Energetic Particle Precipitation Effects on the Electrodynamics of the Coupled Magnetosphere-Ionosphere-Atmosphere

Michael Kokorowski

A dissertation submitted in partial fulfillment of the requirements for the degree of

Doctor of Philosophy

University of Washington

2008

Program Authorized to Offer Degree:
Earth and Space Sciences

University of Washington
Graduate School

This is to certify that I have examined this copy of a doctoral dissertation by

Michael Kokorowski

and have found that it is complete and satisfactory in all respects, and that any and all revisions required by the final examining committee have been made.

Chairs of the Supervisory Committee:

_____
Robert Holzworth

_____
Michael McCarthy

Reading Committee:

_____
Robert Holzworth

_____
Abram Jacobson

_____
Michael McCarthy

Date: _____

In presenting this dissertation in partial fulfillment of the requirements for the doctoral degree at the University of Washington, I agree that the Library shall make its copies freely available for inspection. I further agree that extensive copying of this dissertation is allowable only for scholarly purposes, consistent with "fair use" as prescribed in the U.S. Copyright Law. Requests for copying or reproduction of this dissertation may be referred to Proquest Information and Learning, 300 North Zeeb Road, Ann Arbor, MI 48106-1346, or to the author.

Signature_____

Date_____

University of Washington

Abstract

Energetic Particle Precipitation Effects on the Electrodynamics of the Coupled Magnetosphere-Ionosphere-Atmosphere

Michael Kokorowski

Co-chairs of the Supervisory Committee:
Professor Robert Holzworth
Professor Michael McCarthy
Department of Earth and Space Sciences

In this study, electrodynamic effects on the coupled magnetosphere-ionosphere-atmosphere during energetic particle precipitation events on January 20th and 21st, 2005 are discussed. The largest ground level event (GLE) since 1956 was observed as a result of an extremely hard solar energetic particle (SEP) event on January 20th. Several bursts of relativistic electron precipitation (REP) were observed in conjunction with a sudden storm commencement (SSC) the following day on January 21st. As part of a campaign to study REP events, multiple MINIature Spectrometer (MINIS) balloon payloads were flown in the stratosphere near 32 km altitude from the South African National Antarctic Expedition (SANAE) IV. Onboard instrumentation included an x-ray spectrometer to measure REP bremmstrahlung as well as 3-axis double Langmuir dc electric field probes.

Coincident with SEP event onset on January 20^{th,} a 20-fold increase in the local stratospheric conductivity was measured at MINIS Flight 2 South. Additionally, the total vector electric field vanished at SEP onset. A global, time-dependent conductivity model based, in part, on the Sodankylä Ion Chemistry model, was developed in order to explain the MINIS conductivity observation and describe the effects of SEP precipitation on the larger polar ionosphere and atmosphere. There is good agreement, within the measurement error, between the conductivity model output for the January 20th, 2005 SEP event and the MINIS observations. According to model results, there was a peak enhancement near 45 km that increased the

collisional conductivity 150-fold. Above, 80 km altitude, there was no significant enhancement and also no perturbation to ionospheric potential difference sources due to SEP-ionization. The vanishing horizontal electric fields appear to be related to other physical mechanisms perturbing the ionosphere or SEP-ionization near lower-altitude potential difference sources. The vertical dc electric field decrease is consistent with shorting the global electric circuit (GEC) fair-weather return field.

Bursts of REP x-rays were observed at MINIS balloons in conjunction with two SSC impulses on January 21st, 2005. Coincident with both impulses, simultaneous REP bursts were observed, including the first simultaneous multi-point REP measurements in conjugate hemispheres (with the first impulse). Additional REP bursts were observed that were not coincident with any measured impulse. A correlation study during this two and a half hour bursty period was done comparing the x-ray and horizontal dc electric field observations at the two southern MINIS balloons. There was a moderate, statistically significant correlation between the horizontal electric field observations and only a small statistically significant correlation between x-ray light curve counts at the two payloads (electric field magnitude: $R = 0.68$; x-ray: $R = 0.26$). The general scale size of REP regions was determined to be A) smaller than the scale size of the electric field and B) smaller than the 660 km balloon separation.

TABLE OF CONTENTS

Page

List of Figures v

List of Tables ix

1 Introduction 1

1.1 Broad Research Question: How Does Energetic Particle Precipitation Affect the Coupled Magnetosphere-Ionosphere-Atmosphere? 1
1.2 Motivation: Why Study Energetic Particle Precipitation? 2
1.2.1 Fundamental Geophysics 2
1.2.2 Practical Applications 3
1.3 Coupled Solar Wind-Magnetosphere-Ionosphere System 4
1.3.1 The Dynamic Solar Wind 4
1.3.2 Magnetosphere-Ionosphere Electrical Coupling 5
1.3.3 The Plasmasphere 9
1.3.4 The Radiation Belts 11
1.3.5 Variable Solar Wind Forcing 12
1.4 Solar Energetic Particles 13
1.4.1 SEPs, Solar Flares and Coronal Mass Ejections 13
1.4.2 Dynamic Energetic Proton Motion within the Earth's Magnetosphere 14
1.4.3 Energetic Proton Precipitation in the Polar Caps 16
1.5 Relativistic Electrons 17
1.5.1 Electron Acceleration 17
1.5.2 Precipitation as a Loss Mechanism 19
1.6 Potential Differences in the Collisional Atmosphere 22
1.6.1 Vertical Electric Field and the Global Electric Circuit 22
1.6.2 Horizontal Electric Field Polar Ionosphere 23
1.6.3 Other Potential Sources 24
1.7 Review of Previous Balloon Measurements of Particle Precipitation Events and Associated Electrodynamics 25
1.7.1 Previous Solar Energetic Particle Event Observations 25
1.7.2 Previous Balloon Relativistic Electron Precipitation Event Observations 26
1.8 MINIature Spectrometer (MINIS) Balloon Campaign Overview 28
1.9 Thesis Outline 28

2 Instrumentation for the MINIS Balloon Campaign 31

2.1 MINIS Payload Overview 31
2.2 DC Vector Electric Field Instrumentation 32
2.2.1 Double Langmuir Probe Technique 32
2.2.2 MINIS DC Electric Field Instrument Hardware 36
2.3 Conductivity Measurements Using Relaxation Time Technique 39
2.4 Performance of Electric Field Instrumentation 42

2.4.1 Oscillations in the Vertical DC Electric Field 42
2.4.2 Horizontal DC Electric Field Instrumentation Functioning Properly Before and After Solar Energetic Particle Event Onset 45
2.5 Additional MINIS Balloon Payloads Systems 47
2.5.1 X-Ray Spectrometer 47
2.5.2 Magnetometer 48
2.5.3 Telemetry System 48
2.5.4 Rotation Motor 50
2.5.5 GPS, Housekeeping and Remaining Instruments 51
2.6 Complementary Data Sources 52
2.6.1 ACE Satellite Solar Wind Instrument 52
2.6.2 POES Energetic Proton Detector 52
2.6.3 GOES Particle Detector and Magnetic Field Instrument 53
2.6.4 IMAGE Extreme Ultra-Violet Imager 54
2.6.5 SuperDARN Polar Ionospheric Radars 54
2.6.6 IMAGE Ground-Based Magnetometer Array 54

3 An Atmosphere-Ionosphere Electrical Conductivity Model 56

3.1 Electrical Conductivity within a Plasma 56
3.2 Models of Neutral, Ion and Electron Density Profiles 61
3.2.1 MSISE-90 Neutral Atmosphere Model 62
3.2.2 International Reference Ionosphere Model 63
3.3 Sodankylä Ion Chemistry Model 66
3.4 Full Atmosphere-Ionosphere Electrical Conductivity Model 73
3.5 Additions to the Sodankylä Ion Chemistry Model Particle Precipitation Handling 75
3.5.1 Energetic Protons from Polar Orbiting Satellites 76
3.5.2 Differential Proton Flux Spectra with Estimated Error 87
3.5.3 Adding Relativistic Electron Precipitation Induced Ionization 93

4 Observations During the January 20th, 2005 Solar Energetic Particle Event 104

4.1 Observations of Solar Activity and Energetic Particles from Satellite Instruments 104
4.1.1 Solar Flare and Coronal Mass Ejection Observations 104
4.1.2 Solar Wind Dynamics 107
4.1.3 Energetic Particle Flux Enhancement 112
4.1.4 Geomagnetic Field Fluctuations 118
4.1.5 Cross Polar Cap Potential 120
4.1.6 Summary of Solar Forcing 122
4.2 MINIS Balloon Conductivity and DC Electric Field Observations 122
4.2.1 Direct Observation of Increased Particle Precipitation 122
4.2.2 Large Electrical Conductivity Enhancement and Increased Photoelectric Effect Perturbations 125
4.2.3 Horizontal DC Electric Field Decrease 127

4.2.4 Vertical DC Electric Field Decrease 128
4.2.5 MINIS Flight 2 South Location and Rigidity Cutoff 129

5 Discussion on Effects of January 20th, 2005 Solar Energetic Particle Event ... 132

5.1 SEP-Induced Stratospheric Conductivity Enhancement 132
5.2 Uncertainty in Vertical Electric Field During SEP Event 135
5.2.1 No Accurate Quantitative Description of Dynamic Rigidity Cutoff Motion 136
5.2.2 Conductivity Enhancement Could Account for Vertical DC Electric Field Decrease 138
5.2.3 SEP-Induced Quasi-Static Electric Compared with MINIS Observations 138
5.3 Horizontal Electric Field Decrease 144
5.3.1 Consistent MINIS Observational Environment 145
5.3.2 SEP Ionization Not Responsible for Horizontal Field Decrease 147
5.3.3 Electron Precipitation Not a Likely Source of Conductivity Enhancement 152
5.3.4 Lower-Altitude Source Plausibility 154

6 Relativistic Electron Precipitation and Ionospheric Electrodynamics During the January 21 2005 Storm Sudden Commencement 158

6.1 Solar Wind Impulses on January 21st, 2005 158
6.1.1 Solar Wind Parameters 158
6.1.2 Magnetospheric Compression and Storm Development 162
6.2 MINIS Observations Near Impulse Events 168
6.2.1 Relativistic Electron Precipitation Observations 168
6.2.2 Horizontal DC Electric Field Observations 172
6.2.3 MINIS Field Line Mapping into the Magnetosphere 173

7 Discussion of MINIS Relativistic Electron Precipitation Observations 176

7.1 Correlation Between Horizontal DC Electric Field and REP Observations 176
7.2 Placing Constraints on MINIS-Observed REP Mechanisms 183
7.2.1 Wave-Particle Interactions From a Gyroresoance Perspective 183
7.2.2 Qualitative Usefulness of Horizontal DC Electric Field 188

8 Conclusion and Future Work 192

8.1 A Global Conductivity Model 192
8.2 Effects of the January 20th, 2005 Solar Energetic Particle Event on the Coupled Magnetosphere-Ionosphere-Atmosphere 195
8.3 Relativistic Electron Precipitation and Ionospheric Electrodynamics During the January 21st, 2005 Storm Sudden Commencement 196
8.4 Future Work 198
8.4.1 Particle Precipitation and Energetic Photon Additions to the SIC Model 198

8.4.2 Conductivity Modeling of Multiple SEP Events..... 198
8.4.3 Comparison of Plasmasphere Models with Long-Duration Balloon Horizontal DC Electric Field..... 199
8.4.4 Stratospheric Current Density Fluctuations During an SEP-Induced Vertical DC Electric Field Decrease and Conductivity Increase 200
References 203
Appendix A: MINIS DC Electric Field Instrument..... 217
Appendix B: MINIS Telemetry Allocation..... 220
Appendix C: Model Specifics 222
Appendix D: Electron Ionization Matlab Code..... 223
Appendix E: Electric Field and REP Correlation Study Results..... 230

LIST OF FIGURES

Figure Number Page

Figure 1.3.1 The basic schematic of the magnetosphere. 6
Figure 1.3.2 The classic Dungy cycle..... 6
Figure 1.3.3 Idealized plasma motion and electric field in the polar ionosphere. 7
Figure 1.3.4 Depiction of where the Region 1 and 2 field aligned currents flow into and out of the polar ionosphere. 8
Figure 1.3.5 H^+ number density for several crossings of the plasmapause. 10
Figure 1.4.1 An example Størmer orbit for a single proton with energy of 1.06 GeV. 15
Figure 1.4.2 Rigidity cutoffs determined by a model developed by [*Rodger, et al.*, 2006]. 16
Figure 1.5.1 An example of available phase space transitions for energetic electrons at L = 4.5. 18
Figure 1.5.2 Schematic of the loss cone. 20
Figure 1.7.1 MAXIS x-ray counts on January 24th-25th, 2000..... 27
Figure 2.1.1 Photograph of a southern hemisphere MINIS balloon payload. 32
Figure 2.2.1 Basic design for one set of double Langmuir probes..... 33
Figure 2.2.2. A simplified schematic of the dc potential difference circuit..... 37
Figure 2.2.3 Side view of MINIS payload electric field probes and vertical magnetometer direction..... 38
Figure 2.2.4 Top view of MINIS payload electric field probes, horizontal magnetometer direction and rotation direction..... 38
Figure 2.3.1 An example conductivity measurement. 41
Figure 2.4.1 MINIS Flight 2 South horizontal magnetic and raw vertical electric field. 43
Figure 2.4.2 MINIS Flight 2 South raw vertical electric field and one-minute averaged data. 43
Figure 2.4.3 Raw horizontal electric field data showing instrumentation measurement of slowly-varying geophysical field. 46
Figure 2.5.1 Cartoon of MINIS x-ray spectrometer. 48
Figure 2.5.2 Diagram of the rotation motor assembly..... 50
Figure 3.1.1 Ion and electron cyclotron and collision frequencies as a function of altitude..... 61
Figure 3.2.1 MSISE-90 number density and temperature. 63
Figure 3.2.2 IRI electron density..... 65
Figure 3.2.3 IRI ion and electron density. 65
Figure 3.3.1 GOES 11 integral and differential proton flux at 07:30 UT January 20th, 2005..... 71

Figure 3.3.2 GOES 11 integral and differential proton flux at 09:00 UT January 20th, 2005. 72
Figure 3.4.1 Conductivity profiles based on our new, complete model. 75
Figure 3.5.1 Graphic depiction of POES omni-directional energetic proton detector particle distribution for a solar energetic particle event..... 77
Figure 3.5.2 POES 15 omni-directional energetic proton raw counts for one orbit on January 20th, 2005. 80
Figure 3.5.3 POES 15, 16 and 17 P6 raw counts as a function of L-shell. 80
Figure 3.5.4 POES 15, 16 and 17 raw P9 (>140 MeV) energetic proton counts. 81
Figure 3.5.5 GOES and POES integral and differential proton flux comparison at 07:00 UT January 20th, 2005..... 83
Figure 3.5.6 GOES and POES integral and differential proton flux comparison at 09:30 UT January 20th, 2005..... 84
Figure 3.5.7 GOES and POES integral and differential proton flux comparison at 16:20 UT January 20th, 2005..... 85
Figure 3.5.8 Various GOES and POES particle detector data looking for jump in low-energy channels..... 86
Figure 3.5.9 GOES proton flux calculated from piecewise and nonlinear fits at 09:00 UT..... 88
Figure 3.5.10 GOES proton flux calculated from nonlinear and linear fits at 07:30 UT..... 90
Figure 3.5.11 GOES proton flux calculated from a nonlinear fit at 16:20 UT. 91
Figure 3.5.12 GOES proton flux calculated from a linear fit at 16:20 UT. 92
Figure 3.5.13 Maximum penetration depth for an electron as a function of energy. 94
Figure 3.5.14 Electron stopping power in air. 95
Figure 3.5.15 Ionization due to 100 unidirectional precipitating electrons vertically incident on the upper atmosphere. 97
Figure 3.5.16 Ionization due to 100 precipitating electrons incident on the upper atmosphere isotropically between 0º and 90º off vertical. 97
Figure 3.5.17 Example REP spectrum 102
Figure 3.5.18 Ionization rate profile based on MINIS Flight 2 South observations a 17:12 UT January 20th, 2005. 103
Figure 3.5.19 SIC-calculated ionization rate profiles for SEP (blue) and non-SEP (red) conditions. 103
Figure 4.1.1 GOES 10 x-rays during January 2005..... 105
Figure 4.1.2 SOHO coronagraph images showing the evolution of a CME and an associated SEP event. 106
Figure 4.1.3 SOHO coronagraph taken after the solar flare onset on January 20th, 2005. 107
Figure 4.1.4 Solar wind proton number density measured by ACE during January, 2005. 108
Figure 4.1.5 Solar wind velocity measured by ACE during January 2005..... 110

Figure 4.1.6 Solar wind dynamic pressure measured at ACE in nPa during January 2005. 110
Figure 4.1.7 Interplanetary magnetic field measured at ACE in nT during January 2005. 111
Figure 4.1.8 GOES 10 and 11 integral energetic proton flux during January 2005. 113
Figure 4.1.9 GOES 10 and 11 integral energetic proton flux on January 20th, 2005. 114
Figure 4.1.10 GOES 10 and 11 integral energetic proton flux on January 20th, 2005 with a linear scale. 115
Figure 4.1.11 POES 15, 16 and 17 integral energetic proton flux for the lowest energy channel (> 16 MeV) for L >= 5 during January 2005. 116
Figure 4.1.12 Energetic proton flux data from POES and GOES on January 20th, 2005. 117
Figure 4.1.13 GOES 10 and 12 magnetic field data during January 2005. 119
Figure 4.1.14 GOES 10 and 12 magnetic field data from January 20th, 2005. 119
Figure 4.1.15 SuperDARN cross polar cap potential differences. 121
Figure 4.2.1 MINIS Flight 2 South raw summed light curve counts on January 20th, 2005. 123
Figure 4.2.2 MINIS Flight 2 South x-ray scintillator spectra at 06:35 UT, 06:45 UT and 10:05 UT on January 20th, 2005. 124
Figure 4.2.3 MINIS Flight 2 South conductivity for January 20th, 2005. 125
Figure 4.2.4 MINIS Flight 2 South polar conductivity values for January 19th to January 28th 127
Figure 4.2.5 MINIS Flight 2 South horizontal dc electric field measurements for January 20th, 2005. 128
Figure 4.2.6 MINIS Flight 2 South vertical dc electric field on January 20th, 2005. 129
Figure 4.2.7 POES sub-satellite locations where enhanced energetic proton flux was measured on January 20th, 2005. 130
Figure 4.2.8 POES 17 Omni-directional proton flux near MINIS Flight 2 South. 131
Figure 5.1.1 Conductivity observations from MINIS Flight 2 South and modeled conductivity. 133
Figure 5.1.2 Multiplicative change in modeled parallel conductivity on January 20th, 2005. 134
Figure 5.2.1 Modeled SEP density source example. 140
Figure 5.2.2 Modeled quasi-static vertical electric field caused by SEP charge deposition. 142
Figure 5.2.3 Cartoon of maximum SEP-induced electric field. 143
Figure 5.3.1 Sym-H index for January 20-21, 2005. 146
Figure 5.3.2 IMAGE Magnetometer chain data from stations at the same L-shell as MINIS Flight 2 South on January 20th, 2005. 148
Figure 5.3.3 Modeled parallel, Pedersen and Hall conductivity profiles. 149
Figure 5.3.4 Change in modeled Hall conductivity on January 20th 2005. 150

Figure 5.3.5 Change in modeled Pedersen conductivity on January 20th 2005. 151
Figure 5.3.6 FAST electron flux..... 152
Figure 5.3.7 FAST electron flux..... 153
Figure 5.3.8 Lower-altitude potential difference mapping equivalent circuit..... 156
Figure 6.1.1 ACE solar wind density during January 2005. 159
Figure 6.1.2 ACE solar wind velocity in January 2005. 160
Figure 6.1.3 ACE solar wind dynamic pressure for three hours after 16:30 UT January 21st, 2005. 161
Figure 6.1.4 ACE IMF in January 2005..... 161
Figure 6.1.5 GOES magnetic field data for three hours after 16:30 UT January 21st, 2005. 163
Figure 6.1.6 GOES parallel magnetic field data for three hours after 16:30 UT January 21st, 2005. 163
Figure 6.1.7 Modeled magnetopause with GOES locations. 164
Figure 6.1.8 GOES 10 and 12 >2 MeV electron flux. 166
Figure 6.1.9 Sym-H index during January 2005. 167
Figure 6.2.1 MINIS high time-resolution x-ray counts from three different balloons. 169
Figure 6.2.2 MINIS observed x-ray spectra for Flight 1 North, Flight 2 South and Flight 3 South between 17:10 UT and 17:50 UT on January 21st, 2005. ... 170
Figure 6.2.3 Horizontal dc electric field observations from MINIS Flight 2 South (blue) and Flight 3 South (red). 172
Figure 6.2.4 IMAGE EUV plasmasphere picture taken just before the first compression event. 174
Figure 7.1.1 MINIS light curve and horizontal electric field comparisons. 179
Figure 7.1.2 MINIS light curve and horizontal electric field magnitude and angle comparison. 180
Figure 7.2.1 α^* as a function of L-shell on the magnetic equator assuming a dipole magnetic field for various plasma number densities. 187
Figure 7.2.2 Regions of the magnetosphere where chorus, hiss and EMIC waves are expected to exist for various conditions. 189
Figure 7.2.3 MINIS light curve and electric field data comparison with outward and inward bulk plasma motion highlighted. 190
Figure 8.4.1 Vertical current density at MINIS Flight 2 South on January 20th, 2005. 202

LIST OF TABLES

Table Number Page

Table 1-1 Properties of the outer radiation belt and the plasmasphere. [From *Prölss*, 2004]..... 12
Table 1-2 Summary mechanisms thought to be responsible for REP. 21
Table 3-1 Integral proton flux for a completely isotropic distribution and for an SEP distribution with θ SEP = 75° [*from Evans and Greer,* 2000]. 78
Table 4-1 Summary of notable solar wind fluctuations on January 20th 113
Table 5-1 Vertical electric field magnitude for various characteristic relaxation times..... 145
Table 6-1 Calculated incident REP spectra parameters for Flight 2 South and Flight 3 South between 17:12 UT and 18:55 UT.. 173
Table 7-1 Parameters used in horizontal electric field and x-ray light curve correlation study... 181
Table 7-2 Correlation coefficients for horizontal dc electric field and x-ray light curve observations.... 184
Table 7-3 Summary of general wave characteristics for likely responsible for REP.... 187
Table B-1 MINIS telemetry allocation table..... 223
Table E-1 Full correlation study results between 17:00 UT and 19:30 UT on January 21st, 2005. 243
Table E-1 Full correlation study results between 17:12 UT and 17:27 UT on January 21st, 2005. 244
Table E-1 Full correlation study results between 18:45 UT and 19:00 UT on January 21st, 2005. 245
Table E-1 Full correlation study results between 17:00 UT and 19:30 UT on January 21st, 2005, omitting the impulse events..... 246

ACKNOWLEDGMENTS

I would like to take this opportunity to thank some of the many people who have helped me during the past few years. I would especially like to thank my advisors, Prof. Robert Holzworth and Prof. Michael McCarthy. From the big picture to the tiniest of details, they have taught me so much that I cannot begin to list it all here. Thanks to Prof. Abram Jacobson for helping to make my thesis more comprehendible to "non-tribal members." Thank you to Prof. Robert Winglee who, amoung other things, helped me get my job at JPL. Thanks also to Prof. Erika Harnett, Prof. Walt Harris and John Chin who have each given of their time for my benefit. I would like to give a special thanks to all of the ESS graduate students who have shared their lives with me over the past six years: Jeremy Thomas, Erin Lay, Carol Paty, Ruth O'Connor, Ariah Kidder, Olivia Dawson, Michele Cash, Darci Snowden, Michael Shimogawa, Jim Prager, Race Roberson, Toby Neef and Louis Giersch. Without their comradarie, encouragement, helpful ears and numerous coffee breaks, I never would have been able to finish. Thanks to all of the MINIS team members for producing such a successful project. Thanks to all of the folks at SANAE IV who helped with the balloon launching and also made the 43-44 takeover season so memorable. I would like to give a special thanks to John Sample who spent two seasons with me in Antarctica. I will forever be indebted to him for all of his hard work, and I will always remember the adventures we had. Thank you to all of my extended family who made me feel at home in Seattle. Thank you to all the friends I made here in Seattle, especially Joe, Harrison, George, Claire, Kaori and Gwynne. You were the ones who made Seattle the place I wanted to be. Thank you to my immediate family, who despite great distances, always kept me close to their hearts and minds. Lastly, thank you to my dear wife, Heather. You are everything I could ever have asked for and more.

Over the years, I have been supported by NSF grants (ANT-0230441, ATM-0408356 and ATM-0649489), the Joe Vance research assistantship and several teachings assistantships through the Earth and Space Science Department.

1 Introduction

1.1 Broad Research Question: How Does Energetic Particle Precipitation Affect the Coupled Magnetosphere-Ionosphere-Atmosphere?

Energetic particle precipitation causes a wide range of effects on the near-earth electrical environment. This thesis deals with multiple topics that are directly related to precipitation and its resultant electrodynamic effects. By particle precipitation, we literally mean the "raining down" of charged particles, mainly electrons and protons. The most well known example of particle precipitation is the visible aurora caused by comparatively low energy electrons. In this dissertation, we focus on more energetic particles, which influence the near-earth system differently than visible aurora. Specifically, we focus on solar energetic protons and relativistic electrons. The "near-earth electrical system" refers to the electrical circuit that couples the collisional atmosphere, the ionosphere and the magnetosphere. These regions form a connected circuit through which current can flow. We utilize experimental data from satellites, ground-based instrumentation and the primary MINIature Spectrometer (MINIS) Balloon Campaign to explore effects of energetic particle precipitation. Additionally, we use theoretical modeling techniques from several well-established models as well as the Sodankylä Ion Chemistry (SIC) model. The SIC model has been successfully applied to atmospheric chemistry, but has only recently begun to be applied to atmospheric electrodynamics and space physics.

With this combination of experimental and theoretical work, all of our particular research goals fall under a fundamental overarching question: how does energetic particle precipitation affect the coupled magnetosphere-ionosphere-atmosphere? Within this theme, we explore: A) the function of experimental instrumentation used to collect data; B) new techniques for theoretical conductivity modeling; and C) direct precipitation effects on specific elements of this coupled circuit.

The MINIS campaign made electric field observations on January 20th, 2005, during the hardest solar energetic particle (SEP) event in more than 50 years. The total dc electric field vanished coincidently with the SEP event onset, which has never been observed before. One day later, multiple MINIS balloons observed x-rays from simultaneous MeV relativistic electron precipitation (REP) events as well as associated dc electric fields. Never before has there been multi-point simultaneous REP observations in opposite hemispheres. There is evidence for perturbed vertical dc electric field and x-ray data during the SEP event on January 20th, 2005. We have developed a time-dependent conductivity model, which can include the effects of SEP-induced ionization in the ionosphere and collisional atmosphere. Combining our MINIS electric field data, satellite electron flux data and our new conductivity model, we find that SEP proton precipitation cannot account for the observed horizontal dc electric field decrease, assuming it was caused by increased ionospheric conductivity. We determine that there is only a small statistically significant correlation between REP x-ray observations at the two southern MINIS balloons (separated by 660 km in the afternoon of January 21st) and a moderate horizontal dc electric field correlation. We show that there is no one-to-one connection between REP and electric field magnitude and direction. However, we assert that horizontal dc electric field data are useful in helping to constrain possible precipitation mechanisms.

1.2 Motivation: Why Study Energetic Particle Precipitation?

1.2.1 Fundamental Geophysics

In this thesis, we focus on two distinct types of energetic particles: A) solar energetic particles (SEPs); and B) relativistic electrons. We address a set of fundamental geophysics questions for each type as outlined below.

A) Solar Energetic Particles:

1) Why does the local conductivity increase in the polar stratosphere coincidently with an SEP event onset? What physical mechanisms are responsible? How does the conductivity change at other altitudes? How would altered conductivity affect the larger coupled atmosphere-ionosphere-magnetosphere circuit?

2) Do SEP events alter the current density in the polar caps? What implications might this have for the larger global electric circuit?

B) Relativistic Electrons:

1) What are the temporal and spatial scale sizes of REP events? Are magnetospheric electric fields responsible for moving trapped radiation belt electrons to spatial regions where precipitation occurs?

2) Do REP events cause enhancements in ionospheric conductivity, which then have an effect on the larger coupled circuit?

3) What mechanisms are responsible for REP?

1.2.2 Practical Applications

Aside from fundamental geophysical reasons for studying energetic particle precipitation, there are several similarly compelling and practical reasons for understanding both SEP and REP events. SEP events have been observed to cause polar cap absorption (PCA), during which high-frequency radio waves that normally propagate through the ionosphere become absorbed [*Bailey*, 1964]. This can cause communication outages, especially in isolated polar regions. Specifically, GPS signals and airplane avionics can suffer from outages [*Jones et al.*, 2005]. Any time a large amount of energy is placed into the atmosphere, the chemistry can be affected. SEP events have been shown to cause

fluctuations in ozone and NO_x as well as many other chemical species [*Jackman et al.*, 2005a; *Jackman et al.*, 2005b; *Verronen et al.*, 2005; *Seppälä et al.*, 2006]. SEPs have also been pointed to as the cause of satellite malfunctions and data anomalies [*Iucci et al.*, 2006]. Similarly, relativistic electrons also affect atmospheric chemistry and spacecraft in earth orbit. Unlike solar energetic protons, energetic radiation belt electrons can remain stably trapped for long periods of time, making them a near-constant concern. Relativistic electrons have gained the nickname "killer electrons" because of their ability to cause both hard and soft errors in satellite electronics [*Frederickson et al.*, 1992; *Wrenn*, 1995; *Balcewicz et al.*, 1998]. Effects of REP on atmospheric chemistry include, but are not limited to, winter ozone fluctuations [*Seppälä et al.*, 2007; *Wissing et al.*, 2008]. Both SEP and REP events are important in understanding the natural variability of atmospheric chemical constituents important for current global climate modeling efforts [*Randall et al.*, 2007].

1.3 Coupled Solar Wind-Magnetosphere-Ionosphere System

The solar wind, magnetosphere and ionosphere are coupled through currents and force balances. In this section, we briefly present an overview of the solar wind and the classical picture of bulk plasma motion in the magnetosphere, focusing on the innermost sections. We then connect the magnetosphere to the inner boundary, the ionosphere. Finally, we describe basic solar wind forcing mechanisms to provide a geomagnetic context for energetic particle precipitation measurements and discussions within this thesis.

1.3.1 The Dynamic Solar Wind

The solar wind is a constant, yet dynamic, stream of particles with an imbedded magnetic field that flows from the solar corona. The charged particles are primarily electrons and protons with a few percent of helium ions. The sun's magnetic field, as it permeates the solar system, is called the interplanetary magnetic field (IMF). Charged particles are often trapped on magnetic field lines due to the Lorentz force,

$$\vec{F} = q(\vec{E} + \vec{u} \times \vec{B}). \quad \textbf{(1-1)}$$

Here, $\vec{F}$ is the force on a particle with charge q moving with a velocity $\vec{u}$ in the presence of an electric field $\vec{E}$ and magnetic field $\vec{B}$. At the earth, the solar wind density is often between 3-20 particles cm^{-3} and the velocity ranges between 300 – 900 km s^{-1}. The IMF has a dynamic orientation and often ranges in magnitude between 1 - 30 nT. Of course, all of these values vary on times scales ranging from minutes to years. Extreme events will lead to solar wind properties that are beyond the nominal ranges stated above.

1.3.2 Magnetosphere-Ionosphere Electrical Coupling

The coupled magnetosphere-ionosphere is a complex system connected through electric and magnetic fields as well as flowing currents. Figure 1.3.1 shows a typical overview picture of the magnetosphere in which many boundaries, currents and plasma regions are shown. Solar wind particles and magnetic field, represented on the left-hand-side by a set of arrows, are the dominant external drivers for the system. The ionosphere is the inner conducting boundary that separates the earth from the magnetosphere. We discuss electrical coupling by summarizing how bulk magnetospheric plasma motion supports currents that flow through the ionosphere as well as large-scale ionospheric electric fields.

Figure 1.3.2 shows a noon-midnight meridian schematic of the Dungey cycle, an idealized description of plasma motion in the magnetosphere during times of southward IMF known as magnetospheric convection [*Dungey*, 1961]. A similar but slightly more complicated picture can be drawn for instances of northward IMF. The dark arrows indicate the motion of plasma and imbedded magnetic field. The anti-sunward plasma motion over the polar caps and outside the magnetosphere is a direct result of the flowing solar wind. Inside the magnetosphere, the cold bulk plasma moves sunward. From Equation (1-1), there is no magnetic force acting on charged particles moving along magnetic field lines. Therefore, magnetic field lines are excellent conductors that can often be considered equipotentials. Magnetospheric convection described by the Dungey cycle

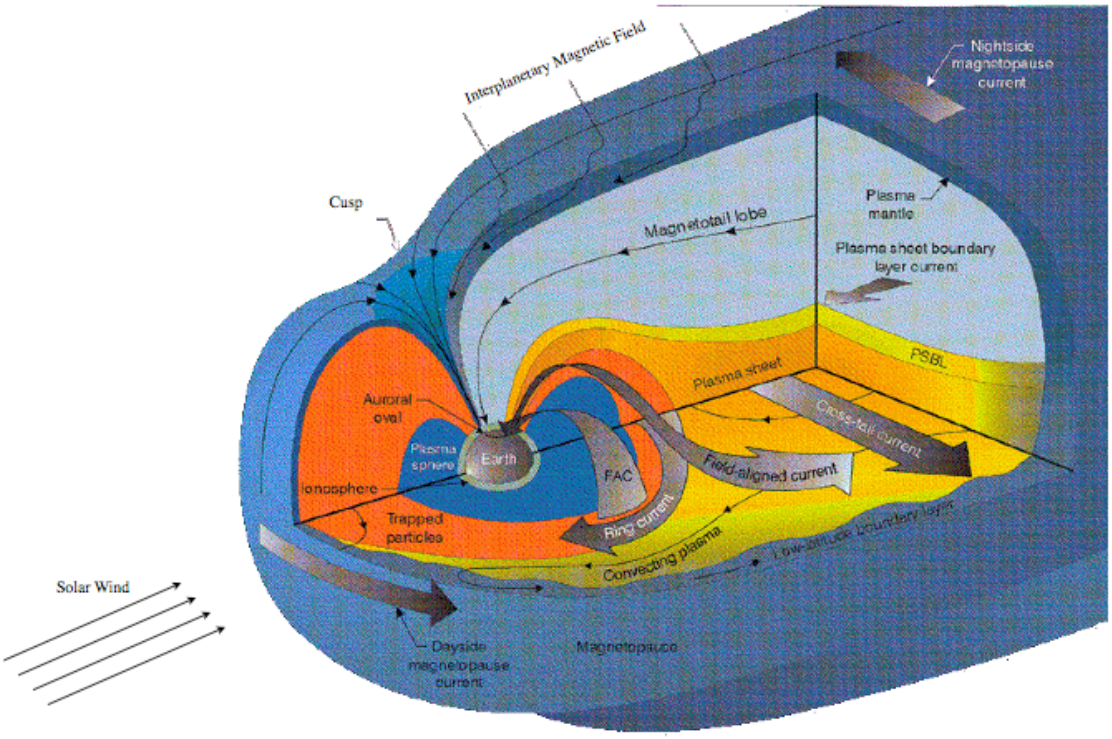

Figure 1.3.1 The basic schematic of the magnetosphere. We focus on the field-aligned currents (FACs), plasmasphere and the trapped radiation belt particles. [Adapted from *Parks*, 1991]

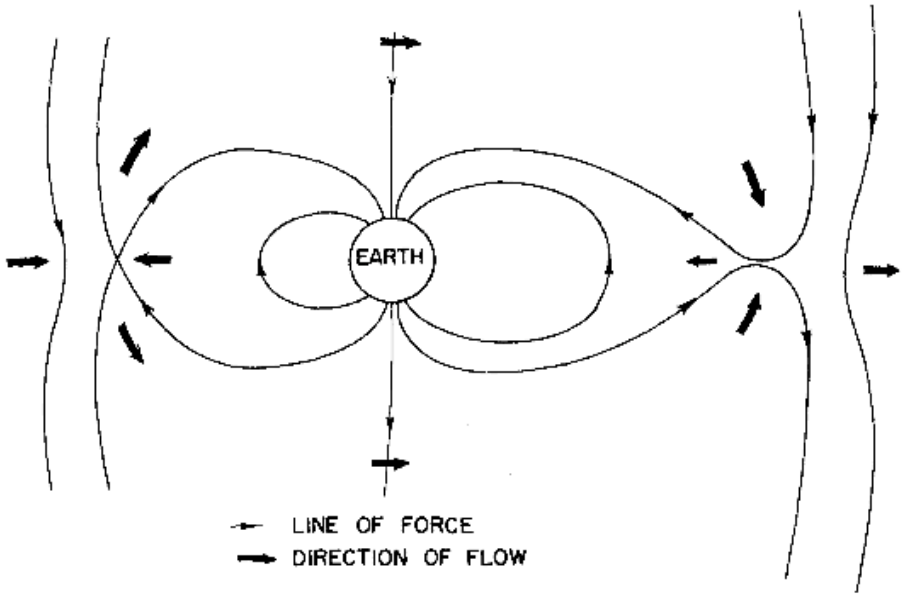

Figure 1.3.2 The classic Dungy cycle. The large arrows depict bulk plasma motion in the magnetosphere for southward IMF. [Adapted from *Dungey*, 1961]

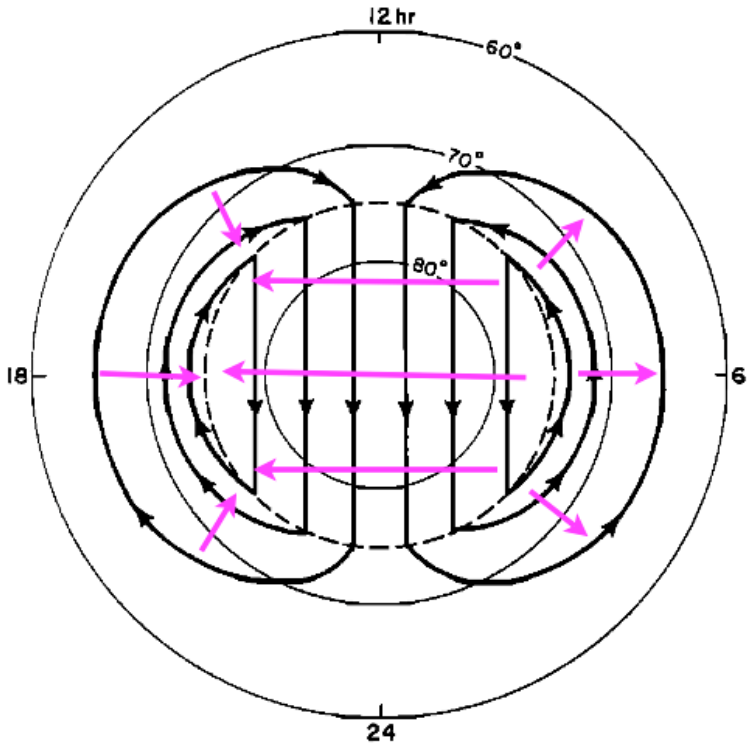

Figure 1.3.3 Idealized plasma motion and electric field in the polar ionosphere. The black contours represent the bulk plasma motion and lines of equipotential. The pink arrows show large-scale electric field vectors. [Adapted from *Spiro et al.,* 1978].

can be projected along conducting magnetic field lines into the polar ionosphere. Figure 1.3.3 shows an idealized example of magnetospheric convection mapped into the ionosphere. The black arrows show the bulk plasma motion in two convection cells and pink arrows show electric field vectors. The black flow contours can also be considered equipotentials because the principle driver of this motion is $\vec{E} \times \vec{B}$ drift. $\vec{E} \times \vec{B}$ drift velocity is orthogonal to the electric and magnetic field vectors and is given by the following equation:

$$\vec{u}_{E\times B} = \frac{\vec{E} \times \vec{B}}{B^2}. \qquad \textbf{(1-2)}$$

Additional drifts that are not represented in the idealized case of Figure 1.3.3 include magnetic field curvature and gradient drifts. Curvature and gradient drift velocities are given by the following equations:

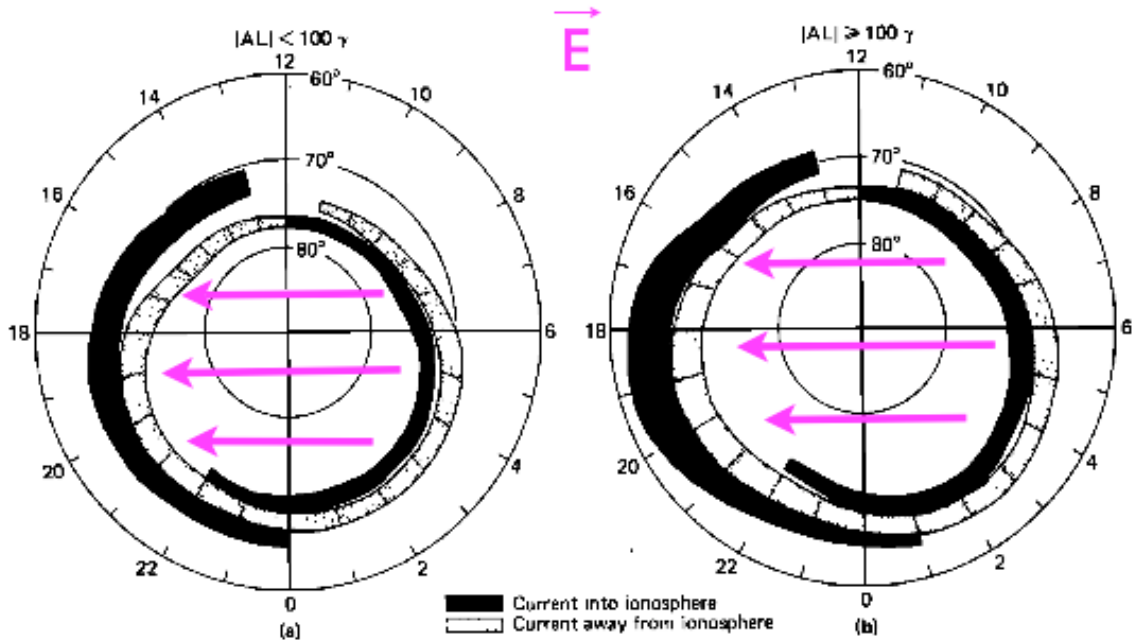

Figure 1.3.4 Depiction of where the Region 1 and 2 field aligned currents flow into and out of the polar ionosphere. The pink arrows show where the currents close in the ionosphere. [Adapted from *Iijima and Potemra*, 1978.]

$$\vec{u}_c = \frac{mv_{\parallel}^2}{qB^4}\left(\vec{B}\times\nabla B/2\right) \tag{1-3}$$

$$\vec{u}_{\nabla B} = \frac{mv_{\perp}^2}{2qB^4}\left(\vec{B}\times\nabla B/2\right) \tag{1-4}$$

Here, m is the mass of the charged particle, q is the particle charge and $v_{\perp}$ and $v_{\parallel}$ are the perpendicular and parallel components of the particle velocity with respect to the magnetic field direction. These additional drift terms preferentially affect more energetic charged particles near the earth where ∇B can become large.

The large-scale electric fields shown in Figure 1.3.3 also support currents that flow from the magnetosphere into the ionosphere (and back out again). A representation of the ionospheric footprint of these currents, called Field-Aligned Currents (FACs), is shown in Figure 1.3.4 from *Iijima and Potemra* [1978]. The spatial distribution of polar FACs as they flow into the ionosphere for geomagnetically quiet (a) and active (b) periods are

shown. The solid and light contours show where current flows into and away from the ionosphere, respectively. The pink arrows are some of the same large-scale electric fields as shown in Figure 1.3.3. Once current flows into the ionosphere, the electric field drives the current through the conducting medium of the ionosphere according to Ohm's law,

$$\vec{J} = \ddot{\sigma}\vec{E}. \tag{1-5}$$

Here, $\vec{J}$ is the current density and $\ddot{\sigma}$ is the tenser conductivity.

All of the parameters that describe the magnetosphere and ionosphere have some role to play when identifying the coupling between the two regions. From the summary above, we see that large-scale potential differences in the ionosphere are directly linked to the currents flowing through the magnetosphere-ionosphere as well as the bulk motion of magnetospheric plasma.

1.3.3 The Plasmasphere

The cold, dense region of plasma that corotates with the earth is called the plasmasphere. The plasmasphere occupies a doughnut-shaped region which extends from the earth up to ~5 earth radii at the equator. A useful parameter for describing particle dynamics in the magnetosphere, especially energetic particle orbits, is the McIlwain L parameter. This parameter defines the magnetic field shell, which crosses the equatorial magnetosphere at a given distance [*McIlwain*, 1961]. For a dipole field, L is given in *Parks* [1991] by the following expression:

$$L = \left(\frac{\mu_0 M}{4\pi B_0} \right)^{\frac{1}{3}}. \tag{1-6}$$

M is the dipole magnetic moment, μ_0 is the magnetic permeability of free space and B_0 is the equatorial dipole field strength. This approximation is valid for the inner magnetosphere during most geomagnetic conditions. However, like most of the magnetosphere, the extent of the plasmasphere varies dramatically. The outer edge of the

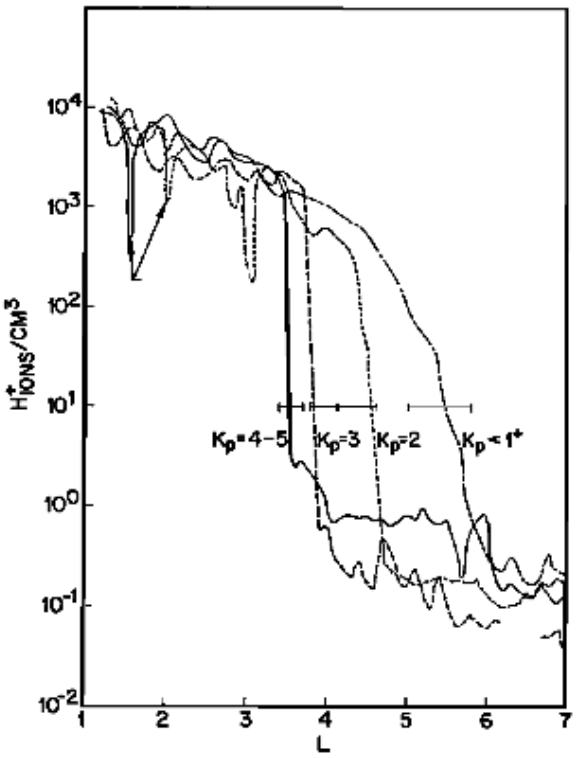

Figure 1.3.5 H^+ number density for several crossings of the plasmapause. [Adapted from *Chappell et al.*, 1970.]

plasmasphere has been observed to vary with geomagnetic activity. Figure 1.3.5 shows plasma number density as a function of L-shell. The density drops sharply at the edge of the plasmasphere, which is called the plasmapause. Magnetic activity is gauged by the Kp index, which ranges from extreme geomagnetic quiet (0-1) to active (9). Kp is calculated by measuring the deviation from quiet conditions in ground-based magnetometers. This means that there will often be a plasmaspheric bulge on the dusk side where sunward convection stagnates.

During times of enhanced geomagnetic activity, the equipotentials near the earth essentially compress, changing the plasmapause boundary. The plasmasphere shrinks when the convection electric field dominates over the corotation field, and the formerly trapped plasmasphere particles convect sunward. This convecting plasma is called a plasmaspheric plume. A review by *Goldstein and Sandel* [2005a] describes the current

state of our understanding of plasmaspheric dynamics associated with plume formation and erosion. Of particular interest, *Goldstein et al.* [2005] showed that there is a direct relationship between the plasmapause and the inner edge of outer radiation belt. Table 1-1 gives characteristic parameter values for the plasmasphere and outer radiation belt.

1.3.4 The Radiation Belts

Stably trapped energetic particles in the magnetosphere form the radiation belts. Due to the Lorentz force, charged particles are free to easily move along magnetic field lines. In the presence of an additional external force, particles can guiding center drift perpendicularly to the magnetic field as well. Bounce motion is an additional type of motion that keeps the energetic particles stably trapped as they move along the magnetic field line toward the earth (and not necessarily continue into the atmosphere). Bounce motion is a result of conservation of magnetic moment in converging (and diverging) magnetic field structures. The force is given by

$$\vec{F}_{\parallel} = -\mu \nabla_{\parallel} B; \qquad \mu = \frac{1}{2}\frac{m v_{\perp}^2}{B}. \tag{1-7}$$

Here, μ is the magnetic moment, B is the magnetic field and $v_{\perp}$ is the velocity component perpendicular to the magnetic field. The force is anti-parallel to the magnetic field convergence and is proportional to the magnetic moment and the gradient of the magnetic field. The force always acts on the particle and can eventually cause the particle to bounce or mirror. In essence, the diverging/converging magnetic field lines form a magnetic bottle that traps the energetic particles. Energy is conserved during bounce motion such that the velocity vector keeps a constant magnitude ($\left(v_{\perp}^2 + v_{\parallel}^2\right) = const.$) even though the individual velocity components themselves change.

There are two sections of the radiation belt called the inner and outer belts. The inner belt extends to about L = 2.5 and is composed of very energetic (> 30 MeV) protons created by a process called cosmic ray albedo neutron decay (CRAND). Inner belt dynamics are

Table 1-1 Properties of the outer radiation belt and the plasmasphere. [From *Prölss*, 2004]

	Particle Population	
	Outer Radiation Belt	Plasmasphere
Energy — Ions	1 - 200 keV	< 1 eV (~5000 K)
Energy — Electrons	< 10 keV	
L shell	$3 < L < 6$	$1.2 < L < 5$
Field Line Footprints	middle and higher latitudes	low and middle latitudes
Particle Density/Flux	$< 10^6$ m^{-3}	$> 10^8$ m^{-3}
Composition	H^+, O^+, He^+, e^-	H^+, e^-
Particle Motion	gyration bouncing drift	gyration corotation
Source Region	plasma sheet, ionosphere	ionosphere
Formation Process	particle transport & acceleration	charge exchange & transport
Loss Process	charge exchange, pitch angle diffusion into loss cone	transport & charge exchange, convection

beyond the scope of this dissertation. We focus only on processes involving the outer belt. The outer belt ranges from approximately L = 3 to L = 6. There is a slot between the two radiation belt regions which is principally a result of atmospheric precipitation driven by coulomb collisions, plasmaspheric hiss, lightning-generated whistlers and man-made VLF transmissions [*Clilverd et al.*, 2008]. We discuss specifics of outer belt sources and sinks in subsequent sections. Table 1-1 summarizes some outer belt properties.

1.3.5 Variable Solar Wind Forcing

As mentioned previously, activity levels in the magnetosphere may be "quiet" or "active." Here we briefly describe what we mean by these terms and describe the basic changes in the magnetosphere between quiet and active periods. The main driver of geomagnetic activity is the variable solar wind, particularly, the *z*-component of the solar wind IMF (the north-south component). As we shown in Figure 1.3.2, the plasma motion in the magnetosphere begins when the IMF turns southward. This allows for an "open" magnetosphere, where the IMF and geomagnetic field are aligned over the polar

caps and anti-aligned at the sub-solar dayside. Since charged particles can easily move along magnetic field lines, and open magnetosphere allows for large amounts of streaming solar wind particles to enter the magnetosphere over the polar caps and in the magnetotail. Thus, the entire plasma motion becomes enhanced or "active." More plasma convects earthward from the tail. During active times with sustained periods of Southward IMF, the large-scale potential differences across the polar ionosphere can reach 250 kV or more. Conversely, during quiet times, the same large-scale potential difference drops to near 20 kV [*Wygant et al.,* 1983].

1.4 Solar Energetic Particles

In this section, we describe solar energetic particles (SEPs) and briefly present their acceleration mechanism, motion within the earth's magnetosphere and finally precipitation into the polar caps.

1.4.1 SEPs, Solar Flares and Coronal Mass Ejections

SEPs are very energetic ions and electrons with energies between 1 -1000 MeV and beyond. They are created in conjunction with solar flares and coronal mass ejections (CMEs). Thus, SEP events are intermittent, unlike the constantly flowing solar wind. SEP events were first observed as enhancements of ground-based ion chamber counts coincident with solar flares in 1942 before CMEs were known to exist [*Forbush*, 1946]. Solar flares are sudden brightening of small regions of the solar surface, which last for minutes to hours. Flares are often emitted from long-lived sunspots, visibly dark regions of intense magnetic field on the sun's surface. The coincidence of solar flares and SEP events was the primary reason that the solar flares were thought to cause charged particle acceleration. Type III radio bursts can be directly tied to 10-100 keV electrons streaming out of the solar corona during solar flares [*Wild et al.*, 1963]. However, type II radio bursts are connected to a shock wave moving through the solar system, not part of the solar flare. This suggests that not all particle acceleration occurs at the sun's surface in conjunction with the solar flare itself [*Wild et al.*, 1963]. After CMEs were discovered, a

strong correlation between large, energetic SEP proton events and CMEs (96%) was found [*Kahler et al.*, 1984]. Currently, it is believed that SEPs are generated at the solar surface, but the more energetic protons are accelerated in CME shocks. The specific acceleration mechanisms are not universally accepted. A review by *Reames* [1999] states that there are two identified mechanisms that dominate very energetic particle populations:

> 1) Stochastic acceleration, involving resonant wave-particle interactions that transfer energy from waves to particles. This occurs in regions of high magnetic field, low-β plasma with high Alfvén speeds, notably the terrestrial aurorae and solar flares.
>
> 2) Shock acceleration that occurs in relatively high-β plasma, including planetary bow shocks, CME-driven shocks, CIR shocks, the heliospheric termination shock, and even supernova shocks. [*Reames*, 1999; p 474.]

These mechanisms are not specific to SEP events, but both types apply to SEP acceleration processes.

1.4.2 Dynamic Energetic Proton Motion within the Earth's Magnetosphere

SEP protons, although very energetic, are still loosely bound to the IMF. The gyroradius of a 100 MeV proton in a 10 nT magnetic field is approximately 5 earth radii (R_e). Thus, SEP protons can stream "along" magnetic field lines toward earth. However, once they reach earth, the SEP distribution is nearly isotropic and not directional like the solar wind. Therefore, we say the SEPs are loosely bound to the IMF. At earth, the magnetosphere is not much larger than the SEP proton gyroradius in interplanetary space. At the edge of the magnetosphere, the geomagnetic field is the same order of magnitude as the IMF. However, the earth's dipole magnetic field falls off as $1/r^3$, making the field strength near earth much larger. The gyroradius of the same 100 MeV proton at 3 R_e in the magnetic equator is about 20 km. SEP protons cannot penetrate straight through the equatorial magnetosphere. They can, however, easily enter along the magnetic lines of force to the polar regions. Thus, due to the dipole-like magnetic geometry, all SEP protons that enter

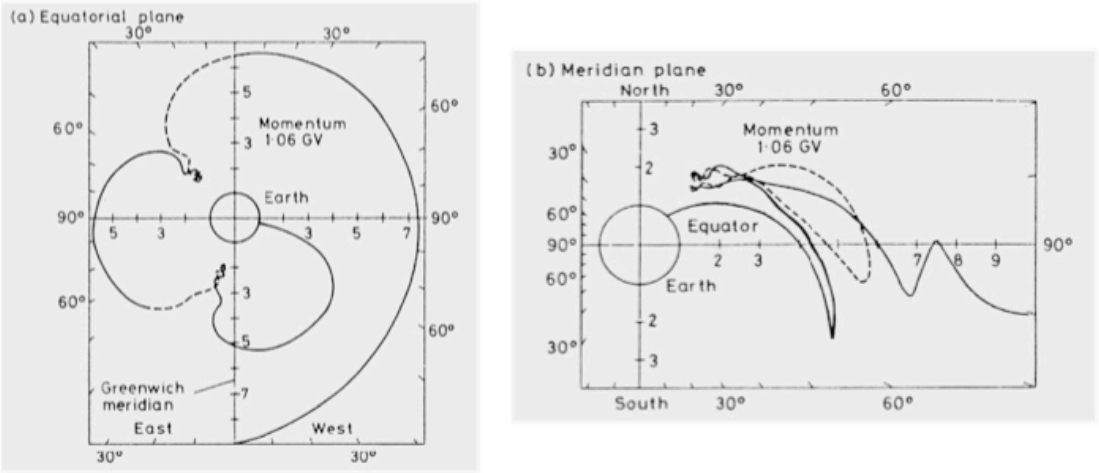

Figure 1.4.1 An example Størmer orbit for a single proton with energy of 1.06 GeV. [From *Hargreaves*, 1992 after *McCracken*, 1962.]

the magnetosphere will either ultimately leave the system or precipitate into the polar regions. The paths the SEPs take are called Størmer orbits. SEP electrons, on the other hand, do not undergo the same kind of motions that SEP protons do because they are more tightly bound to magnetic field lines. For example, a 10 MeV electron would have a 20 km gyroradius at 10 R_e. This electron would not penetrate nearly as deep into the magnetosphere and would not undergo the same Størmer orbits as a heavier proton [*Vampola*, 1969]. Figure 1.4.1 shows one particular Størmer orbit for a 1.06 GeV proton. Protons with more energy have the ability to precipitate closer to the equator than those with less energy. A useful quantity used to discuss the region where a particular particle can precipitate is called rigidity, and is defined as

$$R = \frac{Pc}{ze}, \qquad \textbf{(1-8)}$$

where P is the particle momentum, c is the speed of light, z is the atomic number and e is a positive unit charge. Contours that roughly trace lines of magnetic latitude define rigidity cutoffs. Depending on a particle's individual rigidity, it has the possibility to precipitate anywhere pole-ward of its rigidity cutoff. *Hargreaves* [1992] describes rigidity cutoffs as a function of magnetic latitude of a dipole, λ_m.

$$R_c = 1.49 \times 10^4 \cos^4 \lambda_m \qquad \textbf{(1-9)}$$

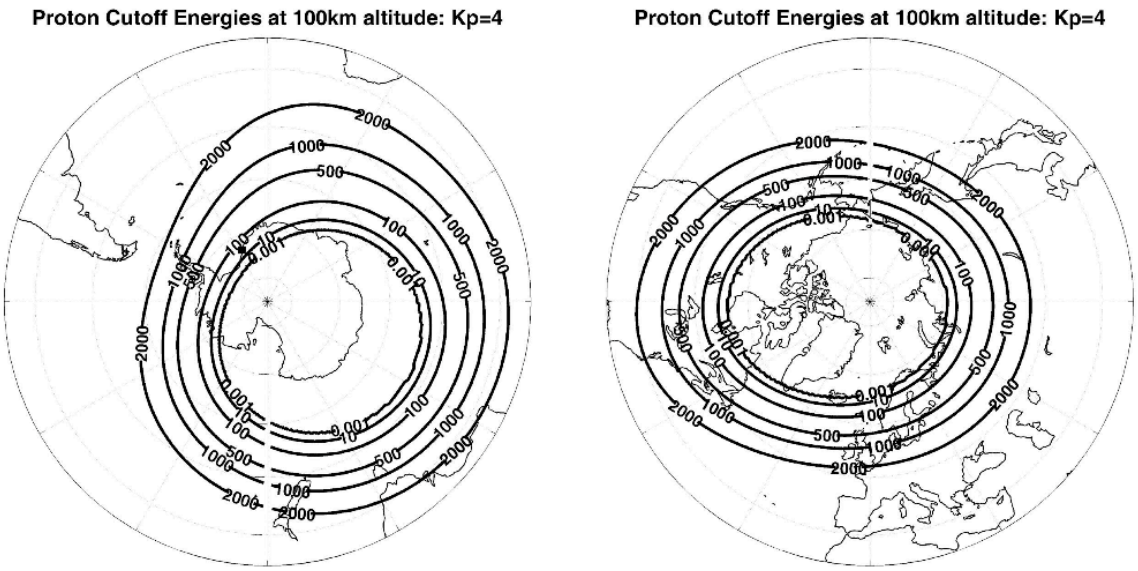

Figure 1.4.2 Rigidity cutoffs determined by a model developed by [*Rodger, et al.*, 2006]. Particles with rigidities labeled on the contours can precipitate anywhere poleward of the cutoffs.

In practice, rigidity cutoffs are not easy to predict for a particular SEP event. This is because SEP particles move through a large part of the magnetosphere and are subject to deviations from an ideal dipole at every moment. Very accurate models of the entire dynamic magnetosphere are required for predictions. One such rigidity model does exist [*Smart and Shea*, 2001]. Additionally, *Rodger et al.* [2006] have developed another model, which also predicts rigidity cutoff values and uses Kp as a proxy for geomagnetic perturbation. Figure 1.4.2 shows several rigidity cutoffs plotted over the northern and southern polar regions for moderate geomagnetic activity (Kp = 4).

1.4.3 Energetic Proton Precipitation in the Polar Caps

Once SEP protons get funneled into the polar cap regions, many precipitate into the atmosphere. Essentially all of the incident SEP energy is lost to collisions with neutrals. When a single proton precipitates, it leaves a trail of ionization behind it. During an SEP event, where large fluxes ($> 10^3$ protons cm^{-2} s^{-1} str^{-1}) of > 1 MeV protons precipitate for multiple hours, enhanced ionization can be significant. Assuming a constant 10^2 (protons cm^{-2} s^{-1} str^{-1}) flux of 10 MeV protons lasting for three hours covering the entire polar cap, $\sim 10^{12}$ joules of energy will be deposited into the atmosphere of each polar region. In

Chapter 3, we discuss in more detail how this ionization affects atmosphere-ionosphere conductivity. Ionization enhancement in the D-region can cause the absorption and reflection of electromagnetic signals, which can normally travel through the ionosphere. Numerous studies have correlated SEP events and radio absorption [e.g., *Stoker*, 1995; *Patterson et al.*, 2001; *Kavanagh et al.*, 2004]. We discuss observations of dc electric field during SEP events in Chapter 4 and Chapter 5. Each SEP event has different incident SEP spectra, duration and rise time. Additionally, the geomagnetic activity is not the same for each event. Therefore, the effects from each SEP events can be quite different.

1.5 Relativistic Electrons

In this section we discuss energetic electrons (> 100 keV), which populate the outer radiation belt. Although relativistic electrons can be stably trapped in the radiation belt for long periods of time, flux rates are extremely dynamic especially during geomagnetically active periods. *Reeves et al.* [2003] showed that magnetic storms have a 50% chance of increasing the net energetic electron flux in the outer radiation belt and 25% chance to reduce the flux or have no net affect at all. Since this result cannot be easily explained, the balance between storm-induced energetic electron source and loss mechanisms is currently ambiguous. Understanding their source and loss mechanisms is vitally important to predicting time-dependent electron flux.

1.5.1 Electron Acceleration

It is believed that electrons can become accelerated up to MeV energies primarily through two types of processes: 1) radial diffusion [e.g., *Fujimoto and Nishida*, 1990; *Hudson et al.*, 2001; *Elkington et al.*, 2003]; and 2) wave-particle interactions [e.g., *Thorne et al.*, 2005; *Summers et al.*, 2007a]. Electrons can be accelerated through radial diffusion by adiabatically moving into a region of enhanced magnetic field while conserving magnetic moment, μ (Equation (1-7)). If magnetic moment is conserved, the electron kinetic energy due to velocity perpendicular to the magnetic field direction is proportional to the

magnetic field strength. Several processes have been proposed for effectively transporting electrons inward. One such mechanism involves ultra low frequency (ULF) waves in resonance with electron drift velocities moving around a distorted dipole magnetic field [*Hudson et al.*, 2001; *Elkington et al.*, 2003]. The other popular idea involves solar wind electron recirculation in the magnetosphere, whereby solar wind electrons enter the magnetotail and drift earthward to low L shells (lower than the outer radiation belt region). Once accelerated, wave-particle interactions could scatter the electrons to higher L-shells with minimal energy loss [*Nishida*, 1976; *Baker et al.*, 1989].

The other proposed acceleration mechanisms are resonant wave-particle interactions. In order to efficiently exchange energy with particles, waves must satisfy the gyro-resonance condition

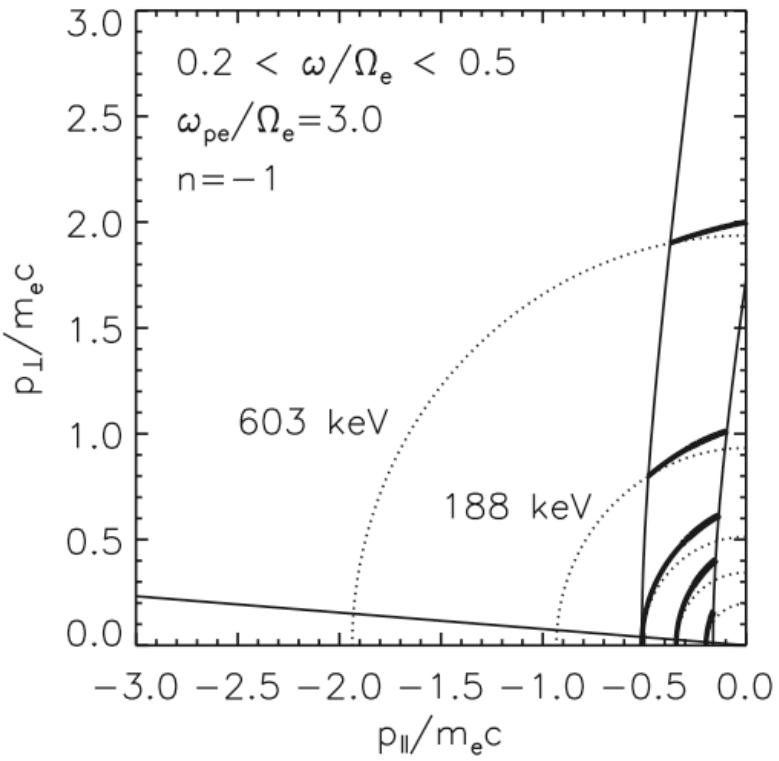

Figure 1.5.1 An example of available phase space transitions for energetic electrons at L = 4.5. The dotted lines represent electrons at 603, 188, 63, 29 and 10 keV. The bold lines are the resonant diffusion surfaces. [From *Horne and Thorne*, 2003].

$$\omega - k_{\|} v_{\|} = \frac{n\Omega_s}{\gamma}; \quad \gamma = \left(1 - \frac{v^2}{c^2}\right)^{-\frac{1}{2}}. \tag{1-10}$$

Here ω is the wave angular frequency, $k_{||}$ is the wave vector parallel to the magnetic field line, $v_{||}$ is the particle velocity along the field line, n is an integer harmonic number, Ω_s is the particle gyrofrequency and γ is the Lorentz factor. When the resonance condition is met, particles can move along defined contours in phase space. Figure 1.5.1 shows one example of possible contours particles may move along when interacting with equatorial chorus plasma wave bands. The solid lines mark the allowable electron motion. Particles can both gain and lose energy through gyroresonant interactions with plasma waves. Depending on the particular conditions (e.g., particle energy, particle population distribution), energy transfer to electrons can be more preferential than energy transfer to the wave. A full review of electron acceleration mechanisms has been performed by *Friedel et al.* [2002].

1.5.2 Precipitation as a Loss Mechanism

Once in the outer radiation belt, relativistic electrons remain there until they are lost either to the magnetopause or to the atmosphere through precipitation. Losses to the magnetopause can occur when the magnetosphere compresses, moving the electron drift path such that it crosses the magnetopause [*Li et al.*, 1997]. Additionally, outward radial diffusion can propagate magnetopause loss even to inner L-shells [*Shprits et al.*, 2006]. In this thesis, we focus on loss to the atmosphere thorough relativistic electron precipitation (REP..

Trapped relativistic electrons in the radiation belt are constantly bouncing along magnetic field lines due to the force applied to a charged particle moving in a diverging magnetic field (Equation (1-7)). Each electron has a pitch angle, α, defined by

$$v_{\perp} = v \sin\alpha \tag{1-11}$$

where $v_{\perp}$ is the component of the particle velocity perpendicular to the magnetic field

vector. Since magnetic moment is conserved, we can write the following equality, which includes pitch angle and magnetic field:

$$\frac{\sin^2 \alpha_1}{B_1} = \frac{\sin^2 \alpha_2}{B_2}. \quad \textbf{(1-12)}$$

The subscripts denote the pitch angle and magnetic field strength at two different locations for one specific particle. We can calculate the magnetic field at the mirror point (i.e., point where the electron reverses its field-aligned direction) by setting the pitch angle at one of the locations in Equation (1-12) to 90° such that the following equation holds true:

$$\sin^2 \alpha = \frac{B}{B_m}. \quad \textbf{(1-13)}$$

Here, B_m is the magnetic field magnitude at the mirror point. α and B are the pitch angle

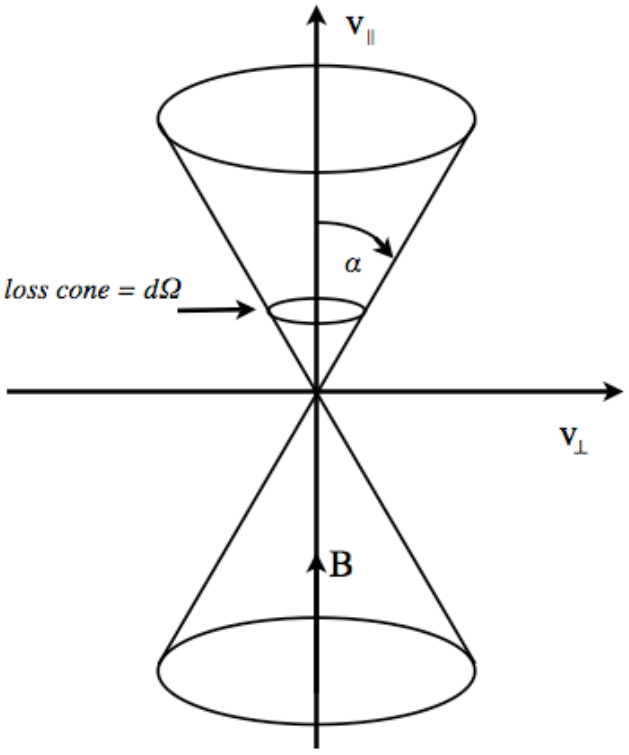

Figure 1.5.2 Schematic of the loss cone. All of the particles that fall into the loss cone are precipitated into (lost to) the atmosphere. Particles outside the loss cone are stably trapped.

Table 1-2 Summary mechanisms thought to be responsible for REP.

	Energy	***Local Time***	***L-Shell***
Current sheet scattering[2,3,6]	*Preferentially high energy*	*Generally night side*	*High trapping boundary*
Whistler mode scattering[1,4,7,8]	*Stronger for low energies (100 keV), can work for MeV energies*	*dawn side*	*Outside plasmapause, L > 3-5*
Electromagnetic Ion cyclotron (EMIC) mode scattering[1,5,7,8,9]	*Preferentially MeV energies*	*dusk side*	*dusk side plasmapause and drainage plume*[2,3,10]
Electrostatic Ion Cyclotron (EIC) mode scattering[8]	*Stronger for low energies (100 keV), can work for MeV energies*	*night side*	?

1. [*Horne and Thorne,* 1998]
2. [*Imhof et al.,* 1991]
3. [*Imhof et al.,* 1979]
4. [*Kennel and Petschek,* 1966]
5. [*Lorentzen et al.,* 2000]
6. [*Sergveev and Tsyganenko,* 1982]
7. [*Summers et al.,* 1998]
8. [*Thorne and Andreoli.,* 1980]
9. [*Thorne and Kennel*., 1971]

and the magnetic field, respectively, at any other point along the electron trajectory. If the magnetic field strength required to mirror the electron is below ~ 100 km, it will become lost to the neutral atmosphere. This loss to the atmosphere is called precipitation. A useful concept when considering precipitation is the loss cone (Figure 1.5.2), which is defined by the solid angle separating particles with pitch angle small enough to precipitate from those that are stably trapped. All of the particles with pitch angles inside the cone will precipitate within one bounce. Those that are outside are stably trapped unless they are pitch-angle scattered, thus moved into the loss cone.

There are various processes that can pitch-angle scatter a stably trapped electron into the loss cone. These include current sheet scattering and wave-particle interactions. Just like wave-particle interactions can accelerate electrons, they can also pitch-angle scatter them through gyro-resonant interactions. Several types of electron and ion cyclotron plasma waves are believed to be candidates for scattering processes. Table 1-2 shows some

characteristics of these pitch-angle scattering processes. There are relatively few direct measurements of REP losses. Satellites in space cannot directly measure a lost particle, they can only measure the absence of particles. Although most of the energy from a relativistic electron goes to ionization, balloon-borne instruments can measure bremsstrahlung x-rays that result from REP.

1.6 Potential Differences in the Collisional Atmosphere

1.6.1 Vertical Electric Field and the Global Electric Circuit

The global electric circuit (GEC), a large-scale electrical system of currents that move through the earth, atmosphere and ionosphere, was initially proposed by *C.T.R. Wilson* [1920]. In the GEC, positive charge is moved from the ground up to the ionosphere by thunderstorm activity. This separation of charge forms a leaky capacitor between the negatively charged, conducting ground and the positively charged ionosphere. Inside this capacitor exists a vertical electric field pointing downward. Since the collisional atmosphere contains a population of charged particles with a non-zero conductivity, it can carry a return current in fair-weather regions where there is no thunderstorm activity. The potential difference between the ionosphere and the ground is 180-400 kV [*Bering et al.*, 1998] and the total downward current flow in fair weather regions is ~ 1 kA. The columnar resistance of the leaky capacitor is ~ 1 x 10^{17} Ω m^2, for a total resistance of 230 Ω. If thunderstorm activity ceased, the capacitor would discharge in less than an hour [*Volland*, 1984]. We use Ohm's law, $\vec{J} = \sigma\vec{E}$, to describe the relationship between current density, conductivity and electric field. Here, we use a scalar conductivity value, not a tenser value as we did in Equation (1-5). Assuming a constant fair-weather return current density of ~ 1 pA m^{-2} (in reality, this current density can fluctuate by a few pico-amps $meter^{-2}$ [*e.g., Holzworth et al.*, 2005]), conductivity and electric field are inversely proportional. Conductivity increases exponentially with altitude because of increased cosmic ray ionization. Electric field, on the other hand, decreases exponentially with altitude. Because it is pertinent to the events in discussed in this thesis, we focus on the

electric field in the fair-weather stratosphere at ~32 km. At this altitude, the downward pointing electric field is ~100 mV m^{-1} and the conductivity is ~10 pS m^{-1}.

1.6.2 Horizontal Electric Field Polar Ionosphere

Within the ionosphere itself, there are potential differences that drive currents horizontally (with respect to the ground). One source of potential differences is solar tidal movement. Daytime heating and nighttime cooling cause ionospheric winds which balance out global pressure differences. S-currents are currents that flow as a result of tidal winds, set up local time-dependent potential differences. However, the magnitude of these potential differences is only a few mV m^{-1}. In the polar regions, much larger potential differences can arise from ionosphere coupling to the magnetosphere. Figure 1.3.3 and Figure 1.3.4 show the large-scale cross polar cap potential (CPCP). The magnitude of the CPCP varies between ~20 kV in geomagnetically quiet conditions and ~240 kV in extremely active periods [*Wygant et al.*, 1983; *Siscoe et al.*, 2002]. The CPCP is tied directly to the conducting magnetic field lines, which also act as lines of equipotential. Solar wind flowing past the earth's magnetic field induces a potential difference across the magnetosphere from the dawn side to the dusk side. When the IMF is southward and the magnetosphere is in an "open" configuration, this potential difference can grow very large. In addition to the solar wind-induced potential, viscous interactions in the low latitude boundary layer (LLBL) appear to create a nearly constant 20 kV potential difference that persists regardless of IMF orientation [*Sonnerup and Siebert*, 2003]. For a simulated polar cap with a 2000 km radius, resultant electric field can be between 0.02 and 0.24 V m^{-1}. Along with the CPCP, smaller scale horizontal potentials can arise in the polar and sub-auroral ionosphere. Polarization caused by spatial separation of proton and electron aurora can create a narrow band of potential difference called a sub-auroral polarization stream (SAPS) between the locations where Region 1 and Region 2 currents flow into the ionosphere [*Brandt et al.*, 2005; *Anderson et al.*, 1993; *Anderson et al.*, 2000]. There can also be polarization within a particular

auroral arc [*de la Beaujardiere et al.*, 1981].

All of these potential differences in the ionosphere map down into the exponentially less-conductive atmosphere below. Making horizontal dc electric field measurements in the stratosphere is an ideal way to essentially remote sense the ionosphere above. In fair weather, away from thunderstorm activity and above the turbulent troposphere, horizontal electric field at 32 km altitude is thought to be the 1-second, >100 km average of the overlying ionospheric electric field [*Mozer and Serlin*, 1969; *Holzworth and Bering*, 1998]. Since the conductivity exponentially increases with altitude in the collisional atmosphere, potential differences can easily map downward but become quickly attenuated above the source location [*Park and Dejnakarintra*, 1977a; 1977b].

1.6.3 Other Potential Sources

The potential differences described above are the dominant, most well-known sources of electric field in the atmosphere. In addition to the aforementioned sources, there are others that are less well understood. Horizontal inertial turbulent stratosphere (HITS) electric field is a large magnitude field that rotates with the same period as atmospheric inertial wave periods [*Holzworth*, 1989; *Hu and Holzworth*, 1997]. It is believed that the source altitude is near the tropopause. HITS electric fields have only been definitively observed by long duration balloon instrumentation at a low (< 25 km) float altitude. However, no altitude-stable long duration balloon flights (which would be capable of observing HITS-like fields) above 26 km have ever been conducted. There is a possibility that any cloud may undergo charge separation processes. Thunderstorm clouds are the best, most extreme example of this. However, there have been observations of electrified clouds, which are not associated with thunderstorm activity (*E. A. Bering*, personal communication) as well as large (> 1 V m^{-1}) vertical electric fields inside noctilucent clouds near 85 km near the mesopause [*Holzworth and Goldberg*, 2004]. None of these electric fields are thought to be the dominant source of vertical or horizontal dc potential differences in the fair weather stratosphere.

1.7 Review of Previous Balloon Measurements of Particle Precipitation Events and Associated Electrodynamics

1.7.1 Previous Solar Energetic Particle Event Observations

There have only been two previous in-situ stratospheric measurements of atmospheric electric field changes during SEP events [*Holzworth and Mozer*, 1979; *Holzworth et al.*, 1987]. The first direct correlation of SEP events and large electric field changes in the stratosphere was made during a large solar flare in August 1972. Geosynchronous orbiting satellite Explorer 41 recorded a four order of magnitude increase in energetic (>60 MeV) protons, which slowly decayed to background levels over a five-day period. Simultaneous vertical electric field measurements by a balloon at ~30 km altitude in the northern polar cap measured a decrease in magnitude from 250 mV m^{-1} to 0 mV m^{-1} [*Holzworth and Mozer*, 1979]. This change was interpreted to be a direct result of enhanced atmospheric conductivity. If the vertical current density ($\vec{J}$) in the global electric circuit is assumed to be nearly constant and the conductivity (σ) is increased, then by Ohm's law, $\vec{J} = \sigma\vec{E}$, it follows that the electric field would decrease. Interestingly, the horizontal component of the electric field during the same period did not suddenly decrease as the vertical component did. It appeared as if the SEP interactions immediately affected the vertical component, but did not immediately affect the horizontal component [*Holzworth*, 1981].

The next direct in-situ measurement was taken more than 10 years later in February 1984 with two important results reported [*Holzworth et al.*, 1987]. First, with both electric field and conductivity measurements made during this event, the change in vertical current density could be directly calculated with Ohm's law. In this case, the vertical current density did not remain constant but increased by a factor of two. The second important result was a measure of the spatial region of the SEP-affected electrical atmosphere. During this event, there were two balloons. The pole-ward balloon (44.6˚ S) measured perturbed conductivity and electric field magnitude while the more equator-ward balloon

(38.7˚ S) did not observe any noticeable changes. In this case, the rigidity cutoff at the pole-ward balloon allowed SEPs to perturb the local electrical environment while the equator-ward balloon was at a cutoff where SEPs could not access, resulting in no noticeable changes to either the conductivity or electric field. This report reinforced the validity of the idea that rigidity cut-offs play an extremely significant role in controlling SEP effects on the electrical atmosphere [*Clilverd et al.*, 2007].

1.7.2 Previous Balloon Relativistic Electron Precipitation Event Observations

There have been two confirmed REP observations made by balloon-borne instrumentation. The first was made in August of 1996 as part of the INTERBOA balloon campaign [*Foat et al.*, 1998]. At 18:35 magnetic local time (MLT) at L = 5.8, x-ray instruments aboard a stratospheric balloon launched from Kiruna, Sweden observed seven x-ray peaks over about 20 minutes. After modeling REP scattering using possible incident electron spectra, it was determined that electrons with energies between 1.5 – 2 MeV must have precipitated. This was the first observation of MeV REP. A 24-minute time delay between satellite observations of 60 keV proton injection was found to be consistent with the time it would take for protons to drift in local time to the longitude over the balloon payload [*Lorentzen et al.*, 2000]. Combining the local time, energy spectrum and proton injection, this led to postulation that EMIC wave gyroresonance was responsible for the REP observation. However, the mechanism that caused the modulation of x-ray flux over the 20-minute event remains unknown.

In 2000, the MeV Auroral X-ray Imaging and Spectroscopy (MAXIS) balloon circumnavigated the south pole for an extended 18-day mission. During its flight, MAXIS observed seven different MeV x-ray bursts, all of which occurred between 14:00 and midnight MLT. One result from the MAXIS campaign, confirming earlier

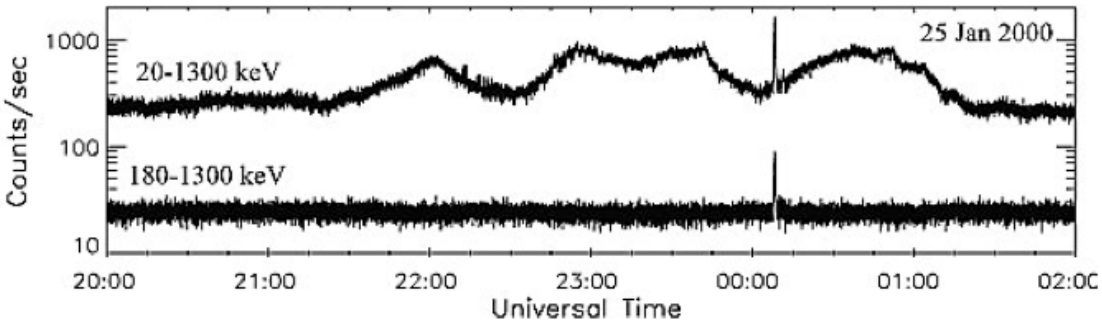

Figure 1.7.1 MAXIS x-ray counts on January 24th-25th, 2000. The energetic burst shortly after midnight appears to be independent of the longer lower energy event. [Adapted from *Millan et al.*, 2002].

observations from Kiruna, was that energetic x-ray bursts are not the tail end of less energetic precipitation, but represent a different phenomenon. Short (minutes), energetic (~800 keV) x-ray bursts were observed to be independent of long periods (several hours) of low-energy (~200 keV) precipitation. Figure 1.7.1 shows x-ray counts in two integral energy bins. The top show energy between 20-1300 keV and the bottom shows 20 -1300 keV. The other major result from MAXIS was the estimation that REP loss could be the dominant loss mechanism for relativistic radiation belt electrons. Based on the average > 700 keV loss rate while MAXIS was between L = 3.7-6.6 (corresponding to the outer radiation belt), the total number of electrons lost over two weeks was ~10^{24}. This is within the range of the total number of > 500 keV electrons expected to be in the outer belts.

The scientific community has learned a great deal from these two balloon campaigns. However, there are many questions left unanswered that are the focus of large magnetospheric research efforts. The MINIS balloon campaign (described below), set out to help constrain the temporal and spatial ambiguity of REP events and to help distinguish the contributions of various precipitation mechanisms. Neither of the two previous balloon campaigns reported a strong connection between observed electric fields in conjunction with REP events. MAXIS had no electric field instrumentation at all. INTERBOA had dc electric field instrumentation similar to MINIS, but limited reports

stemming from these observations provided minimal insight [*Treilhou et al.*, 2000; 2002].

1.8 MINIature Spectrometer (MINIS) Balloon Campaign Overview

The MINIature Spectrometer (MINIS) Balloon Campaign observations are at the heart of this thesis. The primary objective of the MINIS campaign was to observe REP x-rays at multiple locations simultaneously in order to help resolve some of the temporal and spatial ambiguity of previously observed precipitation. Two graduate students were sent to Antarctica via South Africa to hand-launch four balloon payloads. During January of 2005, there were a total of six payloads launched. Four payloads were launched from the South African National Antarctic Expedition (SANAE) IV (71.7° S, 2.8° W geographic), and two from Fort Churchill, Manitoba, Canada (58.8° N, 265.9° E geographic). Each southern payload included an x-ray spectrometer, dc electric field instrumentation, a magnetometer, GPS receiver and an Iridium satellite modem for telemetry. The northern payloads were similar, but had no electric field probes. The southern flights had battery life to last for ~ 8 day flights and the northern payloads were designed to last for ~1-2 days. The payloads were launched from different hemispheres in hopes of making conjugate REP observations.

January, 2005 was an especially active solar period with five X-class solar flares. The solar flares were accompanied by CMEs and SEP events. This extreme solar activity led to the first balloon-borne electric field measurements during an SEP event in over twenty years on January 20th. The first multi-point, simultaneous observation of REP x-rays in separate hemisphere was made in conjunction with a CME impulse arrival at earth with three separate payloads (one in the northern and two in the southern hemisphere) on January 21st.

1.9 Thesis Outline

The remainder of this thesis is divided into the following sections as outlined below.

Chapter 2: Instrumentation. We describe the MINIS balloon payloads with special emphasis on the electric field instrumentation. Also, we give a brief overview of other satellite and ground-based instrumentation, which collected data used in our analysis of the MINIS-observed SEP and REP events in January 2005.

Chapter 3: An Atmosphere-Ionosphere Electrical Conductivity Model. We detail an atmosphere-ionosphere conductivity model which we use later in our data analysis. This conductivity model is built on other standard ionosphere (IRI), neutral atmosphere (MSISE-90) and magnetic field (IGRF) models. For the first time, we employ the Sodankylä Ion Chemisry (SIC) model for ion and electron densities between 20 -120 km altitude. We also make suggestions for alternate ways to include energetic particle precipitation into future versions of the SIC model.

Chapter 4: Observations During the January 20th 2005 Solar Energetic Particle Event. We present an array of geophysical data during the most energetic SEP ground level event since 1956. We focus on electric field and conductivity observations from the MINIS balloon campaign while using additional data to provide context. We show that shortly after the SEP event onset, there was a rapid 20-fold increase in conductivity and an equally sudden decrease in the totel dc electric field in the stratosphere observed at MINIS Flight 2 South.

Chapter 5: Discussion on Effects of January 20th 2005 Solar Energetic Particle Event. We compare results from our conductivity model described in Chapter 3 to the MINIS conductivity observations. We conclude that the measured conductivity enhancement in the stratosphere was caused by direct SEP-induced ionization. Based on the same model results, we conclude that SEP protons could not have altered the conductivity in the ionosphere near 120 km. This means that no ionospheric horizontal dc electric field structures were perturbed by SEP-induced ionization. Therefore, the vanishing horiontal

electric field is not a result of altered ionospheric potential differences.

Chapter 6: Relativistic Electron Precipitation and Ionospheric Electrodynamics During the January 21st 2005 Storm Sudden Commencement. We present geophysical data from multiple satellites, ground-based sources and three MINIS balloons during a sudden storm commencement and the first simultaneous measurements of REP in different hemispheres. We present both x-ray and electric field data from the two southern MINIS balloons during a several hour period of sporadic REP. Complimentary satellite and ground-based data are provided to place the MINIS observations into an appropriate context.

Chapter 7: Discussion of MINIS Relativistic Electron Precipitation Observations. We discuss the MINIS-observed REP events on January 21st, 2005. We show that there is only a small statistically significant correlation between x-ray observations at the two southern balloon payloads, despite there being a moderate correllation in electric field direction and magnitude. There is no one-to-one correlation between horizontal dc electric field and REP x-ray observations. From this lack of correlation, we conclude that the spatial scale size of REP events is often smaller than the 660 km balloon separations (with exceptions directly following sudden compression events) and is smaller than the average scale size of the measured ionospheric horizontal dc electric field. We show that horizontal electric field direction and magnitude can relate to bulk plasma motion in the magnetosphere, but can only qualitatively constrain REP mechanisms.

Chapter 8: Conclusion and Future Work. We begin by reviewing main contributions detailed in the preceding chapters. Then, we propose several problems to address in future studies. Some of this work includes addition of electron and solar-flare photon ionization to the SIC model, conductivity modeling during multiple SEP events and comparison of horizontal dc electric field data with plasmasphere models.

2 Instrumentation for the MINIS Balloon Campaign

2.1 MINIS Payload Overview

The main phase of the MINIature Spectrometer (MINIS) balloon campaign consisted of two sets of balloon payload launches. One set was launched from the southern hemisphere site at the South African National Antarctic Expedition (SANAE) IV, while the other set from Fort Churchill, Manitoba, Canada. The southern and northern payloads differed in instrumentation and intended flight duration. The data presented in this thesis are almost exclusively results of the southern hemisphere payloads. Thus, we will focus on a detailed description of the southern payloads and only mention the differences between the two sets. A photograph of a southern hemisphere balloon payload is shown in Figure 2.1.1.

The primary observation goals of the MINIS balloon campaign were to measure bremsstrahlung x-rays from precipitating relativistic electrons and use the associated electromagnetic field measurements to try to determine the cause of the precipitation. A sodium-iodide x-ray scintillator produced light curves 20 times per second in four broad energy bins between 20 keV and 1500 keV and full spectra in 208 energy bins covering 20 keV to 10 MeV were given every 8 seconds. Three-axis dc electric field was measured using three sets of orthogonal double-langmuir probes. The two sets of horizontal axis probes were sampled once per second and the vertical axis set was sampled four times per second. Electrical conductivity was measured in ten-minute intervals using the same set of dc electric field probes using a relaxation technique. Magnetic field was measured using a TCM2 three-axis magneto-inductive magnetometer. Measurements of very low frequency (VLF) electric and magnetic fields were measured with three-band multi-pole filters connected to one axis of the electric field probe and a separate search coil magnetometer. No reliable VLF data were gathered with this instrument. Thus, we omit

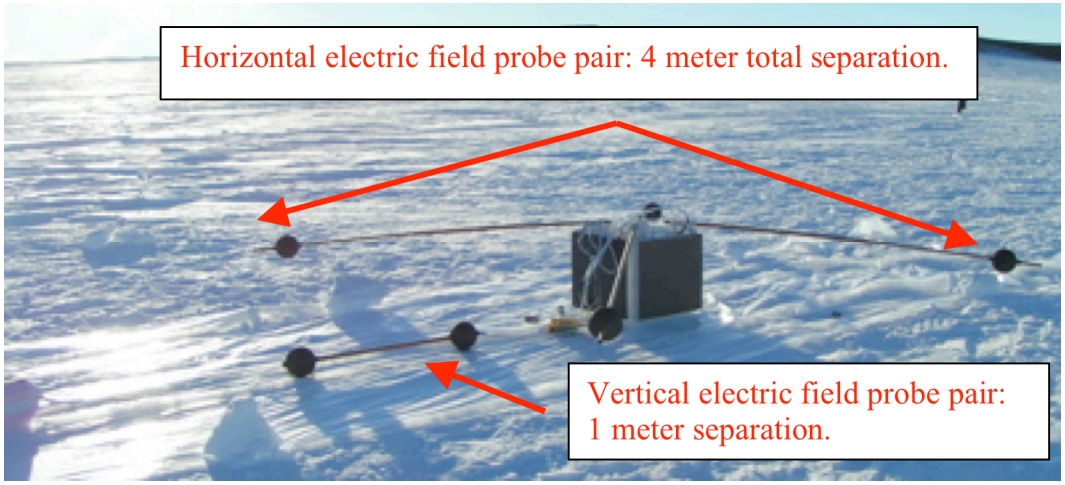

Figure 2.1.1 Photograph of a southern hemisphere MINIS balloon payload.

further discussion of the instrument and the data set. All data were telemetered to a ground station at the Space Sciences Laboratory in Berkeley, California using the Iridium satellite communication network. A global positioning system (GPS) receiver was used to measure geographic latitude, longitude and altitude. The entire payload was rotated about the vertical axis by a dc electric motor with a period of about 45 seconds per rotation. Payload power was provided by several lithium ion battery packs. Each southern flight was expected to have enough battery power to last for eight days.

The southern and northern payloads shared the primary x-ray scintillator instrument as well as the magnetometer, GPS and Iridium telemetry. The northern payloads did not have any electric field instrumentation but did include upward-looking photometers. The flight durations were planned for 1-2 days as opposed to eight, reducing the overall lithium ion battery weight. We will present some x-ray data from the northern hemisphere, but the focus will be on data from the southern payloads.

2.2 DC Vector Electric Field Instrumentation

2.2.1 Double Langmuir Probe Technique

The MINIS balloon campaign utilized the double Langmuir probe technique to

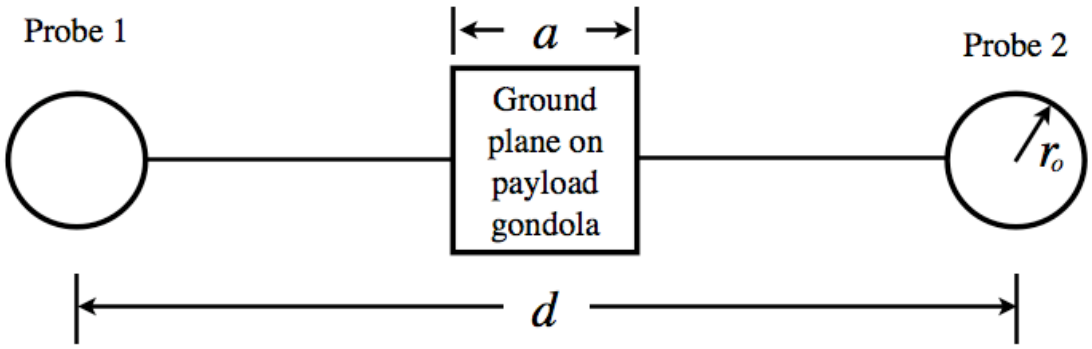

Figure 2.2.1 Basic design for one set of double Langmuir probes. The probes have radius r_o and are separated from each other by length d. The payload gondola has ground planes, which act as the central reference point for potential difference measurements.

measure in-situ stratospheric electric field and remote sense the ionosphere above. At its most basic level, this technique measures the potential difference between two points in space separated by a known distance, from which the electric field is calculated. The double Langmuir probe method has been used on stratospheric balloons as early as the 1960s and has been described in detail in multiple publications [*Kellogg and Weed*, 1968; *Mozer and Serlin*, 1969; *Holzworth and Bering*, 1998]. Balloon-borne double Langmuir probes have been used to study a wide range of ionospheric, magnetospheric, thunderstorm and fair-weather electrical phenomena [*Bering et al.*, 1991; *Hu and Holzworth*, 1996; *Holzworth et al.*, 2005; *Thomas et al.*, 2005].

To make a potential difference measurement in one axis using the double Langmuir probe technique, two probes are extended away from the main payload gondola in opposite directions on electrically isolated booms (Figure 2.2.1.). By including three sets of orthogonal probes, a three-axis electric field can be computed, which leads to a measurement of the total instantaneous vector electric field. Coaxial wires running inside the booms connect the probes to high input impedance electronics in the main payload gondola. The probes must have conducting surfaces and be large enough to gather sufficient charge from the ambient atmosphere to come into electrostatic equilibrium and drive the electronics. As shown in Figure 2.2.1, the electric field between probes 1 and 2

is equal to the negative of the potential difference between probes 1 and 2 divided by the distance between them.

$$\vec{E}_{12} = -\frac{V_2 - V_1}{d} \qquad \textbf{(2-1)}$$

In practice, the potential difference between one single probe and a large conducting surface of the main payload is the measured quantity. This is done for redundancy and to provide a symmetric ground point for all measurements. To ensure that the payload gondola does not significantly distort the ambient electric field the gondola is made as small as possible and the probes are placed as far away as practical from the gondola. According to *Jackson* [1975], a conducting sphere in the presence of a uniform electric field will perturb that field with an induced dipole-like potential. Thus, we estimate that the atmospheric potential difference between a pair of probes will be perturbed by the presence of the gondola by a factor of $\left(\frac{8a^3}{d^3}\right)$, where *a* is the dimension of the gondola and *d/2* is the boom length. In the case of the MINIS payloads, the electric field perturbation factor is ~0.03.

To draw as little current as possible, traditional voltmeters have high input impedances (~10 MΩ) when compared to the resistance within the electronic circuit being analyzed. This allows for precise potential difference measurements. Analogously, when measuring the potential difference within the collisional plasma of the stratosphere, relatively high input impedance must be used. The resistance between the stratospheric plasma and the probes is defined by *Mozer and Serlin* [1969] as

$$R_{atm} = \frac{m_i \nu_{in}}{4\pi n_i e^2 r_0} \qquad \textbf{(2-2)}$$

where m_i is the ion mass, ν_{in} is the ion-neutral collision frequency, n_i is the ion number density, e is the unit charge of an electron and r_0 is the diameter of a spherical probe. In

the case of 15 cm diameter probes like those on the MINIS main-phase payloads, $R_{atm} \approx 10^{13}\Omega$ at ground level and $R_{atm} \approx 10^{10}\Omega$ an altitude of 33 km in the polar stratosphere. Thus, to make potential difference measurements in the polar stratosphere, the input impedance of the electronics must be $>> 10^{10}\Omega$ and in practice are $> 10^{13}\Omega$.

Any time stratospheric electric field measurements are made in the daytime, energetic ultraviolet (UV) radiation bathes the entire payload on the sunlit side. If individual UV photons have more energy than the work function of the illuminated material, they can cause photoemission. These emitted photoelectrons are a positive current flow to the surface. Additionally, they can create small electron clouds, or sheaths, within a few mean free paths of the surface [*Byrne et al.*, 1990]. Photocurrents and space-charge clouds can cause perturbations to the natural electrical environment. To minimize these effects, electric field probes and ground planes are often covered with a water-based colloidal carbon suspension known as Aquadag. The advantage of Aquadag over traditional bare aluminum is that it has a higher work function and can be spread uniformly over desired surfaces. By using Aquadag instead of aluminum, the surface work function can be increased from 4.2 eV to 4.6 eV. This corresponds to reducing the wavelength of UV photons that can contribute to photoemission from 295 nm to 230nm [*Byrne et al.*, 1990]. With a reduced, uniform work function, photocurrents can become small enough to provide absolute accuracy to within 5 mV m^{-1} and relative accuracy to within 1-2 mV m^{-1} [*Mozer*, 1973]. If the electric field probes and the ground planes are not evenly coated and the work function not uniform, errors proportional to the UV photon flux can appear.

In addition to photoelectric effects, there is risk of contamination of the horizontal potential difference measurements by the larger (in nominal fair weather) vertical potential. This can occur if the horizontal probes are tilted out of the horizontal plane (i.e., if the gondola is not perfectly balanced). To separate the contamination from the

real geophysical horizontal electric field, the entire payload can be rotated. When the payload is rotated, vertical contamination becomes dc offsets and slowly varying, or constant, horizontal geophysical fields appear as sinusoids. The magnitude of a real horizontal electric field can then be extracted from the data by fitting the raw output at the spin period. One limitation of this solution is that it decreases the time resolution from the sample frequency to the payload rotation frequency (near 2 rpm, but variable on each MINIS flight).

2.2.2 MINIS DC Electric Field Instrument Hardware

The payloads used during the main phase of the MINIS balloon campaign each had three-axis spherical double Langmuir probes made of foam and coated with Aquadag. As shown in Figure 2.2.3 and Figure 2.2.4, there was one set of probes along the vertical axis and two sets orthogonally spaced in the horizontal plane. Each probe was 15 cm in diameter, large enough to keep the resistance between the probe and the plasma much smaller than the input impedance of the electronics. The horizontal probes were extended out 2 m from the center of the gondola while the two vertical probes were rigidly spaced 1 m apart approximately 3 m above the gondola. The ground plane consisted of four square (0.375 m^2) panels coated with Aquadag on the outside and aluminized mylar on the payload-facing side to reduce thermal emissions, which could heat the central payload electronics. The ground planes were isolated from the main gondola body using one-inch ceramic standoffs.

Figure 2.2.2 is a simplified diagram of the electronics associated with one set of probes. A complete schematic can be found in Appendix A. The spherical probes are connected to the electronics in the main payload using Teflon coaxial cable (RG188). The outer shield of the cable is driven at the same voltage as the input on the center wire to eliminate any

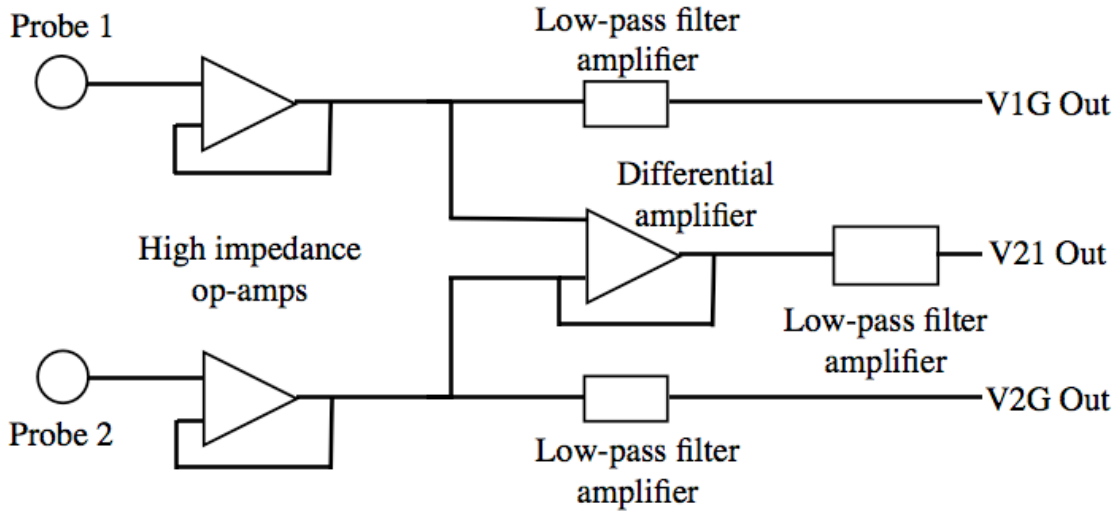

Figure 2.2.2. A simplified schematic of the dc potential difference circuit. From one set of probes, three potentials are output. V1G and V2G are single-sided potential differences between the individual probes and the payload ground. V21 is the difference between the two probes.

voltage drop between the two co-axial conductors, thus reducing leakage current and effective capacitance. High input-impedance operational amplifiers (op-amps) drive the cable shield and pass the probe voltage to the rest of the circuit. The op-amps used for this design are Analog Devices' AD549. Operating in common mode, the input impedance for this amplifier is 10^{15} Ω. This input impedance is more than three orders of magnitude greater than the expected resistance of the stratospheric atmosphere. The operating voltage of the AD549 is ±12 V, limiting the maximum measurable potential. However, the maximum expected potential differences in the fair weather stratosphere are on the order of hundreds of millivolts, well within the operational range. After the input op-amp buffer, the probe voltage is sent to two different follower circuits. One is for the single-sided measurement, which takes the difference between the probe voltage and ground voltage. The other is a two-sided measurement, which takes the difference between a pair of probes. For the vertical probes, the two-sided follower circuit has unity gain, while the horizontal follower circuits have a gain of 2.5. The output from all of the single-sided measurements is inverted, centered on 2.5 V and has a gain of negative 0.165. Complete calibration curves and tables can be found in Appendix A. Each single-sided probe-to-ground potential difference was sampled once per second while the

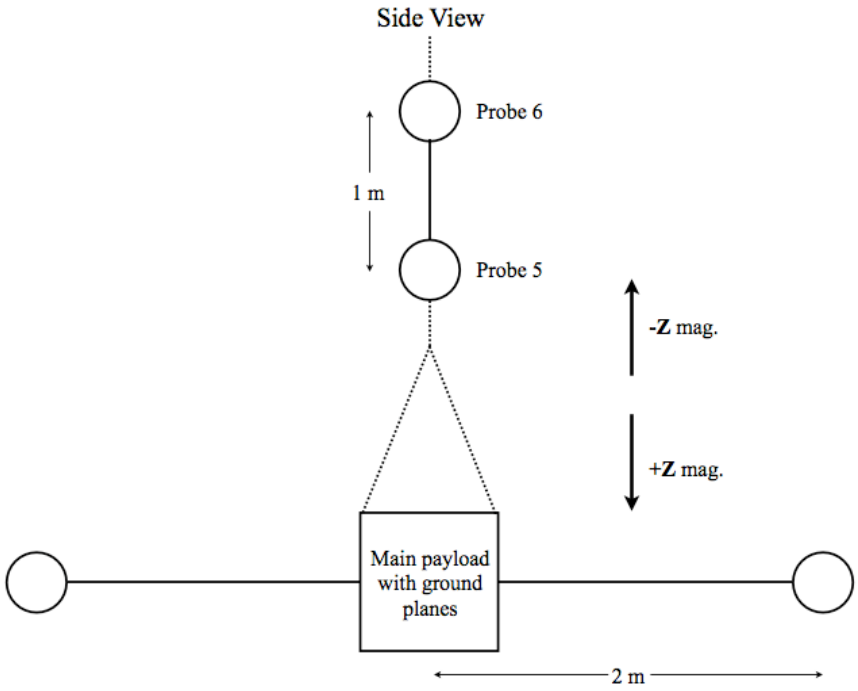

Figure 2.2.3 Side view of MINIS payload electric field probes and vertical magnetometer direction.

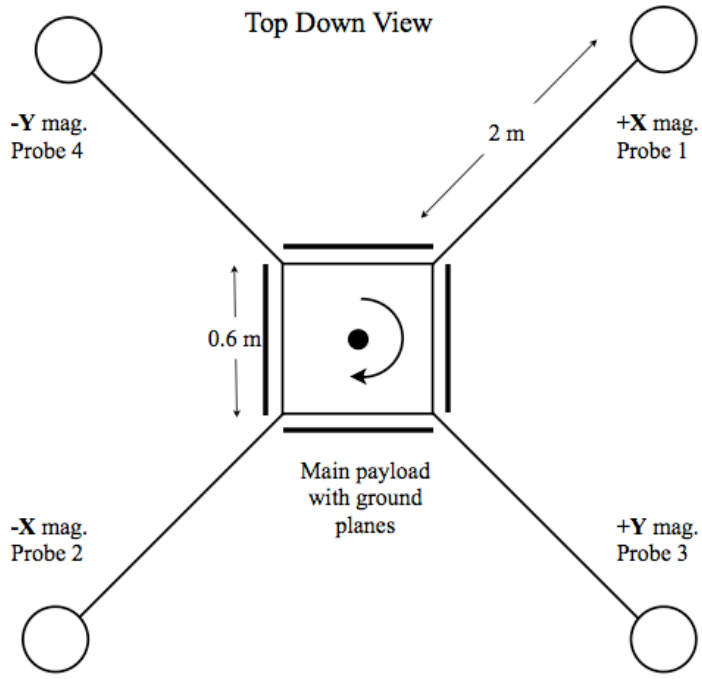

Figure 2.2.4 Top view of MINIS payload electric field probes, horizontal magnetometer direction and rotation direction. Rotation direction is for payloads on flights 1, 2 and 3. Flight 4 had an opposite rotation direction.

vertical double-probe difference was sampled four times per second.

Figure 2.2.3 and Figure 2.2.4 show the payload orientation for all of the electric field probes, the magnetometer and the rotation direction. (The magnetometer and rotation motor are described in Section 2.5.) The probes are paired sequentially with 1, 2, 3 and 4 in the horizontal plane and 5 and 6 along the vertical axis. The magnetometer axes are aligned with the electric field probes. In the horizontal plane, the x-axis is aligned with probes 1 and 2 (positive x pointing toward probe 1) and the y-axis with 3 and 4 (positive y pointing toward probe 3). The positive z-axis points down toward the ground. Payloads 1, 2 and 3 rotate clockwise when looking down on the payload from above, while payload 4 rotates in the opposite direction.

2.3 Conductivity Measurements Using Relaxation Time Technique

Electrical conductivity measurements were made during the MINIS balloon campaign using the relaxation time technique. This method has been used many times for stratospheric balloon observations [*Few and Weinheimer*, 1986; *Byrne et al.*, 1988; *Holzworth*, 1991]. The basic idea of this technique is to place charge onto one of the electric field probes, and then measure the time constant associated with the probe returning to equilibrium. The time constant for relaxation to ambient floating voltage will then depend inversely on the conductivity of the air around the probe. In the case of the MINIS payloads, conductivity is measured during a calibration cycle every ten minutes. During this cycle all six probes were grounded for three seconds. Then, one probe was biased to +5 V and another to -5 V through a high impedance relay while the rest remain held at ground for an additional ten seconds. By opening the relays, the biased probes were allowed to return back to the potential of the surrounding atmosphere by collecting charge carriers of opposite polarity from the collisional plasma. The probes returned to an equilibrium potential with a characteristic exponential time constant τ. This time constant is related to conductivity through the set of relations shown below.

$$\tau = (C_P + C_{in})\frac{R_{atm}R_{in}}{(R_{atm} + R_{in})} \qquad \textbf{(2-3)}$$

Here, C_P and C_{in} are the capacitances of the probe and the high impedance input electronics. R_{atm} is the resistance of the atmosphere and R_{in} is the resistance of the input. In this case, $R_{in} >> R_{atm}$ and $C_{in} << C_P$. Thus, Equation (2-3) reduces to

$$\tau = C_P R_{atm}. \qquad \textbf{(2-4)}$$

For a spherical probe, the capacitance and atmospheric resistance are given by the following:

$$C_P = 4\pi\varepsilon_o r \qquad R_{atm} = \frac{1}{4\pi\sigma r}. \qquad \textbf{(2-5), (2-6)}$$

We can combine Equations (2-4), (2-5), (2-6) to get an expression relating the time constant and conductivity.

$$\sigma = \frac{\varepsilon_o}{\tau} \qquad \textbf{(2-7)}$$

When probes are biased with respect to the ambient plasma, in order to equilibrate, they must gather charge carriers of opposite polarity. Thus, conductivity observations made using this technique are polar (not total) measurements. The total conductivity is the sum of the conductivity due to both positive and negative charge carriers.

$$\sigma = \sigma_+ + \sigma_- = \frac{\varepsilon_o}{\tau_+} + \frac{\varepsilon_o}{\tau_-} \qquad \textbf{(2-8)}$$

In the stratosphere near 33 km, there are very few free electrons and essentially all of the charge carriers are positive and negative ions. Since the average mass and number density of negative and positive ions are nearly equal in the stratosphere, roughly half of the conductivity is a result of each polarity charge carrier. Figure 2.3.1 shows an example of a relaxation curve from which a time constant and conductivity are calculated. Large electrical bursts, large leakage currents, screening layers, and photoemission across the relay can all lead to inaccurate measurements of the conductivity. Large electrical bursts can be due to lightning transients and can even be

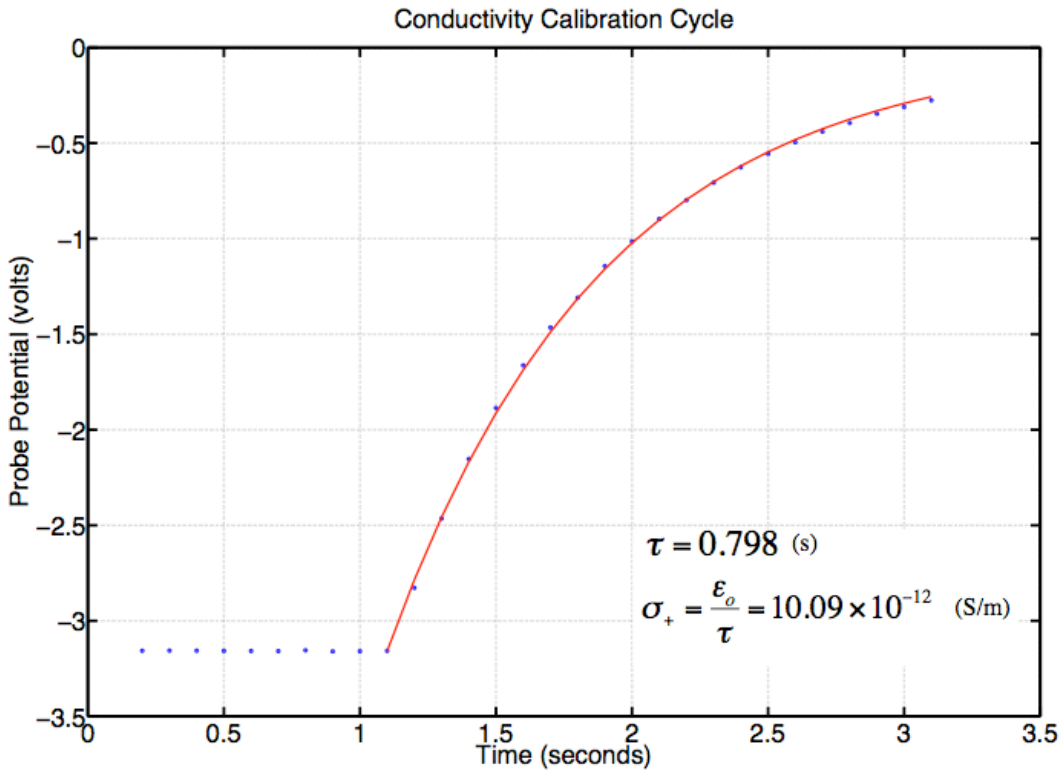

Figure 2.3.1 An example conductivity measurement. The blue dots are data points showing a negative probe bias and positive ion collection. The red line shows an exponential fit to the data (R-square = 0.99) giving a 0.798-second time constant. The exponential decay time constant that fits the curve is a negative number. However, we know that time is positive, so we use the convention where τ is positive as well.

associated with artificial discharges connected to solar panels [*Bering,* personal communication]. The MINIS payloads did not have any solar panels and were at sufficiently high latitude that there were no nearby lightning flashes. To minimize leakage currents, COTO-1240 dry reed relays with an insulation resistance of 10^{14} Ω were used. Screening layers, which build up around a biased probe, were eliminated by a constant flow of air around the probe as it floats [*Holzworth et al.*, 1986]. Photoemission can significantly affect positive conductivity. A photoemission current combined with a current of positive ions causes a probe to relax back into electrostatic equilibrium faster than just the ions. This has the effect of decreasing the relaxation time constant, from which an artificially high positive conductivity can be calculated. [*Byrne et al.*, 1990] determined that under normal circumstances, this photoemission effect is less than 10%

during the daytime for Aquadag-covered spherical probes. The negative conductivity is not subject to the same contamination because the probe is biased positively. When electrons are photo-emitted, they do not have enough energy to surpass the electrical force pulling them back to the probe. Thus, the emitted electrons return to the probe surface resulting in a zero net current.

2.4 Performance of Electric Field Instrumentation

2.4.1 Oscillations in the Vertical DC Electric Field

The vertical electric field data from MINIS Flight 2 South is extremely noisy throughout the entire flight. The noise is in the form of a quasi-periodic oscillation with an amplitude of hundreds of millivolts. Figure 2.4.1 shows MINIS Flight 2 South raw vertical electric field data and payload rotation at 01:35 UT on January 20th, 2005, before the solar energetic particle (SEP) event onset (discussed in Chapters 4 and 5). The rotation is seen as an oscillation of horizontal geomagnetic field in the payload reference frame. There is a clear correlation between the payload rotation and the oscillation in the vertical electric field data. At the SEP event onset, there are drops in the vertical dc electric field magnitude and the noise amplitude.

In order to produce the one-minute averaged vertical electric field data shown in Figure 2.4.2 and again in Figure 4.2.6, calibration ground levels were subtracted from the raw data in Figure 2.4.1 and then averaged in one-minute moving boxes. The result is a less noisy dataset that captures the basic downward-pointing fair weather return electric field (before the SEP event). A comparison of the raw and one-minute averaged data for the first half of January 20th, 2005 can be seen in Figure 2.4.2. The raw electric field oscillations have a much smaller amplitude after the SEP event onset, which leads to much less noisy one-minute averaged data. Here, we show that photoelectron emission could produce potential differences larger than the oscillations observed (shown in Figure 2.4.1) at the payload rotation frequency. This simple model does not account for all aspects of

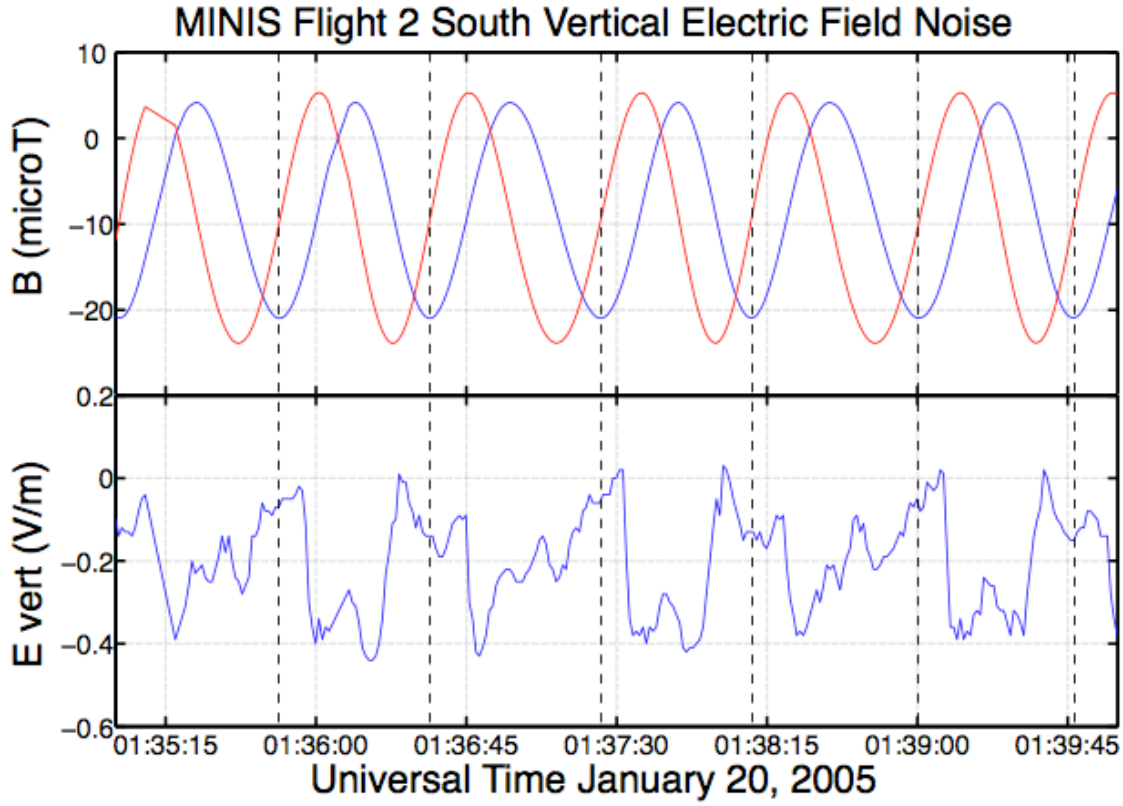

Figure 2.4.1 MINIS Flight 2 South horizontal magnetic and raw vertical electric field. Magnetic field is shown in the top panel and raw vertical electric field is at the bottom. There is a component of the rotation frequency of the payload in the vertical electric field oscillation. The vertical dashed lines mark when the x-axis (blue) of the payload was pointing south.

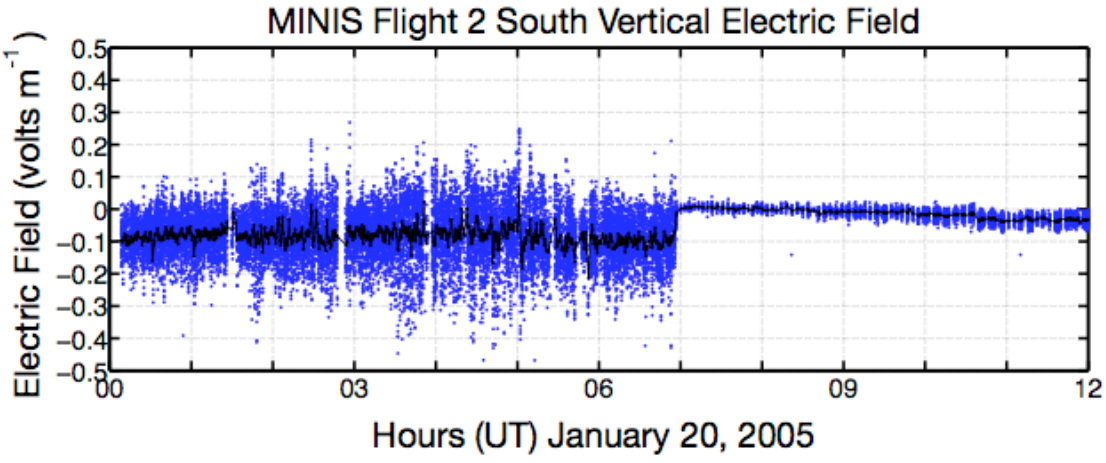

Figure 2.4.2 MINIS Flight 2 South raw vertical electric field and one-minute averaged data. Raw data is shown in blue and the averaged data is in black.

the vertical electric field noise, but provides an example of the kind of mechanism that could produce a similar signature in the dataset.

If the two MINIS Flight 2 South vertical electric field probes had the same, uniform surface work function, then as the probes rotated in the sunlight, there would be a constant, equal flow of photoelectrons off each probe, charging them both positive. This positive charge would then be eliminated by a potential difference measurement because both probes would be charged by the same amount. However, if the two probes did not have the same uniform surface work function, then as the payload rotated, the positive charge on the two probes could have become unequal, thereby distorting the potential difference measurements. At the balloon altitude, ultraviolet photons between 180 nm and 230 nm are the primary source of photoemission [*Byrne et al.,* 1990]. The average photon energy (e.g., for a 200nm photon) is 6.2 eV. The most energy an emitted photon could have is equal to the initial photon energy minus the surface work function. Work functions of aluminum and Aquadag are 4.2 eV and 4.6 eV, respectively. Therefore, the absolute maximum possible potential that could build up on an Aquadag surface is 2 volts. In a model by *Byrne et al.* [1990], the maximum positive probe potential was estimated to be 1 volt. The maximum probe potential caused by photoemission is an order of magnitude larger than the oscillations seen in the vertical electric field data of 100-200 mV. Therefore, it is entirely plausible that a non-uniform work function on the vertical probes could have caused 100 mV oscillations in the vertical data at the spin period.

A photoemission source is also consistent with a drop in the noise after the SEP event onset. When the conductivity increases by a factor of 20 (as shown in Figure 4.2.3), the photoemission charge can only accumulate for $1/20^{th}$ the amount of time as it could before the SEP event onset (as discussed in Section 2.3). Accordingly, the potential difference that can develop as a result of photoemission decreases by a factor of 20. This would

take a 300 mV p-p oscillation and reduce its magnitude to 15 mV p-p. Directly after the SEP event onset, the oscillations measure approximately 25 mV p-p.

The MINIS electric field probes were made of porous foam, making a uniform cover of Aquadag difficult to attain and uniformity difficult to evaluate before launch. Additionally, there where other objects on the balloon payload load line that could have also charged due to photoemission including the rotation motor, metal electronics instrumentation housing and the Iridium antenna. Previous University of Washington balloon campaigns with double Langmuir probe dc electric field instrumentation, where there were no vertical oscillations like those in the MINIS data, have used metal probes as opposed to porous foam ones. Similar vertical oscillations can be found in the vertical dc electric field data from MINIS Flight 1 South and Flight 3 South. Poor quality double-sided probe data from Flight 4 South make it difficult to ascertain if there are oscillations in data from this flight as well. For each flight, the amplitude of these oscillations is similar (within a factor of ~2). This plausibility discussion is not, by itself, capable of describing all of the vertical dc electric field noise. For example, one argument against photoemission as a source of noise in the vertical electric field is lack diurnal signal coinciding with a modulation in ultraviolet photon flux present in any payload data. Without knowing the precise noise source, the best option is to remove as much of the contamination as possible, as shown in Figure 2.4.2.

2.4.2 Horizontal DC Electric Field Instrumentation Functioning Properly Before and After Solar Energetic Particle Event Onset

The horizontal dc electric field data from MINIS Flight 2 South does not have the same noise as the vertical data. However, the magnitude of the horizontal field drops to zero at SEP event arrival. (See Figure 4.2.5.) We show that the instrumentation appears to be working continuously from before the SEP event onset onward. In order to remove any

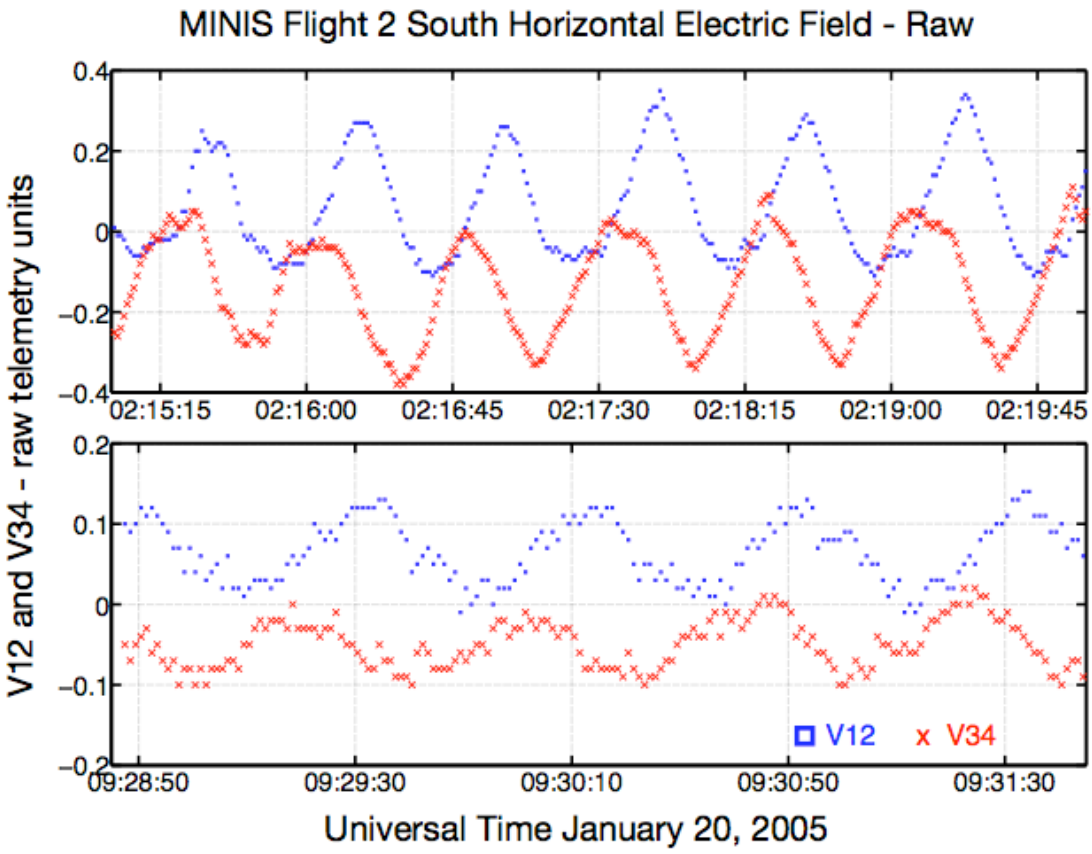

Figure 2.4.3 Raw horizontal electric field data showing instrumentation measurement of slowly-varying geophysical field. Data are from several hours before SEP event onset (top) and several hours after (bottom). The blue squares are data from probes 1 and 2 in the x-axis of the payload frame and the red x's are data from probes 3 and 4 in the y-axis.

non-geophysical dc offsets in the horizontal electric field data, the MINIS payloads were rotated about a vertical axis. Any slowly varying horizontal electric field can be seen in the data as a sinusoidal oscillation. If the electric field is a real geophysical field, the sinusoids from the two sets of orthogonal horizontal probes will be consistently 90° out of phase. Figure 2.4.3 contains two examples of periodic sinusoids that show that the horizontal probes were measuring a slowly varying electric field. The line series show raw telemetered values representing potential differences between the two orthogonal pairs of horizontal probes before any post-processing. The difference in rotation period occurred because the rotation motor spun slower in colder temperatures (night time). There is a constant 90-degree phase shift between the two line series in each plot. This

confirms that the probes are indeed measuring a real, slowly varying external electric field because each orthogonal set of probes measures a maximum (for instance) 90-degrees out of phase with each other. DC offsets occur when the payload is off-balance and the vertical component of the electric field (which generally has a much larger amplitude than the horizontal components in fair weather) is projected onto the horizontal plane of the payload. The top panel of Figure 2.4.3 shows a time period before the SEP event onset and the bottom panel shows a time period after onset. This provides a high degree of confidence that this instrument was working correctly throughout the flight.

2.5 Additional MINIS Balloon Payloads Systems

2.5.1 X-Ray Spectrometer

Onboard each MINIS payload was an x-ray spectrometer used to detect bremsstrahlung x-rays from precipitating relativistic electrons. Each spectrometer had a (three inch diameter by three inches tall) cylindrical scintillator crystal made of sodium iodide (NaI) and an attached photomultiplier tube (PMT). (See Figure 2.5.1.) When x-rays pass through the NaI crystal, small pulses of visible light are emitted based on the amount of energy deposited. The PMT then converts the light pulse into an amplified electronic signal, which is then passed to further electronics for counting and sorting.

The MINIS x-ray spectrometer electronics provided two different output products. High energy-resolution spectra were provided every 8 seconds while high time-resolution light curves were provided every 50 milliseconds. Simultaneous high time and energy resolution was not possible due to telemetry limitations. The high energy-resolution spectra had 208 separate energy bins. These bins covered energy ranges from 20 keV all the way to 10 MeV. Alternately, the light curves had only four energy bins: 20–175 keV, 175–540 keV, 540–825 keV and 825–1500 keV. *McCarthy and Parks* [1985] provide a description of a similar instrument. *Sample* [2008] provides a more comprehensive description of the MINIS x-ray spectrometer.

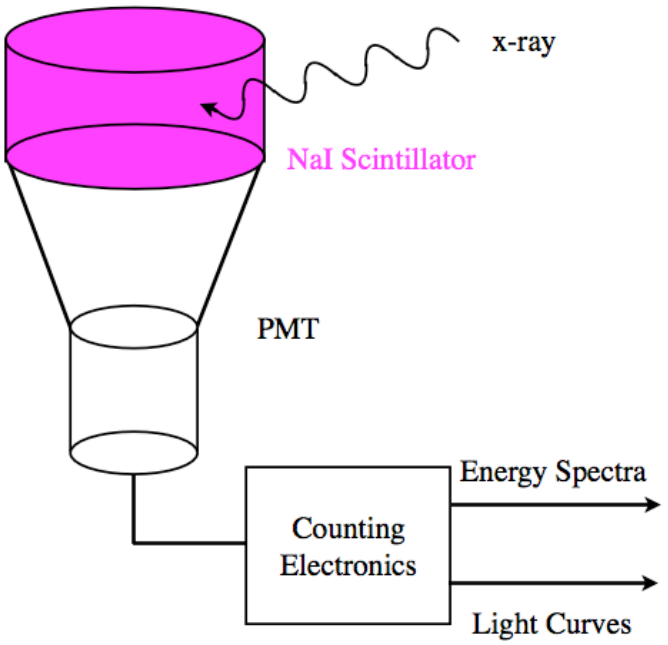

Figure 2.5.1 Cartoon of MINIS x-ray spectrometer.

2.5.2 Magnetometer

Each of the MINIS balloon payloads carried a TCM2 magneto-inductive magnetometer made by Tri-M Systems/PNI Corporation. The magnetometer was used to provide geomagnetic directional information as well as scientific data. DC magnetic field values from all three axes were sampled once per second. The horizontal axes were aligned with the electric field double Langmuir probe pairs in the horizontal plane and the positive *x* direction was aligned with probe 1. The vertical axis had positive *z* pointing down toward the ground. (See Figure 2.2.3 and Figure 2.2.4 for a diagram of the payload alignment, including magnetometer orientation.) Output from the magnetometer was in units of micro-Tesla (e.g., an output of 30 means 30 μT).

2.5.3 Telemetry System

There was no intention of recovering any of the MINIS payloads. Thus, all of the data were telemetered from each payload to a ground station at the Space Sciences Laboratory

in Berkeley, California via the Iridium Satellite Network [*Lemme et al.*, 1999]. This network is a constellation of satellites, which allow for voice and data communication through portable, handheld phones and modems. Each MINIS payload had one Iridium (NAL Research Corporation A3LA-I) modem and antenna. The average data transmission rate for the modems is 2.4 Kbits/second (as provided by the manufacturer). This is slightly more than one second of 256 bytes (2048 bits) of data that each payload was designed to send. The complete telemetry allocation can be found in Appendix B.

Aside from the limited data transmission rate, the largest problem with the Iridium telemetry was the frequency of dropped calls. The payload computer was designed to redial the ground station when a disconnection occurred. Even with this measure, data were lost throughout the flights when new calls were not successfully established before the onboard data buffer began to overwrite data which had not yet been transmitted.

One important note to make regarding data transmission by the MINIS payloads relates to gaps during a specific time period. The data acquisition systems on each payload were designed to give priority to incoming counts from the x-ray spectrometer. Essentially, all data collection would momentarily stop while x-ray counts were sent to the computer. In normal circumstances, this would not be a problem because the data acquisition system could sample each instrument and housekeeping value with plenty of time to count each x-ray pulse from the spectrometer. However, as we will discuss in later sections, when there are many more counts than expected (i.e., during a hard Solar Energetic Proton event), the data acquisition system can, and did, become overloaded. The result was that data from other instruments were lost. It initially appeared as though the telemetry failed during this time, but in fact, the problem originated with the data handling system. This happened for several hours on January 20th, 2005 for Flight 2 South.

2.5.4 Rotation Motor

Each MINIS payload was rotated about the vertical axis in order to help identify and eliminate non-geophysical electric field contamination. The desired payload rotation rate was about 2 rpm. Along with the rotation rate requirement, the motor needed to be light, cheap, operable in extreme temperatures and consume minimal power. The motor used for the main phase of the campaign was a Faulhaber/MicroMo 1524-012SR dc-micromotor (Figure 2.5.2.). The no-load rotation speed was 9,900 rpm when operating at 12 V. Combined with the motor, there was an in-line gear head with a 262:1 gear reduction (Faulhabeer 15/5 262:1). The motor/gear head package was then attached to the horizontal input of a 24:1 right angle worm gear using a flexible coupler. A large, steel bolt passed through the vertical axis of the worm gear and was coupled using a lynchpin.

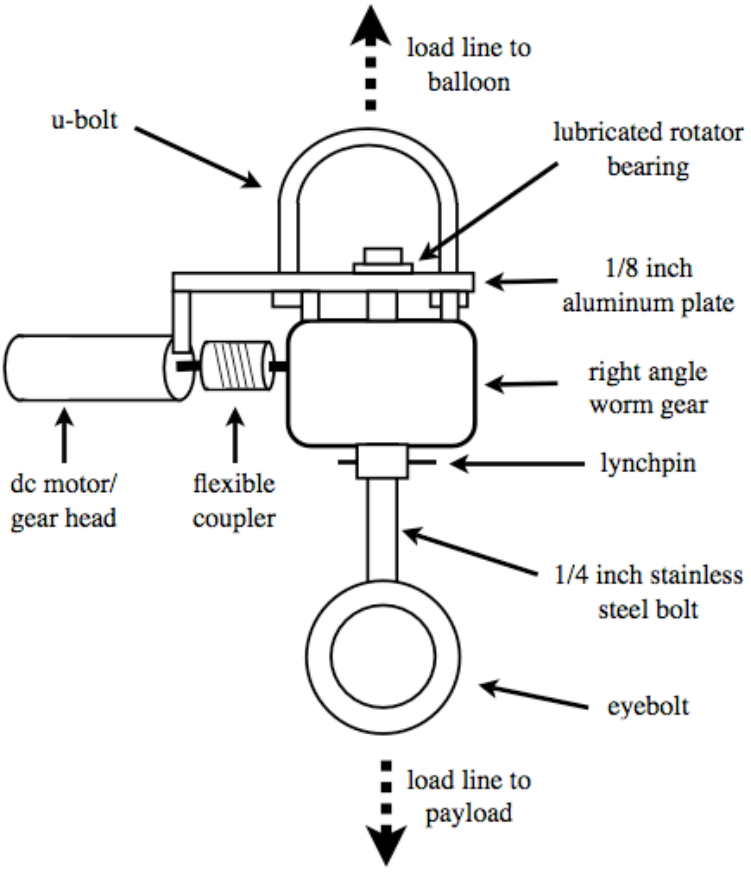

Figure 2.5.2 Diagram of the rotation motor assembly.

The payload was then suspended from an eyebolt on the bottom of the steel bolt secured by another lynchpin. All force of the payload pulling downward and the balloon tension upward was placed on an eighth inch aluminum plate.

The actual rotation rate of the payload gondola varied as a function of temperature. In pre-flight testing, the temperature seemed to affect the viscosity of the motor lubrication. When the motor and rotator bearing lubrication was replaced with synthetic automobile oil, the rotation rate became slightly less dependant on temperature. The result is that nighttime MINIS payload rotation rates were near 1 rpm and daytime rotation rates were near 2 rpm.

2.5.5 GPS, Housekeeping and Remaining Instruments

One key instrument, crucial to the success of the MINIS campaign, was a GPS receiver used for location finding. The receiver used for each payload was a Lassen SQ GPS Receiver. The GPS data were telemetered once every 15 seconds giving latitude, longitude and altitude. A suite of housekeeping voltages were regularly telemetered to keep a record of instrument operation conditions. A complete list of all data telemetered can be found in Appendix B.

In addition to the instrument systems listed above, the southern MINIS balloon payloads each carried sun sensors and very low frequency (VLF) electric and magnetic field filters. The sun sensors were simply photodiodes with orthogonal look directions. Their purpose was to provide calibration and backup to the magnetometer, which provided directional information. Thus far, the sun sensor data have been used solely for general comparison with magnetometer data for spin-rate analysis. The VLF field filters were attached to a magnetic search coil and to one set of electric field potential difference output (before the cut off filter in the electric field circuit). Despite pre-flight testing and calibration, none of the VLF filters appear to have provided any useful data.

2.6 Complementary Data Sources

In this section we will briefly describe the instruments used to gather complementary data used to put the MINIS observations into the larger context of global geophysical dynamics. The MINIS team did no direct work on any of the instruments described here. For each instrument, we will simply provide a basic overview of the instrument, references for further reading and locations where data can be found on the internet.

2.6.1 ACE Satellite Solar Wind Instrument

The Advanced Composition Explorer (ACE) satellite was launched in August 1997 with the primary goal of measuring solar wind characteristics. A review article describing the mission in detail was written by *Stone et al.* [1998]. ACE orbits the L1 Lagrange point (a point in space between the sun and the earth where gravitational and centripetal forces balance) upstream of the earth about 235 earth radii. At this location, the various instruments can measure solar wind characteristics including composition, velocity, density, magnetic field orientation and energetic particle flux. All of the data can be found in online data centers managed by the National Oceanic and Atmospheric Administration Space Environment Center [*NOAA/SEC*, 2008]. Data used in our analysis come from the Solar Wind Electron, Proton and Alpha Monitor (SWEPAM) and the ACE/MAG three axes fluxgate magnetometers.

2.6.2 POES Energetic Proton Detector

The Polar Operational Environment Satellites (POES) are a constellation of polar, low earth orbiters. They each contain a large suite of instruments for earth observation and polar space environment observation. Each satellite completes an orbit in 102 minutes at an altitude of 833 km at an inclination of 81º [*NASA/POES*, 2008]. At the time of the MINIS balloon campaign, there were three POES satellites in operation (NOAA 15, 16 and 17). For our study, we focus on the Space Environment Monitor (SEM) package and in particular, the Medium Energy Proton and Electron Detector (MEPED). The MEPED instrument has three electron telescope channels (30-1100 keV, 100 - 1100 keV and 300 –

1100 keV) and six proton telescope channels (30 – 80 keV, 80 – 250 keV, 250 – 800 keV, 800 – 2500 keV, 2500 – 6900 keV and > 6900 keV). Additionally, there is a set of omni-directional proton detectors, which detect higher energy protons (> 16 MeV, 35 MeV, > 70 MeV, and > 140 MeV). A detailed description of all the SEM instruments and data products is given by *Evans and Greer* [2000].

2.6.3 GOES Particle Detector and Magnetic Field Instrument

The Geosynchronous Operational Environment Satellites (GOES) are very similar to their polar-orbiting relatives, POES. The primary difference between the two constellations is the orbit. GOES are in a geo-stationary orbit. Thus, each GOES satellite remains at the equator ~6.7 earth radii away from the center of the earth. However, GOES and POES have similar Space Environment Monitor (SEM) packages [*NASA/GOES*, 2008]. For this analysis, we focus on the high-energy protons and electrons. GOES has 11 differential proton channels. We have used data from the three telescope (0.8 - 4 MeV, 4 - 9 MeV and 9 - 15 MeV) and four dome (15 – 40 MeV, 40 – 80 MeV, 10 – 165 MeV and 165 – 500 MeV) channels. There are three energetic electron dome detector channels (≥ 0.6 keV, ≥ 2 MeV and ≥ 4.0 MeV). In addition to telescope and dome detectors, there is a separate solid state High-Energy Proton and Alpha Detector (HEPAD), which has a dynamic range for both protons (350 - >700 MeV) and alpha particles (4 - > 3400 MeV). Along with the particle detector, each GOES satellite has an x-ray detector with two wavelength bands. Flux is measured in short (0.5 – 3 Å) and long (1 – 8 Å) bands using two different ion chambers. The last instrument that we utilize is the three-axis magnetometer. The GOES magnetometer data product gives the three components of the magnetic field as H_p (parallel to the satellite/earth spin axis), H_e (earthward), and H_n (normal to H_p and H_e, westward). A complete GOES data book describing each instrument on the GOES platform was prepared by Loral Space Systems and NOAA for NASA [*Hawkins*, 1996].

2.6.4 IMAGE Extreme Ultra-Violet Imager

The Imager for Magnetopause-to-Aurora Global Exploration (IMAGE) satellite was launched in March, 2000 with a mission to observe plasma dynamics through various imaging techniques including energetic neutral atom (ENA) emissions, plasmaspheric imaging in the extreme ultraviolet (EUV) and auroral emissions in the far-ultraviolet (FUV). IMAGE has a very elliptical orbit with an apogee of 7.2 earth radii so that it can capture images of an entire polar cap and plasmasphere in one frame. A compete mission overview is given by *Burch* [2000] and the more information can be found at the Southwest Research Institute's IMAGE page [*SwRI*, 2008]. IMAGE was operational during the MINIS balloon campaign in January, 2005. In this thesis, we will present images of the FUV proton aurora as well as the plasmasphere.

2.6.5 SuperDARN Polar Ionospheric Radars

The Super Dual Auroral Radar Network (SuperDARN) is comprised of twelve northern hemisphere and seven southern hemisphere high frequency (HF) ionospheric radars. A review of the most recent decade of SuperDARN operation is given by *Chisham et al.* [2007]. The individual radar sites are established to maximize the field of view of the entire network. The basic mode of operation of the system involves sending short pulses in the HF band and listening for echoes. An auto correlation function, based on the doppler shift of the sequence pulse echoes, allows for back-scattered power and doppler velocity of plasma irregularities to be determined. Polar circulation can be estimated by combining the doppler velocity measurement from the whole array with an empirical model. Large-scale plasma circulation patterns can help describe the global magnetosphere-ionosphere current flow. SuperDARN data products, including convection maps for northern and southern hemispheres, can be found at the Johns Hopkins Applied Physics Laboratory SuperDARN web site [*JHU/APL*, 2008].

2.6.6 IMAGE Ground-Based Magnetometer Array

The International Monitor for Auroral Geomagnetic Effects (IMAGE) is a ground-based

magnetometer array located in northern Europe. (Not to be confused with the IMAGE satellite.) The array covers geographic latitudes from 58º to 79º north. Each fluxgate magnetometer provides a three-axis magnetogram in an X (north), Y (east) and Z (downwards) component system. A complete description of the magnetometer chain, including station locations and access to data can be found at the Finnish Meteorological Institute's IMAGE website [*FMI*, 2008].

3 An Atmosphere-Ionosphere Electrical Conductivity Model

In this chapter, we discuss a conductivity model that uses several standard, freely available atmospheric, ionospheric and magnetic field models as well as the relatively new Sodankylä Ion Chemistry (SIC) model. Our conductivity model can be applied at any location on earth at a specific time for altitudes between 20 km and 120 km and can include SEP-induced ionization effects. There are atmospheric conductivity models based on neutral atmospheric scale-height assumptions [*e.g., Dejnakarintra,* 1974]. Additionally, there is a global, semi-empirical model by Hu [1994] that estimates conductivity at 26 km altitude as a function of geomagnetic latitude and longitude. However, there is no published model that provides location and altitude information as the model we present here.

We present theory that explains conductivity above 20 km in a collisional plasma in Section 3.1. With expressions for the different conductivity components in hand, we move on to describe the various models we utilize to build our conductivity model. In Section 3.2, we describe the Mass Spectrometer – Incoherent Scatter (MSIS) model and the International Reference Ionosphere (IRI) model. In Section 3.3, we discuss the SIC model with a special emphasis on how it incorporates ionization caused by energetic proton precipitation. The ability to include effects of energetic protons is a relatively new SIC model feature. We present examples of our new, complete conductivity model in Section 3.4. Lastly, in Section 3.5, we present suggestions for adding functionality to the SIC model by: A) using data from polar orbiting as opposed to geosynchronous satellites for proton input into the atmosphere; B) changing the routine for converting integral into differential proton flux; and C) including energetic electron precipitation as an additional ionization source term.

3.1 Electrical Conductivity within a Plasma

Electrical conductivity is the measure of a medium's ability to conduct an electric current.

Conductivity values are extremely important for understanding nearly every aspect of electrical phenomena in the atmosphere, ionosphere and the magnetosphere. There are many examples of how conductivity influences the electrodynamics of thunderstorm activity, the global electric circuit, particle precipitation, ionospheric current flow and geomagnetic storm processes [e.g., *Hale et al.*, 1981; *Holzworth et al.*, 1985; *Kirkwood et al.*, 1988; *Driscoll et al.*, 1992; *Rycroft et al.*, 2000; *Galand and Richmond*, 2001; *Holzworth et al.*, 2005]. Indeed, conductivity is such a fundamental quantity that within the context of this dissertation, we will touch on how polar atmospheric and ionospheric conductivity relates to each of the processes listed above with the exception of thunderstorms.

The medium we are considering is the plasma in the collisional atmosphere and ionosphere. By collisional atmosphere, we mean the region of the atmosphere where there are no free electrons (generally below 60 km) and we neglect the altitudes below 20 km because of modeling limitations that will be made clear later. In the strictest sense, the collisional atmosphere is not a traditional plasma because there are no free electrons. However, we can describe conductivity of these neighboring regions in a similar way.

We begin with a general statement of current density $\vec{J}_s$ for a single charged particle species *s*.

$$\vec{J} = n_s q_s \vec{u}_s \tag{3-1}$$

Here, n_s and q_s are the number density and charge of the species *s*, respectively. The vector velocity of the particle species is given by $\vec{u}_s$, which depends on any applied external forces and mobility (defined below). We define $\vec{u}_s$ in the presence of an external force $\vec{F}$ and with mobility k_s as follows.

$$\vec{u}_s = k_s \frac{\vec{F}}{q_s} \tag{3-2}$$

Mobility is defined in terms of the particle charge, mass $m_s$and the collision frequency

ν_{sn} between the charged species and neutrals.

$$k_s = \frac{q_s}{m_s \nu_{sn}} \tag{3-3}$$

For our purposes, we are interested in an electromagnetic force, which we insert, along with our expression for mobility, into Equation (3-2).

$$\vec{u}_s = \frac{q_s}{m_s \nu_{sn}} (\vec{E} + \vec{u}_s \times \vec{B}) \tag{3-4}$$

Then, we can combine Equations (3-1) and (3-4) to get an expression for the current density comprised of charged particles of species *s*.

$$\vec{J}_s = n_s q_s \vec{u}_s = \frac{n_s q_s^2}{m_s \nu_{sn}} (\vec{E} + \vec{u}_s \times \vec{B}) \tag{3-5}$$

Equation (3-5) is a vector equation comprised of three separate components. We make a simplifying assumption that the magnetic field is only in the $\hat{z}$ direction. This is nominally the case in the polar regions, where the earth's magnetic field is nearly vertical. Using this assumption, we can break Equation (3-5) into Cartesian $\hat{x}, \hat{y}$ and $\hat{z}$ components.

$$\begin{aligned} J_{s,x} &= n_s q_s u_{s,x} = \frac{n_s q_s^2}{m_s \nu_{sn}} (E_x + u_{s,y} B_z)\, \hat{x} \\ J_{s,y} &= n_s q_s u_{s,y} = \frac{n_s q_s^2}{m_s \nu_{sn}} (E_y + u_{s,x} B_z)\, \hat{y} \\ J_{s,z} &= n_s q_s u_{s,z} = \frac{n_s q_s^2}{m_s \nu_{sn}} E_z\, \hat{z} \end{aligned} \tag{3-6}$$

The set of three equations in (3-6) have three unknown velocity components. After a bit of algebra, we can eliminate each velocity component such that we are left with expressions for the current density in terms of known quantities.

$$\begin{aligned} J_{s,x} &= \frac{n_s q_s^2}{m_s} \left[\left(\frac{\nu_{sn}}{\nu_{sn}^2 + \Omega^2} \right) E_x + \left(\frac{\Omega_s}{\nu_{sn}^2 + \Omega_s^2} \right) E_y \right] \\ J_{s,y} &= \frac{n_s q_s^2}{m_s} \left[\left(\frac{\nu_{sn}}{\nu_{sn}^2 + \Omega_s^2} \right) E_y - \left(\frac{\Omega_s}{\nu_{sn}^2 + \Omega_s^2} \right) E_x \right] \\ J_{s,z} &= \frac{n_s q_s^2}{m_s \nu_{sn}} E_z \end{aligned} \tag{3-7}$$

We have taken advantage of the definition of gyrofrequency for a charged particle in the presence of a magnetic field $\Omega_s = \frac{q_s|B|}{m_s}$. Equation (3-7) is a complete, though cumbersome expression for the current density. We can construct a conductivity tenser such that all of the information in Equation (3-7) is expressed in a simple, compact version of Ohm's law. Let us make the following substitutions.

$$\sigma_{P,s} = \frac{n_s q_s^2}{m_s}\left(\frac{\nu_{sn}}{\nu_{sn}^2 + \Omega_s^2}\right) \tag{3-8}$$

$$\sigma_{H,s} = \frac{n_s q_s^2}{m_s}\left(\frac{\Omega_s}{\nu_{sn}^2 + \Omega_s^2}\right) \tag{3-9}$$

$$\sigma_{0,s} = \frac{n_s q_s^2}{m_s \nu_{sn}} \tag{3-10}$$

Equations (3-8), (3-9) and (3-10) are called the Pedersen, Hall and parallel (to the magnetic field) conductivity for a single charged particle species, respectively. Using these substitutions, we can now construct a compact version of Ohm's law with a tenser conductivity $\ddot{\sigma}_s$.

$$\vec{J}_s = \ddot{\sigma}_s \bullet \vec{E}; \qquad \ddot{\sigma}_s = \begin{bmatrix} \sigma_{P,s} & \sigma_{H,s} & 0 \\ -\sigma_{H,s} & \sigma_{P,s} & 0 \\ 0 & 0 & \sigma_{0,s} \end{bmatrix} \tag{3-11}$$

Accounting for all charged particle species, we simply sum the contribution for each individual species.

$$\vec{J} = \sum_s \vec{J}_s = \sum_s \ddot{\sigma}_s \bullet \vec{E} = \ddot{\sigma} \bullet \vec{E} \tag{3-12}$$

$$\ddot{\sigma} = \sum_s \ddot{\sigma}_s = \sum_s \begin{bmatrix} \sigma_{P,s} & \sigma_{H,s} & 0 \\ -\sigma_{H,s} & \sigma_{P,s} & 0 \\ 0 & 0 & \sigma_{0,s} \end{bmatrix} = \begin{bmatrix} \sigma_p & \sigma_H & 0 \\ -\sigma_H & \sigma_P & 0 \\ 0 & 0 & \sigma_0 \end{bmatrix} \tag{3-13}$$

Our final form of Ohm's law with a complete conductivity tenser becomes

$$\vec{J} = \vec{\vec{\sigma}} \bullet \vec{E}; \qquad \vec{\vec{\sigma}} = \begin{bmatrix} \sigma_P & \sigma_H & 0 \\ -\sigma_H & \sigma_P & 0 \\ 0 & 0 & \sigma_0 \end{bmatrix} \qquad \textbf{(3-14)}$$

The terms along the diagonal allow for current flow in the direction of the electric field, while the Hall term allows for current flow perpendicular to both $\vec{E}$ and $\vec{B}$. If the collision frequency is significantly large ($\nu_{sn} >> \Omega_s$), then the Pedersen conductivity term simply reduces to the parallel term and the Hall term is smaller yet by a factor of (Ω_s / ν_{sn}). Thus, in the collisional atmosphere, we can approximate Equation (3-14) with a scalar equation.

$$\vec{J} = \sigma \vec{E}; \qquad \sigma = \sum_s \frac{n_s q_s^2}{m_s \nu_{sn}} \qquad \textbf{(3-15)}$$

The diagonal terms of the tenser conductivity all reduce to the same expression, which we call the collisional conductivity. We can ignore the Hall cross term because $(\Omega_s / \nu_{sn}) << 1$. Conversely, if the cyclotron frequency is large ($\Omega_s >> \nu_{sn}$), then the Hall term reduces to $\sigma_H = n_s q^2 / m_s \Omega_s$ and the Pedersen term is smaller by a factor of (ν_{sn} / Ω_s). The reduced Hall term is simply another way of expressing $\vec{E} \times \vec{B}$ guiding center drift. We can estimate where the maximum Pedersen conductivity will be by setting its first derivative to zero and holding Ω constant (which is nearly true for an altitude profile between 20 – 150 km in a given location since the magnitude of the magnetic field is almost constant). This estimation excludes an effects of hydration, which can increase the charge-carrier mass and increase the gyrofrequency. The result is that we get a maximum Pedersen conductivity when the collision and cyclotron frequencies are equal $(\nu_{sn} = \Omega_s)$. Figure 3.1.1 shows calculated collision and cyclotron frequencies for electrons and constituent ions. (We will discuss models used to make these calculations in the coming sections.) We can see that we expect local maxima for the Pedersen conductivity at 70 km (due to electrons) and just above 120 km (due to ions). The ion-neutral collision frequency is much smaller at 120 km than the electron-neutral collision frequency is at 70 km.

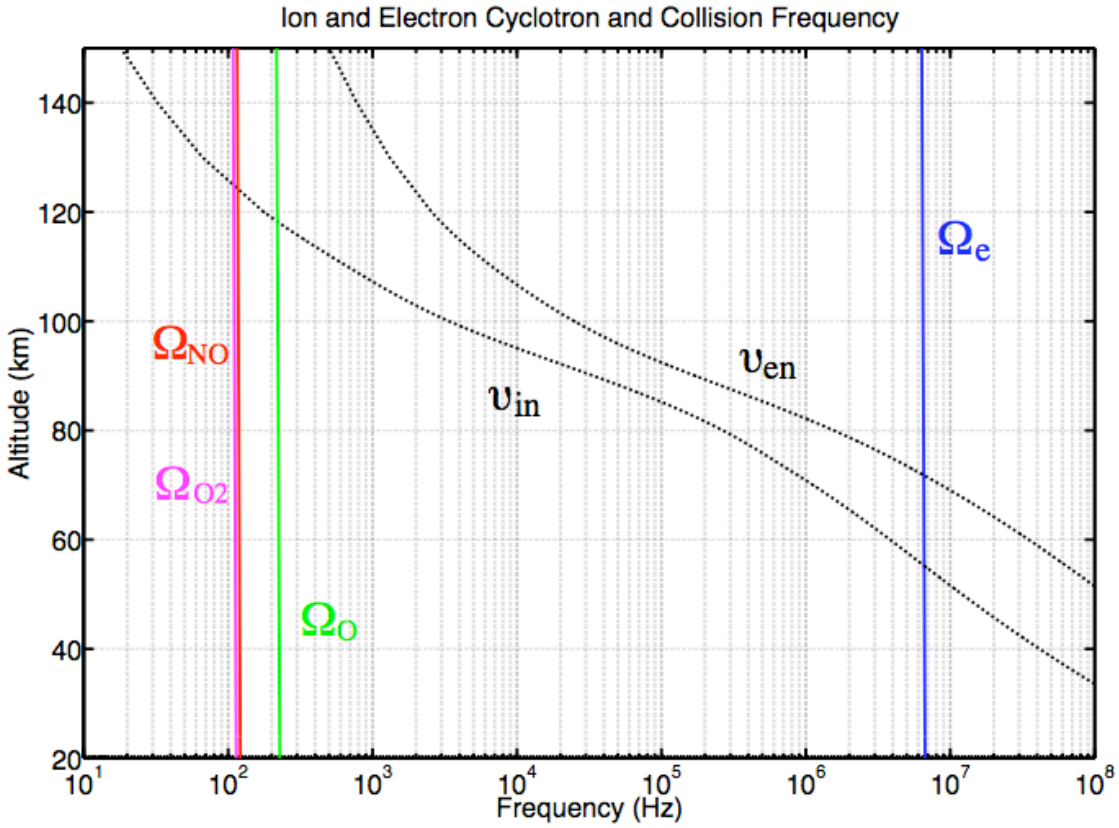

Figure 3.1.1 Ion and electron cyclotron and collision frequencies as a function of altitude. Collision frequencies are the dashed black lines. Electron cyclotron frequency is the solid blue line and ion cyclotron frequencies for O2, NO and O ions are given by solid magenta, red and green lines, respectively. These values are computed using MSISE-90 neutral density and temperature profiles for 70º S, 345º E, 06:00 UT January 20th, 2005.

3.2 Models of Neutral, Ion and Electron Density Profiles

When looking at the equations in the previous section, it is clear that in order to calculate atmospheric and ionospheric conductivity at a given location, we need to know about the neutral and charged populations. Because it is impossible to make simultaneous measurements on a fine, global scale, we must use models to estimate neutral and charged population characteristics. We use the Mass Spectrometer – Incoherent Scatter (MSIS, specifically MSISE-90) model for neutral atmosphere composition, density and temperature. For the ionosphere above 120 km, we use the International Reference Ionosphere (IRI) model for charged particle composition, density and temperature. From

20 km to 150 km (in some cases 120 km), we use the Sodankylä Ion Chemistry (SIC) model for charged particle composition and density. Each of these three models is described in the following sub-sections.

3.2.1 MSISE-90 Neutral Atmosphere Model

The original Mass Spectrometer – Incoherent Scatter (MSIS) model was first introduced in a pair of papers by *Hedin et al*. [1977a; 1977b]. The basis of this empirical model comes from mass spectrometer measurements of N_2 from five different spacecraft (AE-B, Ogo 6, San Marco 3, Aeros A and AE-C) and temperature measurements from four incoherent radar ground stations (Arecibo, Jicamarca, Millstone Hill and St. Santin) during an epoch that spans 1965 to 1975. MSIS sorted the data into different regimes based on latitude, altitude, average UV flux (given by $\overline{F}_{10.7}$), day of the year, local time, UV flux deviation from the average ($F_{10.7} - \overline{F}_{10.7}$) and geomagnetic activity (A_p index). The output of the model provided global temperature and N_2 density, which resolved annual, seasonal, diurnal and semi-diurnal fluctuations. The original model also output global O, He, Ar, O_2 and H densities to varying degrees of accuracy. The 1980s saw improvements to the original MSIS formulation, which included more satellite data, rocket composition data as well as re-evaluation and addition of empirical fit constants [*Hedin*, 1983; 1987]. MSISE-90, the version used in this analysis, extended the range of the previous (MSIS-86) model into the mesosphere and lower atmosphere. Most of the data used for the extension came from the Middle Atmosphere Program 16 Handbook [*Barnett and Corney*, 1985]. A complete description of the MSISE-90, along with various error estimates can be found in a paper by *Hedin* [1991]. The best estimate for errors in density below 90 km is 5% whereas above 90 km errors are estimate to be as high as 20% (and could be a result of lightning activity). The MSISE-90 model can be downloaded or run in an online version through NASA's Model Web [*GSFC*, 2008]. Figure 3.2.1 shows number density of O, N_2 and O_2 as well as temperature from the ground to 350 km for a specific location and time (70º S, 345º E, 0600 UT January 20th, 2005).

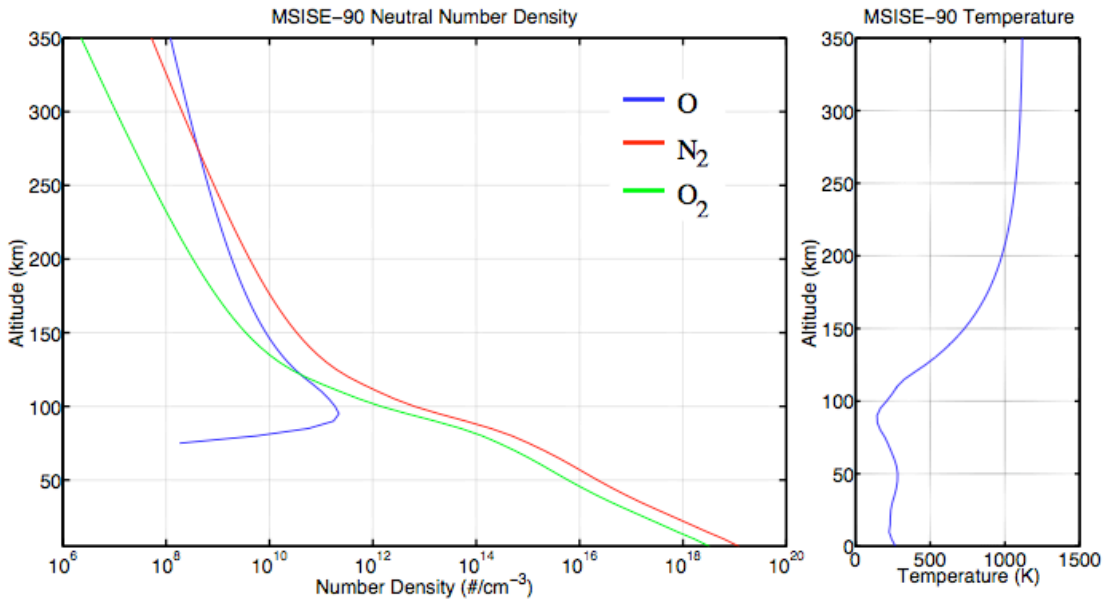

Figure 3.2.1 MSISE-90 number density and temperature. On the left, densities of O, N_2 and O_2 in cm^{-3} and on the right, temperature in Kelvin. Each is given as a function of altitude for 70º S, 345º E, 06:00 UT January 20th, 2005.

There is a newer version of the MSIS model, NRLMSISE-00, developed by the Naval Research Laboratory. This newest version was not used for conductivity modeling for consistency with the SIC model, which uses the MSISE-90 version.

3.2.2 International Reference Ionosphere Model

The International Reference Ionosphere (IRI) is the standard model used for specification of ionospheric parameters. It has been described by working groups of the Committee On SPAce Research (COSPAR) and the International Union of Radio Science (URSI) as the "best of the best" [*Szuszczewicz et al.*, 1998]. The IRI model describes the ion and electron densities, temperatures and velocities. Much like the MSIS model, the IRI is constantly being upgraded. However, the basic function of the model remains consistent. The main external drivers for the IRI model are sunspot number (R) and solar radio flux ($F_{10.7}$) [*Bilitza*, 2001]. $F_{10.7}$ solar radio flux is used as a proxy for EUV ionizing solar radiation because EUV cannot be monitored from the ground and there are no long-term

(greater than one solar cycle) space-based EUV records. (NASA's TIMED spacecraft was launched in 2001 and has a EUV sensor. This data has not yet been incorporated into the IRI model.) Sunspot number and $F_{10.7}$ radio flux have long ground-based data records. The IRI model is capable of describing long-term (yearly) ionospheric parameters and is less accurate in shorter timescales (i.e., monthly, weekly, daily) [*Bilitza*, 2001]. Therefore, in order to gain better temporal resolution, other drivers are being investigated and added. These include the global ionospheric index (*IG*) [*Liu et al.*, 1983] derived from representative radiosonde data as well as total electron content from GPS satellites.

Comprehensive error estimates for IRI output parameters are not well defined because the IRI model is a collection of other models designed to work under various conditions in different ionospheric regions. However, to get an idea of the error associated with our use of the IRI model, let us look at electron density in the least well-defined regions: the D and E regions. The natural electron density at a particular altitude in these regions can vary by more than three orders of magnitude due to day-night asymmetries, seasonal and solar cycle dependences, and geomagnetic activity. There have been a large number of observations (~275 rocket flights launched from a handful of locations) of these variable regions aimed at characterizing spatial and temporal fluctuations. With this in mind, let us look at summertime D-region electron density measurements along with IRI model predictions in Figure 3.2.2 [based on *Danilov et al.*, 1995]. This figure shows that although there is some variability, model estimations generally agree with observations. Unfortunately, Danilov et al. did not include quantitative fit coefficients. The estimated mean error for IRI electron densities between 60 km and 120 km is a factor of 2.6 [*Friedrich and Torkar*, 2001]. *Barnum* [1999] showed that IRI-modeled peak electron densities above 200 km could be as much as a factor of 2 lower than calculations based on rocket-based whistler wave dispersion measurements. Figure 3.2.3 is a sample number

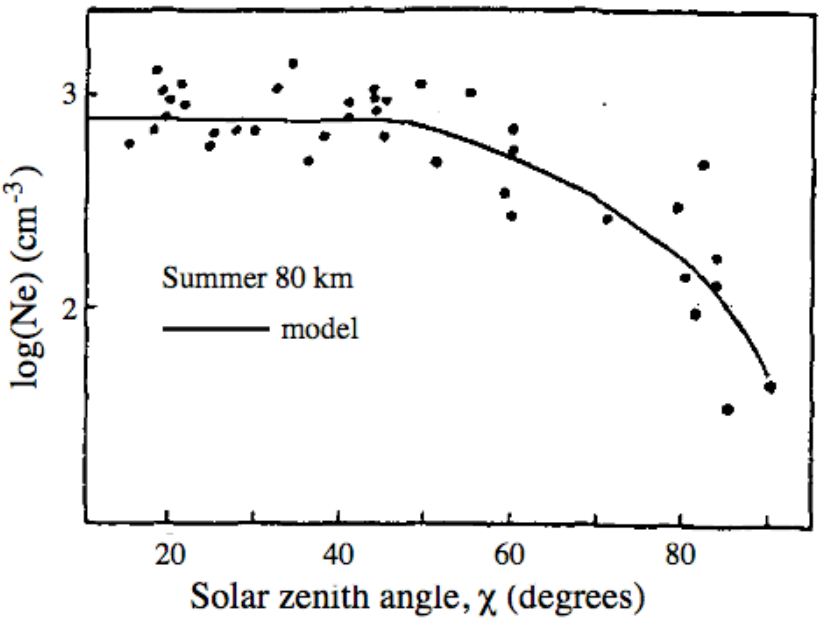

Figure 3.2.2 IRI electron density. Model output (solid line) and rocket measurements (dots) are shown in the summer time D-region at 80 km as a function of solar zenith angle. Based on *Danilov et al.* [1995].

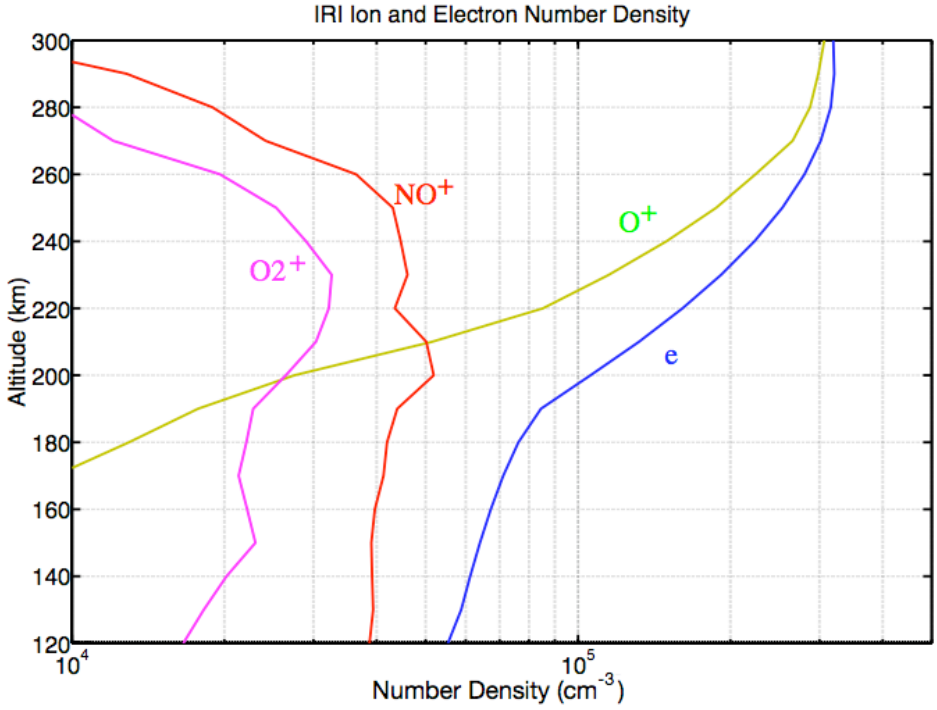

Figure 3.2.3 IRI ion and electron density. Electron (blue), O+ (green), NO+ (red) and O2+ number densities are given as a function of altitude from 120 km to 300 km. This profile is for 70º S, 345º E, 06:00 UT January 20th, 2005.

density output of the IRI model for 70º S, 345º E, 06:00 UT January 20th, 2005.

A complete description of the IRI model is given by Bilitza in a NASA technical memorandum [*Bilitza and World Data Center*, 1990]. An online web-based IRI model can be found on NASA's modelweb page along with links to the most current IRI version [*GSFC*, 2008]. For the work presented in this text, IRI -2001 was used. Detailed parameters can be found in Appendix C.

3.3 Sodankylä Ion Chemistry Model

The 1-D Sodankylä Ion Chemistry (SIC) model is similar to the IRI model in that it describes ion and neutral densities as a function of altitude for a given location and time. What sets the SIC model apart from the IRI model is: A) the comprehensive inclusion of many (79) ion and neutral species; B) the ability to include energetic particle precipitation directly into species continuity calculations; and C) a validity range from 20 – 150 km, where energetic particle precipitation effects are greatest. These advantages make the SIC model ideal for case studies of lower atmosphere and ionosphere dynamics during energetic particle precipitation events. However, the SIC model is relatively new. Earnest development efforts to evolve SIC into a tool began in the late 1990s. Thus, the SIC model is just beginning to be used within the field of space physics. The SIC model has been used to study various phenomena during energetic particle precipitation events, including whistler-induced electron precipitation [*Rodger et al.*, 2007], VLF radio wave propagation [*Clilverd et al.*, 2006] and ozone population dynamics [*Seppälä et al.*, 2006], to name just a few. The work described in this text is the first application of the SIC model to atmospheric and ionospheric conductivity. Because this application is a new endeavor, we will present the SIC model in greater detail than either the MSIS or IRI models.

Originally, the 1-D SIC model was developed to help describe quiet-time D-region

dynamics by keeping track of concentrations of multiple ion species (24 positive and 11 negative) [*Turunen et al.*, 1996]. After several revisions, the SIC model now includes 79 different ion and neutral species (36 positives, 28 negatives and 15 neutrals) over an altitude range of 20 – 150 km. The most complete description of the most recent SIC version used in this analysis is in the Ph.D. dissertation of *Verronen* [2006]. In order to calculate the concentration of each species, a time dependent continuity equation of the following form is solved.

$$\frac{\partial n_s}{\partial t} = P_s - L_s n_s - \nabla \cdot (n_s \overline{\upsilon}_s) \qquad \textbf{(3-16)}$$

Here, n_s is the number density, P_s is the local production rate, $L_s n_s$ is the local loss rate and $\overline{\upsilon}_s$ is the average velocity for a given species *j*. The last term on the right hand side, $\nabla \cdot (n_s \overline{\upsilon}_s)$, is atmospheric vertical transport (e.g., an upward wind). Although Equation (3-16) is a straightforward definition for a given species' number density, the challenge of the SIC model comes from the large number of species and the complex chemistry involved. Detailed flow diagrams of that representative chemistry can be found in Figures 4.3 and 4.4. of *Verronen* [*2006*]

One of the primary ionization and dissociation sources in the collisional atmosphere and ionosphere are energetic UV and EUV photons. Based on the SIC model description by *Verronen* [2006], the SIC model uses daily average 1 AU photon flux rates determined by the SOLAR2000 model [*Tobiska et al.*, 2000]. Specifically, radiation flux is taken in 1 nm bins between 1 - 423 nm, 39 individual EUV spectral lines between 1.86 – 105.0 nm and the Lyman-α line. These various radiation inputs are standard outputs from the SOLAR2000 model and an empirical approximation for the Lyman-α given by Thomas and *Bowman* [1986]. Using the Beer-Lambert law, solar flux is determined at each altitude for each wavelength by the following:

$$I(\lambda, z, \chi) = I_\infty(\lambda) e^{-\tau(\lambda, z, \chi)} \qquad \textbf{(3-17)}$$

On the left hand side of Equation (3-17), I is the solar flux as a function of wavelength,

λ, altitude, z and solar zenith angle, χ. On the right hand side, I_∞ is the incident solar flux at the top of the atmosphere and τ is the optical depth of the atmosphere. Based on Equation (3-17), ionization rates at each altitude can be calculated by the following:

$$Q_s(z,\chi) = \int_\lambda I(\lambda,z,\chi)\eta_s(\lambda)\sigma_s(\lambda)n_s(z)d\lambda \qquad \textbf{(3-18)}$$

Here, Q_s is the ionization rate, η_s is the efficiency for ionization/dissociation, σ_s is the absorption cross-section, and n_s is the number density for a given species *s*. (See *Turunen et al.* [1996] for a more complete derivation of Equation (3-18).

The last ionization input to the SIC model is energetic particle precipitation. Here, we describe how protons are presently handled by the SIC model. As of now, only proton precipitation is directly handled by the SIC model. Effects from electrons and photons are not yet included directly. (See Section 3.5.3 for more discussion of electron ionization.) Here, we will outline the process of calculating ionization rates due to solar energetic proton precipitation as detailed by *Verronen* [2006]. Energetic proton flux from the geosynchronous GOES spacecraft in integral channels between >1 MeV and >100 MeV is used for the SIC proton input. The GOES integral proton flux is converted into a differential flux between 600 keV and 2000 MeV. Based on a case study of six different SEP events, *Freier and Webber* [1963] concluded that each event was best represented by an exponential number rigidity spectrum of the following form:

$$J = J_0 e^{-P/P_0} \qquad \textbf{(3-19)}$$

Here, J is the integral proton flux and P is the proton rigidity (momentum p per unit charge q). Over the course of an individual SEP event, *Freier and Webber* [1963] determined that the flux spectrum was not constant, but the exponential nature of the flux spectrum held true. We define rigidity P as a function of the individual proton kinetic energy E, proton mass m_p and the speed of light c.

$$P = \frac{p}{q} = \frac{1}{qc}\sqrt{E(E + 2m_p c^2)} \qquad \textbf{(3-20)}$$

From the GOES observations (or observations from similar spectrometers), we know the integral proton flux as a function of energy *J(E)* at several discrete energy values. We can calculate integral flux as a function of rigidity *J(P)* using Equation (3-20). With our assumed relation for integral flux in terms rigidity, we can solve for the characteristic rigidity P_0 and the characteristic proton flux J_0 using Equation (3-19) for each pair of GOES energy channels E_i and E_{i+1} (and therefore rigidity channels P_i and P_{i+1}).

$$P_0 = \frac{P_i - P_{i+1}}{\ln J_{i+1} - \ln J_i} \tag{3-21}$$

$$J_0 = \exp\left(\frac{P_i \ln J_{i+1} - P_{i+1} J_i}{P_{i+1} - P_i}\right) \tag{3-22}$$

By employing this method, we are assuming that the exponential relation in Equation (3-19) for integral proton flux is valid between each pair of energy channels E_i and E_{i+1}. Substituting back into Equation (3-19), we can calculate the integral flux *J(E)* at any energy. Using a grid of *k* intervals, the integral spectrum is then described by the following:

$$J_k = J_0 e^{-P_k / P_0}. \tag{3-23}$$

Here, J_0 and P_0 are different for rigidities bins corresponding to different energy channel pairs E_i and E_{i+1}. Then, we can easily convert integral flux into a differential flux F_d on a grid with *k* intervals of our choosing.

$$F_d = \frac{J_k - J_{k+1}}{E_{k+1} - E_k} \tag{3-24}$$

The energy bins are then centered at E_d, given by

$$E_d = \frac{E_{k+1} + E_k}{2}. \tag{3-25}$$

Finally, we have differential proton flux F_d at a set of discrete of energy values E_d. We call this method the "piecewise" method because it treats pairs of data points as separate pieces of an integral proton spectrum that are independent of each other. If we were to convert from integral to differential energy spectra using Equations (3-24) and (3-26)

without assuming a spectral shape (here, using Equation (3-19)), then we would only have $(i - 1)$ differential spectrum values (where i is the number of integral energy bins). We use the exponential integral spectral shape assumption to provide a higher resolution in the resultant differential spectrum.

Freier and Webber [1963] assert that Equation (3-19) is generally a good fit to the integral proton flux spectrum for solar proton events. However, for any given measurement, we do not know how well the actual proton spectrum fits this assumption. Using the method described above, discontinuities appear when the assumed integral spectrum does not accurately describe the real measured spectrum. Figure 3.3.1 and Figure 3.3.2 give examples of both integral and differential spectra one half of an hour after a solar proton event onset on January 20th, 2005 and two hours after onset. Figure 3.3.1 has a relatively poor fit compared with Figure 3.3.2 because our initial assumption that the integral spectrum could be well described by Equation (3-19) does not readily apply. Looking at Figure 3.3.1, it is evident that some care must be taken when examining individual spectra. We discuss methods that could be employed in the future to avoid discontinuities and calculate the error associated with converting from integral to differential spectra in Section 3.5.2.

After calculating a differential proton flux spectrum, the incident protons are propagated through an ionization model of the atmosphere using a method based on the range-energy relation for protons in air [*Bethe and Ashkin*, 1953]. Range (R) describes the amount of material the protons travel through and is given in units of mass per area (often g cm^{-3}). The range-energy relation can be written in the following form:

$$R(E) = aE^b. \qquad \textbf{(3-26)}$$

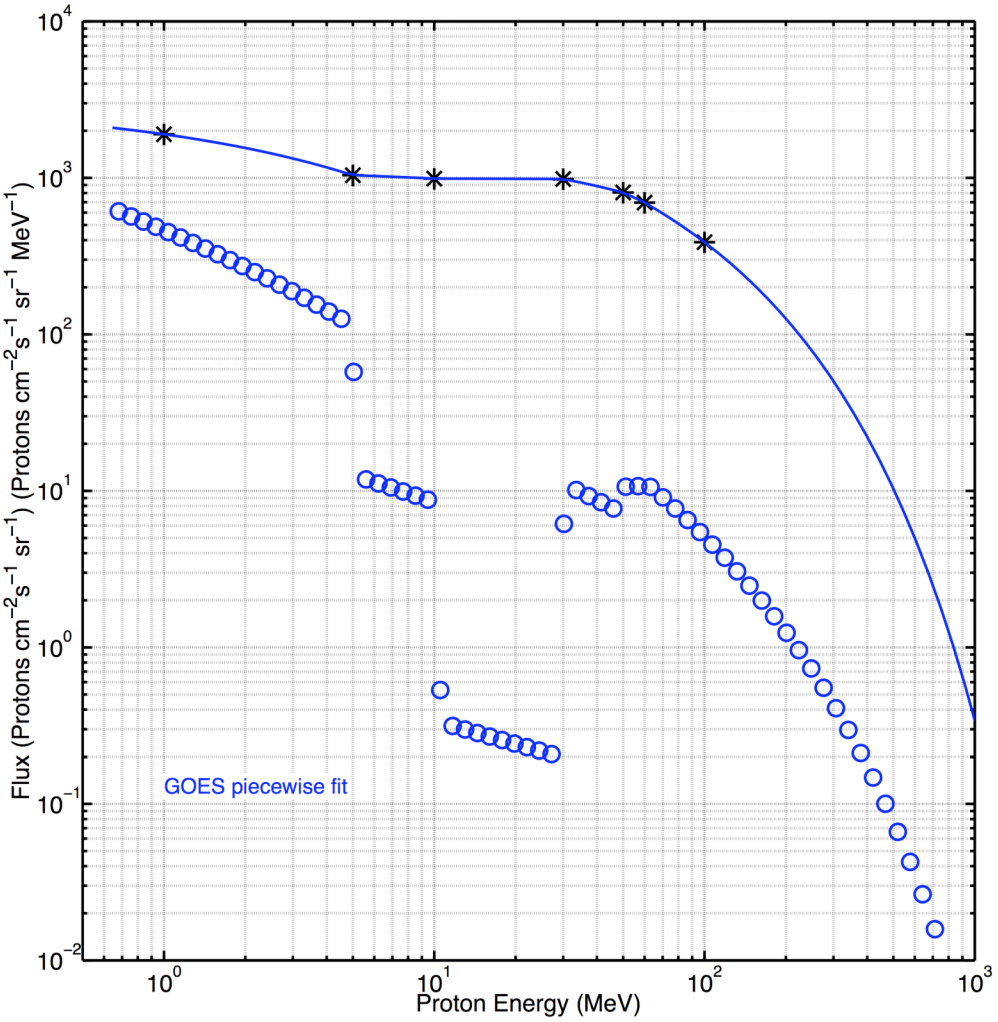

Figure 3.3.1 GOES 11 integral and differential proton flux at 07:30 UT January 20th, 2005. Proton flux one half of an hour after SEP event onset (07:30 UT after onset at nearly 07:00 UT). The black stars are the GOES 11 integral measurements. The solid blue line is the piecewise fit to the observations. The blue circles are the calculated differential proton flux values. The error bars on the data (marking the estimated 15% uncertainty) are not easily noticeable because they are small with respect to the marker size.

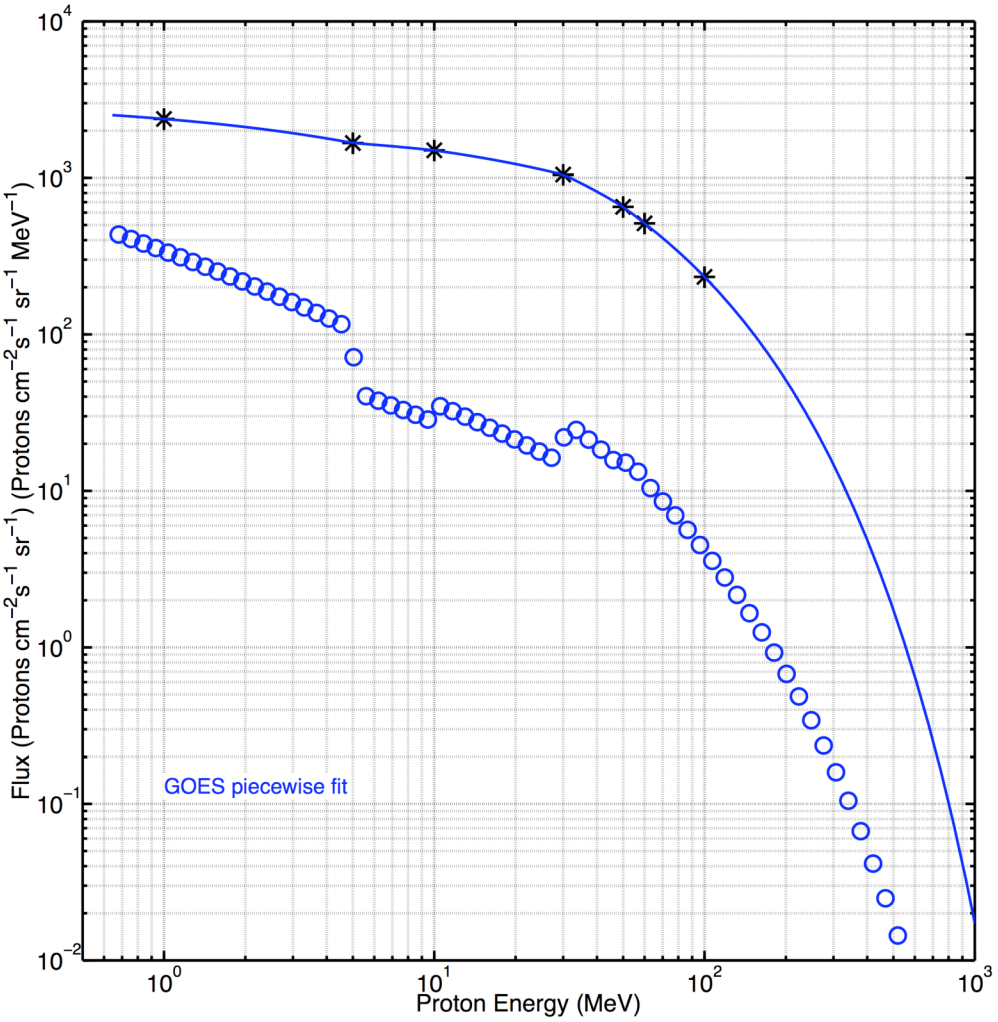

Figure 3.3.2 GOES 11 integral and differential proton flux at 09:00 UT January 20th, 2005. This plot is very similar to Figure 3.3.1, except the data are from two hours after the SEP event onset (09:00 UT after onset at nearly 07:00 UT). The black stars are the GOES 11 integral measurements. The solid blue line is the piecewise fit to the observations. The blue circles are the calculated differential proton flux values. The error bars on the data (marking the estimated 15% uncertainty) are not easily noticeable because they are small with respect to the marker size.

Here, R is the range, E is the kinetic energy of the proton and a and b are experimentally determined parameters. It is assumed that all energy deposited by a precipitating proton is lost to ionization [*Rees*, 1982]. Based on procedures originally used by *Reid* [1961] and again by *Rees* [1989], the amount of energy deposited at a given altitude (z_0) with a pitch angle θ is given by

$$\frac{dE}{dx} = \left(\frac{dR(E, z_0, \theta)}{dE} \right)^{-1}, \tag{3-27}$$

where

$$R(E, z_0, \theta) = R(E) - \frac{1}{n(0)} \int_{z_0}^{\infty} \frac{n(z)}{\cos\theta} dz \tag{3-28}$$

is the range remaining at altitude z_0 while $n(0)$ and $n(z)$ are neutral number density values at the ground and altitude z, respectively. The right hand side of Equation (3-28) gives the total range of a proton with energy E less the range into the atmosphere already traveled to reach altitude z_0. We can find the ionization rate due to a single proton by dividing the energy lost at a specific altitude, $\frac{dE}{dx}$, by the average ionization energy, $\Delta\varepsilon = 35eV$ [*Rees*, 1989]. Then, in order to get the total ionization rate Q, we need to multiply Equation (3-27) by the proton flux, *F(E),* and integrate over energy and angle.

$$Q(z_0) = \frac{1}{\Delta\varepsilon} \int\int\int \left(\frac{dE}{dx} \right) F(E) \sin\theta d\theta d\phi dE \tag{3-29}$$

With Equation (3-29), we can take a solar energetic proton spectrum and calculate an ionization rate profile. This SEP-induced ionization rate is used as an ion production term in Equation (3-16).

3.4 Full Atmosphere-Ionosphere Electrical Conductivity Model

After describing the basis for our atmosphere-ionosphere conductivity model, we can now put all the pieces together for a final product. We can directly solve Equation (3-14) using the model values calculated using a combination of the MSISE-90 neutral atmosphere, IGRF magnetic field, IRI ionosphere charged particle density and SIC

atmosphere/lower ionosphere charged particle density and our own ionization rate models. The only parameter we do not get from one of the sources listed above is the ion neutral collision frequency. For this, we use the following empirical formula derived from EICSAT radar measurements given in [*Kirkwood et al.*, 1988].

$$\begin{aligned} \nu_{in} &= 4.305 \times 10^{-16} \, (nN_2 + 0.98nO_2 + 0.57nO) \, s^{-1} \\ \nu_{en} &= 1.5 \times 10^{-17} \, (n \, T_e) \, s^{-1} \end{aligned} \quad \textbf{(3-30)}$$

Here nN_2, nO_2, nO and n are the number densities (m^{-3}) of molecular nitrogen, molecular oxygen, atomic oxygen and the total neutral number density, respectively. The electron temperature is given by T_e (K), which we assume to be equal to the neutral temperature in the collisional atmosphere (SIC model) where we do not have explicit model temperature estimations.

Figure 3.4.1 shows one set of model outputs taken at 70º S, 345º W at 06:00 UT on January 20th, 2005. The parallel, Pedersen and Hall conductivity profiles are given by black, red and green lines, respectively. There is a discontinuity at 120 km, which is the boundary of where the SIC (below 120 km) and IRI (above 120 km) charged particle densities are used. Hall conductivity is not calculated above 120 km because the IRI model does not give separate ion and electron densities. Combined with a collision frequency that is much lower than the cyclotron frequency above 120 km, the ion and electron terms effectively cancel out. Geophysically, the Hall term will drastically decrease with increasing altitude above 120 km. For this particular time and location, there is relatively little residual solar energetic proton precipitation resulting from the SEP event that began on January 17th, 2005. The maximum hall conductivity occurs near 300 km with the maximum electron density. Meanwhile, the maximum Pedersen conductivity is near 120 km where the ion cyclotron and ion-neutral collision frequencies are equal. The parallel term is monotonically increasing with altitude as the neutral density decreases. In the lower atmosphere, just above 40 km, there is a knee in the

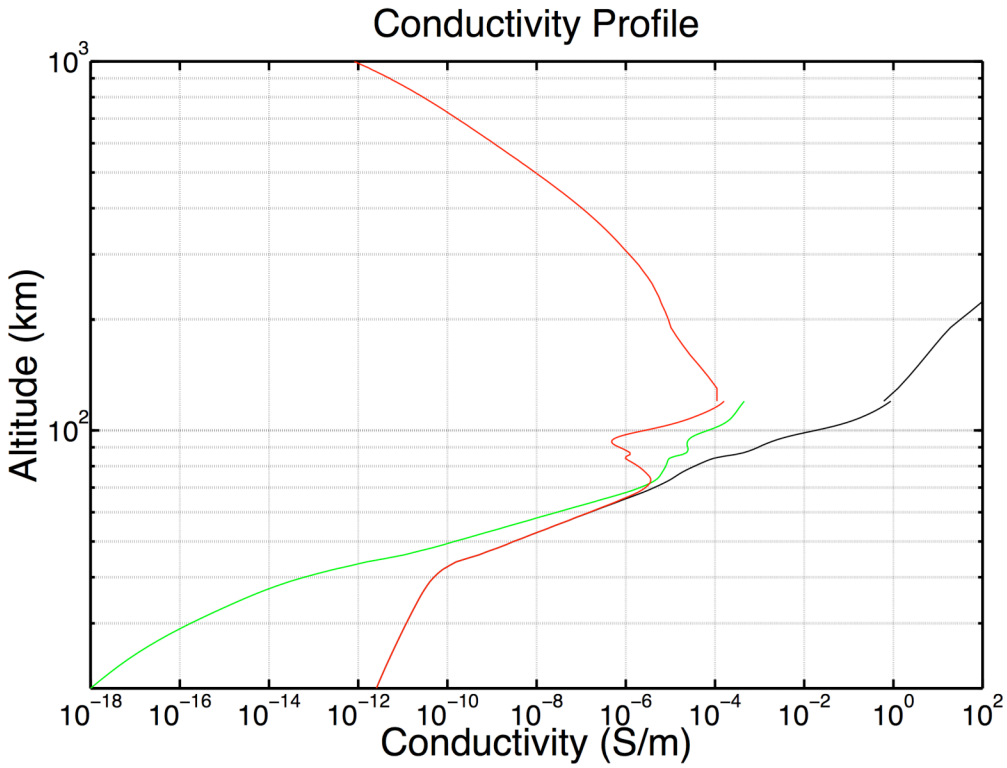

Figure 3.4.1 Conductivity profiles based on our new, complete model. Parallel, Pedersen and Hall conductivity is represented by the black, red and green lines, respectively. The model is for 70º S, 345º W at 06:00 UT on January 20th, 2005.

parallel/Pedersen conductivity. Below this knee, water group ions carry a significant amount of charge. If water group ions are ignored in this region, conductivity values can be off by more than an order of magnitude.

We can build a conductivity profile for any location on any day for which we have the appropriate model data and input conditions. As mentioned in Section 3.1 knowing conductivity values is extremely important for many electrical phenomena. In subsequent chapters, we apply our new conductivity model during energetic precipitation events and compare the results to MINIS balloon observations.

3.5 Additions to the Sodankylä Ion Chemistry Model Particle Precipitation Handling

The SIC model has proven to be extremely useful for producing estimates of ion densities

in the collisional atmosphere and lower ionosphere. In our work using the SIC model, we have successfully built a new atmosphere-ionosphere conductivity model that includes ionization from precipitating energetic protons. After working with the SIC model output and the energetic proton input, we feel that the model can be improved by: A) taking solar proton spectra from polar orbiting satellites instead of geosynchronous; B) calculating the differential proton flux spectrum with an estimated error; and C) including ionization from energetic electron precipitation. These modifications have not yet been included in the SIC model and are described in detail in the sections that follow.

3.5.1 Energetic Protons from Polar Orbiting Satellites

The first new feature to add to the SIC model is the capability to use the polar-orbiting POES satellite high-energy proton measurements instead of the geosynchronous GOES detectors to determine incident proton flux. This has the benefit of using a measured particle flux only a few hundred kilometers above the affected atmosphere and removes some of the assumptions that are needed when taking proton flux data from tens of thousands of kilometers down geomagnetic field lines. In addition, since the POES satellites sample all rigidities, this method could be used to probe the rigidity cutoff transition region. In this case, however, we will limit our discussion to the deep polar cap region. GOES satellites at geosynchronous are assumed to sample the energetic proton spectrum that will have direct access to the polar cap in the current version of the SIC model.

The most energetic proton data from POES is supplied as count rates in four omni-directional detector channels. We must convert count rates into flux rates by following a method described in the POES space environment monitor technical handbook [*Evans and Greer*, 2000]. In order to find the number flux N, we solve

$$N = \int\int\int J(\phi,\theta)\sin\theta\cos\theta d\theta d\phi dA, \qquad \textbf{(3-31)}$$

where θ and ϕ are polar and azimuthal angles with respect to the detector surface element

dA. The procedure for solving Equation (3-31) involves integrating over the detector faces to get a geometric factor and subtracting count rates from lower energy bins to get differential proton flux. However, since the detector is omni-directional, assumptions need to be made on the angular distribution of the particle counts and thus, the limits of integration for Equation (3-31). Two common angular distributions are isotropic and isotropic to a given polar angle, which is typical for solar energetic particle events [*Evans and Greer,* 2000]. Figure 3.5.1 shows a typical solar energetic proton distribution incident on a POES detector in polar coordinates with the vertical axis pointing along the

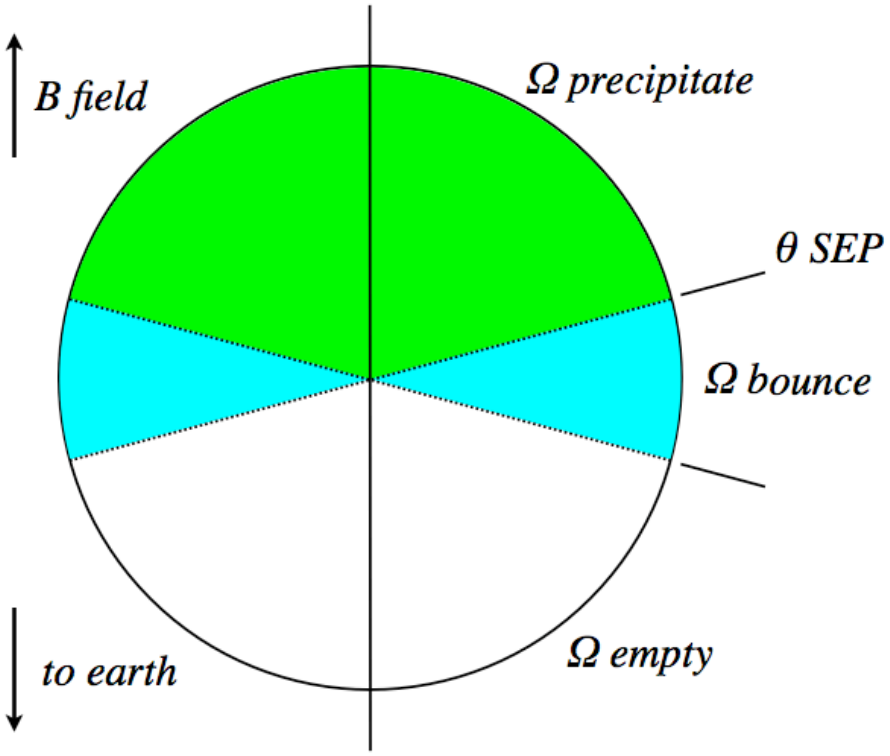

Figure 3.5.1 Graphic depiction of POES omni-directional energetic proton detector particle distribution for a solar energetic particle event. Proton flux is assumed isotropic over the entire green and cyan shaded area and zero for the white area. The green area represents the solid angle of protons that will eventually precipitate and the cyan area represents protons that are bouncing and not being lost to the atmosphere.

Table 3-1 Integral proton flux for a completely isotropic distribution and for an SEP distribution with θ SEP = 75° [*from Evans and Greer,* 2000].

Integral Proton Flux J (protons cm^{-2} s^{-1} str^{-1})

E min	Isotopic	θ SEP = 75°
16 MeV	0.849 CR_6 – 0.667 CR_8	0.849 CR_6 – 0.508 CR_8
35 MeV	0.849 CR_7 – 0.667 CR_8	0.849 CR_7 – 0.508 CR_8
70 MeV	0.182 CR_8	0.341 CR_8
140 MeV	0.182 CR_9	0.341 CR_9

geomagnetic field line. (Each pie wedge indicates particles traveling from a given direction toward the center of the circle.) The image is a cross section of an axially symmetric sphere. The shaded regions depict regions of solid angle where the proton distribution is isotropic. The white area stands for the solid angle that has no particle counts at all. When considering which particles of those counted actually precipitate, we must only include the green shaded area, denoted $\Omega_{\text{precipitate}}$, and not the cyan shaded area, Ω_{bounce}. The particles in the bounce solid angle are downward moving protons (θ_{SEP} to 90°) that then bounce below the satellite detector and pass through again (90° to 90° + θ_{SEP}). Assuming that protons with a 90° pitch angle can bounce at 150 km above the earth's surface, the smallest θ_{SEP} can be is 60°. However, a more typical value for θ_{SEP} is 75° [*Evans and Greer*, 2000]. Without additional information, there is no way to know for sure what θ_{SEP} is for any given solar proton event or for a particular observation. Table 3-1 gives the integral proton flux in terms of count rates in the four omni-directional detectors for an isotropic distribution and SEP distributions for θ_{SEP} = 75°. The values for J listed in Table 3-1 are not the final flux we are interested in because they include particles counted in $\Omega_{\text{precipitate}}$ and Ω_{bounce}. We assume that all particles in the Ω_{bounce} solid angle mirror somewhere between the satellite in LEO and the top of the atmosphere (150 km). Therefore, to get the precipitating integral proton flux, $J_{precipitate}$, at the top of the atmosphere, we count only the protons in the solid angle, $\Omega_{\text{precipitate}}$. We assume that the protons in the solid angle $\Omega_{\text{precipitate}}$ measured at the satellite will change their pitch angle such that θ_{SEP} = 90° at 150 km. This means that the SEP distribution that once covered

the solid angle $\Omega_{\text{precipitate}}$, is distributed over 2π steradians at the top of the atmosphere. We must normalize the integral flux values determined using Table 3-1 by a ratio of solid angle. Our expression for $J_{precipitate}$ then becomes

$$J_{precipitate} = J\frac{\Omega_{precipitate}}{2\pi}. \quad \textbf{(3-32)}$$

With the GOES data set, there are continuous measurements of energetic proton flux at geosynchronous which are assumed to precipitate into the polar caps. Therefore, it is possible to get a continuous proton flux estimate from one single spacecraft. However, with POES sampling all L-shells, we must pick the correct spacecraft location and proton spectra to use for a particular analysis. Fortunately, there are multiple POES spacecraft in orbit to choose from (three in January 2005), providing near-continuous observations. In order to compare with GOES measurements and evaluate the full solar proton spectrum (and not a partial spectrum where lower rigidity protons are cut off), we only evaluated periods of enhanced flux above L=6.

Figure 3.5.2 shows raw omni-directional proton channel counts for one single POES orbit during the solar proton event on January 20th, 2005. The solar energetic protons are represented by the large plateaus. We select only the proton spectra corresponding to time between the vertical dashed lines with high count rate and L>=6 (for P6, these points are highlighted with black markers). We want to ignore the South Atlantic Anomaly (SAA) and the other unknown enhanced particle distribution (labeled "?" in Figure 3.5.2). One hypothesis is that the unknown distribution is a result of energetic electrons contaminating the proton detectors. However, the source of these counts is beyond the scope of this work. We will simply not include them in our analysis because we are focusing on precipitation at higher L-shells. Figure 3.5.3 shows the count rate for POES 15, 16 and 17 as a function of L-shell. The SAA is clear between L=1 and L=2. The unidentified distribution of particle counts can be seen at L=2 and spreading perhaps as far as L=4.5. SEP proton counts can be seen above L = 3.5 extending all the way to the

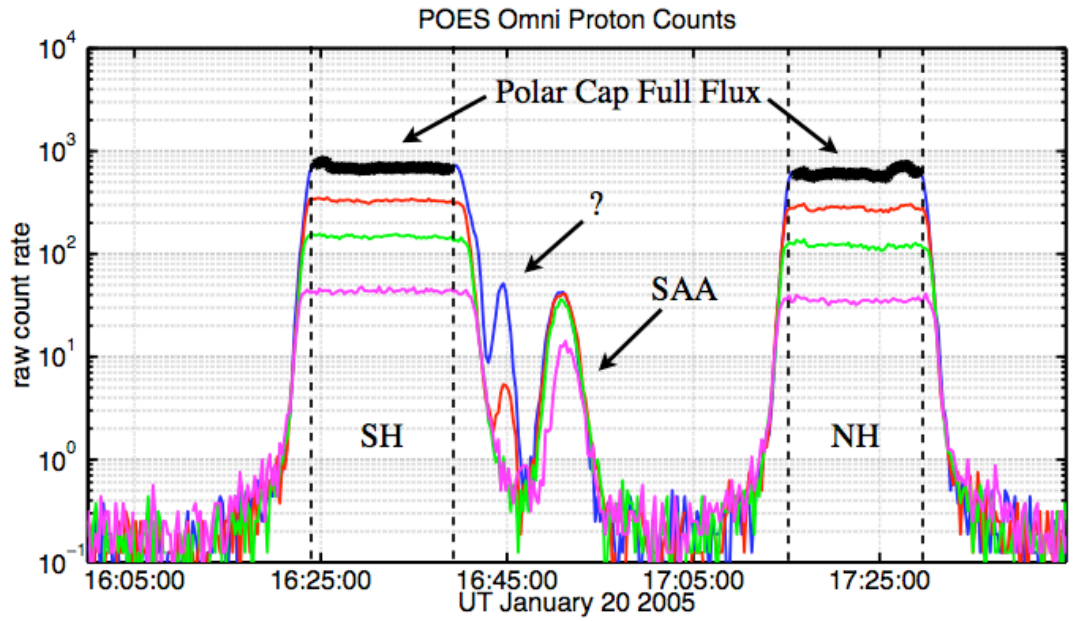

Figure 3.5.2 POES 15 omni-directional energetic proton raw counts for one orbit on January 20th, 2005. The blue, red, green and magenta lines are the count rates for P6 (>15 MeV), P7 (>35 MeV), P8 (>70 MeV) and P9 (>140 MeV), respectively. The areas between the vertical dashed lines represent times when POES 15 was above L=6 in the southern (SH) and northern hemisphere (NH). Times where there is an acceptably high P6 count rate are highlighted with black markers. The South Atlantic Anomaly and an unidentified particle population are also clearly visible.

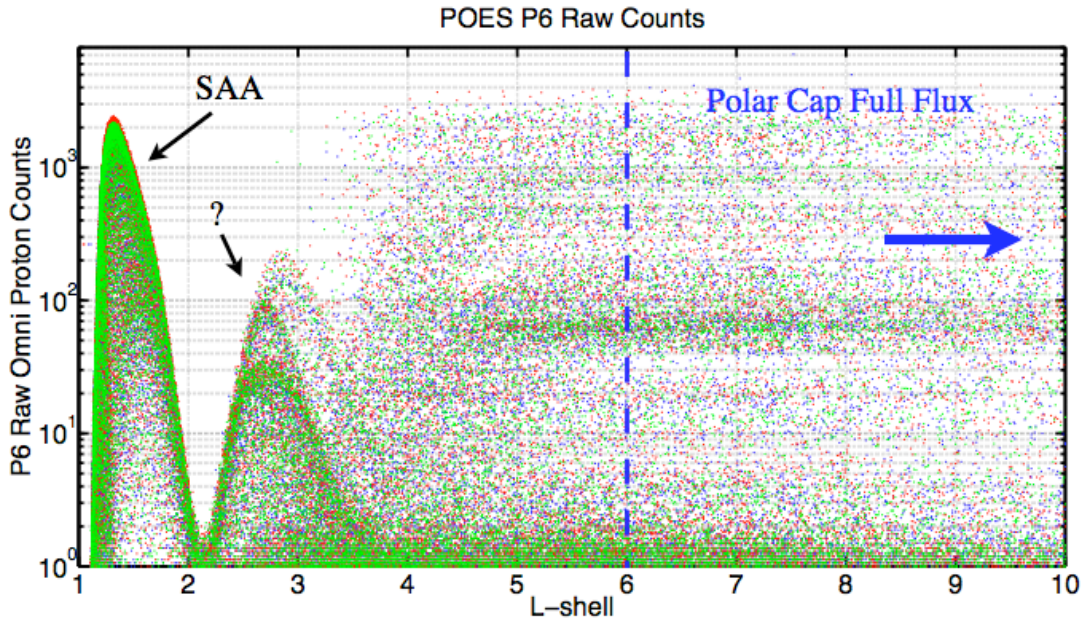

Figure 3.5.3 POES 15, 16 and 17 P6 raw counts as a function of L-shell. Both the South Atlantic Anomaly and the unidentified particle population are clearly evident. For use in comparing with GOES data, we only use POES proton flux data when each satellite is above L=6, marked by the dashed vertical blue line.

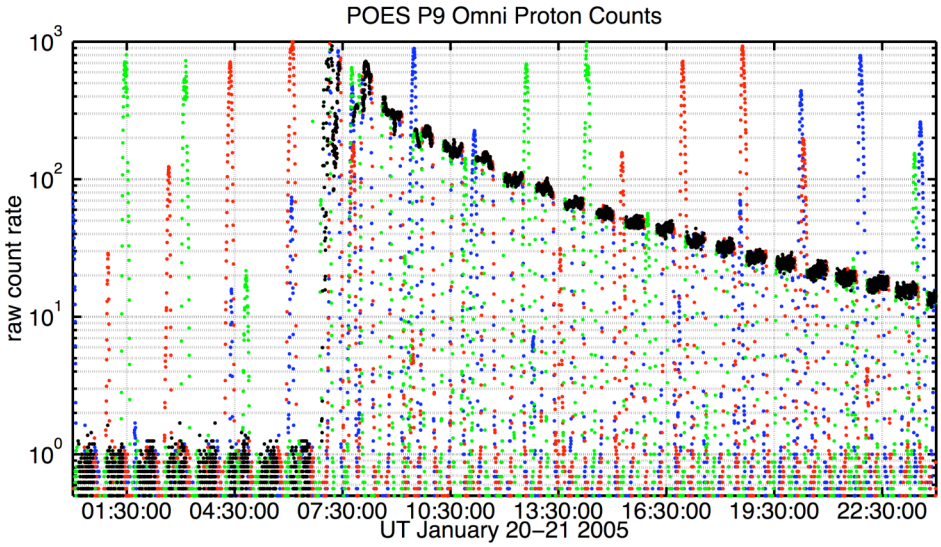

Figure 3.5.4 POES 15, 16 and 17 raw P9 (>140 MeV) energetic proton counts. The black dots represent the proton data collected above L=6. There are no large north-south asymmetries.

pole in a nearly uniform distribution. The counts to the right of the vertical blue line in Figure 3.5.3 represent the same L-shell cut off highlighted with black markers in Figure 3.5.2. By using only time periods where a POES satellite is observing SEP protons above L=6, we can eliminate contamination from the SAA and unknown sources.

Since the POES spacecraft sample both hemispheres alternately, we must check to see if there are any asymmetries between the northern and southern hemisphere. Figure 3.5.4 shows the P9 counts from POES 15, 16 and 17 for the entirety of January 20th, 2005. It is apparent that the general trend of the count rate after SEP onset is monotonically decreasing. There are no large north-south asymmetries. The POES spacecraft are essentially sampling the same energetic proton population while they are in either polar cap. Since this is the case, we use a 10-point average (five nearest earlier and later points) when creating an integral proton spectrum to feed into the SIC model. This has the effect of ceasing to give precise time or location measurements and instead can be treated as temporal and spatial averages applicable to either hemisphere.

Let us now take a look at three example comparisons between the GOES and POES high-energy proton spectra. In Figure 3.5.5, we show that POES data produce continuous differential spectra shortly after SEP event onset. Figure 3.5.6 shows typical differential proton spectra from POES and GOES from January 20th, 2005 after the SEP event. The integral and differential proton spectra usually have similar shapes although the GOES spectra often have larger discontinuities. This suggests that the integral proton spectra observed at POES fit the assumed exponential in Equation (3-19) better than those observed at GOES. Figure 3.5.7 presents a common feature in the GOES data set where an enhancement occurs in the lowest-energy channel (>1 MeV). Figure 3.5.7 shows an instance where the lower energy proton channels in the GOES data set become enhanced. This kind of enhancement occurred several times on January 20th, 2005. GOES 11 and GOES 10 (GOES 10 data not shown here) both observe enhancements in the lowest energy proton channels at the same time (to within the 5 minute time-steps). There are no coincident enhancements in the POES energetic proton data. However, the minimum omni-directional energy channel on POES is generally too high (>16 MeV). Figure 3.5.8 shows a comparison of the energetic proton flux data from GOES as well as energetic omni-directional proton flux, lower-energy directional proton flux, and electron flux data from POES. Only the POES 0° pitch angle electron channels observe flux enhancements at 14:00 and 16:00 UT, coincident with the GOES proton enhancements. There are no enhancements in the lower energy directional proton channels. It is entirely possible that the GOES proton enhancements represent a localized equatorial enhancement that did not extend into the polar regions. If this indeed is the case, then using the POES proton observations, as opposed to those from GOES, would provide a more accurate input to any SEP precipitation model.

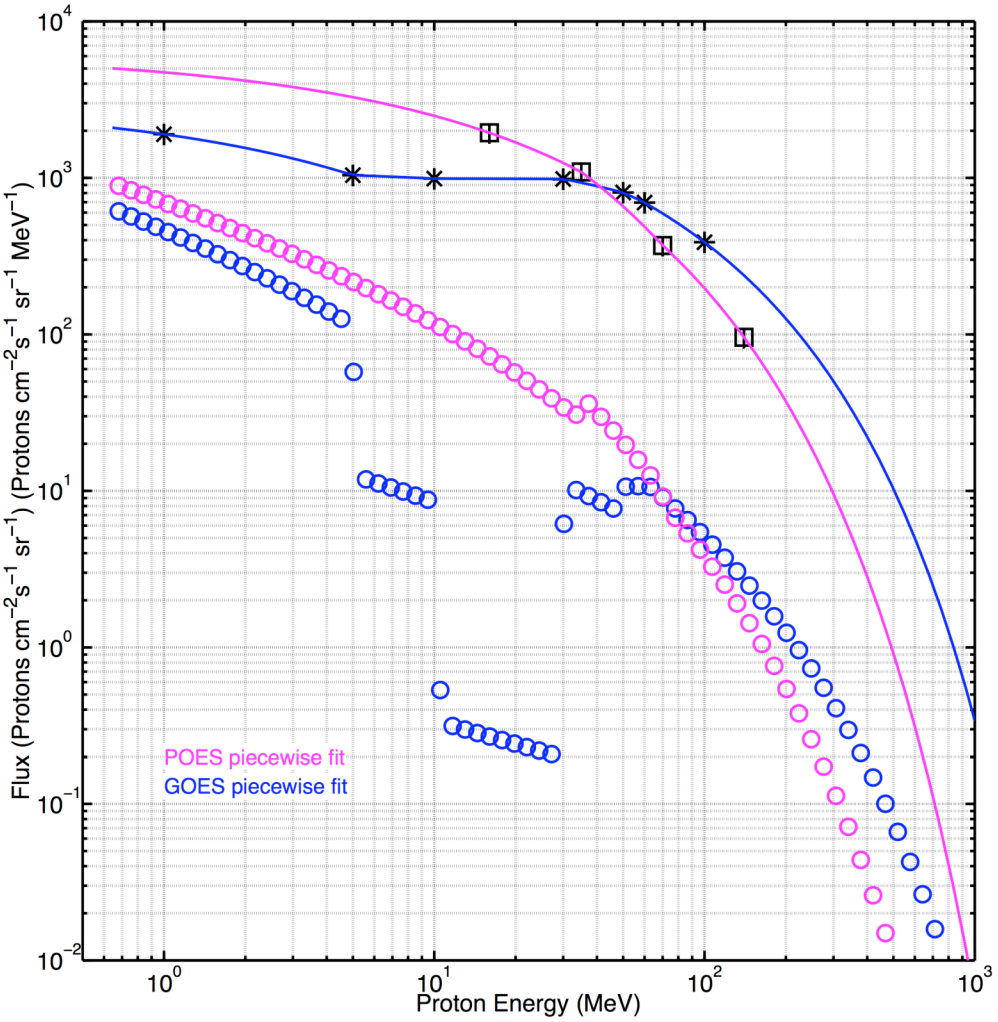

Figure 3.5.5 GOES and POES integral and differential proton flux comparison at 07:00 UT January 20th, 2005. Black asterisks and squares mark the GOES and POES observations, respectively. The solid curves show the integral fit to the observations. The circles are the calculated differential flux spectra. This is the same GOES 11 data as in Figure 3.3.1. The POES data produce a much smoother differential spectrum at this specific time. The error bars on the data (marking the estimated 15% uncertainty) are not easily noticeable because they are small with respect to the marker size.

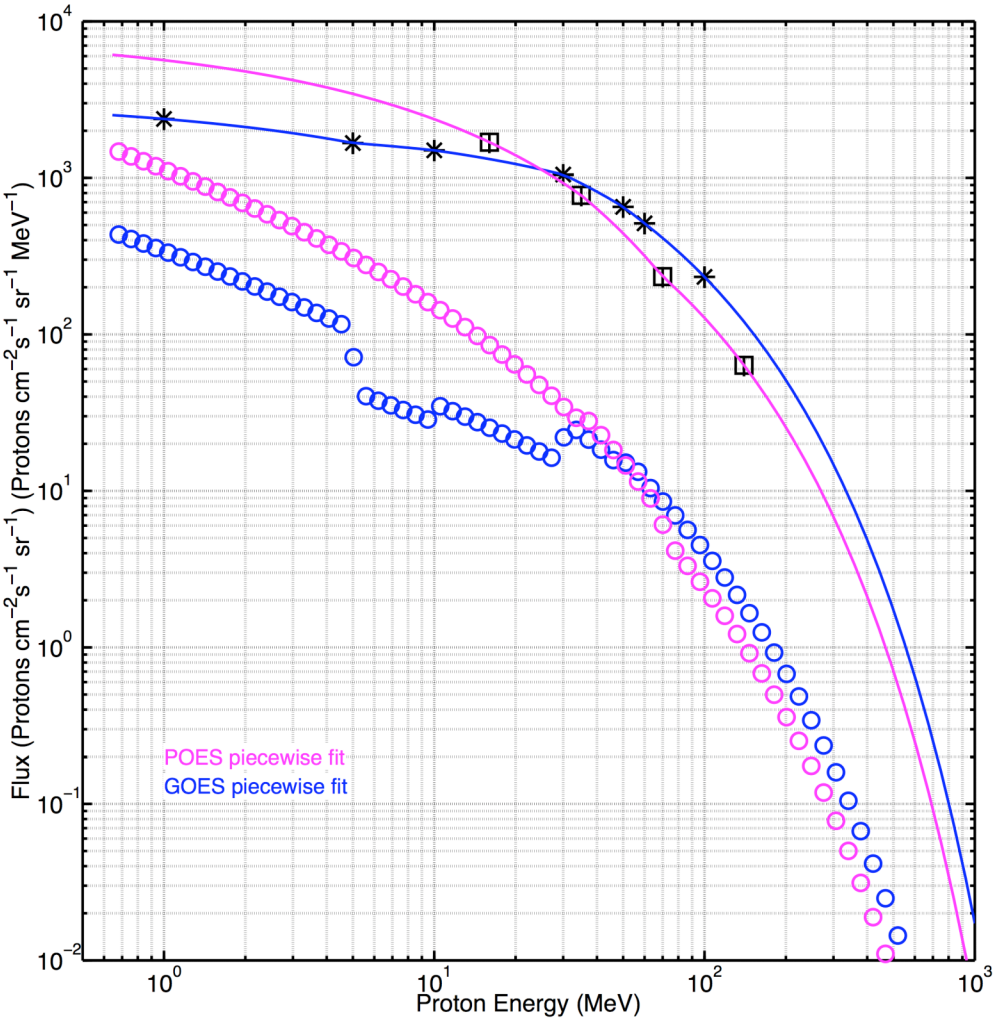

Figure 3.5.6 GOES and POES integral and differential proton flux comparison at 09:30 UT January 20th, 2005. Black asterisks and squares mark the GOES and POES observations, respectively. The solid curves show the integral fit to the observations. The circles are the calculated differential flux spectra. This is the same GOES 11 data as in Figure 3.3.2. The GOES and POES data produce similar differential spectrum at this specific time, but the GOES spectrum still has jumps. This is a typical comparison for measurements on January 20th, 2005. The error bars on the data (marking the estimated 15% uncertainty) are not easily noticeable because they are small with respect to the marker size.

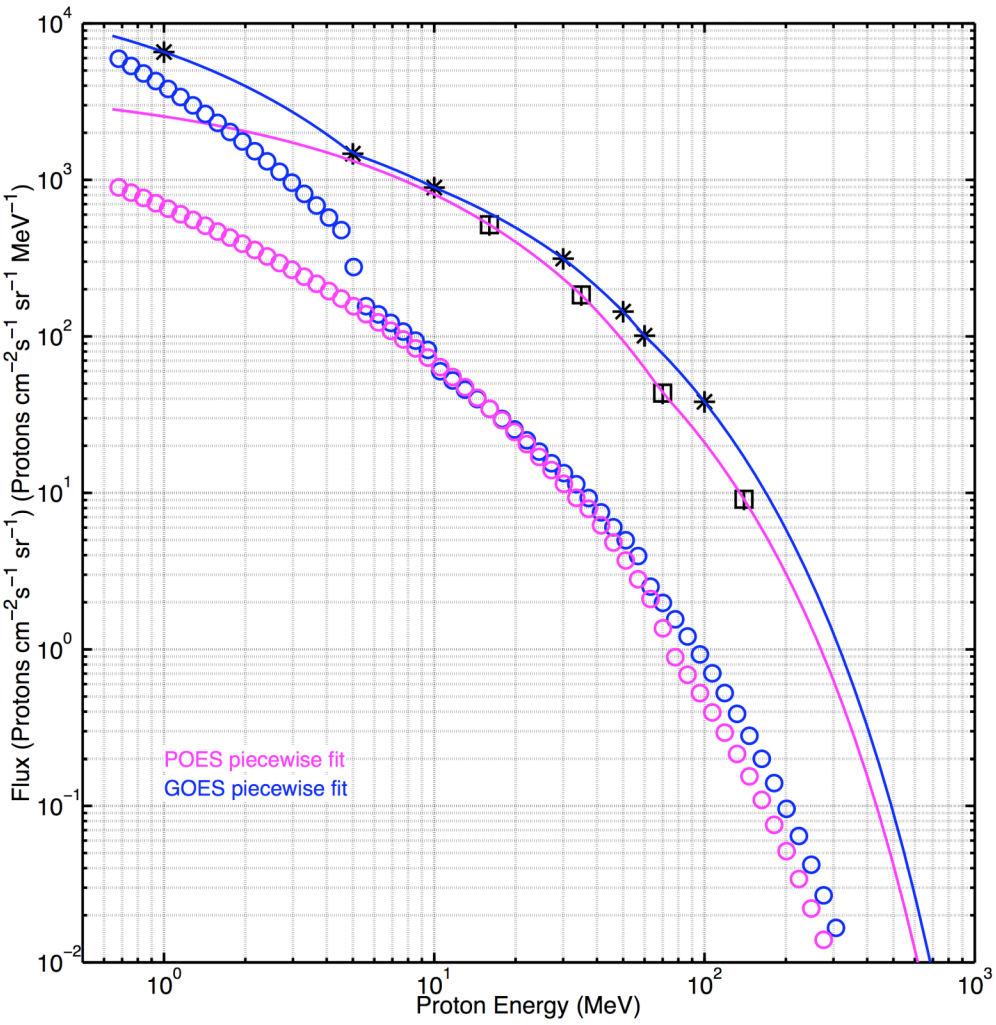

Figure 3.5.7 GOES and POES integral and differential proton flux comparison at 16:20 UT January 20th, 2005. Black asterisks and squares mark the GOES and POES observations, respectively. The solid curves show the integral fit to the observations. The circles are the calculated differential flux spectra. The GOES low energy proton flux (> 1 MeV) is enhanced with respect to the expected spectral shape. POES does not have a > 1 MeV channel. The error bars on the data (marking the estimated 15% uncertainty) are not easily noticeable because they are small with respect to the marker size.

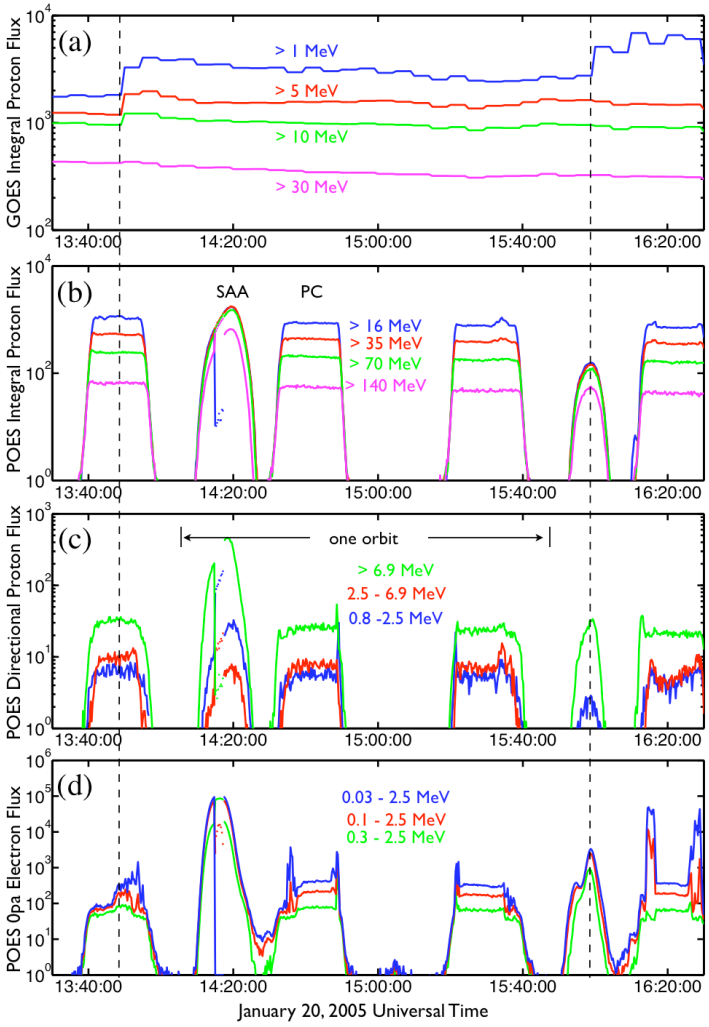

Figure 3.5.8 Various GOES and POES particle detector data looking for jump in low-energy channels. Here, we show: (a) GOES energetic proton flux; (b) POES omni directional protons; (c) directional protons; and (d) directional electrons. Only the POES 0 degree pitch angle measures an increased count rate at the same time as GOES proton enhancements.

Taking POES energetic proton data is an acceptable replacement for GOES data based on the comparisons made in this section. The advantages to using POES data are: 1) nearly in-situ energetic proton measurements near the precipitation region; 2) the ability to select a specific L-shell or location to take a proton spectra; and 3) the ability to check for north-south asymmetries in precipitation. There are disadvantages to using POES as well, namely: 1) non-continuous temporal coverage; and 2) as of now, the data require

much more processing and an assumption about the loss angle.

3.5.2 Differential Proton Flux Spectra with Estimated Error

One problem with the procedure for taking the GOES and POES integral energetic proton flux data and producing a differential flux spectrum (outlined in Section 3.3) is that there is no real measure of the error in doing so. Essentially, Equation (3-19) was solved for each pair of integral flux data points and no account for the rest of the spectrum was made. At certain times, this resulted in step functions with discontinuities at the minimum threshold energy (e.g., Figure 3.3.1 at 5, 10 and 30 MeV). There is no physical reason for the discontinuities and no measure of the error associated with the current fitting method. In order to address these issues, we introduce an alternate method for calculating the differential flux spectra that evaluates each temporal observation as a whole and provides an error estimate. We provide multiple examples that compare this alternate method with the method used in previous analyses.

The basic notion of this alternate method is to assume that Equation (3-19) fits the entire integral flux proton spectrum and not simply values in adjacent bins. We will call this the "complete" method because it fits the complete data set to an exponential at one time and does not separate pairs of data points as the earlier method did. Restating Equation (3-19), the integral flux J as a function of rigidity P becomes

$$J = J_0 e^{-P/P_0}. \qquad \textbf{(3-33)}$$

Taking an integral flux spectrum at a given time, we use both a nonlinear and linear least squares fit (using a Trust-Region algorithm) to find the constants J_0 and P_0. Along with the constants, we can provide an error estimate for the fit in the form of goodness of fit statistics adjusted R-square. We provide several examples comparing the piecewise method outlined earlier with our alternate nonlinear and linear fits using GOES and POES observations. For each of our alternate fits, we also include 95% confidence bounds as well as adjusted R-square values.

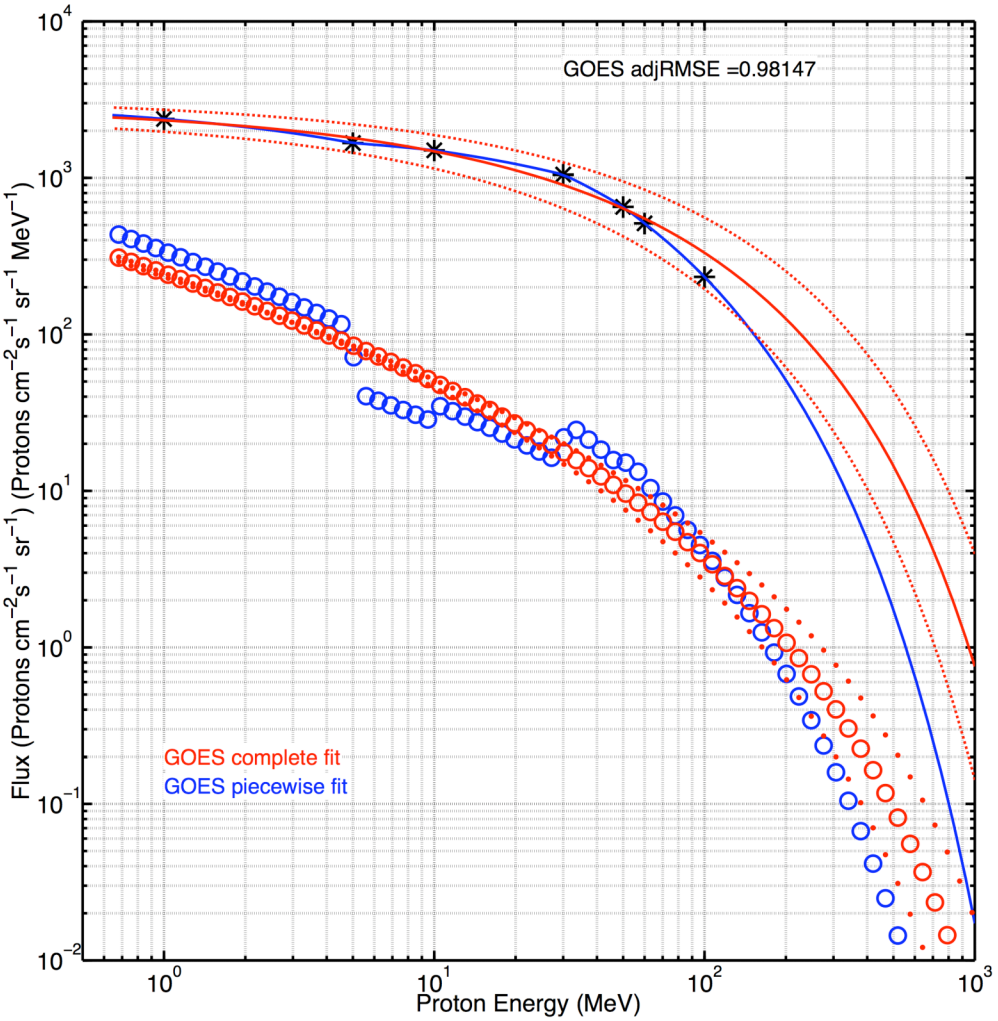

Figure 3.5.9 GOES proton flux calculated from piecewise and nonlinear fits at 09:00 UT. The black asterisks are the GOES integral flux observations. The solid blue line and blue circles are the piecewise fit calculated integral and differential spectra, respectively. The solid red line is the nonlinear integral proton spectrum. The dashed lines are the 95% confidence bounds for the integral spectrum. The red circles mark the nonlinear differential spectrum. The red dots are differential spectra calculated using the 95% confidence bound values from the nonlinear fit. Estimated errors of 15% in the measurements are plotted. They are not noticeable because the error bars are nearly the same size as the markers themselves.

In Figure 3.5.9 we show GOES data from 09:00 UT on January 20th, 2005 along with a piecewise fit and a non-linear fit. There are two distinct advantages clearly evident. The nonlinear fit to the entire integral energy spectrum results in smooth spectra. There are no piecewise-induced discontinuities. We also have an estimate of the error given by the adjusted R-square value. With a value near unity, we have a quantifiable confidence in our nonlinear fit.

With the advantages of providing continuous spectra and estimates of fitting error, we proceed by comparing the difference between nonlinear and linear fits. The linear fitting method is exactly the same as the nonlinear except we fit the natural logarithm of Equation (3-33). We provide five examples comparing the fit methods, three using GOES and two from POES. In Figure 3.5.10, we show GOES integral proton observations along with spectra calculated from nonlinear (red) and linear (green) fitting methods one half of an hour after SEP event onset at 07:30 UT. Directly after SEP onset, the piecewise fitting method produced discontinuities as large as three orders of magnitude (see Figure 3.3.1). Both of our alternate methods produce no discontinuities and give adjusted R-square values of > 0.75. We see that the linear fit has an adjusted R-square value closer to unity (0.82 as opposed to 0.76). The linear fit 95% confidence intervals are also smaller. This is typical for the period of time directly after the SEP event onset on January 20th, 2005. For much of January 20th, 2005 following the SEP event onset, however not immediately afterward, the linear and nonlinear fitting methods have similar adjusted RMSE values (within 0.01) closer to unity (often about 0.97).

The last example differential spectra we show involves the enhancements in the lowest GOES energetic proton channels as discussed in Section 3.5.1. We present GOES data and integral spectra fits using the nonlinear method in Figure 3.5.11 and the linear method in Figure 3.5.12 (separated for clarity). We see that the nonlinear fit method is much

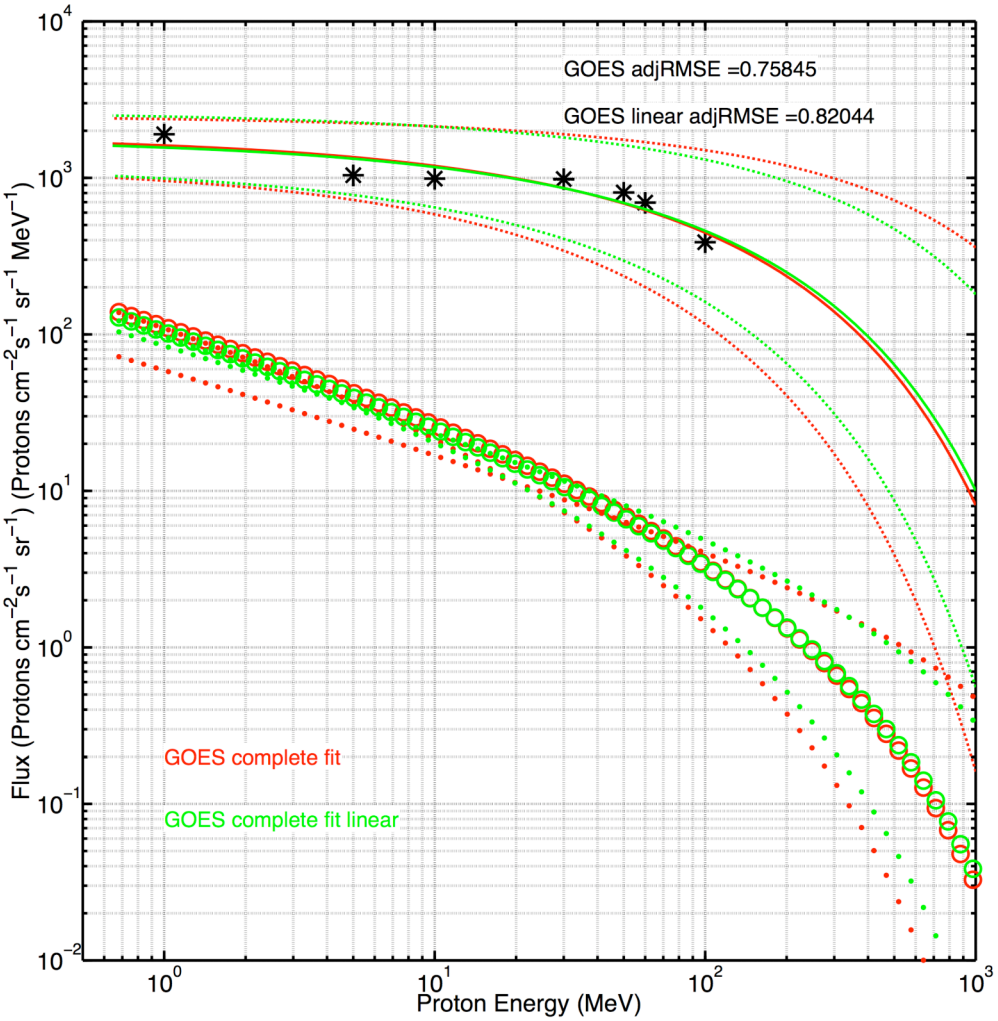

Figure 3.5.10 GOES proton flux calculated from nonlinear and linear fits at 07:30 UT. The black asterisks are the GOES integral flux observations. The nonlinear fit spectra are in red and the linear fit spectra are in green. The solid lines and circles are the calculated integral and differential spectra, respectively. The dashed lines are the 95% confidence bounds for the integral spectrum. The dots are differential spectra calculated using the 95% confidence bound values from the fit. Estimated errors of 15% in the measurements are plotted. They are not noticeable because the error bars are nearly the same size as the markers themselves. The adjusted R-square values are labeled simply "GOES adjRMSE" for the nonlinear fit and "GOES linear adjRMSE" for the linear fit.

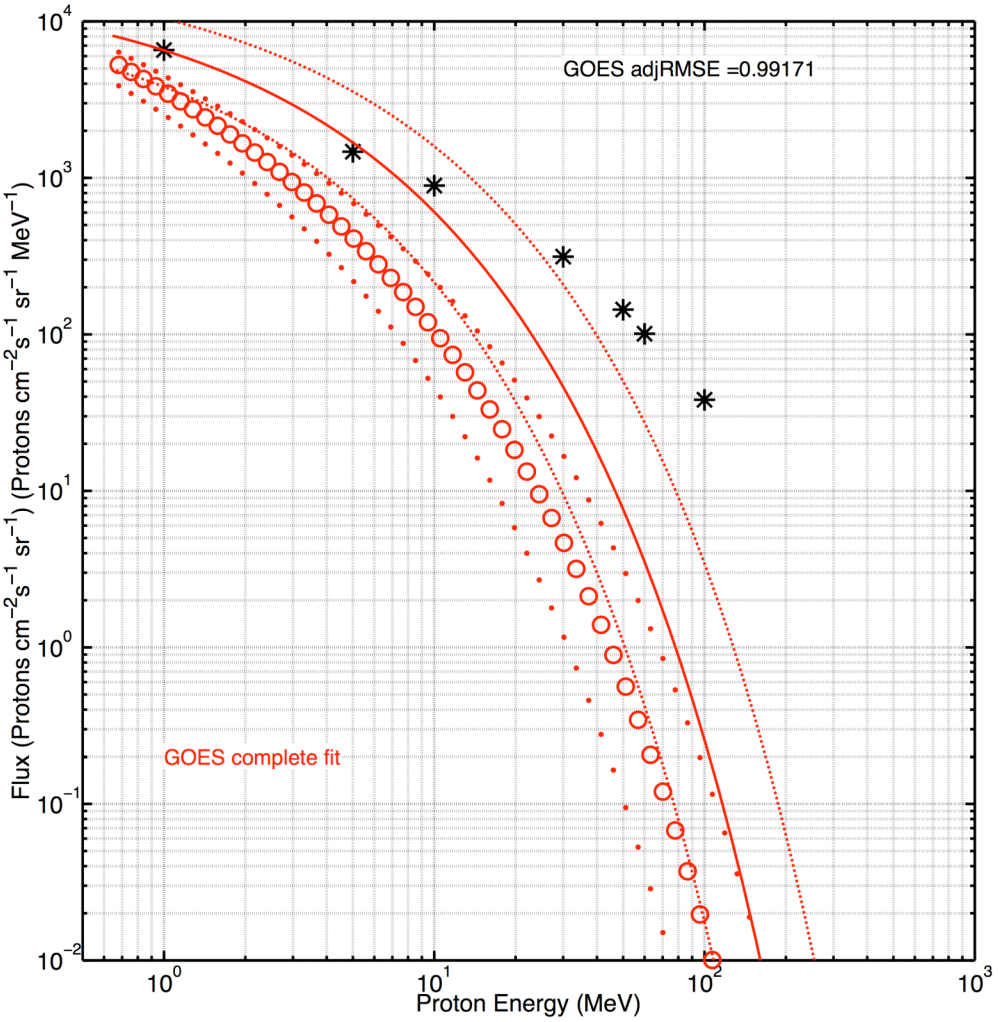

Figure 3.5.11 GOES proton flux calculated from a nonlinear fit at 16:20 UT. The black asterisks are the GOES integral flux observations. The solid red line and red circles are the nonlinear fit calculated integral and differential spectra, respectively. The dashed lines are the 95% confidence bounds for the integral spectrum. The red dots are differential spectra calculated using the 95% confidence bound values from the nonlinear fit. Estimated errors of 15% in the measurements are plotted. They are not noticeable because the error bars are nearly the same size as the markers themselves.

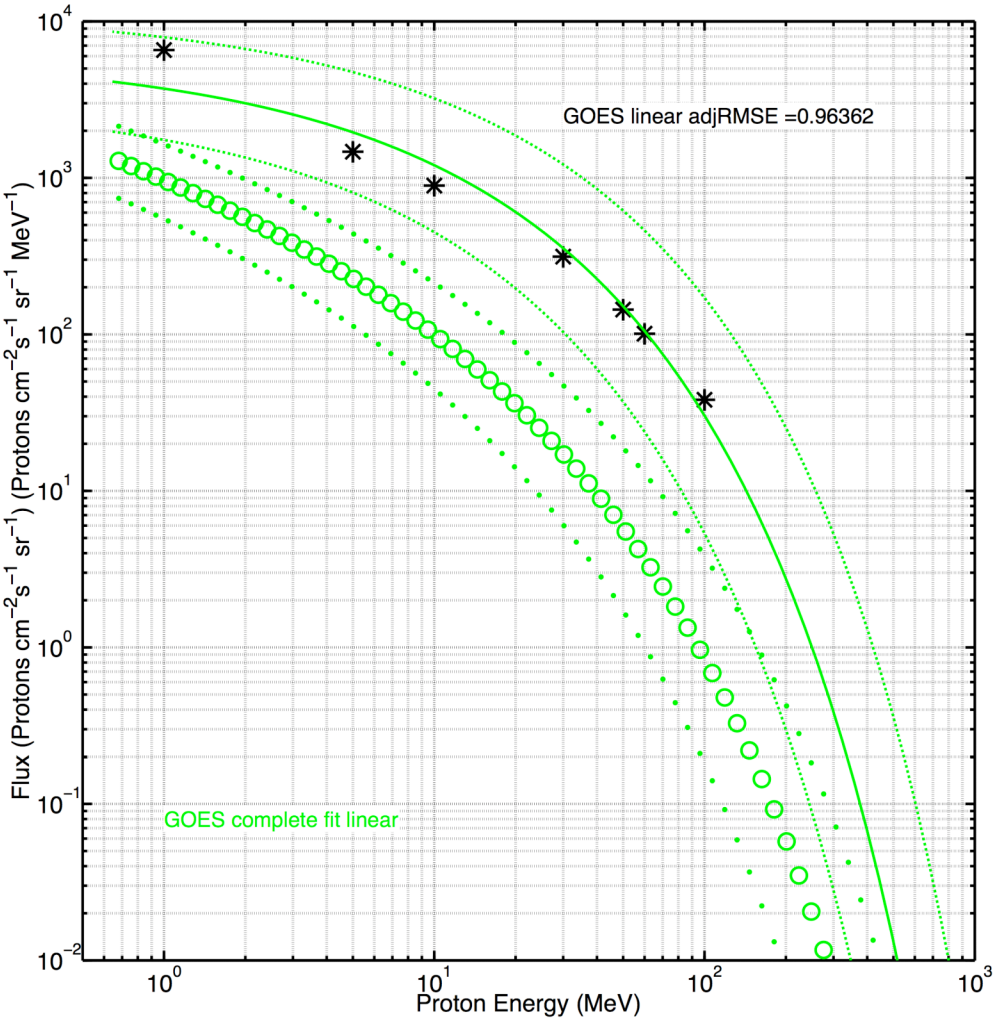

Figure 3.5.12 GOES proton flux calculated from a linear fit at 16:20 UT. The black asterisks are the GOES integral flux observations. The solid green line and green circles are the nonlinear fit calculated integral and differential spectra, respectively. The dashed lines are the 95% confidence bounds for the integral spectrum. The red dots are differential spectra calculated using the 95% confidence bound values from the nonlinear fit. Estimated errors of 15% in the measurements are plotted. They are not noticeable because the error bars are nearly the same size as the markers themselves.

more sensitive to the low energy enhancement. In contrast, the linear method follows the higher energy data points more closely. In light of our supposition that the low energy enhancement is not likely to represent precipitating protons, the linear method is more useful for SEP precipitation studies.

In summary, our alternate "complete" fitting method successfully provides continuous integral and differential spectra with a quantified estimate of error. In all of the cases we examined during the January 20th, 2005 SEP event, the linear fitting method is nearly as good (adjusted R-square values within 0.01) or better than (adjusted R-square values closer to unity by 0.06) the nonlinear method. Additionally, the linear method is less susceptible to low energy enhancements, which do not necessarily indicate a change in SEP precipitation, found in the GOES data.

3.5.3 Adding Relativistic Electron Precipitation Induced Ionization

As of now, the SIC model does not have a built-in method for taking ionization from relativistic electrons into account. The framework of the SIC model is such that an ionization rate profile due to precipitating electrons can simply be added as an additional source term. In this section we describe how to take an incident relativistic electron spectrum and determine the ionization as a function of altitude. Simply put, the method propagates an electron down through the atmosphere, keeping track of the energy lost at each altitude. From this energy loss, we calculate the ionization.

From empirical studies, electrons follow a range-energy relationship. This means that electrons with a given energy can propagate through a given range of air. The range z of an energetic electron is not a distance, but rather a mass density integrated along a distance given in units of mass per area (often g cm^{-2}). An electron precipitating vertically into the top of the atmosphere (200 km) will travel to a specific altitude (on average). The range

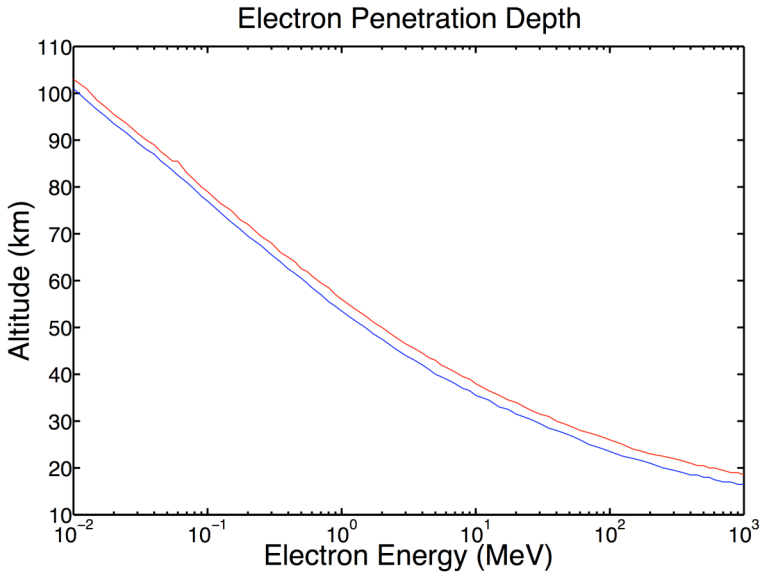

Figure 3.5.13 Maximum penetration depth for an electron as a function of energy. The blue and red lines are for electrons with zero and 45 degrees off-vertical angles of incidence, respectively.

that an electron travels into the atmosphere is the integrated mass density of the atmosphere vertically above the stopping altitude. If that same electron precipitated at an angle θ with respect to vertical, then its range will be given by

$$z = \frac{h}{\cos\theta}, \qquad \textbf{(3-34)}$$

where h is the integrated mass density along the vertical from the top of the atmosphere to a given altitude. Figure 3.5.13 shows the range for electrons precipitating vertically (blue) and at 45º from vertical (red) using range values determined from *Berger and Seltzer* [1982] and MSISE-90 model atmospheric mass density. Instead of plotting range as a function of energy, range has been converted into an altitude to which electrons can penetrate.

The two primary ways for a precipitating electron to lose energy are through collisions with neutrals and radiation. Electron energy lost over a given range Δz is given by

$$\Delta E = [\varepsilon_{col}(E) + \varepsilon_{rad}(E)]\Delta z. \qquad \textbf{(3-35)}$$

The stopping power (or the energy lost per unit range) for collisions and radiation is ε_{col}

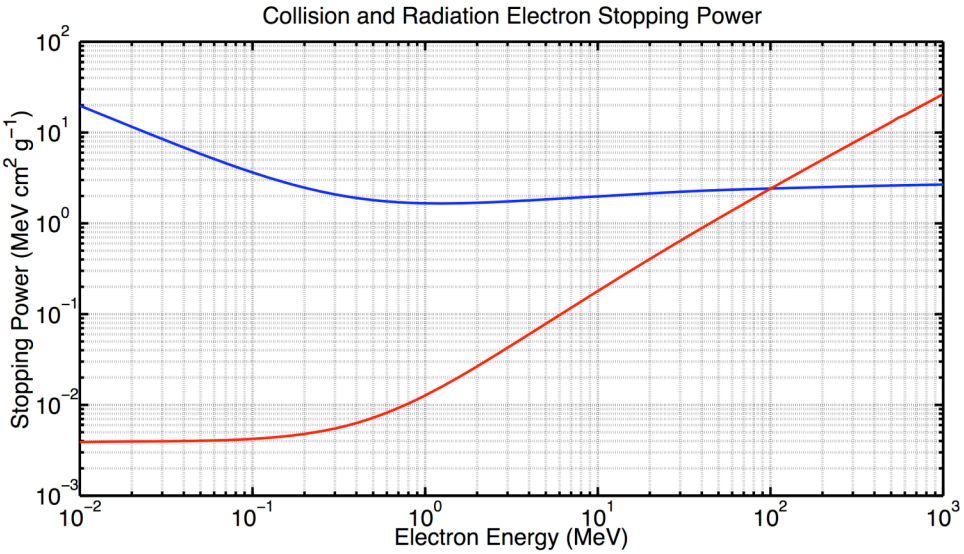

Figure 3.5.14 Electron stopping power in air. The blue line represents collision stopping power and the red line is radiation stopping power.

and ε_{rad}, respectively. Each of these stopping powers is a function of the electron energy. Figure 3.5.14 shows experimentally-determined radiation (red) and collision (blue) stopping power in air as a function of electron energy. For electrons with energy below 10 MeV (true for most precipitating relativistic electrons), much more energy is lost to collisions than to radiation. If an electron with energy $E_{initial}$ propagates through a thickness of air with range Δz, then that electron will have lost energy ΔE according to the following:

$$E_{initial} - \Delta E = E_{initial} - [\varepsilon_{col}(E_{initial}) + \varepsilon_{rad}(E_{initial})]\Delta z. \quad \textbf{(3-36)}$$

By taking the stopping power of $E_{initial}$ (and not a combination of $E_{initial}$ and ΔE, e.g., $(E_{initial} - \Delta E)/2$), we introduce an error, which is small as long as Δz and/or $E_{initial} - \Delta E$ remain small. (For the step sizes used in the full ionization model, the typical error size is less than a few percent.) It has been experimentally shown that the energy lost by an electron per ionization $E_{ionization}$ in N_2 and O_2 is 33 eV and 37 eV, respectively. It is a common practice to use 35 eV as an average value in air [*Rees*, 1989]. Thus the total ionization in the range Δz becomes

$$\Delta Q = \frac{\Delta E}{E_{ionization}} \Delta z. \qquad \textbf{(3-37)}$$

If Equation (3-37) were used for an electron incident on the top of the atmosphere for a step size of fixed height (1 km used in the full model), then ΔQ is small because Δz is small. We can then calculate the ionization within the next range step Δz by repeating the calculation with the 'initial' electron energy now $E_{initial} - \Delta E$. This is repeated again and again until all of the electron energy $E_{initial}$ is lost. The electron is assumed to travel in a straight line and not deviate from its trajectory. For high energies, this is a valid approximation because the momentum of the precipitating electrons is much larger (by several orders of magnitude) than the momentum of the newly formed ion-electron pair. Based on a simple random walk analysis, we estimate that the error introduced by this assumption is less than 10% with the largest deviations occurring in the lowest 20 km of a given electron track. For an electron precipitating vertically, we can simply sum the mass of air above a given altitude to calculate the range an electron must travel to reach that altitude. Using the MSISE-90 model for neutral density and the National Bureau of Standards tables for range and stopping power values [Berger and Seltzer, 1982], we can calculate ionization due to precipitating electrons at a given altitude. Figure 3.5.15 gives an ionization profile due to 100 vertically incident electrons at several different energies. The normalizing constant A represents the area over which the electrons were initially incident and since they are propagating vertically downward, the width of the column of air they travel through. In reality, we do not expect that all electrons have a vertical precipitation angle and that there is a distribution of electrons. By repeating the process described for a mono-directional beam over a range of incidence angles and normalizing, we can produce an ionization rate profile for an isotropic distribution. Figure 3.5.16 shows a similar ionization profile due to 100 electrons isotropically incident between 0º and 90º off vertical. Here, the normalizing constant A is equal to only the horizontal area affected by the electrons at a given altitude and not the incident precipitation area. We use this normalizing convention to show that given an equal number of precipitating

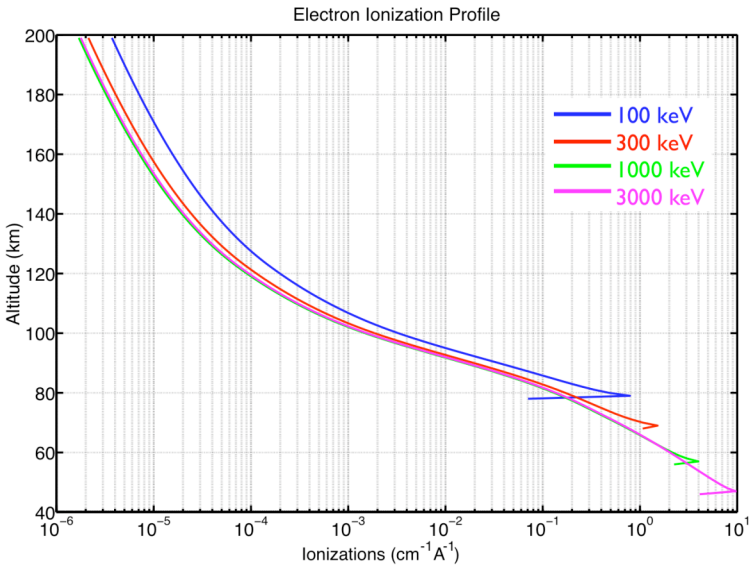

Figure 3.5.15 Ionization due to 100 unidirectional precipitating electrons vertically incident on the upper atmosphere. The horizontal axis units are ionizations per volume where A is a normalizing constant representing the effected horizontal area.

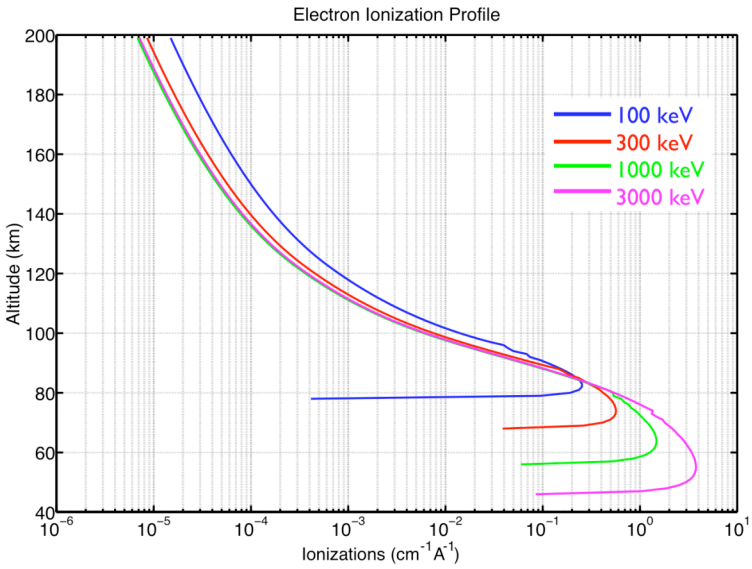

Figure 3.5.16 Ionization due to 100 precipitating electrons incident on the upper atmosphere isotropically between 0º and 90º off vertical. The horizontal axis units are ionizations per volume where A is a normalizing constant representing the effected horizontal area.

electrons, isotropic and mono-directional distributions deposit different amounts of energy at a particular altitude.

With a method for describing ionization due to energetic electrons, we take realistic input spectra based on MINIS observations as input. Based on work described in *Sample* [2008], we characterize precipitating electron spectra by the following:

$$f = f_0 e^{-E/E_0}. \tag{3-38}$$

Equation (3-38) describes the integral flux f as a decaying exponential function of energy E and e-folding energy E_0. This is not the only way to describe a precipitating electron spectrum, but it accurately describes the energetic precipitation events observed by MINIS (above ~ 200 keV).

Now that we have described the method for producing ionization rate profiles given an incident energetic electron flux, we can examine the entire process from the point of view of writing a code to do the calculations. The entire process detailed below is a approximation used to evaluate the ionization rate given in Equation (3-29). Essentially, we take a unit set of electrons with initial energy E, propagate them through that atmosphere with an initial angle of incidence θ and keep track of the energy lost (and therefore the number of ionizations) at each altitude. Then, we replace our unit set of electrons with a spectrum based on observations. Let us begin with vectors giving the altitude a and range z. We use 200 km as the upper bound of our atmosphere and calculate the range from this height.

$$\begin{bmatrix} a_1 = 200 \\ \vdots \\ a_i \\ \vdots \\ a_n = 0 \end{bmatrix} \qquad \begin{bmatrix} z_1 = 0 \\ \vdots \\ z_i \\ \vdots \\ z_n \end{bmatrix} \qquad z_i = z_{i-1} + \Delta z_{i-1} \tag{3-39}$$

Δz_i is the range between z_{i-1} and z_i given by the following equation where ρ is the

atmospheric mass density, Δa is the height step size and θ is the angle of incidence off vertical:

$$\begin{bmatrix} \Delta z_1 \\ \vdots \\ \Delta z_i \\ \vdots \\ \Delta z_n = 0 \end{bmatrix}; \qquad \Delta z_i = \frac{\Delta a}{\cos\theta}\frac{(\rho_{i+1} - \rho_i)}{2}. \tag{3-40}$$

With the range steps Δz, we can now calculate the electron energy as a function of altitude. Depending on the initial energy of the electron, it will lose a portion of its energy in each altitude step based on the range of air it must travel through. We build a unit set of electrons with initial energies between E_{min} and E_{max} and a constant angle of incidence. From this initial incident set, we can define the energy of a particular unit electron as a function of altitude using Equation (3-41). Each column represents an initial energy bin separated by a specified value (often 1 keV for complete model application) and each row represents an altitude. Thus, in a particular column, the energy values represent the energy of an electron at a given altitude after starting with initial energy E_{1j} at the top of the atmosphere and then losing energy to collisions and radiation.

$$\begin{matrix} E_{\min} & & & & E_{\max} \end{matrix}$$
$$\begin{bmatrix} E_{11} & \cdots & E_{1j} & \cdots & E_{1m} \\ \vdots & & \vdots & & \vdots \\ E_{i1} & \cdots & E_{ij} & \cdots & E_{im} \\ \vdots & & \vdots & & \vdots \\ E_{n1} & \cdots & E_{nj} & \cdots & E_{nm} \end{bmatrix} \qquad E_{ij} = E_{i-1,j} - [\varepsilon_{total}(E_{i-1,j})]\Delta z_i \tag{3-41}$$

Then, we can calculate the number of ionizations in a given altitude step due to electrons within each specific initial energy bin by dividing the energy lost at each altitude by the average ionization energy.

$$\begin{matrix} E_{\min} & & & & E_{\max} \end{matrix}\begin{bmatrix} \Delta Q_{11} & \cdots & \Delta Q_{1j} & \cdots & \Delta Q_{1m} \\ \vdots & & \vdots & & \vdots \\ \Delta Q_{i1} & \cdots & \Delta Q_{ij} & \cdots & \Delta Q_{im} \\ \vdots & & \vdots & & \vdots \\ \Delta Q_{n1} & \cdots & \Delta Q_{nj} & \cdots & \Delta Q_{nm} \end{bmatrix} \qquad \Delta Q_{ij} = \frac{E_{ij}}{E_{ionization}} \tag{3-42}$$

Equation (3-42) describes the ionizations in the i[th] altitude bin due to one single electron precipitating in the j[th] energy bin. Realistic energetic electron precipitation spectra are not flat with one electron per unit energy, thus we introduce an electron energy spectrum. We use the following form to describe incident electron flux spectra:

$$\begin{bmatrix} f_1 & \cdots & f_j & \cdots & f_m \end{bmatrix}; \qquad f_j = f_0 e^{-E_{1j}/E_0}. \tag{3-43}$$

Then, we can multiply the electron flux spectrum f (in counts sec^{-1} energy^{-1}) by the transpose of the ionizations due to an electron in each energy bin ΔQ to get the transpose of the ionization rate altitude profile Δq. In other words, we multiply the number of ionizations ΔQ from our unit set of electrons based on the number of electrons in our precipitation spectrum *f*.

$$\begin{bmatrix} \Delta q_1 \\ \vdots \\ \Delta q_i \\ \vdots \\ \Delta q_n \end{bmatrix}^T = \begin{bmatrix} f_1 & \cdots & f_j & \cdots & f_m \end{bmatrix} \begin{bmatrix} \Delta Q_{11} & \cdots & \Delta Q_{i1} & \cdots & \Delta Q_{n1} \\ \vdots & & \vdots & & \vdots \\ \Delta Q_{1j} & \cdots & \Delta Q_{ij} & \cdots & \Delta Q_{nj} \\ \vdots & & \vdots & & \vdots \\ \Delta Q_{1m} & \cdots & \Delta Q_{im} & \cdots & \Delta Q_{nm} \end{bmatrix} \tag{3-44}$$

We have assumed a mono-directional electron beam up until this point. If we want to consider an isotropically-distributed source, we have to normalize the ionization rate profile from Equation (3-44). Let us assume an isotropic source over a solid angle defined by a cone with half-angle θ_N such that our electron spectrum f (which has no directional dependence) becomes spread out. We keep the same total number of electrons, but change the angle of incidence. We split up the solid angle into annuli with a given angular step size (usually 2.5 degrees for our model runs). Following the equations above, we

propagate a mono-directional electron spectrum f through the atmosphere assuming an angle of incidence θ. We repeat this multiple times for angles of incidence between zero and θ_N. At this point, we have over-estimated the ionizations by using the entire electron spectrum f for every angle of incidence as opposed to using only the fraction expected to be incident at that angle. Thus, we need to normalize each calculated ionization rate profile. We can multiply by the fraction of solid angle annulus for one angle step size ($\theta_{max} - \theta_{min}$ where the angle of incidence is the mean of these two) over the total solid angle of the source region to normalize each ionization rate profile.

$$\begin{bmatrix} \Delta q_{N1} \\ \vdots \\ \Delta q_{Ni} \\ \vdots \\ \Delta q_{Nn} \end{bmatrix} = \left(\frac{\cos\theta_{\min} - \cos\theta_{\max}}{1 - \cos\theta_N} \right) \begin{bmatrix} \Delta q_1 \\ \vdots \\ \Delta q_i \\ \vdots \\ \Delta q_n \end{bmatrix} \quad \textbf{(3-45)}$$

Thus, we have a series of normalized ionization rate profiles, one for each angle of incidence we considered. Finally, to get the total ionization rate as a function of altitude, we have to sum all of the normalized ionization rates from Equation (3-45) over all angles of incidence.

$$\begin{bmatrix} q_1 = \sum_{\theta} \Delta q_{N1} \\ \vdots \\ q_i = \sum_{\theta} \Delta q_{Ni} \\ \vdots \\ q_n = \sum_{\theta} \Delta q_{Nn} \end{bmatrix} \quad \textbf{(3-46)}$$

An example incident precipitating relativistic electron spectrum is shown in. This spectrum corresponds to one specific measurement at MINIS Flight 2 South at 17:12 UT January 21st, 2005. We assume that there are no electron counts below 200 keV. In actuality, there most likely are electrons below 200 keV, but the spectrum is unconstrained by the MINIS x-ray observations.

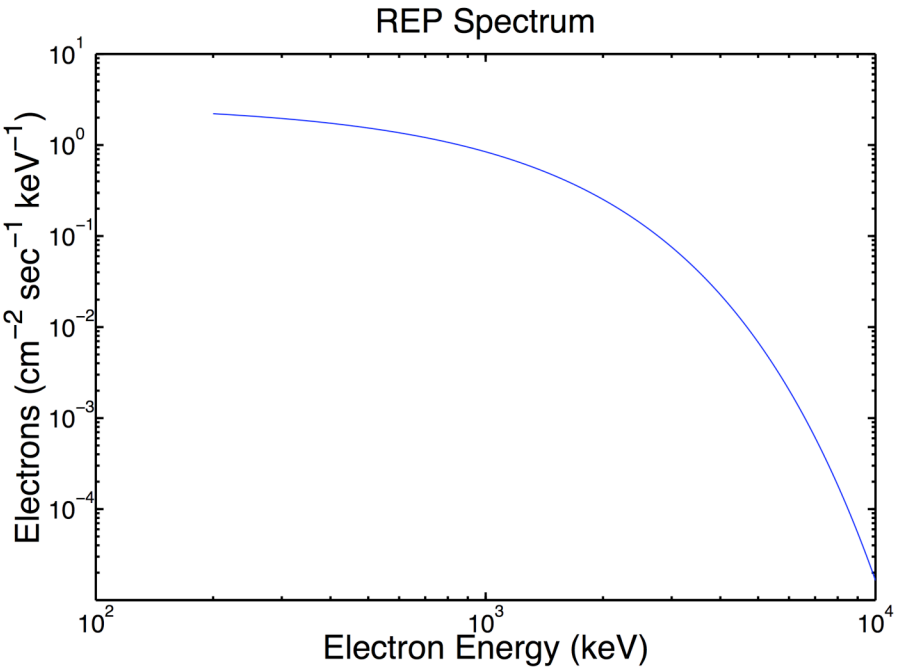

Figure 3.5.17 Example REP spectrum determined by J. Sample from MINIS Flight 2 South x-ray measurements at 17:12 UT on January 21st, 2005. The e-folding energy is 830 keV and nothing has been calculated below 200 keV.

Figure 3.5.18 shows an example of an ionization rate profile based on the spectrum in Figure 3.5.17. All electrons are assumed to be vertically incident. REP-induced ionization is small when compared with the SIC-calculated ionization rate profiles shown in Figure 3.5.19. In order to have a noticeable effect on atmospheric conductivity, REP would have to be much more intense than the example provided by MINIS. Alternately, a large low-energy component to the spectrum shown in Figure 3.5.17 could possibly have a significant effect.

Given any energetic electron flux spectrum, like those produced from MINIS observations, an ionization rate profile can be made using the method described. The Matlab routine written to calculate total ionization rate profiles for the MINIS observations can be found in Appendix D. This routine can easily be modified for application to future observations.

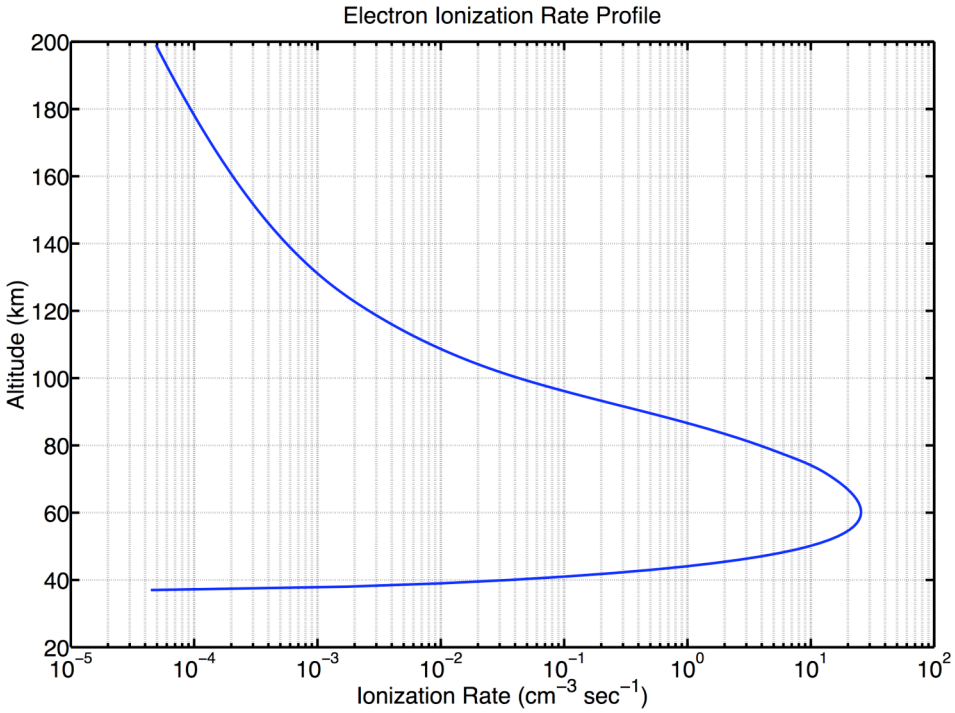

Figure 3.5.18 Ionization rate profile based on MINIS Flight 2 South observations a 17:12 UT January 20th, 2005. The source electrons are assumed to be vertically incident. The altitude step size is 1 km and the energy step size is 1 keV.

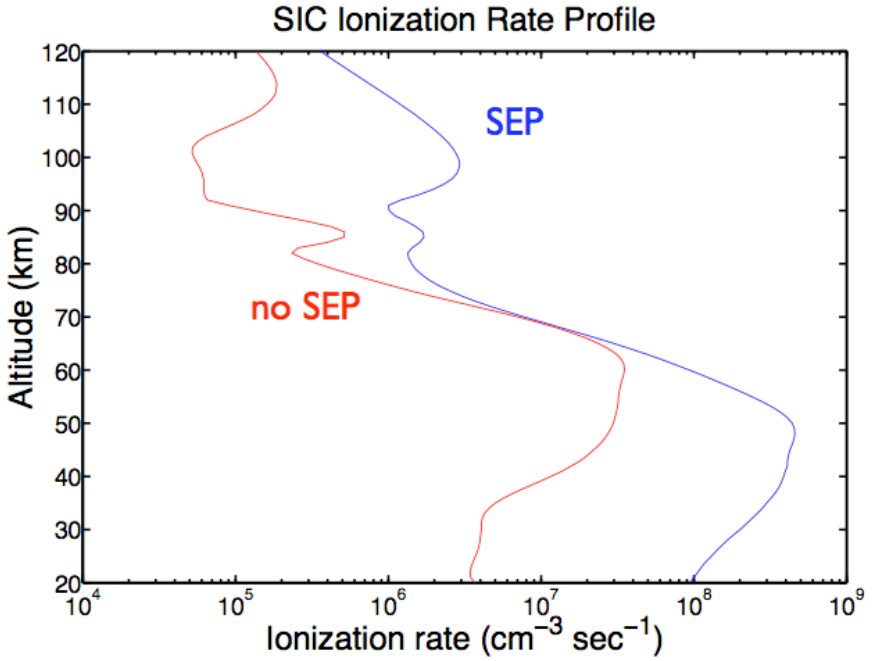

Figure 3.5.19 SIC-calculated ionization rate profiles for SEP (blue) and non-SEP (red) conditions.

4 Observations During the January 20th, 2005 Solar Energetic Particle Event

January 2005 was a particularly active period for the sun. During the declining phase of solar cycle 23, between January 15th and 24th, there were five X-class solar flares observed by the GOES x-ray detectors. In conjunction with some of these solar flares, several halo coronal mass ejections (CMEs), and solar energetic particle (SEP) events occurred. Solar flare x-rays, bulk CME plasma and energetic particles each affect the earth's coupled magnetosphere-ionosphere-atmosphere system. In this chapter, we will examine effects of the largest solar flare (X 7.1) and hardest SEP event, which occurred on January 20th, 2005. First, we will examine the solar activity and solar wind to provide context for the events on January 20th. Then, we will present the effects on the electrical environment from the point of view of the MINIS balloon observations. These effects include an increase in electrical conductivity and a vanishing of the dc electric field in the polar stratosphere. The presentation of data in Chapter 4 is followed, in Chapter 5 by a description of proposed physical mechanisms which we believe are most likely to explain the balloon observations and implications for the larger global system.

4.1 Observations of Solar Activity and Energetic Particles from Satellite Instruments

In this section, we will present satellite data describing the solar activity between January 16th and 24th with a special focus on January 20th, 2005. On this day, a large X 7.1 solar flare occurred in conjunction with a halo CME and SEP event. We focus on the solar wind parameters, solar flare x-rays and SEPs that began to arrive at earth shortly after the flare onset (within one half of an hour). We discuss the bulk CME plasma, which did not arrive at earth until the following day, in Chapters 6 and 7.

4.1.1 Solar Flare and Coronal Mass Ejection Observations

The first indicators of a solar flare come from x-ray radiation observations. Since x-

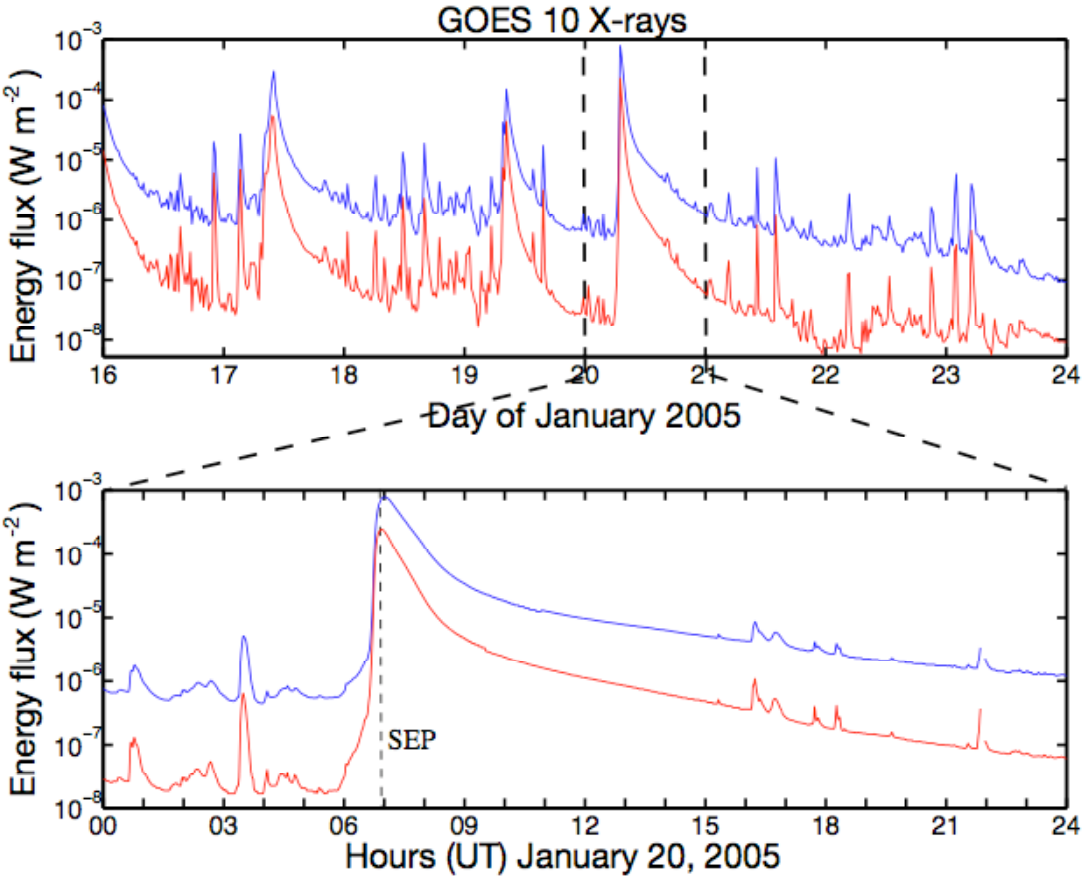

Figure 4.1.1 GOES 10 x-rays during January 2005. The top panel spans January 16th to 24th and the bottom panel shows January 20th. The blue and red lines are the long (1 – 8 Å) and short (0.5 – 3 Å) wavelength bands, respectively. The top panel is coarsely sampled every 20 minutes and the bottom panel is sampled once a minute. The vertical dashed line in the bottom panel marks the SEP (not x-ray) arrival at earth.

rays travel at the speed of light, they are the first to arrive at earth, before SEPs and bulk plasma. If there is a CME eruption at the same time as a solar flare, light emissions from the expelled CME plasma near the sun will arrive almost simultaneously with the initial x-rays. The GOES satellites all have instruments that measure two discrete bands of x-ray radiation (short 0.5 – 3 Å and long 1 – 8 Å). Figure 4.1.1 shows GOES 10 x-ray observations between January 16th and 24th in the top panel and only January 20th in the bottom panel. GOES 12 x-rays are also available for this time period and show a nearly identical time series. In the top panel of Figure 4.1.1, three X-class x-ray peaks can be seen (X-class flares are any with peak intensities in

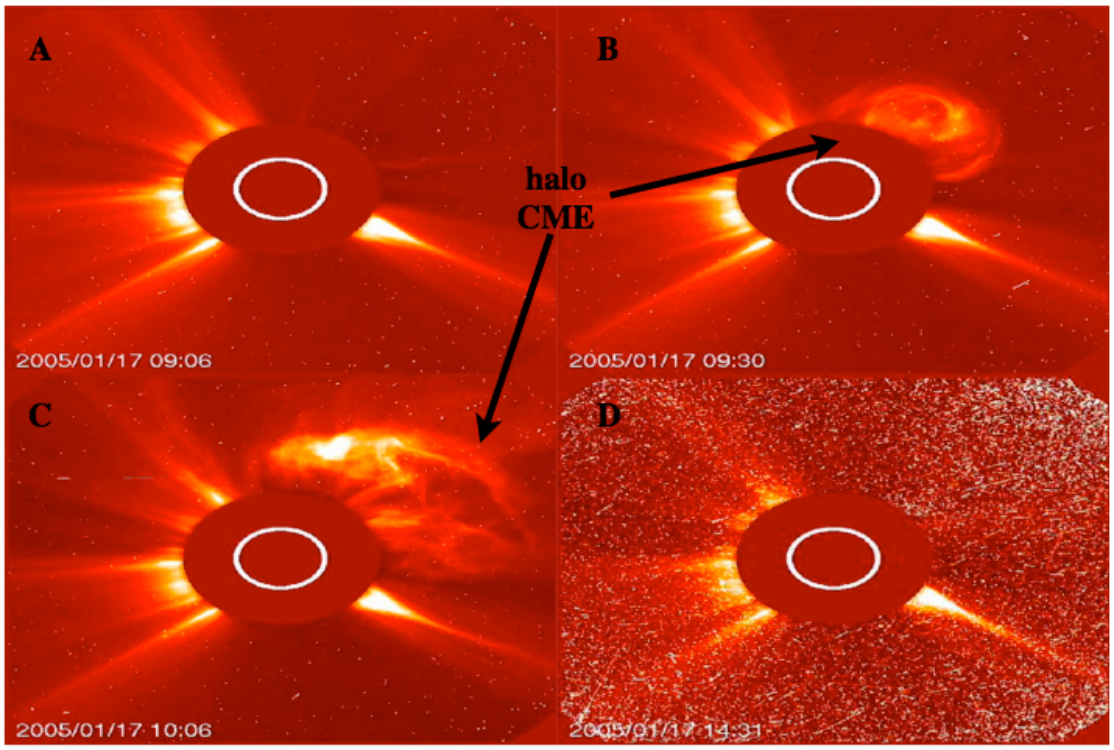

Figure 4.1.2 SOHO coronagraph images showing the evolution of a CME and an associated SEP event. The halo CME develops as the flare occurs while the SEPs are observed hours later. Time stamps are give for each panel: A) 09:06 UT B) 09:30 UT C) 10:06 UT and D) 14:31 UT.

the long band greater than 10^{-4} W m^{-2}). There are two additional X-class flares on January 15th (not shown). The purpose of showing the x-rays in Figure 4.1.1 is simply to show that the sun was especially active during this time. Also, notice that the last X-class flare occurred on January 20th. This means we need to take into account the activity before January 20th when analyzing the data, but we need not be concerned with effects from additional flares on subsequent days. Figure 4.1.1 shows that there are solar flares occurring during January 2005, but we cannot tell if there were any CMEs or SEP events. Initial evidence for these events can be attained from Solar Heliospheric Observatory (SOHO) coronagraph images. We will use SOHO images, taken near the L1 Lagrange point, as qualitative evidence for CMEs and SEP events. Figure 4.1.2 shows a time series from January 17th before and after an X-class solar flare. Panel A shows the corona just before the flare with streamers, but no CME. Panels B and C show the development of a halo CME. The peak x-ray flux observed at GOES 10 occurs at 09:50 UT, between the

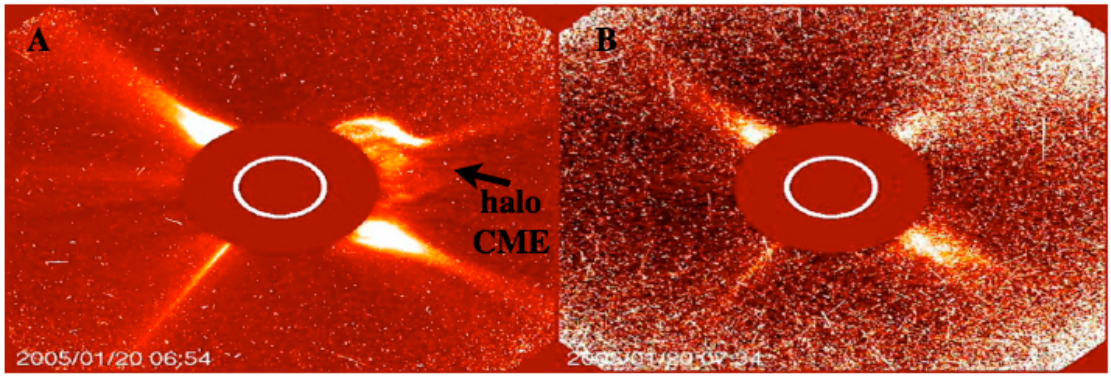

Figure 4.1.3 SOHO coronagraph taken after the solar flare onset on January 20th, 2005. Panel A shows the beginnings of a halo CME at 06:54 UT and panel B shows a significant saturation of the CCD by SEP protons at 07:34 UT.

time stamp of panels B and C. SEP protons hitting the CCD of the coronagraph camera can be seen in panel D as white fuzz. The peak SEP fuzz is shown at 14:31 UT. The peak SEP occurs nearly 4 hours after the beginning flare and CME. This time evolution is typical for solar flare, CME and SEP events. From a similar analysis, we can see that the events of January 20th differ significantly from those on January 17th. Figure 4.1.3 shows SOHO coronagraphs for the January 20th events. In panel A, we can see the initial developments of a halo CME at 06:54 UT. In the very next frame, taken at 07:34 UT, the CME is completely obscured by the SEP particles saturating the CCD. This is not a typical SEP evolution because the protons arrive much faster than they normally would. We will show more quantitative evidence illustrating the uniqueness of the January 20th event later. For now, we have established that during January 2005 there were CMEs and SEP events associated with some of the solar flares and that the events of January 20th occurred in unusually rapid succession.

4.1.2 Solar Wind Dynamics

The best satellite monitor for solar wind characteristics is the Advanced Composition Explorer (ACE), which orbits the L1 Lagrange point about 221 earth radii upstream from the earth toward the sun. Onboard ACE, there are instruments that can measure

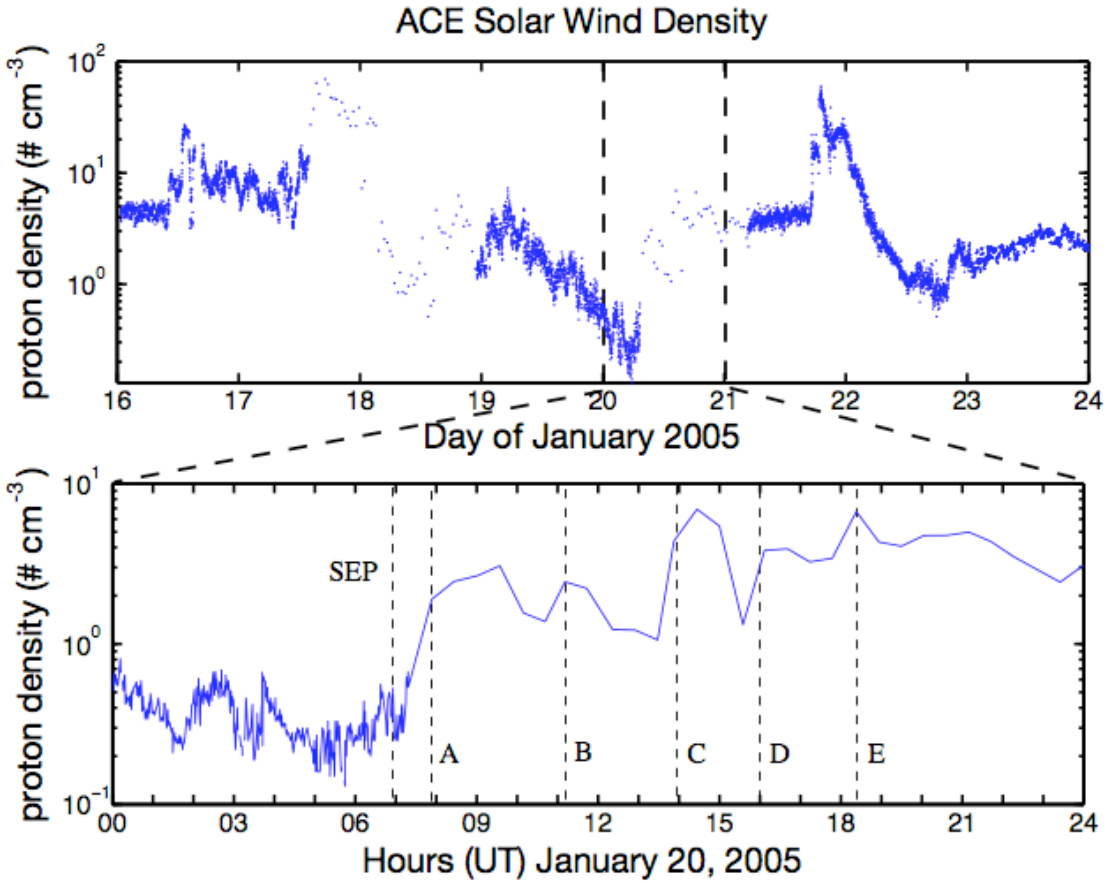

Figure 4.1.4 Solar wind proton number density measured by ACE during January, 2005. The top panel shows January 16th to 24th. The bottom panel shows January 20th. The vertical dashed lines represent the SEP event onset at ACE (SEP) and five additional density fluctuations (A – 07:53 UT, B – 11:10 UT C - 13:56 UT, D - 15:54 UT and E - 18:22 UT).

the density, velocity and imbedded magnetic field of the solar wind. Figure 4.1.4 shows the solar wind proton number density between January 16th and January 24th, time delayed for arrival at earth. (All ACE data presented in this chapter are time delayed for earth arrival for easier comparison with near-earth observations.) One of the most noticeable characteristics of the plot is the inconsistent measurement rate. During the two largest SEP events of this time period, normal instrument operation is affected. Higher time-resolution measurements are not available. However, during regular half-hour intervals, density measurements are attained using a different instrument mode (*R. Skoug,* private communication). This affects the density and velocity measurements, but not the magnetic field data. The next point to notice is the dynamic nature of the solar wind

density itself. It is clear that there are multiple rapid changes mainly caused by fast, dense CME bulk plasma streams in the top panel. In the lower panel, we can see the solar wind proton density for January 20th. The vertical dashed lines represent the time when the SEP event onset (labeled SEP) along with five additional times (A - 7:53 UT, B - 11:10 UT, C - 13:56 UT, D - 15:54 UT and E - 18:22 UT). The special circumstances related to these notable times become more evident as more observational data is presented. However, by simply looking at only Figure 4.1.4, we note that the five labeled dashed lines A, B, C, D and E are all associated with density increases. It is important to keep in mind that these density fluctuations all occur when data points are taken every half of an hour (not averaged over one half of an hour). This means that despite large fluctuations, we cannot say how quick the fluctuations are, only that they occur on half-hour timescales. These density fluctuations are part of the dynamic solar wind pressure exerted onto the earth's magnetosphere. Dynamic pressure is a function of solar wind density and velocity, so let us also look at the velocity term.

Figure 4.1.5 has the same format as Figure 4.1.4 except that it shows ACE solar wind velocity instead of proton number density. The GSE coordinates used have positive $\hat{x}$ pointing towards the sun. Thus, flow towards the earth is represented as a negative value of the *x*-component of the velocity. Vertical dashed lines mark the SEP event onset (SEP) and the same five notable times as in Figure 4.1.4. The solar wind velocity increases sharply by 200 km sec^{-1} at A, modestly increases by 25 km sec^{-1} at B and modestly decreases by 50 km sec^{-1} at C. As with the density shown in Figure 4.1.4, we cannot definitively say how quickly these fluctuations occur nor determine their absolute magnitude change.

Combining the solar wind density and velocity data we can get the solar wind dynamic

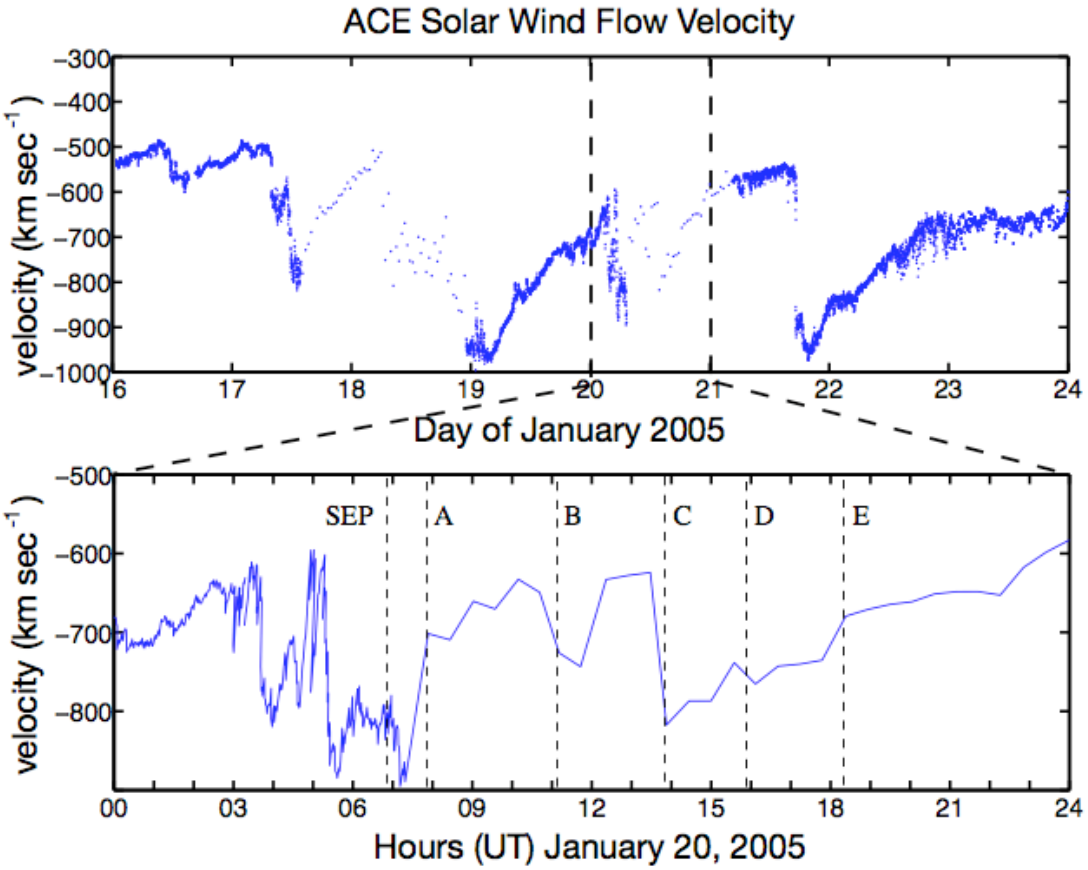

Figure 4.1.5 Solar wind velocity measured by ACE during January 2005. The top panel shows January 16th to 24th. The bottom panel shows January 20th. The vertical dashed lines represent the SEP event onset at ACE (SEP) and the five times with a density fluctuation (A – 07:53 UT, B – 11:10 UT C - 13:56 UT, D - 15:54 UT and E - 18:22 UT).

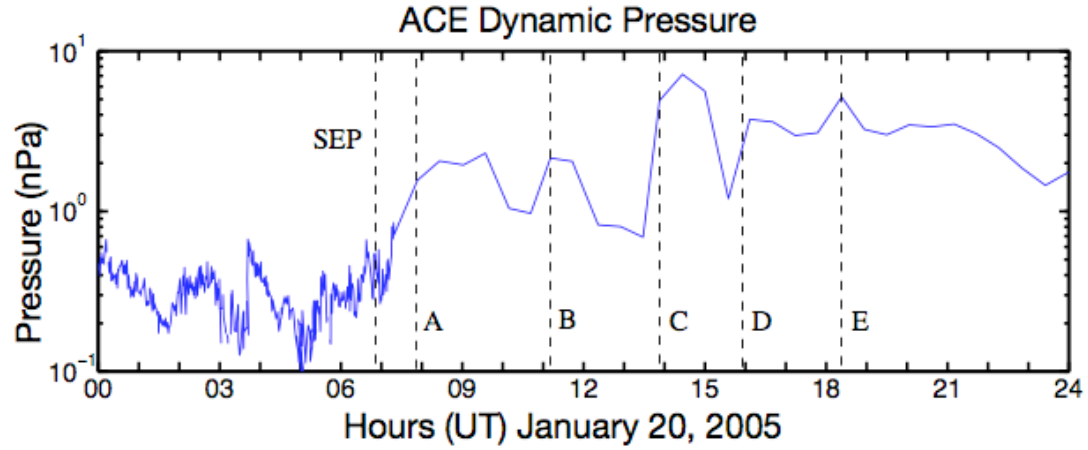

Figure 4.1.6 Solar wind dynamic pressure measured at ACE in nPa during January 2005. The vertical dashed lines represent the SEP event onset at ACE (SEP) and five distinct pressure increases (A – 07:53 UT, B – 11:10 UT C - 13:56 UT, D - 15:54 UT and E - 18:22 UT).

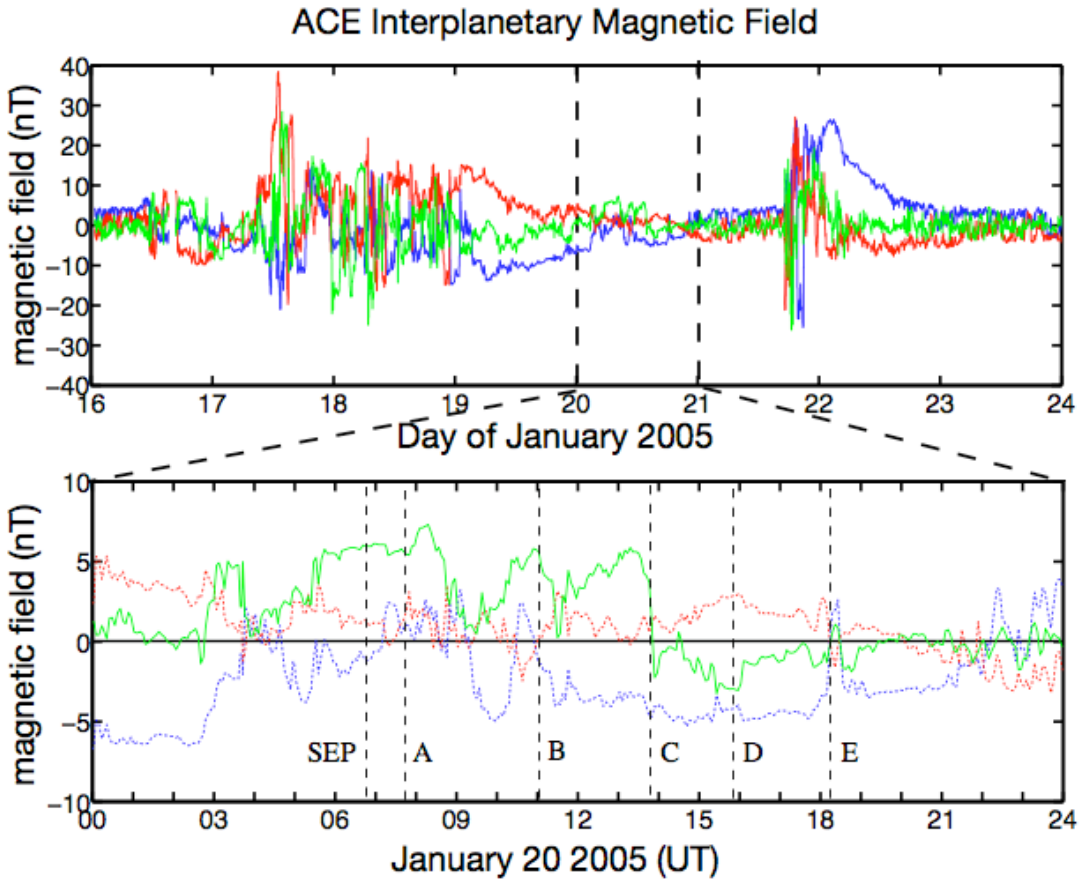

Figure 4.1.7 Interplanetary magnetic field measured at ACE in nT during January 2005. The top panel shows January 16th to 24th. The bottom panel shows January 20th. The x, y and z components are in blue, red and green, respectively. In the lower panel, B_x and B_y are shown as dashed lines to make fluctuations in B_z easier to see. The vertical dashed lines represent the SEP event onset at ACE (SEP) and the same five time labeled in earlier plots (A – 07:53 UT, B – 11:10 UT C - 13:56 UT, D - 15:54 UT and E - 18:22 UT).

pressure, shown in Figure 4.1.6. The same six times are marked on the figure. At each time, there is a marked increase in solar wind dynamic pressure.

The last piece of the solar wind to examine is the interplanetary magnetic field. Figure 4.1.7 shows the interplanetary field measured at ACE. The top panel shows the time between January 16th and 24th, while the bottom panel shows January 20th in more detail. From the top panel, we can see that the largest magnetic field fluctuations occur on January 17th, 18th, 21st and 22nd, while January 20th is comparatively calm. The large fluctuations in the top panel of Figure 4.1.7 are consistent with the arrival of bulk CME

Table 4-1 Summary of notable solar wind fluctuations on January 20th. Times are based on the coarse density and velocity measurements unless there is evidence of fluctuations from other data sources. Each set of data values show the value before the times listed and then the value at the time listed.

	A	B	C	D	E
Time (UT)	07:53	11:10	13:56	15:54	18:22
Δ *density (# cm^{-3})*	0.5-2	1.4-2.5	1.1-4.4	1.3-3.8	3.4-6.7
Δ *velocity (km s^{-1})*	890-702	649-726	624-817	738-765	738-765
Δ *dyn. pres (nPa)*	0.7-1.6	1.0-2.1	0.7-4.9	1.2-3.7	3.1-5.2
Δ *Bz (nT)*	6-5	5-4	4-(-3)	(-3)-(-3)	(-1.5)-1

plasma on January 17th and 21st.

Upon closer inspection of January 20th, B_z is northward for most of the day until C at 13:56 UT. This indicates a closed magnetospheric configuration with no significant low latitude geomagnetic activity before 13:56 UT and an open configuration ripe for storm activity for several hours afterward while B_z is south. Only points C and E have significant coincident interplanetary magnetic field fluctuations. There are relatively large, rapid B_z fluctuations that do not coincide with each solar wind pressure change. However, after the SEP event onset, the only two moments where B_z flips sign are coincident with times when the dynamic pressure changes (C - 13:56 UT C and E – 18:22 UT).

Table 4-1 contains a summary of the solar wind fluctuations at the indicated notable times. The largest dynamic pressure change is coincident with the largest magnetic field change at point C. Point D has the second largest pressure increase and point E has a similarly large pressure increase and the only instance of B_z flipping northward. With this view of the solar wind environment as a context, let us next examine the energetic particle flux at earth.

4.1.3 Energetic Particle Flux Enhancement

In the preceding sections, we have only provided qualitative evidence for the SEP events

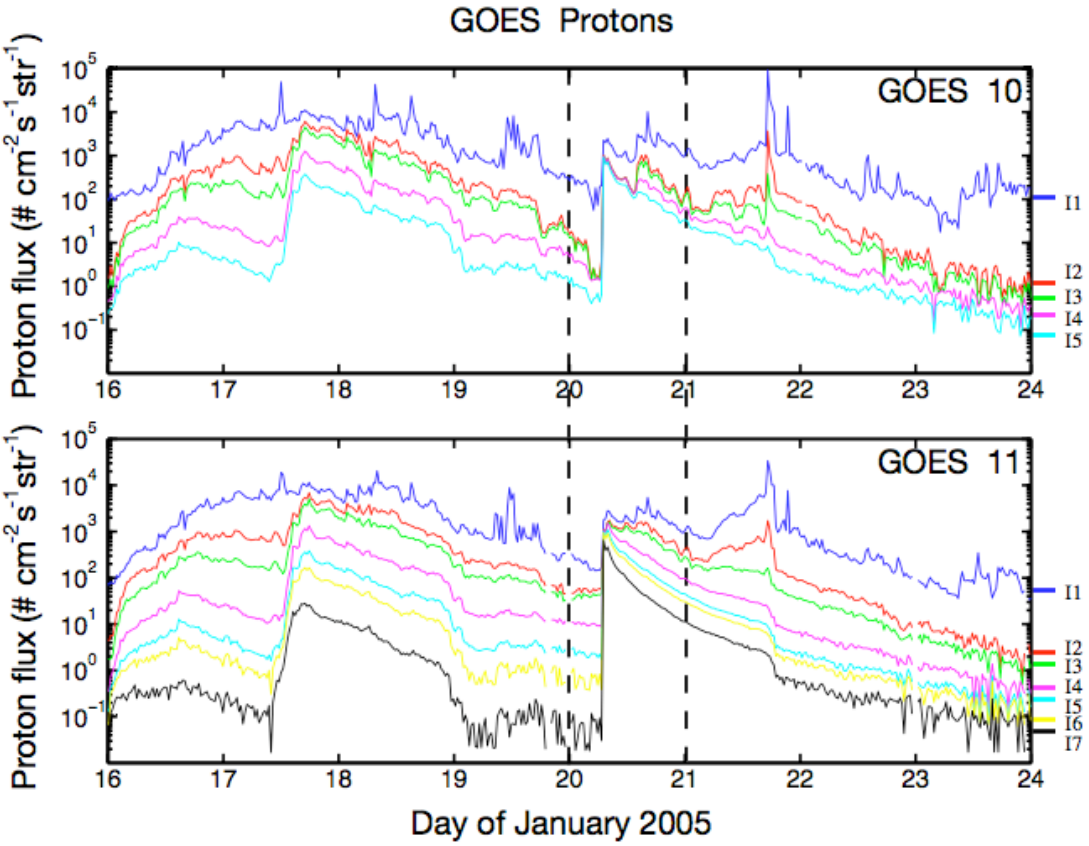

Figure 4.1.8 GOES 10 and 11 integral energetic proton flux during January 2005. The seven integral channels, I1 to I7, are shown in blue, red, green, magenta, cyan, yellow and black, respectively. The minimum proton energy for each channel is I1 > 1 MeV, I2 > 5 MeV, I3 > 10 MeV, I4 > 30 MeV, I5 > 50 MeV, I6 > 60 MeV and I7 > 100 MeV. The vertical dashed lines indicate the section of data shown in Figure 4.1.9.

by showing contamination of both the SOHO images and ACE solar wind data. These are good examples of the kinds of problems SEPs can have on space instrumentation. Let us now present some quantitative measurements of increased energetic proton flux from earth-orbiting GOES and POES satellites. Figure 4.1.8 shows GOES energetic protons from GOES 10 and 11 between January 16th and January 24th. In January 2005, GOES 10 was the west operational satellite at 135º W and GOES 11 was in a back-up position at 105º W. GOES 12 proton data is not available for this time period. Integral proton flux is given in seven different channels (I1 > 1 MeV, I2 > 5 MeV, I3 > 10 MeV, I4 > 30 MeV, I5 > 50 MeV, I6 > 60 MeV and I7 > 100 MeV). GOES 10 channels I6 and I7 were not operational during this time period. Figure 4.1.8 shows the dynamic energetic proton

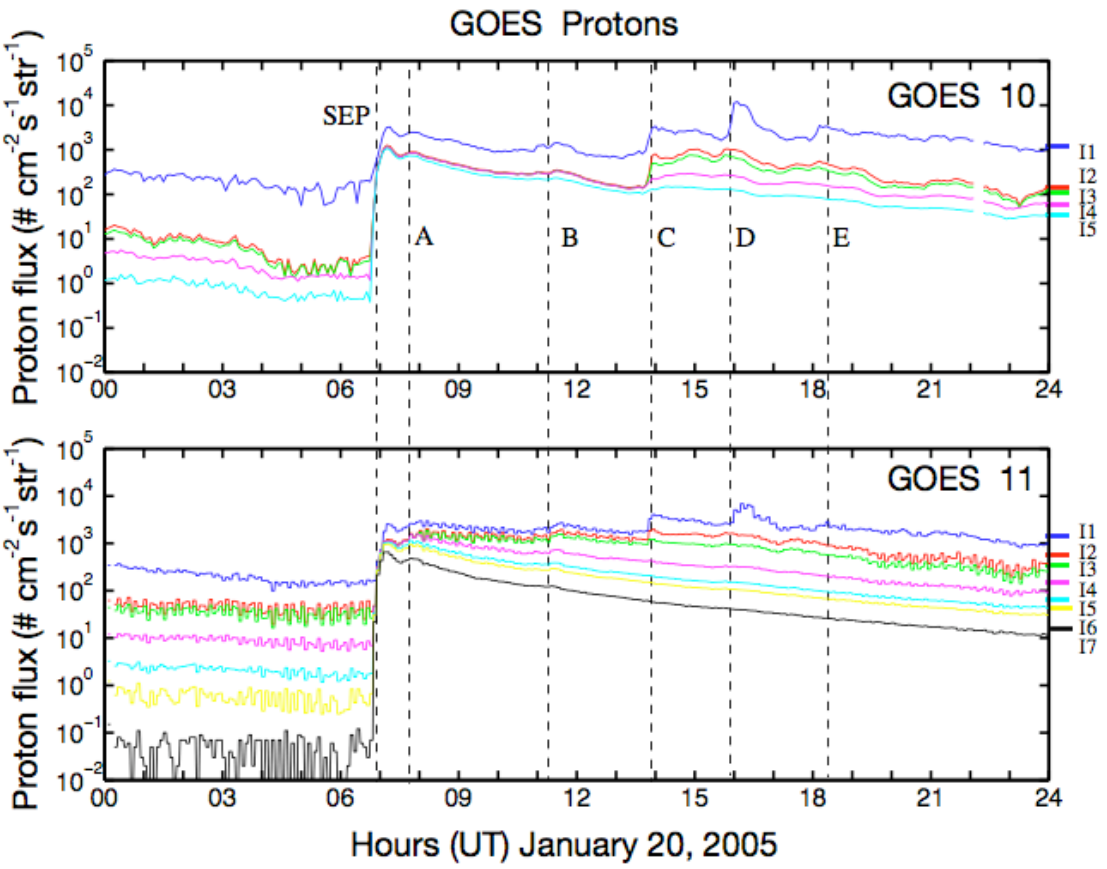

Figure 4.1.9 GOES 10 and 11 integral energetic proton flux on January 20th, 2005. The seven integral channels, I1 to I7, are shown in blue, red, green, magenta, cyan, yellow and black, respectively. The minimum proton energy for each channel is I1 > 1 MeV, I2 > 5 MeV, I3 > 10 MeV, I4 > 30 MeV, I5 > 50 MeV, I6 > 60 MeV and I7 > 100 MeV. The vertical dashed lines represent the SEP event onset at GOES 10 and 11 and the same five dynamic pressure enhancements seen at ACE (A – 07:53 UT, B – 11:10 UT C - 13:56 UT, D - 15:54 UT and E - 18:22 UT).

populations at geosynchronous. The flux measurements for GOES 10 and 11 are not identical, but share the same basic features. The two large SEP event onsets can be seen on January 17th and 20th. The rise-time for the January 17th event is nearly seven hours while the rise time for the event on January 20th is about 30 minutes. The maximum flux is larger for the January 17th event with a peak of near 10^4 protons cm^{-2} s^{-1} str^{-1} in the I1 channel compared with only 2.5 x 10^3 protons cm^{-2} s^{-1} str^{-1} for the January 20th event. However, there are many more of the most energetic protons (those with energies > 100 MeV) in the January 20th event compared with the January 17th event (6 x 10^2 and 2 x 10^1 protons cm^{-2} s^{-1} str^{-1}, respectively). This agrees with the qualitative observations from

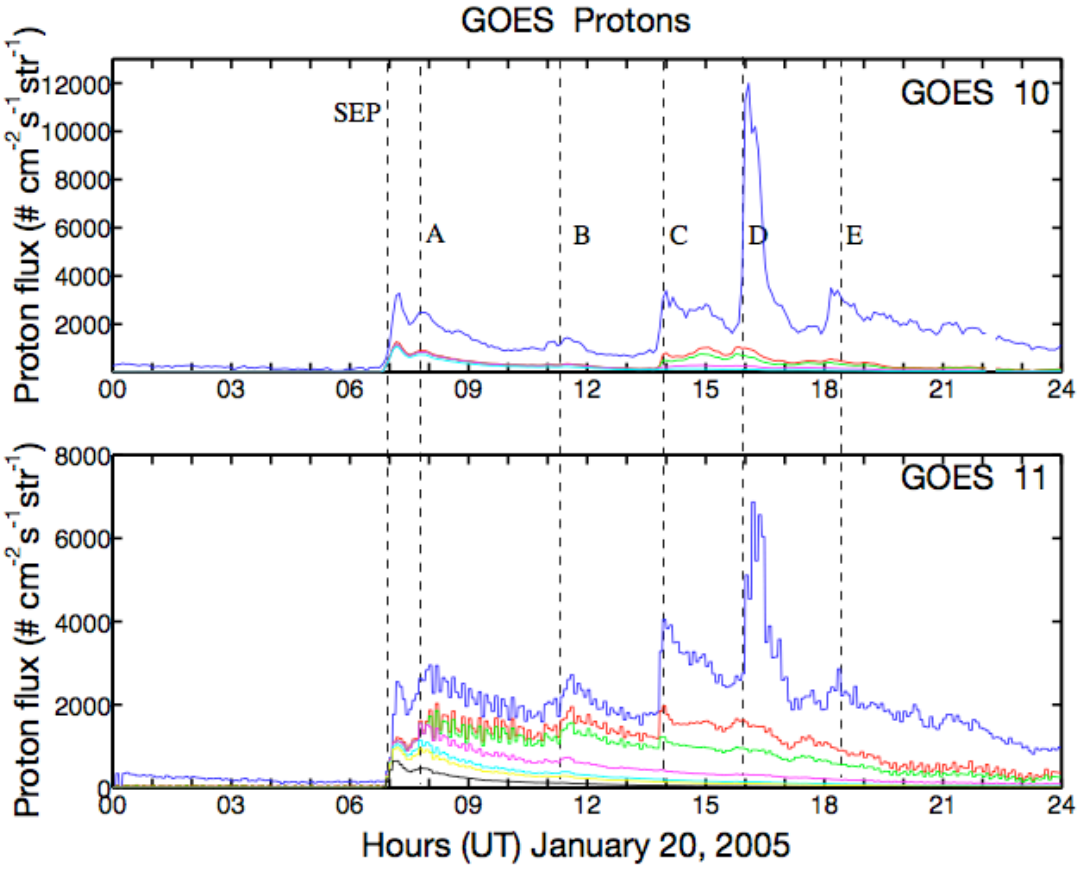

Figure 4.1.10 GOES 10 and 11 integral energetic proton flux on January 20th, 2005 with a linear scale. The colors and vertical dashed lines are the same as Figure 4.1.9. Enhancements in the lowest energy channel, I1, are easier to see.

the SOHO coronagraph images shown in Figure 4.1.2 and Figure 4.1.3. Figure 4.1.9 focuses on January 20th and allows us to see more detail in the harder of the two SEP events. The SEP event onset is apparent and marked with a vertical dashed line labeled SEP. The other vertical dashed lines marked A, B, C, D and E are at the same times as previous figures of ACE solar wind data. In Figure 4.1.9 and Figure 4.1.10 (same as Figure 4.1.9, but with a linear y-axis scale), increased proton flux is very noticeable in the lowest energy channels. Each labeled time shows solar wind dynamic pressure increases coincident with GOES energetic proton flux enhancements in the lowest energy channels (except for E which is not quite in alignment, but is consistent with a dynamic pressure increase just before 18:22 UT). This points to a solar wind modulation of energetic proton flux at geosynchronous over a range of local time (22:00 LT – 11:00 LT, from pre

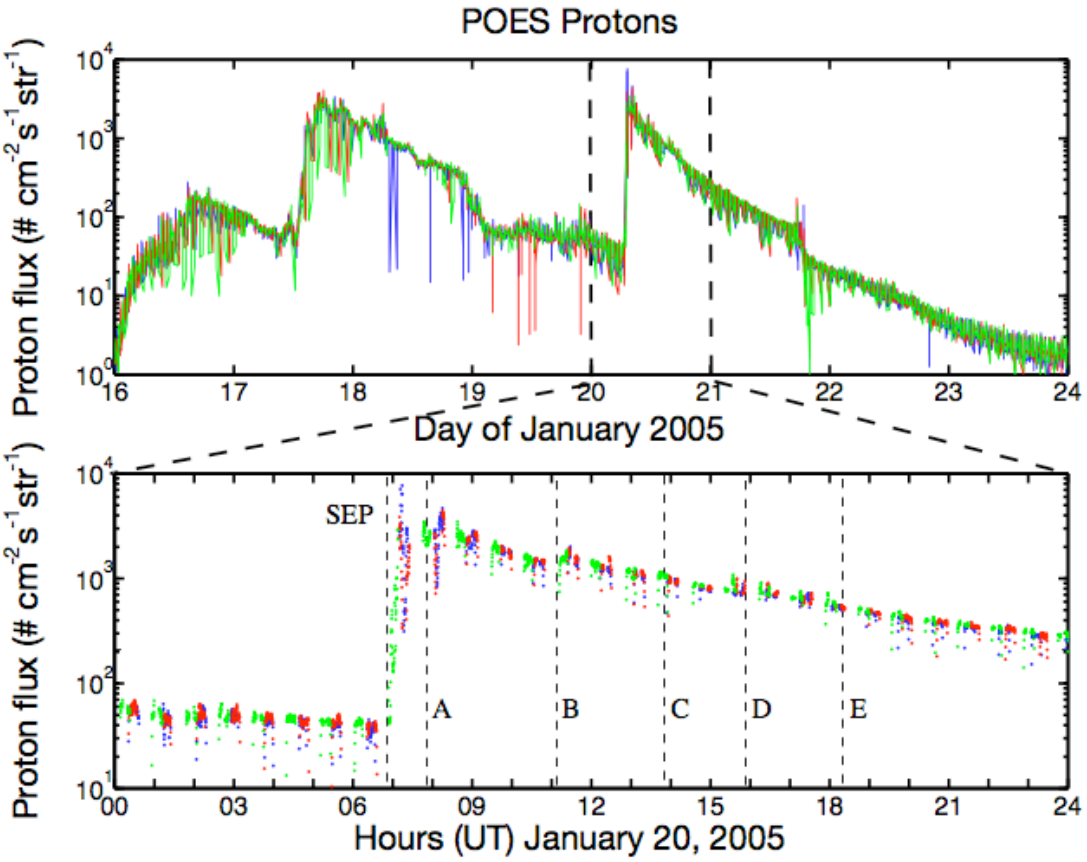

Figure 4.1.11 POES 15, 16 and 17 integral energetic proton flux for the lowest energy channel (> 16 MeV) for L >= 5 during January 2005. The top panel shows data between January 16th and January 24th. The lower panel shows data on January 20th. The blue, red and green curves mark data from POES 15, 16 and 17, respectively. The vertical dashed lines in the bottom panel represent the SEP event onset and the same five notable flux fluctuations as in earlier figures (A – 07:53 UT, B – 11:10 UT C - 13:56 UT, D - 15:54 UT and E - 18:22 UT).

midnight to pre-noon).

In addition to energetic proton flux at geosynchronous, we can examine flux at polar low-earth orbit by examining data from the POES spacecraft. Figure 4.1.11 shows the lowest omni-directional integral proton channel (>16 MeV) from POES 15, 16 and 17. Only measurements taken at L >= 5 are included. The large increase at SEP onset is clear, while additional flux increases are not as easily apparent. However, there are flux enhancements at A (~ 2500 to 5000 protons cm^{-2} s^{-1} str^{-1}) and at B (~ 1500 to 2000 protons cm^{-2} s^{-1} str^{-1}) although it is not easy to distinguish between temporal and

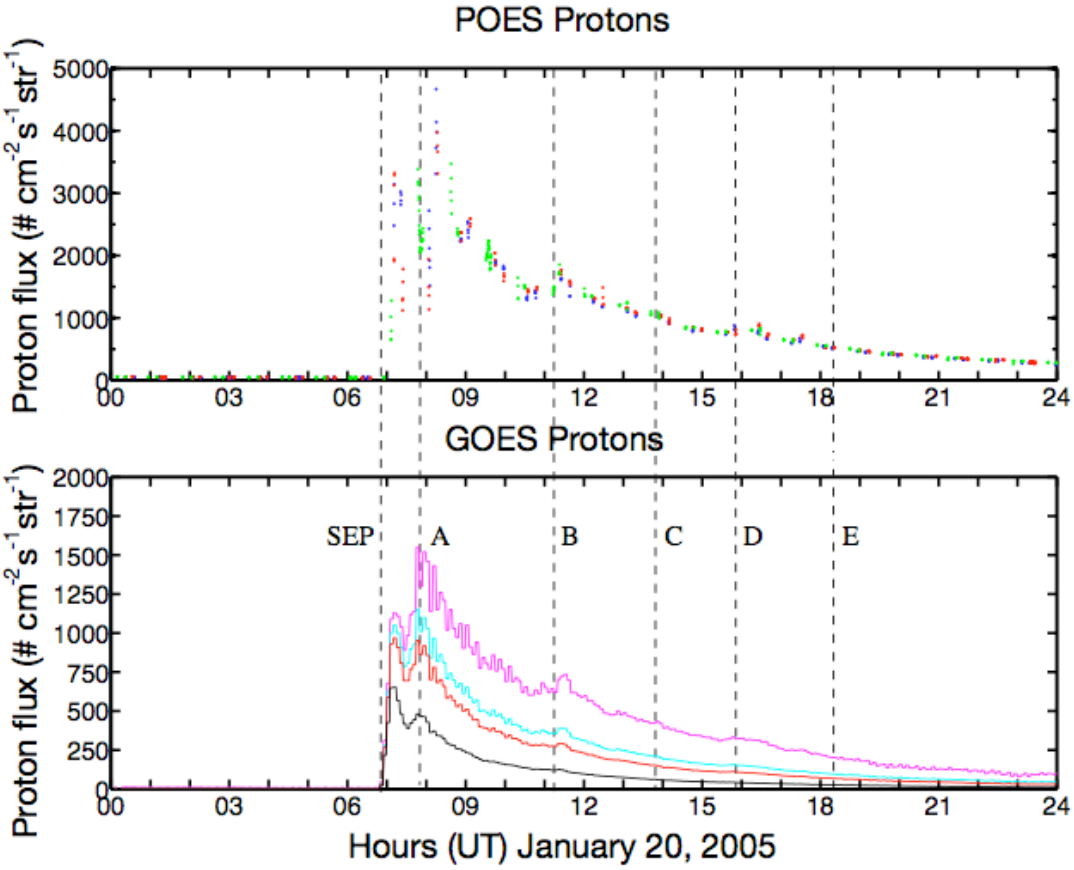

Figure 4.1.12 Energetic proton flux data from POES and GOES on January 20th, 2005. The top panel shows data from lowest energy channel (> 16 MeV) on POES 15, 16 and 17 (blue, red and green, respectively) while the spacecraft were between 6 < L < 8. For comparison, the bottom panel shows the highest energy channels for GOES 11 (I4 > 30 MeV, I5 > 50 MeV, I6 > 60 MeV and I7 > 100 MeV).

spatial enhancements. With the GOES satellites, all rapid (< 2 hour) fluctuations are temporal since the spacecraft remains in the same position relative to the surface of the earth. However, POES satellites sample different polar caps and have different trajectories over the polar caps. POES 15 and 16 orbits are nearly in the dawn-dusk plane while POES 17 orbits close to the noon-midnight plane. As the earth rotates under the POES spacecraft, they sample different slices of the polar caps. This time and space ambiguity makes direct comparison with GOES observations more difficult. In order to remove some of the ambiguity, we can look at the same data shown in Figure 4.1.11 but only plot data points taken between 6 < L < 8, which are the L-shells where the GOES spacecraft orbits lie. From Figure 4.1.12, we can see the noticeable increases at A and B.

There also appear to be slight enhancements at C and D manifested as changes to the overall slope of the data SEP flux decay rate. The timing and relative magnitude of all of these enhancements qualitatively agree with the GOES 11 observations in the bottom panel of Figure 4.1.12, where there are enhancements seen at A and B in the more energetic channels, and slight fluctuations at C and D.

The GOES and POES energetic proton observations give a consistent view of the particle flux in the near earth environment. On January 20th, 2005, there was a large, rapid enhancement of energetic proton flux at 06:54 UT, the SEP event onset. Subsequent fluctuations in the flux are coincident in time with solar wind dynamic pressure increases and, in some cases, changes in the IMF. This suggests that SEP flux observations at specific locations are sensitive to solar wind dynamics and not to rapid changes in the intrinsic SEP spectrum incident at earth.

4.1.4 Geomagnetic Field Fluctuations

Along with the energetic particle flux, we also examine the magnetic field fluctuation in the near space environment by looking at data from GOES 10 and 12 (GOES 11 magnetometer data is not available during this time). Figure 4.1.13 shows GOES 10 and 12 magnetic field data between January 16th and 24th. Three axis data are shown with the H_p (parallel to the earth's spin axis) component in blue, H_e (pointing towards the earth) in red and H_n (normal to H_p and H_e) in green. In the H_p component, diurnal oscillations caused by the tilt of the spacecraft orbit with respect to the geomagnetic field are evident in the quieter periods. On January 20th, a perturbation to the diurnal signal can be seen for both GOES 10 and 12. Perturbations of this kind are common and not, in and of themselves, incredibly special. We take notice of this specific perturbation because it is evidence of solar wind pressure and/or IMF dynamics acting on the geomagnetic field during the time we are interested in. Figure 4.1.14 shows the same data as Figure 4.1.13 but only for January 20th. Here, the same five times are delineated at A, B, C, D and E.

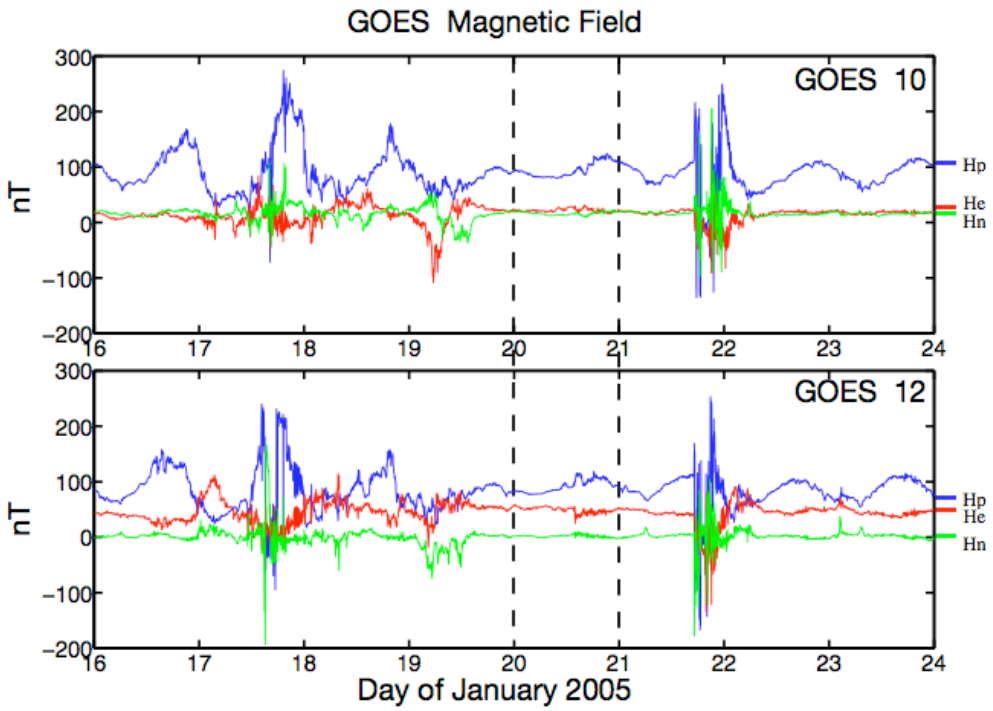

Figure 4.1.13 GOES 10 and 12 magnetic field data during January 2005. The H_p, H_e and H_n components are in blue, red and green, respectively.

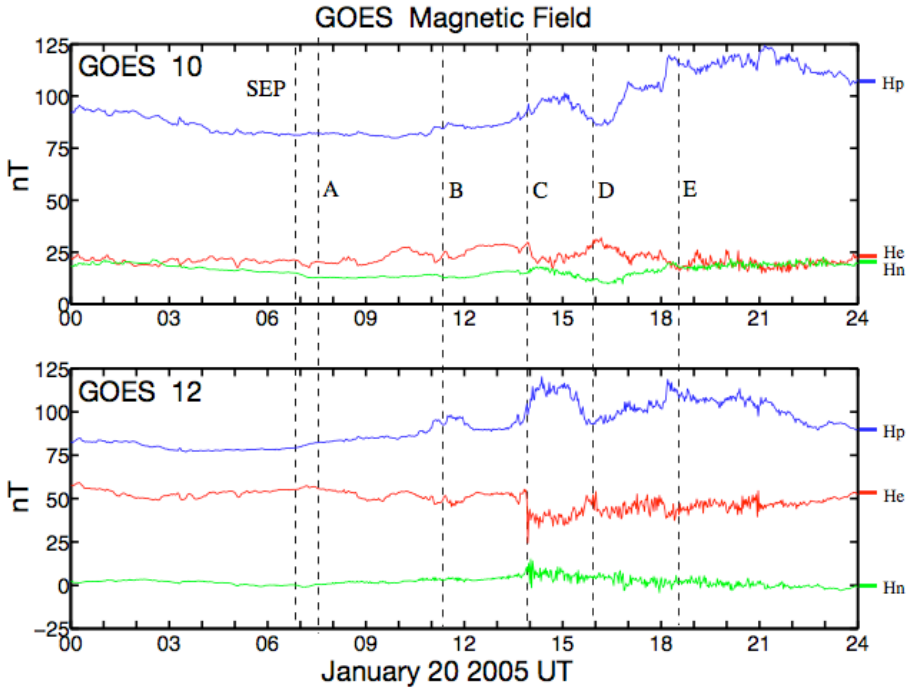

Figure 4.1.14 GOES 10 and 12 magnetic field data from January 20th, 2005. The H_p, H_e and H_n components are in blue, red and green, respectively. The dashed lines are at the same times as in previous figures (A – 07:53 UT, B – 11:10 UT C - 13:56 UT, D - 15:54 UT and E - 18:22 UT).

At the SEP event onset and at A, there are no significant magnetic fluctuations at either GOES 10 or 12 to speak of. Between C and D, there is an enhancement in the parallel component of 25 nT at GOES 12 and 10 nT at GOES 10. At this time (15:00 UT), GOES 12 is at 11:00 LT near the nose of the magnetosphere and GOES 10 is at 07:00 LT near the dawn side flank. After C (13:56 UT), every component for both satellites becomes more variable until about 21:00 UT. This is nearly the same time that the IMF is southward. If we zoom in further at the transition at C, we can see that the observations have oscillating structure to them that are most evident in the H_e and H_n components of GOES 12 (11:00 LT).

4.1.5 Cross Polar Cap Potential

The classic Dungey Cycle depicts plasma convection in the magnetosphere (see Figure 1.3.2). Plasma motion in this cycle is primarily driven by $\vec{E} \times \vec{B}$ drift in a dawn to dusk electric field with a southward IMF (anti-sunward drift) and the constant northward geomagnetic field (sunward drift). Therefore, when the cross polar cap potential is large and/or the southward component of the IMF grows, the anti-sunward plasma drift velocity increases. This results in an enhancement of the entire plasma circulation cycle in the magnetosphere. Thus, by looking at the cross polar cap potential and the IMF orientation, we have a proxy for magnetospheric convection. In Figure 4.1.15, we show that the cross polar cap potential remains small and that magnetospheric convection is low both before and immediately after SEP event onset at 07:53 UT on January 20th, 2005.

In the lower panel of Figure 4.1.7, which shows ACE magnetic field data, the z-component of the IMF was northward for three hours before the SEP event onset and remained northward for 11 hours until 13:56 UT. Based on *Wygant et al.* [1983], magnetospheric plasma convection has some inertia and large cross polar cap potential differences established in times of southward IMF decay to background levels near 20 kV

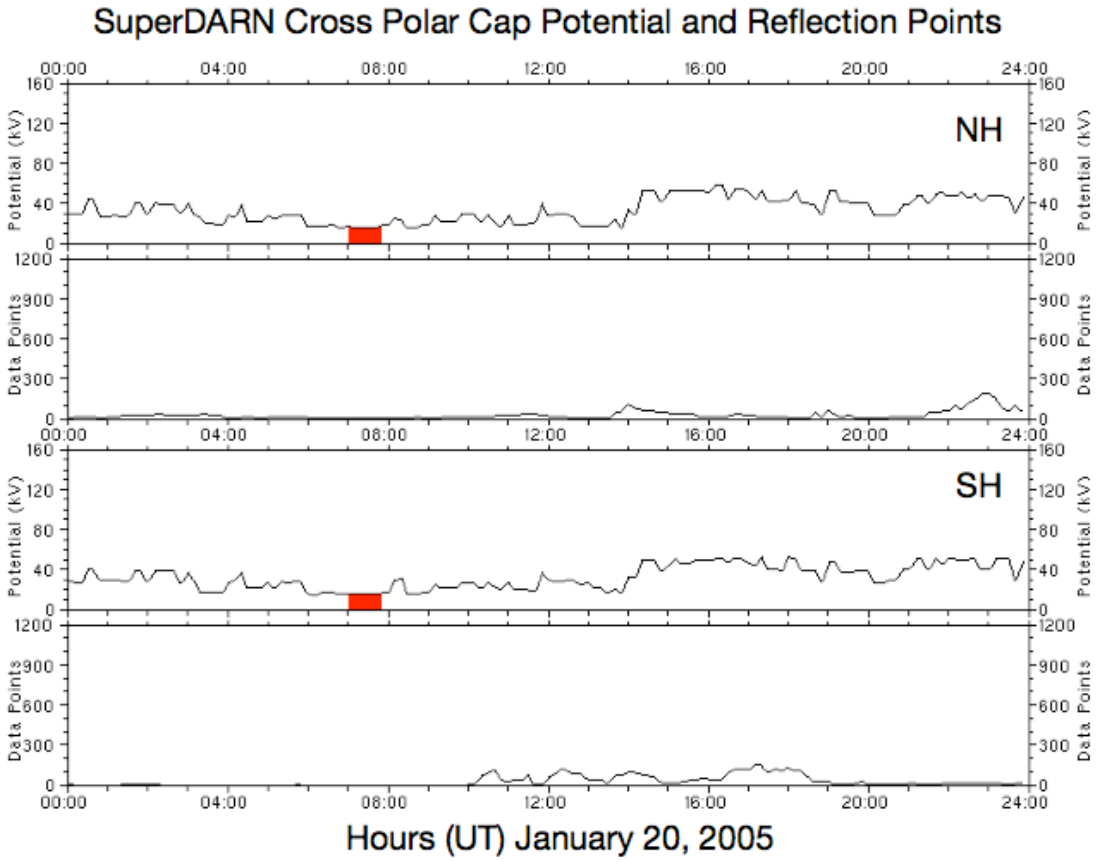

Figure 4.1.15 SuperDARN cross polar cap potential differences. Estimations of the northern (top panels) and southern (bottom panels) cross polar cap potentials and the number of radar echoes used for each calculation. The red highlights the hour after SEP event onset.

after three hours. Ground-based SuperDARN radar and magnetometer arrays provide more indications of a quiet, closed magnetosphere. SuperDARN radar reflections during January 20th point to a quiet magnetosphere with little to plasma convection. Figure 4.1.15 shows the calculated polar cap potential difference in both the northern and southern hemisphere on January 20th, 2005. The potential stays very low, near 20 kV, between 04:00 UT and 14:00 UT. We note that there are relatively few (< 15) radar echoes for each snapshot used to build the convection maps and cross polar cap potentials. The combination of the ACE and SuperDARN data sets indicate that: A) there is little convection in the magnetosphere; and B) the large scale horizontal electric fields in the ionosphere are as small as they ever become.

4.1.6 Summary of Solar Forcing

During January 2005, there were several halo CMEs and associated SEP events. On January 20th, the last and largest of the X-class flares was accompanied by an extremely hard SEP event with a rapid rise time. SEPs arrived at earth within one half of an hour after the solar flare x-rays. There are two main points to take away from the observational data presented in Section 4.1: 1) coincident with the SEP event onset, there are no significant fluctuations in the solar wind, the IMF or the geomagnetic field; and 2) at several times after SEP event onset, solar wind dynamic pressure increases (and IMF fluctuations at C and E) are responsible for varying degrees of geomagnetic field fluctuations and enhancements in satellite-observed energetic proton flux. We are not directly interested in quantifying the specifics of how each dynamic pressure increase affected magnetic field or proton flux observations at various locations. Rather, we are interested in how energetic proton precipitation affects the earth's electrical environment. In the section that follows we will use the observations presented here to help place the MINIS balloon observations into the proper context.

4.2 MINIS Balloon Conductivity and DC Electric Field Observations

During the events of January 2005, there were four southern MINIS balloon flights, allowing the extreme SEP event on January 20th, 2005 to be completely recorded from before onset until complete relaxation several days later. Only one payload (Flight 2 South) was aloft for the entire duration, although a second payload was launched about 14 hours after the SEP event onset. Upon the SEP event onset at 6:54 UT, MINIS Flight 2 South was at 70.9° S, 10.9° W geographic and 30.9 km altitude. Over the course of the day, the balloon drifted nearly 400 km to 71.4° S and 21.5° W and reached a maximum altitude of 33.2 km. In this section, we present observations exclusively from MINIS Flight 2 South.

4.2.1 Direct Observation of Increased Particle Precipitation

Each MINIS balloon had an x-ray scintillator instrument designed to measure

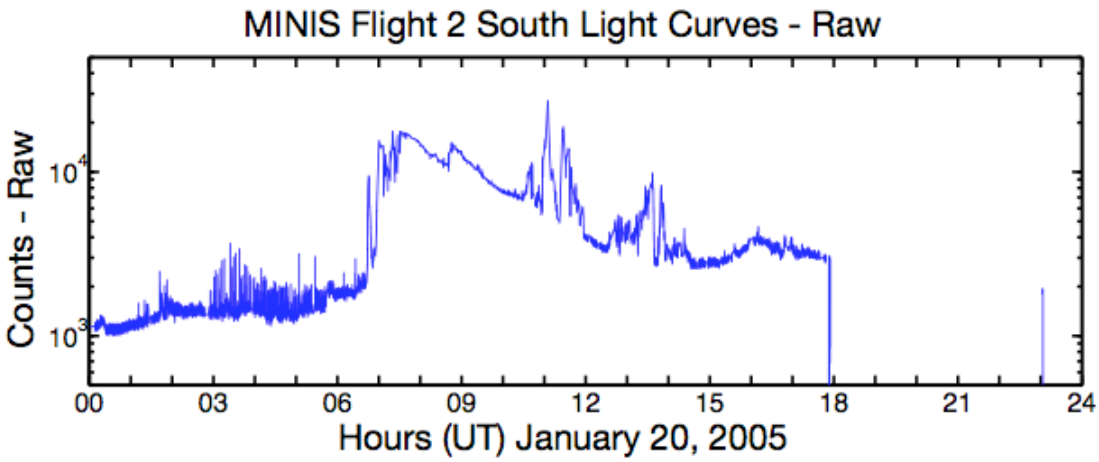

Figure 4.2.1 MINIS Flight 2 South raw summed light curve counts on January 20th, 2005.

bremsstrahlung from relativistic electron precipitation. However, any energetic particle passing through the scintillator crystal can deposit energy, ultimately leading to a count in the PMT. The MINIS x-ray instrument was not intended to resolve energetic proton precipitation. During the January 20th, 2005 SEP event, there was undoubtedly proton and secondary particle flux passing by the balloon. Figure 4.2.1 shows the total summed counts in the four light curve channels from MINIS Flight 2 South on January 20th. A large flux enhancement is clear at SEP onset. After SEP onset and lasting into January 21st, the spectra from the x-ray scintillator are not easily interpreted. There is a high-energy hump that wanders with time (between 2 MeV and 3 MeV at 10:05 UT in) and the characteristic 511 keV annihilation line migrates with time. Also, minutes before the SEP event onset, during the rise of the solar flare x-rays measured by GOES (06:45 UT), there is a distinct enhancement. This enhancement occurs before any odd instrument behavior. Figure 4.2.1 shows spectra from the x-ray instrument before the solar flare (06:35 UT), just before SEP event onset during the aforementioned enhancement (6:45 UT) and after SEP onset (10:05 UT).

There are clear differences between each spectrum. In the spectrum taken at 06:35 UT before any enhancement or the SEP event, the characteristic 511 keV line is evident. The

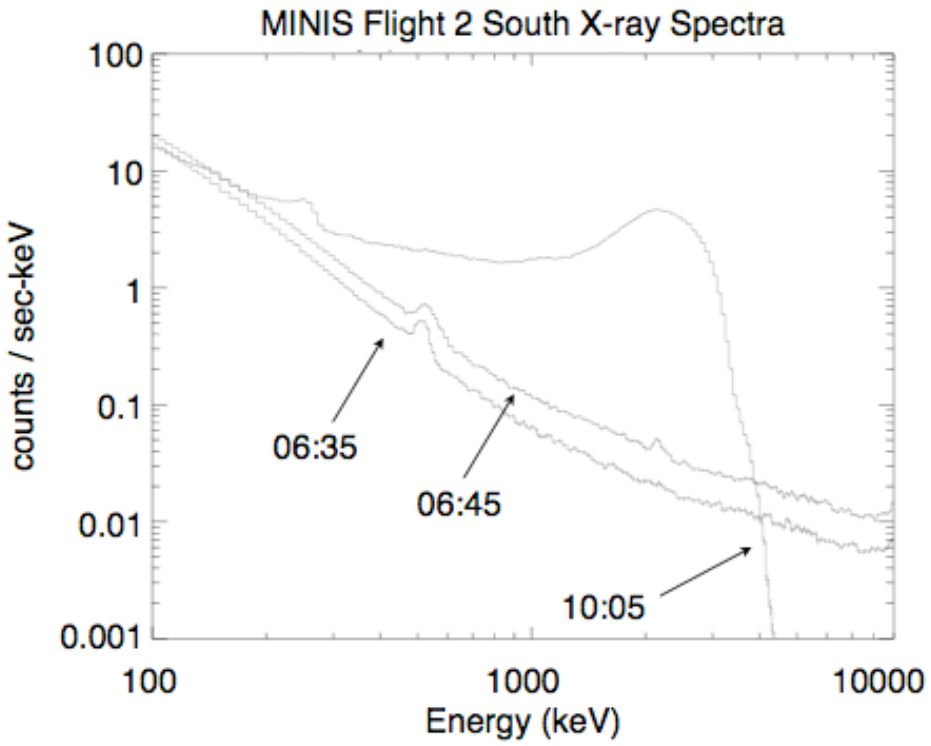

Figure 4.2.2 MINIS Flight 2 South x-ray scintillator spectra at 06:35 UT, 06:45 UT and 10:05 UT on January 20th, 2005. (Adapted from work by M. McCarthy.)

spectrum taken at 06:45 UT shows an enhancement across all energies and an additional spectral line near 2.2 MeV. This is consistent with energetic solar flare x-rays directly from the flare itself, also observed by the RHESSI satellite [*J. Sample* and *A. Shih*, private communication]. The spectrum taken at 10:05 UT has a large hump centered near 2 MeV which wanders with time. Also, the 511 keV line is shifted to near 280 keV. Migration of the 511 keV annihilation line is not explicitly shown in Figure 4.2.2, but the line seen at 280 keV at 10:05 UT slowly shifts position until it reaches the correct location and reliably remains at 511 keV after 16:35 UT on January 21st, 2005. After the SEP event onset, we can take the MINIS particle data and confidently say that there is indeed a large increase of energetic particles at MINIS Flight 2 South. We cannot provide much more insight about the spectra of the particles or about the identity of the particles themselves. Protons with energies greater than 100 MeV can precipitate down to the MINIS balloon stratospheric altitude. Thus, we expect there to be a mix of primary protons and

secondaries generated from collisions with atmospheric neutrals.

4.2.2 Large Electrical Conductivity Enhancement and Increased Photoelectric Effect Perturbations

Shortly after the SEP event onset on January 20th, 2005, the local electrical conductivity at MINIS Flight 2 South was observed to increase by a factor of about 20. Figure 4.2.3 shows the conductivity for January 20th, 2005. There are a few points to note about the conductivity measurements on this day. First, the frequency of the data points decreases dramatically after the SEP event onset. This is a result of how the onboard computer was programmed to accept data and place it into the telemetry stream. Counts from the x-ray scintillator were the highest priority data for the campaign and were placed into the data stream preferentially. When the count rate during the SEP event greatly exceeded the expected REP count rate for a sustained period of time, other data were lost, including conductivity data. The second point to note is that the error bars after the SEP event onset are much larger than previously. This is a result of sampling frequency. During conductivity calibration cycles, the voltages on the electric field probes were sampled ten times per second. This is sufficient for relaxation times longer than the sample frequency. The nominal relaxation time in the stratosphere near 30 km is about 1 second. However,

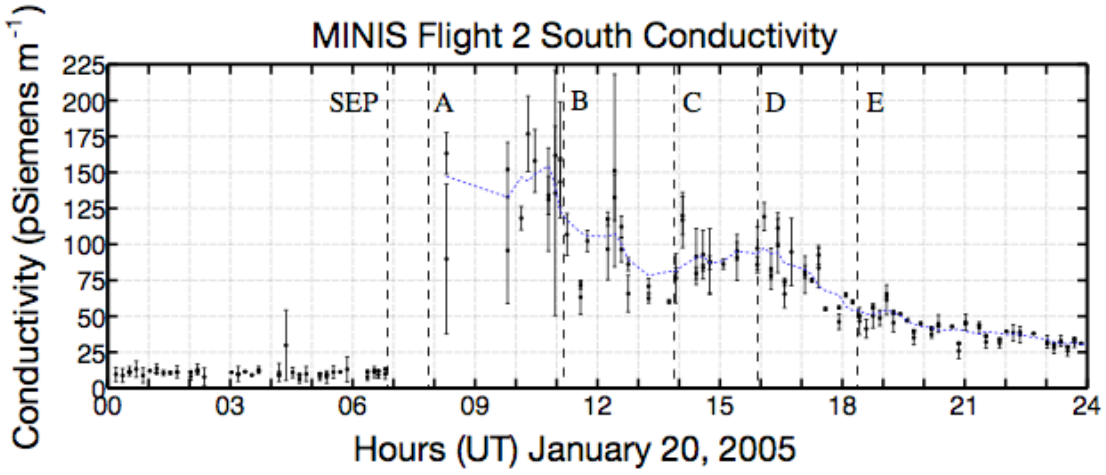

Figure 4.2.3 MINIS Flight 2 South conductivity for January 20th, 2005. The vertical dashed lines are at the same times as in previous figures (A – 07:53 UT, B – 11:10 UT C - 13:56 UT, D - 15:54 UT and E - 18:22 UT).

with a 20-fold increase of conductivity, the goodness of fit statistics for the calculated exponential decay time constants worsened. Despite these instrumental issues, the basic trend is clear. After the SEP event onset, conductivity increased. In Figure 4.2.3, the same times A, B, C, D and E are marked. There are not enough data points to resolve changes near A. At B and D, it is hard to make strong arguments for changes in conductivity. However, because the error bars are large, changes in conductivity may indeed have occurred. We have more confidence that conductivity increased by a factor of two at C, from 60 pS m^{-1} to 120 pS m^{-1}.

Another point to note about the conductivity values shown in Figure 4.2.3 is that they are not the combined positive and negative polarity conductivity, but rather they are double the measured value for the negative polar conductivity. The reason for this is the large divergence of the positive and negative polarity conductivity values. *Byrne et al.* [1990] showed that during the daytime, when UV flux is at its highest, conductivity values made using the relaxation technique in the polar stratosphere in non-SEP conditions can differ by factors of two. During an SEP event, when ozone is depleted above the balloon altitude, UV flux can increase at the balloon. According to a combination measurements from the European Space Agency's GOMOS instrument aboard the ENVISAT satellite and Sodankylä Ion Chemistry (SIC) model results, the tertiary ozone maximum near 72 km was decreased by more than 70% during the January 20th, 2005 SEP event. SIC model results predict an SEP ionization enhancement of HO_x, which reacts with ozone and destroys it [*Seppälä et al.*, 2006]. Similar results linking SEP precipitation to HO_x and ozone depletion were found for the October 2003 SEP events as well [*Degenstein et al.*, 2005]. Even though we expect a UV flux enhancement when ozone is depleted during an SEP event, to the best of our knowledge, there have been no direct quantitative measurements confirming this. This ozone decrease and UV flux increase can have the effect of making the polar conductivity measurements even more

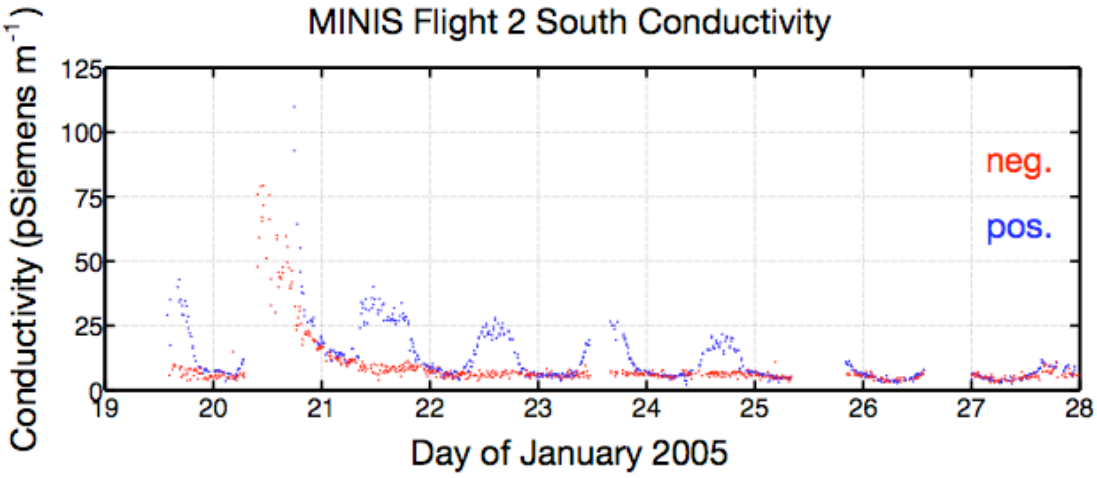

Figure 4.2.4 MINIS Flight 2 South polar conductivity values for January 19th to January 28th. Positive polar conductivity values regularly double in the daytime compared with negative polarity measurements.

divergent. Figure 4.2.4 shows Flight 2 South positive (blue) and negative (red) polar conductivity values between January 19th and January 28th. Universal time and local times differ by a few hours (increasing difference as time goes on) such that universal and local noon are about the same. At local noon for many days, the conductivity values diverge by more than a factor of two.

The basic points to take away from the conductivity measurements are that: A) the conductivity increased dramatically after the SEP event onset; and B) fluctuations at the demarcated points are possible, but the resolution is not sufficient to add much certainty in most instances (Figure 4.2.3).

4.2.3 Horizontal DC Electric Field Decrease

Along with the rise in local stratospheric conductivity, the horizontal dc electric field at MINIS Flight 2 South suddenly decreased to near zero at the SEP event onset. The data are one-minute averages taken every 30 seconds. Before the onset, there are nominal fluctuations in the electric field on the order of 10 mV m^{-1}. However, directly afterward, there are fluctuations of similar timescales, but significantly decreased magnitude. There have been no previous observations of the total horizontal dc electric field magnitude

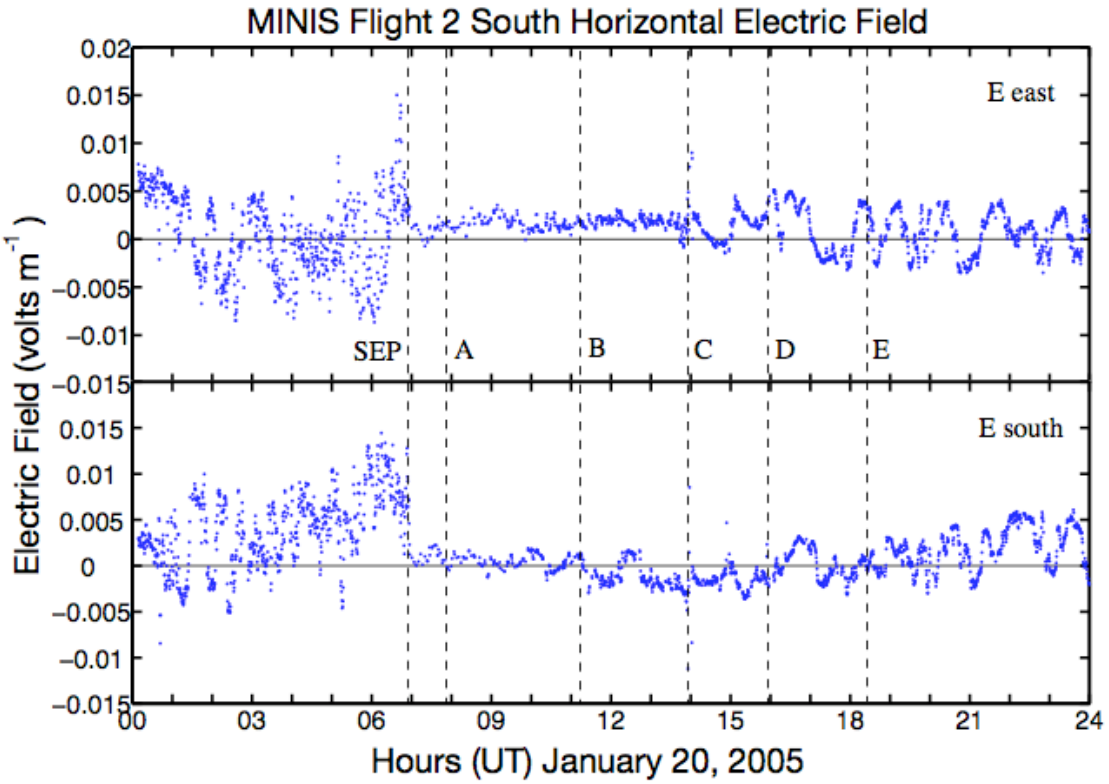

Figure 4.2.5 MINIS Flight 2 South horizontal dc electric field measurements for January 20th, 2005. The data are one-minute averages taken every 30 seconds. The vertical dashed lines are at the same times as previous figures (A – 07:53 UT, B – 11:10 UT C - 13:56 UT, D - 15:54 UT and E - 18:22 UT).

decreasing coincident with an SEP event onset. This measurement is the first of its kind.

4.2.4 Vertical DC Electric Field Decrease

Along with the horizontal dc components, the vertical dc component of the electric field also decreased in magnitude near the SEP event onset. Figure 4.2.6 shows the vertical dc electric field measured by MINIS Flight 2 South on January 20th, 2005. The data points are one-minute averages taken every 30 seconds. There are a few points to notice in this figure. The first is that at the SEP event onset, there was a sudden decrease in electric field magnitude from about 100 to near 0 mV m^{-1}. This is generally consistent with previous measurements by *Holzworth and Mozer* [1979]. The second point to note is that before the SEP event onset, the data are quite noisy, with most data point values ranging between 0 and -200 mV m^{-1}. In contrast, after the SEP event onset, the apparent noise in the data goes away. In Section 2.4.1, we show that a photoemission charging

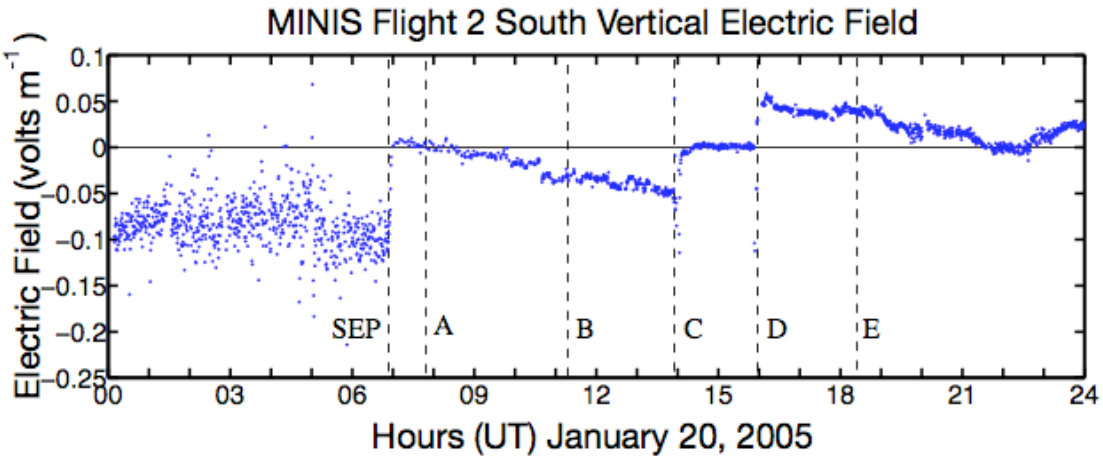

Figure 4.2.6 MINIS Flight 2 South vertical dc electric field on January 20th, 2005. The data are one-minute averages taken every 30 seconds. The vertical dashed lines are at the same times as previous figures (A – 07:53 UT, B – 11:10 UT C - 13:56 UT, D - 15:54 UT and E - 18:22 UT).

could be a large source of this noise. The last point to notice are two jumps in the dc electric field magnitude at C (13:56 UT) and D (15:54 UT). There are no previous observations of similar dc electric field jumps during an SEP event. We describe in Section 5.3 several physical mechanisms that could possibly have caused this observation despite there being no completely satisfying explanations currently available.

4.2.5 MINIS Flight 2 South Location and Rigidity Cutoff

In order to place the MINIS Flight 2 South observations into context, we want to know where, in relation to the areas of SEP precipitation, MINIS Flight 2 South was located. In other words, we want to define the incident SEP spectrum directly above Flight 2 South. Figure 4.2.7 shows a map of the world overlain with markers showing where the POES satellites observed increased proton flux over the course of January 20th, 2005. Each pink data point represents the sub-satellite point of a POES spacecraft when it measured flux in the > 140 MeV proton channel higher than 20 counts sec^{-1}. By choosing the highest energy channel, we are using the protons that have sufficient energy (> 100 MeV) to penetrate to the MINIS balloon altitude in the stratosphere. In the deep polar cap regions, flux in this energy channel is often greater than 100 counts sec^{-1}. Thus, the area we are demarcating does not receive uniform flux, but is regulated by the geomagnetic field

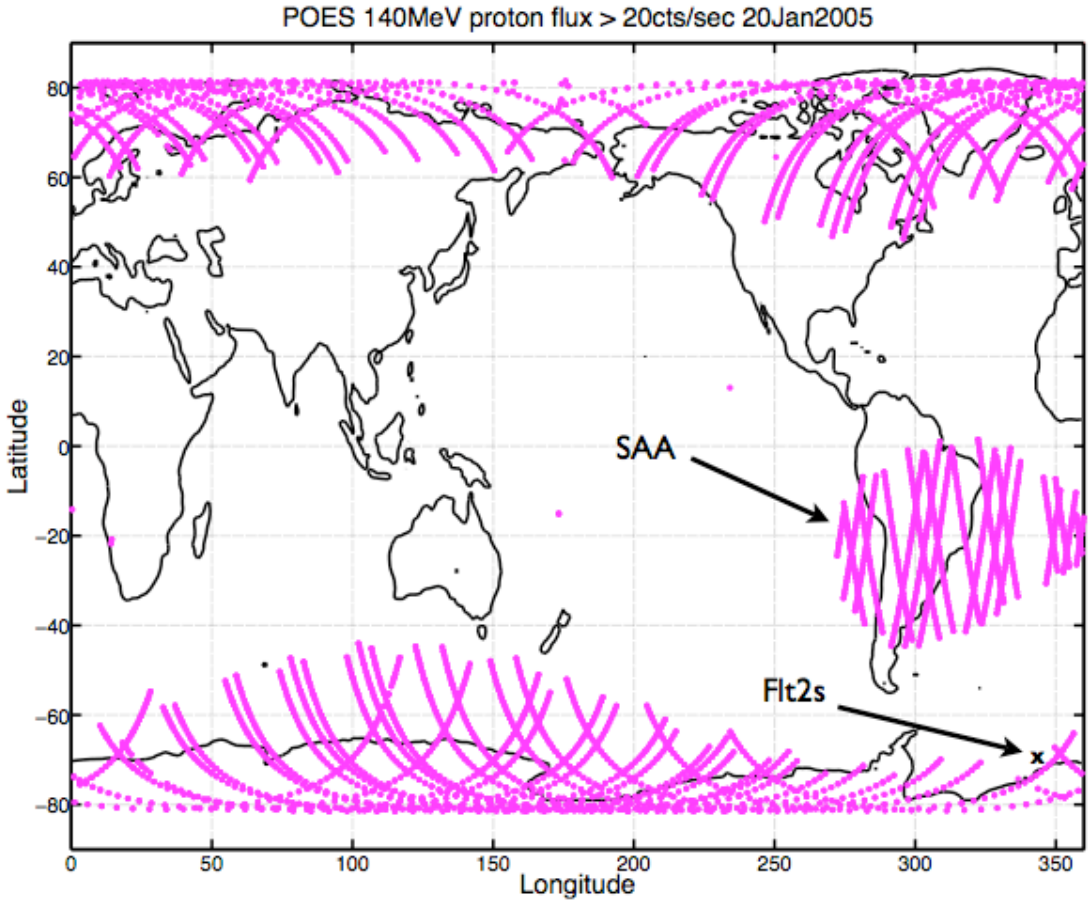

Figure 4.2.7 POES sub-satellite locations where enhanced energetic proton flux was measured on January 20th, 2005. Each pink dot marks a location where the >140 MeV proton channel surpassed 20 counts sec^{-1}. MINIS Flight 2 South (Flt2s) is in the bottom right corner. The region labeled SAA covers the South Atlantic Anomaly and is a result of inner radiation belt protons, not SEP protons.

in the form of rigidity cutoffs. Over the course of the day, MINIS Flight 2 South moves 400 km to the west. This means that it is moving into an area of slightly higher rigidity cutoff as the day progresses. For most of the day on January 20th, the POES satellites do not pass directly above MINIS Flight 2 South. On one occasion, however, the POES 17 sub satellite point passes within 300 km of MINIS Flight 2 South. Figure 4.2.8 shows the POES 17 omni-directional energetic proton spectrum as it passes near Flight 2 South. The vertical dashed line (09:27:45 UT) marks the time when the POES 17 sub satellite point is at 71° S and 4° W and MINIS Flight 2 South is at 71° S and 12° W, a separation of 290 km. At the marked time, the count rate in the > 16 MeV (blue), > 35 MeV (red) and > 70 MeV (green) channels are all nearly equal and 50% higher than the count rate in the

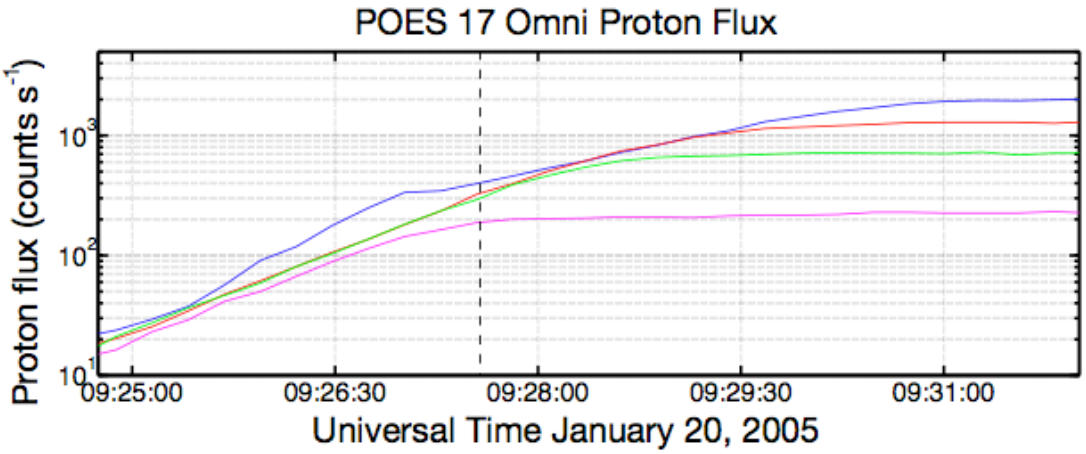

Figure 4.2.8 POES 17 Omni-directional proton flux near MINIS Flight 2 South. Data is shown for the >16 MeV (blue), > 35 MeV (red), >70 MeV (green) and > 140 MeV (magenta) energy channels. The vertical dashed line is the location of closest approach to MINIS Flight 2 South.

> 140 MeV channel (pink). This means that the rigidity cutoff is between 70 MV and 140 MV at this time. Thus, we postulate that the rigidity cutoff at MINIS Flight 2 South is also likely to be in that same range.

5 Discussion on Effects of January 20th, 2005 Solar Energetic Particle Event

In this chapter, we discuss the effects of the January 20th, 2005 SEP event on coupled electrodynamic atmosphere and ionosphere. In Section 5.1 we investigate anomalies observed in the electric field data that are not geophysical, but rather instrumental affects resulting from SEP precipitation. In Sections 5.2-5.4 we pose several questions that are addressed in the subsequent text. We begin with an analysis of the electric field instrumentation during this time so that we gain appropriate confidence in our analysis.

5.1 SEP-Induced Stratospheric Conductivity Enhancement

Questions addressed in this section: 1) why does the local conductivity increase at MINIS Flight 2 South coincidently with the SEP event onset; 2) what physical mechanisms are responsible; and 3) how does the conductivity change at altitudes other than the balloon altitude in the stratosphere?

Answer Summary: Precipitating SEP protons are the dominant source of ionization, and therefore conductivity enhancement, in the polar stratosphere on January 20th, 2005. We take the MINIS Flight 2 South conductivity observations, shown in Figure 4.2.3, and compare them with our SIC-driven conductivity model that includes SEP proton precipitation described in Section 3. We show that there is good agreement between the data and model at balloon altitude. Based on our conductivity model, we show that the maximum conductivity enhancements are centered near 45 km altitude and that there is essentially no enhancement higher than 80 km altitude.

Figure 5.1.1 shows the same conductivity data as in Figure 4.2.3 with modeled conductivity overlaid. The red curve assumes a rigidity cutoff of 100 MV and the green curve assumes a 200 MV cutoff (translating into >100 MeV and >200 MeV protons). The input spectrum used for making Figure 5.1.1 was taken from GOES 11 and the

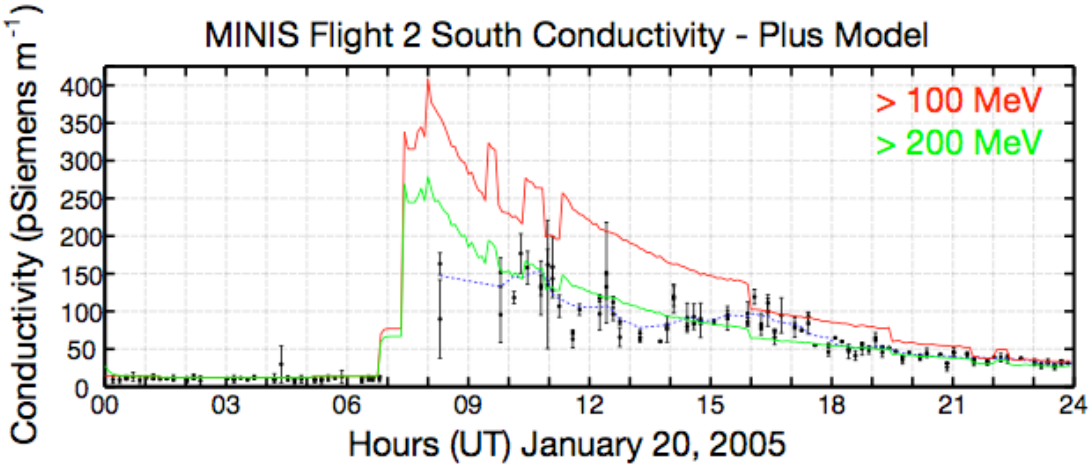

Figure 5.1.1 Conductivity observations from MINIS Flight 2 South and modeled conductivity. The observations (black) are the same as those in Figure 4.2.3. The red curve is a model result assuming a rigidity cutoff of 100 MV and precipitation of > 100 MeV protons. Similarly, the green curve assumes a 200 MV cutoff. Incident protons are taken from GOES 11.

original method for producing a differential spectrum (as described in Section 3.3) was used. Not shown in Figure 5.1.1 are curves for lower rigidity cutoffs. Protons with energy below 100 MeV will not precipitate directly to the balloon altitude. Since the method used for modeling SEP-induced ionization is limited to direct proton collisions (neglecting radiation and other secondaries), lowering the rigidity cutoff will not have a noticeable effect. The incident protons simply do not precipitate deep enough into the atmosphere. Different geographic locations will have different rigidity cutoff values, which modulate the access of SEP proton precipitation. In Section 4.2.5, we showed that the rigidity cutoff of MINIS Flight 2 South is constrained between 70 MV and 140 MV shortly after the SEP event onset (09:27:45 UT). Therefore, we have plotted the model runs that used the nearest cutoff values. In Figure 5.1.1, the model run that assumes a higher rigidity cutoff of 200 MV agrees with the MINIS Flight 2 South observations more closely. SIC-calculated ion densities are currently estimated to be accurate to within a few tens of percent (*A. Seppälä,* private communication). Combining the error of the SIC-ion densities with the error of the conductivity observations makes a more precise

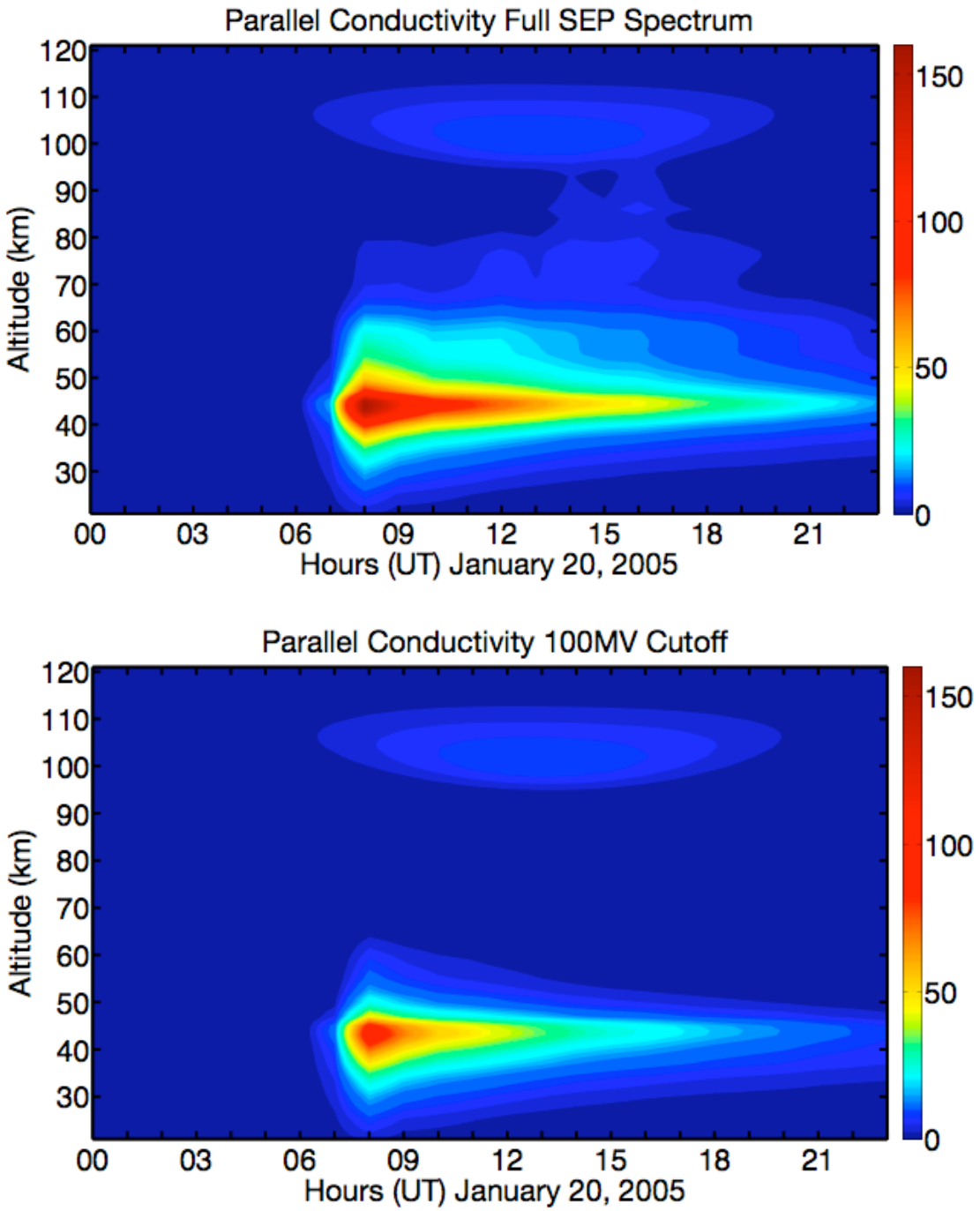

Figure 5.1.2 Multiplicative change in modeled parallel conductivity on January 20th, 2005. The top panel assumes a full incident SEP spectrum and the bottom panel assumes a 100 MV rigidity cutoff. Each hour, a conductivity profile is normalized by the profile at midnight. The color bar values represent the multiplicative change in the local conductivity (e.g., 50 = conductivity 50 times greater than base value at midnight).

comparison difficult. From the model comparison with the measurements, we can say that direct ionization of neutrals by incident precipitating SEP protons can account for most, if not all, of the conductivity increase observed by MINIS Flight 2 South.

Generalizing this one case study, direct SEP proton precipitation should be the dominant mechanism responsible for conductivity enhancements in the stratosphere for any SEP event with sufficient > 100 MeV proton flux. An added benefit of this model is that we are not limited to making model predictions at only the balloon altitude, rather we can predict the electrical conductivity at any altitude between 20 km and 120 km. Figure 5.1.2 shows the change in the parallel (to the magnetic field) component of the conductivity tensor on January 20th, 2005 for altitudes between 20 and 120 km assuming a vertically-oriented magnetic field. The color indicates the parallel conductivity profile over the course of the day, normalized by the parallel conductivity profile values at midnight. The top panel uses model output assuming a full SEP spectrum while the lower panel assumes a rigidity cutoff of 100 MV. In each case, there is an enhancement greater than two orders of magnitude centered near 45 km. At higher altitudes, centered near 105 km, there is another enhancement less than one order of magnitude. This higher altitude enhancement is due to daytime solar radiation and is not related to the SEP event.

5.2 Uncertainty in Vertical Electric Field During SEP Event

Question addressed in this section: why is there a sudden vertical dc electric field jump at 13:56 UT as well as a jump *and* reversal at 15:54 UT in the MINIS Flight 2 South data?

Answer Summary: The answer to this problem is not well constrained and is hard to confidently determine. We cannot accurately constrain rigidity cutoff dynamics and therefore changes in precipitating SEP spectrum are simply speculation. We present some examples of plasuible physical mechanisms that could explain the sudden observed fluctuations. We show that conductivity enhancements could be responsible for rapid

electric field changes, but not a reversal. An upward quasi-static electric field established by SEP protons could become large enough to cancel (and reverse) the net vertical dc electric field measured at MINIS Flight 2 South only if the characteristic relaxation time is long (>100 seconds).

In this section, we investigate possible physical mechanisms that could cause the vertical dc electric field measured by at MINIS Flight 2 South to suddenly fluctuate at 13:56 UT and 15:54 UT as seen in Figure 4.2.6. With no identifiable source of instrumental errors and coincidence with other observable geophysical fluctuations, we look for geophysical forcing mechanisms. We attempt to quantify the movement of rigidity cutoffs and the affect that moving cutoffs would have at the balloon location. We find that accurately quantifying rigidity cutoff locations and therefore SEP precipitation spectrum is non-trivial. By itself, a sudden change in overhead flux would not cause an electric field fluctuation. However, an SEP-induced conductivity enhancement could cause a rapid electric field fluctuation (as we show in Section 5.1). We determine that a conductivity enhancement could account for the observed sudden electric field jump at 13:56 UT, but not the jump and reversal at 15:54 UT. We investigate the possibility that an upward pointing quasi-static vertical electric field could form as a result of an SEP-produced charge imbalance in the stratosphere below the balloon altitude. We use a time-dependent model to show that an upward pointing vertical quasi-static electric field is simply too small to be measured by Flight 2 South, let alone be responsible for the observed fluctuations.

5.2.1 No Accurate Quantitative Description of Dynamic Rigidity Cutoff Motion

In an attempt to constrain the incident SEP proton flux above MINIS Flight 2 South at 13:56 UT and 15:54 UT, we pull from much of the data presented in Sections 4.1 and 4.2 beginning with ACE solar wind data. Figure 4.1.6 and Figure 4.1.7 show the solar wind

dynamic pressure and IMF. There are several times (labeled A, B, C, D and E) where there are enhancements in the solar wind dynamic pressure. However, only at two of these times (C and D) were there vertical DC electric field jumps. Why are only some of these solar wind dynamic pressure enhancements coincident with a jump in the dc vertical field at MINIS Flight 2 South? One commonality that times C and D share is that they are the only two times with a dynamic pressure increase and southward IMF. We suppose that for January 20th, 2005, at C and D (13:56 UT and 15:54 UT), the SEP rigidity cutoffs are at their most equator-ward location. *Rodger et al.* [2006] showed that rigidity cutoffs move equator-ward with increasing geomagnetic activity index Kp, which increases with southward IMF. However, Kp is a 3-hour average, while the time it takes an SEP to enter the magnetosphere and precipitate is significantly shorter (seconds). Clearly, SEP trajectory is based on the instantaneous state of the magnetosphere, not the 3-hour average. Unfortunately, we do not have an accurate magnetospheric snapshot, nor is there a good data source that can provide the specific rigidity cutoff at MINIS Flight 2 South as a function of time. It may be possible that a complete, dynamic energetic particle-tracking model, coupled with an accurate time-dependent geomagnetic field could help determine local rigidity cutoffs. Indeed, there have been several intensive efforts to model rigidity cutoffs [e.g., *Smart and Shea*, 2001; *Rodger et al.*, 2006]. However, there is no current SEP model that can resolve time-dependent magnetic field fluctuations like those observed in the later half of January 20th, 2005. Without an applicable model, nor the resources to develop a truly complete dynamic, we can only make estimates about how the rigidity (and therefore the incident proton flux above MINIS Flight 2 South) shifted at 13:56 UT and 15:54 UT. We cannot confidently give a quantified estimate of SEP precipitation dynamics at a specific location. We can only suppose that the rigidity cutoffs moved equator-ward at both times when the IMF turned southward and the solar wind dynamic pressure increased. An analysis by *Rodger et al.* [2006] agrees with this basic idea that a more disturbed magnetosphere (higher Kp in their analysis) moves rigidity cutoffs equator-ward.

5.2.2 Conductivity Enhancement Could Account for Vertical DC Electric Field Decrease

We examine the observed conductivity and electric field variations without a quantified description of incident SEP flux over MINIS Flight 2 South, which caused the enhanced conductivity. Looking at Figure 5.1.1, we can see that there are increases in conductivity at both C and D (13:56 UT and 15:54 UT). The change in conductivity is about a factor of two from 60 – 120 siemens m^{-1} at 13:56 UT and a 25% increase from 100 – 125 siemens m^{-1} at 15:54 UT. Here, we use Ohm's law in the same way we did in Section 5.1. The conductivity increase by a factor of 2 at 13:56 UT could explain a drop in the vertical electric field from 50 mV m^{-1} before 13:56 UT to roughly 25 mV m^{-1} afterward if the current density were constant (see Figure 4.2.6). However, this same explanation does not work for the jump at 15:54 UT where the vertical dc field reverses polarity. A 25% increase in conductivity is not large enough to account for the observed electric field magnitude increase from nearly nothing to 50 mV m^{-1} upward. A conductivity enhancement could decrease the magnitude of the original downward pointing electric field, but it could not have caused it to switch directions.

5.2.3 SEP-Induced Quasi-Static Electric Compared with MINIS Observations

We investigate the possibility that an upward pointing quasi-static vertical electric field could grow large enough to be of comparable magnitude to the MINIS Flight 2 South observations. A build-up of positive charge below the balloon, deposited by SEPs themselves, will result in a quasi-static dc electric field. We quantify the resultant electric field that could counter the downward GEC return electric field by building a cylindrically-symmetric, time-dependent atmospheric electricity model. A very similar field model was employed by *Thomas* [2005] to successfully model the quasi-static electric field following a lightning discharge. Our model was split into two parts: A) a static solution for the atmospheric potential; and B) a time-dependent fourth order

Runge-Kutta solution for the continuity equation, which governs the movement of free charge. The set of electrostatic equations used were:

$$\sigma = \frac{ne^2}{m\nu} \tag{5-1}$$

$$\vec{J} = \sigma\vec{E} \tag{5-2}$$

$$\nabla^2\phi = -\frac{\rho}{\varepsilon_0} \tag{5-3}$$

$$\frac{\partial\rho}{\partial t} + \nabla \bullet \vec{J} = \Pi \tag{5-4}$$

Here, (5-1) is the collisional conductivity, (5-2) is Ohm's law, (5-3) is Gauss' law and (5-4) is the continuity equation, with Π as the SEP source term.

Our model is "2.5-D" and is cylindrically-symmetric about a local vertical axis, with altitude and radial horizontal distance as the independent variables. The balloon is in the middle (radius equals zero) at 32 km altitude. We assume that there is a uniform SEP precipitation only in the inner section of our cylindrical space (out to radius of 45 km). As the engine for this model, we used FISHPAK, a package of fortran subprograms for the solution of separable elliptic partial differential equations (written by J. Adams, P. Swarztrauber and R. Sweet of NOAA Boulder). This package was designed with this "2.5-D" structure in mind. Our spatial grid size is 60 by 90, where the grid spacing represents 1 km spacing in the altitude (60 km in altitude and 90 km radial distance). We use collisional conductivity values calculated by our conductivity model described in Chapter 3 and assume that there was no initial space charge. We use satellite energetic proton flux (both from GOES and POES) as the space charge source. First, we take the satellite integral proton flux measurements and convert them into 2150 differential flux bins between 0.64 and 2150 MeV following the method described in Section 3.3. Then, we calculate what the stopping altitude for each differential energy bin would be by using a range-energy relation determined by [*Sternheimer*, 1959].

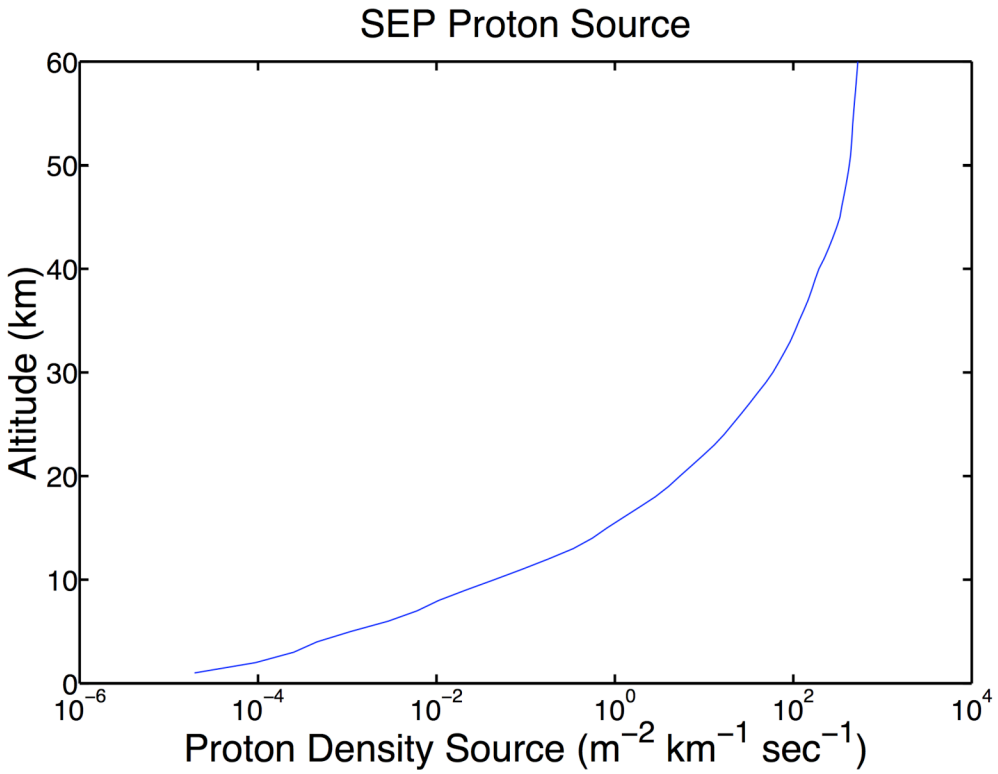

Figure 5.2.1 Modeled SEP density source example**.** This profile was calculated using the full GOES SEP spectrum at 12:00 UT on January 20th, 2005.

$$R = A(E)^B \qquad \textbf{(5-5)}$$

Here, $A = 2.71 \times 10^{-3}$, $B = 1.72$ and E is energy in MeV. We then translate range into altitude by summing the mass of air above a particular stopping altitude using the MSISE-90 model described in Section 3.2.1. This gives us the number of protons stopping at a particular altitude per second. Simply multiplying the time step by this value gives us the charge deposited at each grid point during each time step.

We assume uniform proton precipitation incident vertically down between 0 and 45 km in the radial direction in order to minimize outer edge effects. This is a relatively good first order approximation although a more realistic approach would be to assume a much larger horizontal area with SEP incidence at a variety of angles. We do not expect that this an error is large enough to alter the final vertical electric field by the several orders of

magnitude needed to become comparable to the MINIS Flight 2 South observations. The upper and lower boundaries were assumed to be infinitely conducting. At the ground, this is a fair assumption since the conductivity of the ground is ten orders of magnitude greater than the conductivity of the air just above it. At 60 km, the neutral density is low enough that there are free electrons contributing to the conductivity. However, there is no distinct boundary like that on the ground. Once a static solution was found, we moved the charge according to a modified continuity equation which is a combination of (5-2), (5-3) and (5-4)

$$\frac{\partial \rho}{\partial t} + \vec{E} \bullet \nabla \sigma + \frac{\sigma \rho}{\varepsilon_0} = \Pi. \qquad \textbf{(5-6)}$$

Equation (5-6) was solved numerically using a fourth-order Runge-Kutta method for differential equations. After the charge was moved, a new static solution for Equations (5-1), (5-2), (5-3) and (5-4) was found. Specifically, we wanted the vertical electric field component inside the SEP-affected region.

We ran a simple validity test by placing a single layer of uniform charge near the balloon altitude (30 km) between 0 km and 45 km horizontal distance. We expected the electric field at a simulated balloon location (32 km altitude, 0 km horizontal distance) to initially be equal to that of a charged conducting plate ($\frac{\rho}{2\varepsilon_0}$, where ρ is surface charge density) and decay away afterwards with a characteristic time constant. With time constants and electric fields on our coarse grid within a factor of about two of our expectations, this test confirmed that we had a reasonably working model.

This routine was run until it reached an equilibrium charge density. Figure 5.2.2 shows that the resultant vertical dc electric field is very small with respect to the fluctuations seen in the MINIS Flight 2 South dataset. The magnitude of the SEP-induced quasi-static electric field is on the order of microvolts per meter, four orders of magnitude less than

the field it would need to cancel. We perform a simple order of magnitude calculation to check the reasonability of our model output by constructing an idealized SEP-induced charge distribution shown in Figure 5.2.3. Assume that the balloon payload is in a 100 MeV cutoff regime and that all of the SEP protons greater than 100 MeV precipitate down to the same altitude at 30 km. This will establish a layer charge at 30 km with a surface charge density equal to the total SEP flux times a characteristic relaxation time. This characteristic relaxation time could be equal to the local relaxation time measured by the balloon instrumentation. However, since we do not know for certain what the characteristic relaxation time its, we will select a range of values in our calculation. There is a negative charge layer of equal and opposite charge density at 60 km formed by electrons that cannot precipitate down to 30 km. This scenario represents the maximum expected SEP-induced upward vertical electric field.

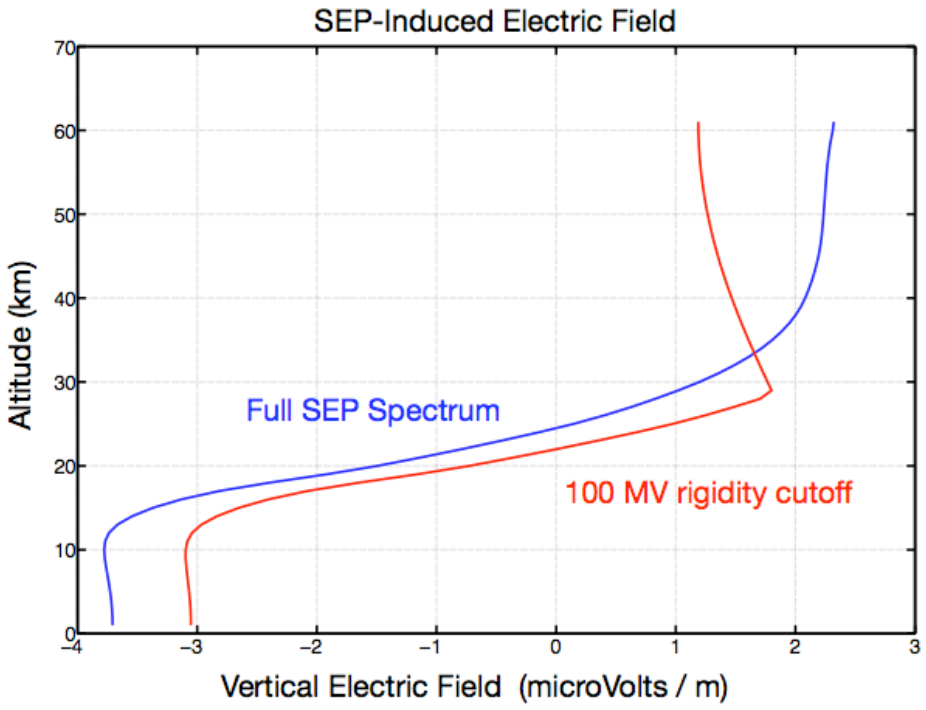

Figure 5.2.2 Modeled quasi-static vertical electric field caused by SEP charge deposition. The blue line assumes a full SEP spectrum and the red line assumes no protons under 100 MeV. This is a cut from our cylindrical model along the middle vertical axis at radius equals zero.

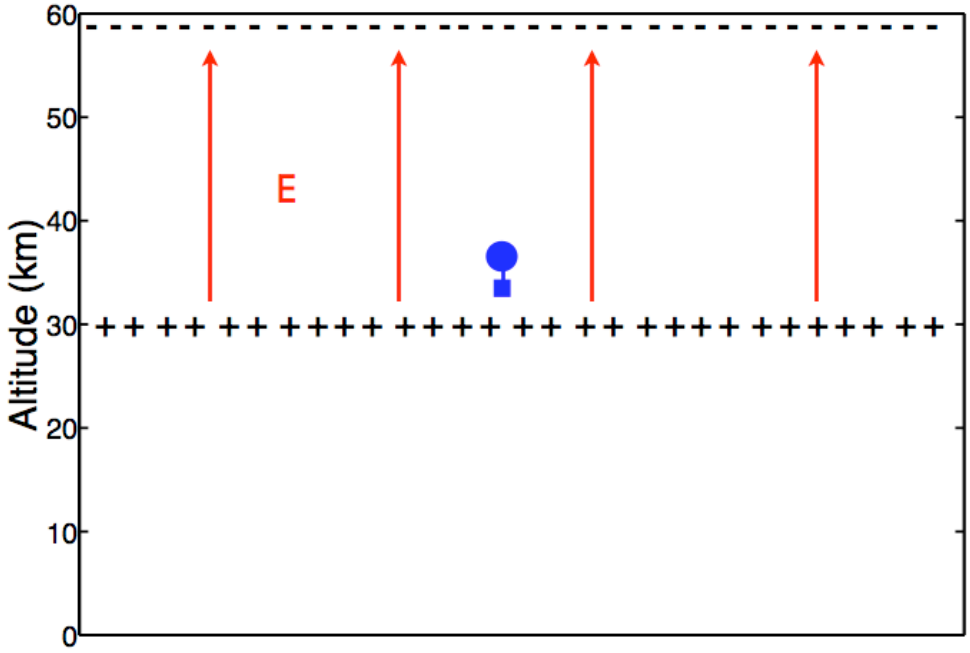

Figure 5.2.3 Cartoon of maximum SEP-induced electric field. There is a positive charge layer at 30 km and a negative charge layer at 60 km forming a parallel plate capacitor-like configuration.

Table 5-1 Vertical electric field magnitude for various characteristic relaxation times. Proton flux values are based on GOES measurements at 09:00 UT and 14:00 UT on January 20th, 2005. A range of characteristic relaxation times are given between 0.01 sec (less than the MINIS-observed local relaxation time during the SEP event) and 1000 sec (same order of magnitude as the estimated GEC relaxation time.

	$4.925\times10^{3}\ protons\ m^{-2}s^{-1}$	$3.68\times10^{2}\ protons\ m^{-2}s^{-1}$
0.01 sec	$8.9\times10^{-7}\ V/m$	$6.7\times10^{-8}\ V/m$
0.1 sec	$8.9\times10^{-6}\ V/m$	$6.7\times10^{-7}\ V/m$
1.0 sec	$8.9\times10^{-5}\ V/m$	$6.7\times10^{-6}\ V/m$
10.0 sec	$8.9\times10^{-4}\ V/m$	$6.7\times10^{-5}\ V/m$
100.0 sec	$8.9\times10^{-3}\ V/m$	$6.7\times10^{-4}\ V/m$
1000.0 sec	$8.9\times10^{-2}\ V/m$	$6.7\times10^{-3}\ V/m$

The flux of protons with energy greater than 100 MeV precipitating in the polar region at 09:00 UT on January 20th, 2005 is $4.925\times10^{3}\ m^{-2}s^{-1}$. This corresponds to charge flux of $7.88\times10^{-16}\ C\ m^{-2}s^{-1}$. If this charge all stopped at 30 km remained there for 0.1 seconds

(same order of magnitude as the MINIS-observed local relaxation time), then the surface charge density, σ, would be $7.88 \times 10^{-17}\ C\ m^{-2}$. We assume a similar, but oppositely charged, layer forms at 60 km. The electric field between two a charge layers is given by: $E = \sigma / \varepsilon_0$. The resultant electric field has a magnitude of $8.9 \times 10^{-6}\ V\ m^{-1}$. This value is nearly two orders of magnitude larger than our 2.5-D model predicts. Our 2.5-D model uses a distributed source as opposed to a charged layer. Therefore, we would expect our model to produce a smaller magnitude. This provides confidence that our 2.5-D model is not over-estimating the upward electric field magnitude. Table 5-1 summarizes the upward vertical electric field calculated from this simple model using two different proton flux values and a range of characteristic relaxation times. According to our simple model, the characteristic relaxation time would need to be at least 100 seconds in order for a quasi-static upward dc electric field to cancel the downward pointing fair-weather electric field. Therefore, we determine that in order for an upward quasi-static dc electric field resulting from SEP precipitation to cause a reversal in the MINIS data set, the characteristic relaxation time also needs to be greater than 100 seconds.

5.3 Horizontal Electric Field Decrease

Questions addressed in this section: 1) is there evidence for a changing observational environment; and 2) assuming potential difference sources in the ionosphere and also at lower-altitudes, could an SEP-induced conductivity enhancement perturb constant current electric field sources?

Summary: The MINIS-observed horizontal dc electric field decrease does not appear to be a result of a change to the observational environment (e.g., a sudden polar cap compression or alteration of potential difference mapping). We initially suppose that the source of the stratospheric horizontal dc electric field measured at MINIS is ionospheric. Using our conductivity model described in Chapter 3, we determine that SEP-induced

conductivity enhancements are too small near 120 km to significantly affect the ionospheric horizontal dc electric fields. We present evidence suggesting that electron precipitation is also too small at this time to affect the ionospheric electric fields. Alternately, we present a plausibility argument suggesting that lower altitude sources, which could have been effected by an SEP conductivity enhancement, may have been the source for the MINIS-stratospheric observations.

5.3.1 Consistent MINIS Observational Environment

The largest source of horizontal dc electric fields in the stratosphere during fair weather is commonly thought to be large-scale potential differences in the ionosphere [*Mozer*, 1971]. In this section we begin by assuming that the source region for the MINIS-observed horizontal dc electric field is, in fact, ionospheric. We eliminate changes to the observational environment, namely; (1) polar cap compression and (2) modification of potential difference mapping from the ionosphere.

(1) Polar Cap Compression. As mentioned in Chapter 1, the largest magnitude horizontal electric fields observed in the stratosphere by stratospheric balloon payloads at high latitudes in fair weather are usually a result of large spatial scale ionospheric electric fields. Although variable on timescales of minutes to hours, these fields could be 25-50 mV/m in magnitude on average for a mild to moderately active period. Outside of the polar cap, we might expect significantly smaller ionospheric potential differences up to 15-20 mV/m. A rapid compression event on the timescale of the SEP rise time (<20 minutes) could have the effect of shrinking the polar cap region where we expect to see these large ionospheric electric fields. Thus, if MINIS Flight 2 South, at 61° S magnetic latitude, was near the edge of the polar cap (which we believe it was, based on nominal polar cap size and POES satellite precipitation data shown in Figure 4.2.7), then a sudden compression could effectively move the balloon from inside to outside the polar cap. This could potentially have the effect of moving the balloon from a region where there is a

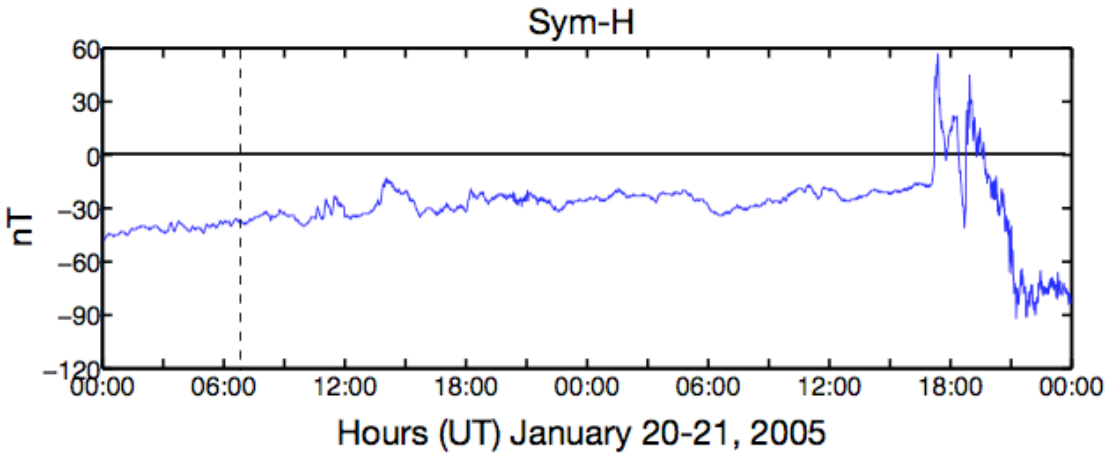

Figure 5.3.1 Sym-H index for January 20-21, 2005. This can be read just like Dst, but the values are given every minute as opposed to every hour. There is no large fluctuation at the January 20th SEP event onset (vertical dashed line). For comparison, a sudden compression event is shown near 16:00 UT January 21st.

large horizontal electric field in the ionosphere to an area with no such field overhead. This could explain the MINIS measurements (at least in part). If there were a sudden compression event, we would expect there to be similarly rapid magnetic field fluctuations as well. Because there is no evidence for any substantial fluctuations in space-based magnetometers like GOES 10 (Figure 4.1.14) or in the global Sym-H index (Figure 5.3.1), we disregard polar cap compression as a possible mechanism to explain the horizontal electric field decrease.

(2) Potential Difference Mapping Modification. Another possible observation condition change is a modification to the mapping of horizontal fields from the ionosphere down to the balloon altitude in the stratosphere. If the conductivity enhancement between the balloon and the source changes significantly, as it certainly did on January 20th, 2005, would there be a change in the attenuation factor? A model of electric field mapping by *Park and Dejnakarintra* [1977a] provide examples of ionospheric potential differences and the attenuation at lower altitudes using conductivity profiles for nominal conditions. For very large spatial-scale sources of 1000 km, there is essentially no attenuation as the horizontal ionospheric electric field is mapped down to 30 km in the stratosphere.

Smaller scale fields of 100 km will have an attenuation of nearly half. *Park and Dejnakarintra* [1977a] determined that an SEP event will have little to no impact on the attenuation of horizontal electric fields measured in the stratosphere from ionospheric sources. We can therefore rule out enhanced conductivity as a change in observation conditions as a probable cause for MINIS electric field observations.

5.3.2 SEP Ionization Not Responsible for Horizontal Field Decrease

We assume that the current flowing through the polar ionosphere remained constant during the SEP event onset on January 20th, 2005. If there were large, rapid changes in the current flow, we would see evidence in ground-based magnetometers like those in the IMAGE chain. Figure 5.3.2 shows the x-component (east-west) of several magnetometers at magnetic latitudes corresponding to the same L-shell that MINIS Flight 2 South was on during January 20th, 2005. There are no fluctuations coincident with SEP event onset. Additionally, polar-orbiting magnetometer observations can provide an estimate current flow into and out of the ionosphere by measuring the deflection of the earth's magnetic field. Based on FAST magnetometer data, there were no observed rapid changes in magnetic deflection coincident with the SEP event onset [*C. W. Carlson*, private communication]. We note the lack of evidence for rapid fluctuations in GOES magnetometers (Figure 4.1.14) and SuperDARN radar observations (Figure 4.1.15). The addition of SEP particle charge carriers through precipitation lends to a possible current increase, while a drop in current density seems less likely. With this evidence, we cannot completely rule out small total current changes (e.g., form a small current to an even smaller current). However, the assumption that the current flowing through the ionosphere was slowly varying is a very reasonable one. We apply Ohm's law ($\vec{J} = \ddot{\sigma} \bullet \vec{E}$) and say that if the current density is slowly varying, and we observe an electric field decrease at MINIS Flight 2 South, we expect a conductivity enhancement at the location of the source potential differences (~120 km).

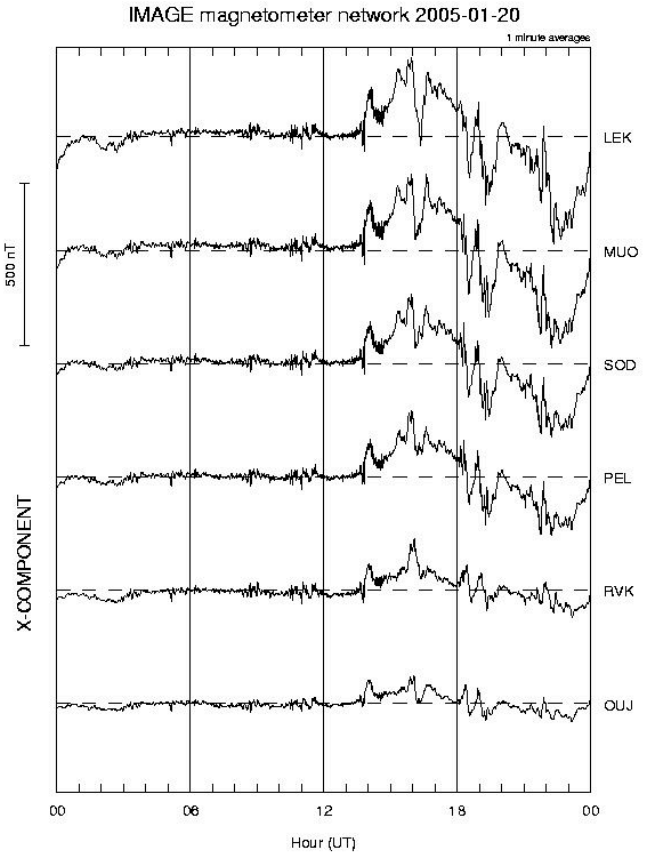

Figure 5.3.2 IMAGE Magnetometer chain data from stations at the same L-shell as MINIS Flight 2 South on January 20th, 2005. There are no noticeable magnetic field changes at SEP event onset just before 07:00 UT.

SEP-induced conductivity enhancements are not large at 120 km, the source altitude for large-scale horizontal potential differences. The ionization from precipitating SEP protons is simply too low. Horizontal current in the polar ionosphere is carried by the horizontal conductivity tenser components: the Pedersen and Hall terms. We apply our conductivity model from Chapter 3 to show that SEP precipitation has a negligible effect on conductivity values in the source region. Figure 5.3.3 shows results from our conductivity model at two times on January 20th, 2005 assuming a full SEP spectrum (no rigidity cutoffs). The solid lines are for 06:00 UT, one hour before the SEP event onset,

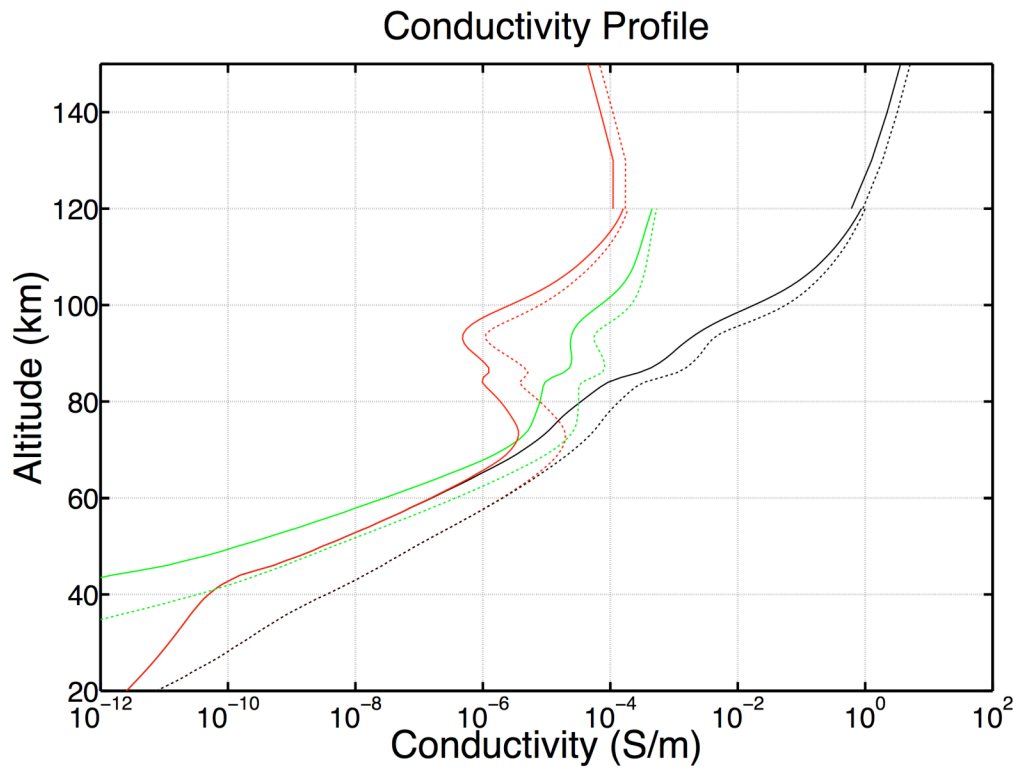

Figure 5.3.3 Modeled parallel, Pedersen and Hall conductivity profiles.Parallel, Pedersen and hall conductivities are shown in black, red and green, respectively. The solid lines are at time 06:00 UT, one hour before SEP event onset, and the dashed lines area at time 09:00 UT, two hours after SEP event onset. All profiles calculated assuming a full incident SEP spectrum.

and the dashed lines are for 09:00 UT, two hours after onset. There are discontinuities at 120 km. The conductivity was calculated using SIC-derived ion and electron densities below 120 km and using the IRI model output above 120 km. The SIC model has taken the SEP proton precipitation into account, whereas the IRI model has not. There is an increase in each component of the conductivity above 120 km from 06:00 UT to 09:00 UT. This is due simply to solar radiation forcing and not SEP proton precipitation. The peak of the Pedersen conductivity, which carries a bulk of the current from the magnetosphere through the ionosphere, is near 120 km. This means that our ionospheric source potential is also near 120 km (the same altitude where the ion cyclotron and ion collision frequencies are equal; see Figure 3.1.1). There needs to be an enhancement of the horizontal conductivity components near 120 km in order to decrease the source electric field. However, from Figure 5.3.3, both the Hall and Pederson conductivity see negligible

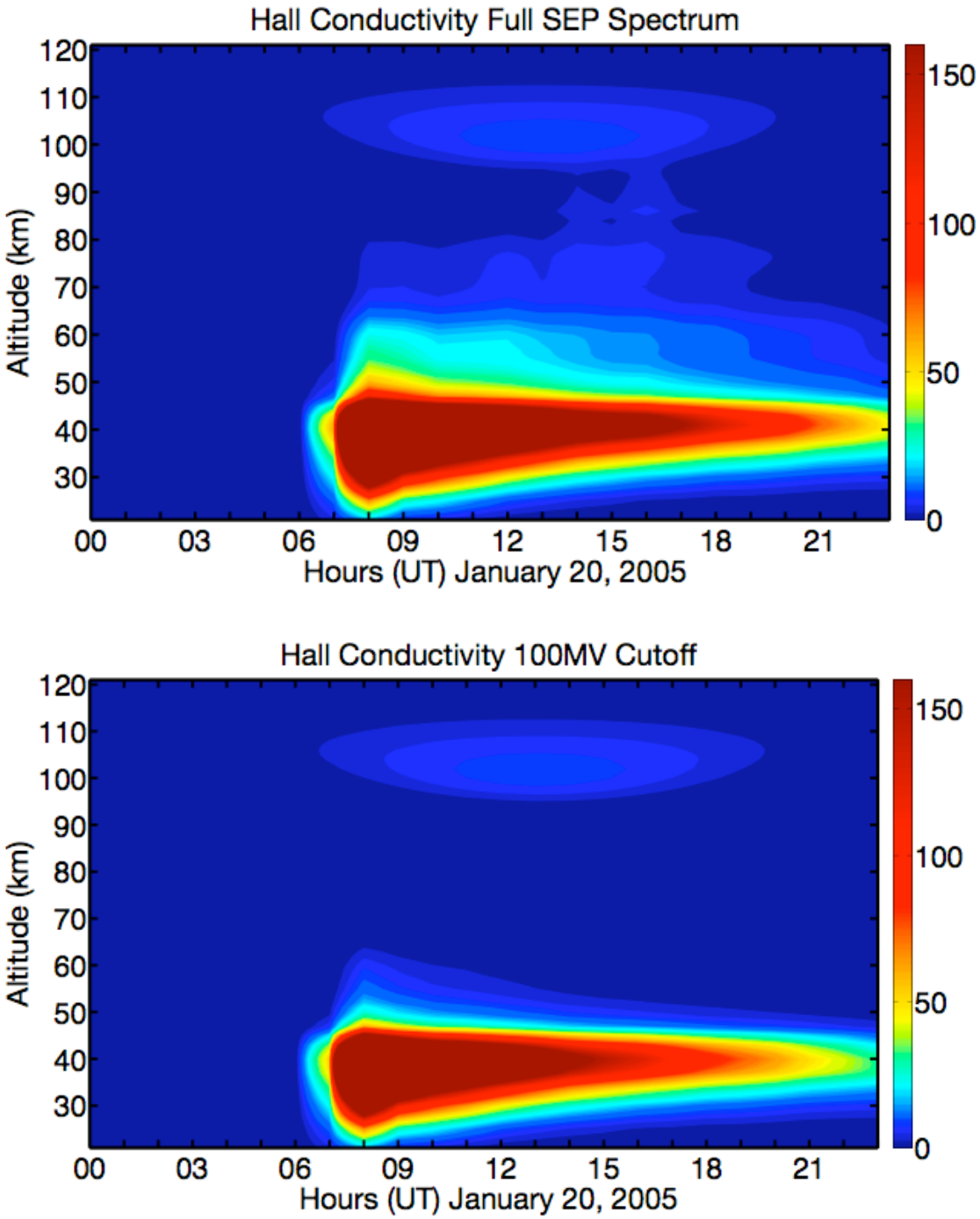

Figure 5.3.4 Change in modeled Hall conductivity on January 20th 2005. The top panel assumes a full incident SEP spectrum and the bottom panel assumes a 100 MV rigidity cutoff. Each hour, a conductivity profile is normalized by the profile at midnight. The color bar values represent the multiplicative change in the local conductivity (e.g., 50 = conductivity 50 times greater than base value at midnight).

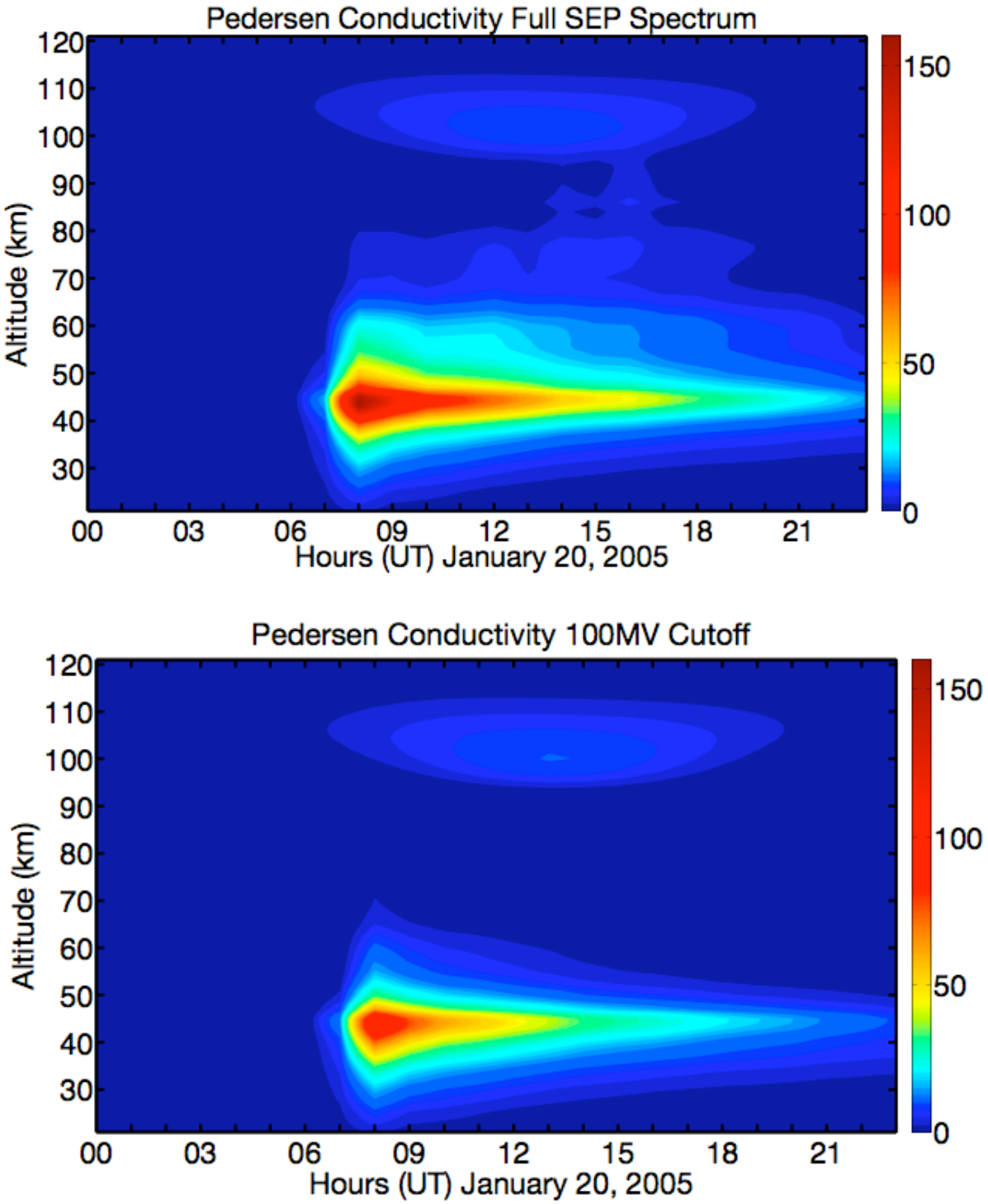

Figure 5.3.5 Change in modeled Pedersen conductivity on January 20th 2005. The top panel assumes a full incident SEP spectrum and the bottom panel assumes a 100 MV rigidity cutoff. Each hour, a conductivity profile is normalized by the profile at midnight. The color bar values represent the multiplicative change in the local conductivity (e.g., 50 = conductivity 50 times greater than base value at midnight).

changes from before to after SEP event onset. We can also look at the relative change of the Pederson and Hall terms as a function of time in Figure 5.3.4 and Figure 5.3.5. The large conductivity enhancements are all lower than 120 km, too low to affect the source region. There is a small enhancement centered near 110 km due to nominal solar radiation (not including any solar flare effects). From our model, it is clear that the SEP protons simply deposit their energy too low in the atmosphere to explain the horizontal electric field observations.

5.3.3 Electron Precipitation Not a Likely Source of Conductivity Enhancement

We argue that there is insufficient evidence for electron precipitation, leaving solar flare radiation as one remaining possibility to explain the conductivity enhancement observed during MINIS Flight 2 South. The onboard x-ray spectrometer, designed to measure electron precipitation, was flooded with counts during the SEP event, making extraction

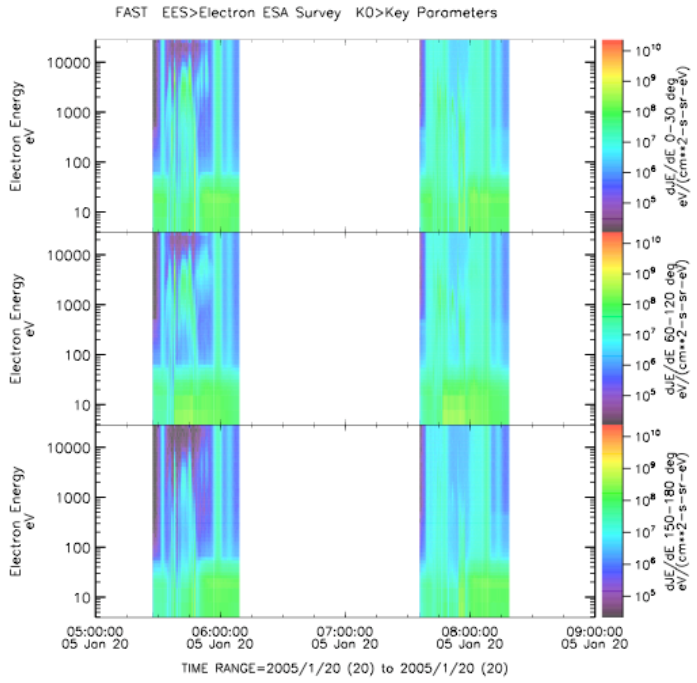

Figure 5.3.6 FAST electron flux. These data are for electrons between 5 eV and 30 keV for 05:00 UT to 09:00 UT on January 20th, 2005. There is an increase in apparent electron flux after the SEP event onset just before 07:00 UT. However, the data is very likely heavily contaminated by SEP protons after onset. (Figure courtesy of C. W. Carlson and the FAST Team).

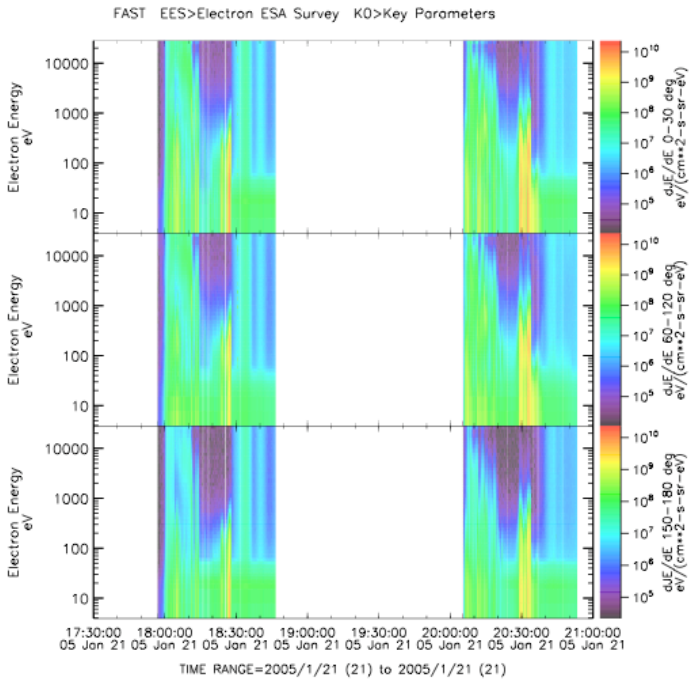

Figure 5.3.7 FAST electron flux. These data are for electrons between 5 eV and 30 keV for 17:30 UT to 21:00 UT on January 21st, 2005. The electron flux levels are comparable to those on the previous day when there is an SEP event. (Figure courtesy of C. W. Carlson and the FAST Team).

of any energetic electron component impossible. Thus, we look at the polar orbiting FAST satellite electron flux data to see if there were any significant enhancements. Figure 5.3.6 shows energetic electron data for two FAST polar passes (one before and one after SEP event onset) for energies between 5 eV and 30 keV in three pitch angle bins. There does appear to be an increase in electron flux, but the SEP protons themselves are likely responsible for heavily contaminating the data set during this time (*C.W. Carlson*, private communication). Thus, what we see in Figure 5.3.6 is an extreme upper limit on the electron flux. We can also compare the data from January 20th, 2005 to data from the next day (January 21st, 2005), when there was no SEP event and the horizontal dc electric field did not vanish or decrease at MINIS Flight 2 South (see Chapters 6 and 7). Figure 5.3.7 shows enhancements of similar magnitude as those in Figure 5.3.6. We expect that electrons between 2 keV and 5 keV will cause the most ionization per electron near 120

km [*Rees*, 1989]. Remembering that Figure 5.3.6 is likely an extremely high limit on the actual electron flux, we assert that electron precipitation could not have caused a conductivity enhancement on January 20th, 2005 because there was not a significant increase of electron flux in the necessary energy range at the SEP event onset.

5.3.4 Lower-Altitude Source Plausibility

It is possible that the source of a significant fraction of the horizontal dc electric field measured at MINIS is not ionospheric at all, but rather from a lower-altitude source. Two possible candidate sources for horizontal fields with amplitudes large enough to match the MINIS observations are electrified clouds and a horizontal inertial turbulent stratosphere (HITS) source [*Holzworth*, 1989]. Although thunderstorms can have extremely large electric fields associated with them, at MINIS Flight 2 South's southerly position, thunderstorms are practically non-existent. According to data from the World Wide Lightning Location Network [see *Lay et al.*, 2004; *Rodger et al.*, 2004] for more WWLLN details), the nearest thunderstorm activity to MINIS Flight 2 South on January 20th, 2005 was well over 1000 km away [*E. Lay,* private communication] and was therefore not a viable source for large electric fields.

HITS fields, on the other hand, have been definitively identified by altitude-stable (26 km) balloon instrumentation, in the middle latitude stratosphere. The signatures of HITS fields are large-amplitude day time magnitudes and a rotation at the local inertial period. It was suggested by *Holzworth* [1989], that most stratospheric balloon-based electric field measurements would miss HITS fields for several reasons. A) Upward mapping of potential differences is not as efficient as downward mapping [*Park and Dejnakarintra*, 1977a; 1977b]. Therefore, even one scale height further above the source altitude could damp out any signature. B) Night time, or 24-hour fully-illuminated polar, HITS electric field amplitudes should be relatively small. For optical auroral observations (which account for a majority of high-latitude balloon flights), balloon payloads were flown at

night. C) Without an altitude-stable payload, it could be easy for a rotating, turbulent HITS fields signature to become obscured by vertical balloon motion. Most stratospheric balloon flights are not altitude-stable. Despite these obstacles, there is evidence that a HITS-like signature was also observed in high altitude Polar Patrol Balloons, which were not altitude stable [*R. H. Holzworth* and *E. A. Bering*, private communication].

There is reason to believe that the MINIS-observed horizontal dc electric field observations, near the time of the SEP event on January 20th, 2005, may have been heavily influenced by a HITS field or another lower-altitude source. In order for the horizontal dc electric field to be dominated by a lower-altitude source, the ionospheric source would have to be small. For most of January 20th, 2005, conditions were such that the ionospheric horizontal electric field was as small as it could be. For several hours before the SEP event and for several hours afterward, the IMF was northward. (See Figure 4.1.7.) *Wygant et al.* [1983] show that after about three hours of northward IMF, the cross polar cap potential drops to a minimum value. There are practically no SuperDARN radar echoes during the same period that the IMF was north, implying small (< 20 mV/m) ionospheric electric field within the radar field of view. (See Figure 4.1.15.) Because the ionospheric electric field was small and radars cannot measure such small field signatures, there are no other independent measurements besides the balloon at this time. There is no way to conclusively eliminate a lower-altitude source as the dominant signature in the MINIS data. However, we have no independent observation confirming the existence or strength of a lower-altitude source on January 20th either.

Supposing that a lower-altitude source was the dominant feature in the MINIS horizontal dc electric field data on January 20th, 2005, we might well expect that the field would completely vanish at the SEP event onset. In one possible scenario, a constant current electric field source at the tropopause is established, perhaps, by a horizontal wind-induced charge separation. This is similar to a proposed HITS mechanism [*Holzworth*,

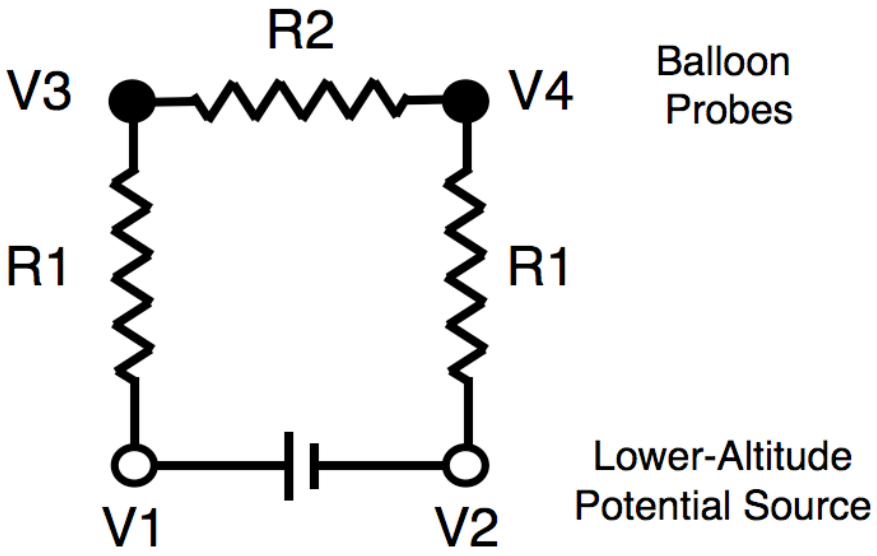

Figure 5.3.8 Lower-altitude potential difference mapping equivalent circuit. The lower-altitude source is represented by the potential difference between V1 and V2. The potential difference between the two horizontal balloon probes is represented by the difference between V3 and V4. R2 is the geophysical resistance between the probes due to the collisional plasma of the stratosphere. R1 is the resistance between the balloon altitude and the lower altitude.

1989]. Using our conductivity model, we have shown that there were SEP-induced conductivity enhancements below the balloon altitude and above the proposed tropopause source. (See Figure 5.1.2 and Figure 5.3.5.) We expect that lower-altitude potential differences will be rapidly attenuated above the source in regions of higher conductivity [*Holzworth* 1989; *Dejnakarintra*, 1974; *Park and Dejnakarintra*, 1977b]. The horizontal electric field could have vanished at 32 km for one of two reasons. First, the source, itself, could have been shorted out by an enhanced conductivity at the source altitude. A factor of five increase in the local conductivity at the source with a constant current density could result in vanishing horizontal dc electric fields similar to the MINIS observations. Second, we might expect a horizontal dc electric field decrease if there is a conductivity enhancement at the balloon altitude and below, but not extending all the way to the source altitude. An equivalent circuit for this is scenario is shown in Figure 5.3.8.

The gain, *G*, between the lower-altitude source and the balloon-observed potential difference is given by the following equation.

$$G = \frac{R_2}{2R_1 + R_2} \tag{5-7}$$

We make the simplifying assumption that $R_1 \geq R_2$. This assumption is reasonable because the conductivity between the balloon altitude and the lower-altitude source is larger than the conductivity at the balloon altitude itself. Also, we assume the vertical distance between the balloon and the source altitude is much larger than the probe separation. This simplifying assumption reduces Equation (5-7) to

$$G = \frac{R_2}{2R_1}. \tag{5-8}$$

If the resistance values, R_2 and R_1, were to decrease as a result of a conductivity enhancement, then the gain will change. The gain will decrease if R_2 decreases more than R_1. Returning to our hypothetical situation, the conductivity at the balloon altitude and below becomes enhanced, decreasing R_2 of the equivalent circuit. The conductivity near the source remains unchanged, leaving R_1 relatively unchanged. The result would be a decreased horizontal dc electric field observed at the balloon altitude. With these plausibility examples of how a lower-altitude source might become heavily and suddenly attenuated, we cannot rule out similar circumstance during MINIS Flight 2 South.

6 Relativistic Electron Precipitation and Ionospheric Electrodynamics During the January 21 2005 Storm Sudden Commencement

One day after the X 7.1 solar flare and solar energetic particle (SEP) event described in Chapters 4 and 5, the bulk coronal mass ejection (CME) plasma arrived at earth. This fast moving CME plasma caused a two-step impulsive solar wind dynamic pressure observed at earth at 17:11 UT and 18:45 UT on January 21st, 2005. These impulses resulted in rapid compression of the magnetosphere and a storm sudden commencement (SSC). There were three MINIS balloons aloft in the dusk-side polar stratosphere (although only two had electric field instrumentation). Each observed bremsstrahlung x-rays from relativistic electron precipitation (REP) associated with these impulse events. There were horizontal dc electric field increases measured at the two southern balloon payloads consistent with normal geomagnetic storm progression as well as rapid decreases coincident with particular REP observations. In this chapter, we present data describing the impulse events and SSC in the solar wind and within the magnetosphere. Then, we present the MINIS x-ray and electric field observations. This combined data set is important because it is the first to contain multi-point balloon-borne REP observations during SSC impulse events. All of the data present in this chapter is aimed to place all of the observations into proper context. Later, in Chapter 7, we discus some of the scientific connections between satellite and MINIS balloon observations.

6.1 Solar Wind Impulses on January 21st, 2005

In this section, we present data indicating the arrival of two solar wind impulses. We show solar wind parameters measured by the ACE spacecraft, magnetospheric magnetic field and electron flux data from GOES as well as the Sym-H storm indicator.

6.1.1 Solar Wind Parameters

To illustrate evidence for the two CME impulses in the solar wind, we show ACE proton density and velocity and then combine them to get dynamic pressure. The top panel of

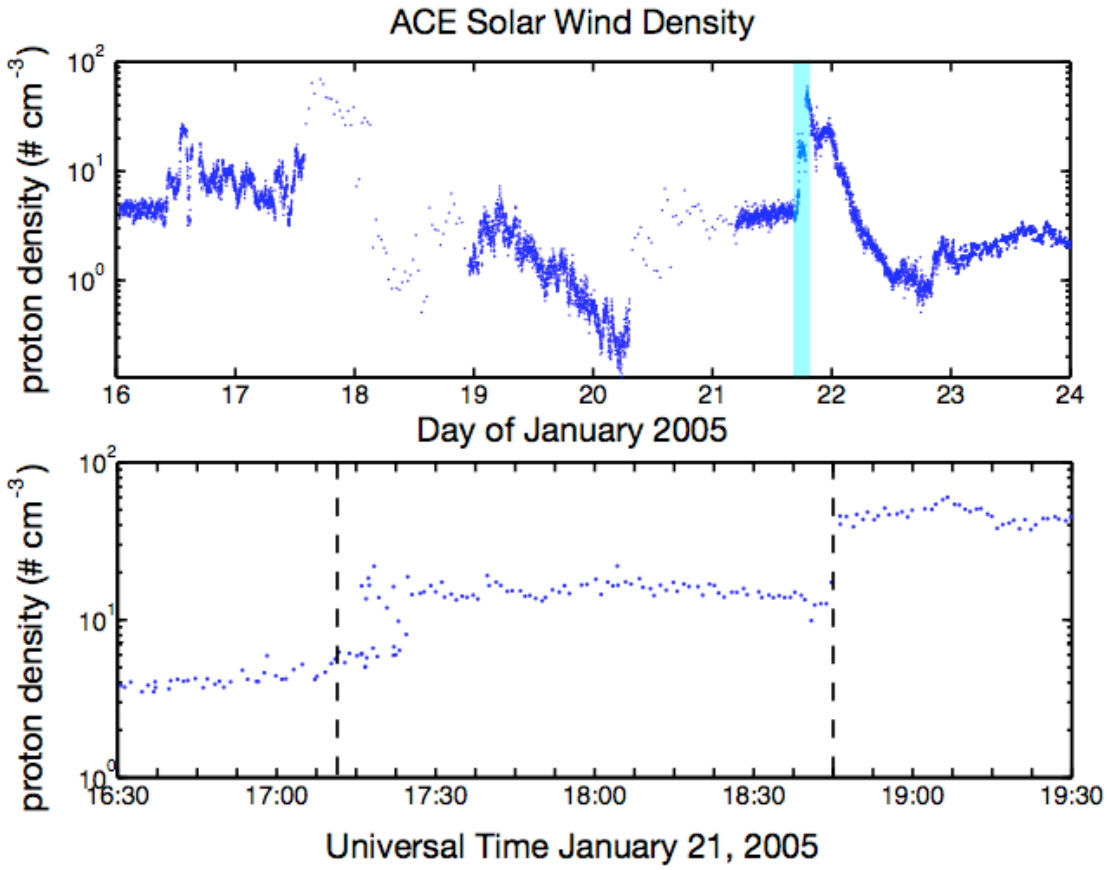

Figure 6.1.1 ACE solar wind density during January 2005. The top panel shows the time between January 16th and 24th. The shaded region indicates the time represented in the bottom panel. The bottom panel ranges from 16:30 UT to 19:30 UT on January 21st, 2005. The two vertical dashed lines indicate general earth arrival times of the two impulses at 17:12 UT and 18:45 UT.

Figure 6.1.1 shows solar wind density for January 16th to 24th (similar to Figure 4.1.4). In the lower panel, we focus on January 21st, 2005 between 16:30 UT and 19:30 UT. The data are time-shifted for estimated earth arrival. There is a shaded region in the top panel indicating the time period represented in the bottom panel. The two vertical dashed lines in the bottom panel are representative of the impulse arrival times at earth (17:12 UT and 18:45 UT). In reality, effects from the impulse interaction with the magnetosphere take some time to propagate. Thus, the time at which the effects from the impulses are noticed at different locations (e.g., GOES satellites or MINIS balloons) can vary by about a minute. Additionally, the time delay from ACE (221 earth radii upstream in the solar wind) to earth is an estimate based on the velocity of the solar wind as it passes by.

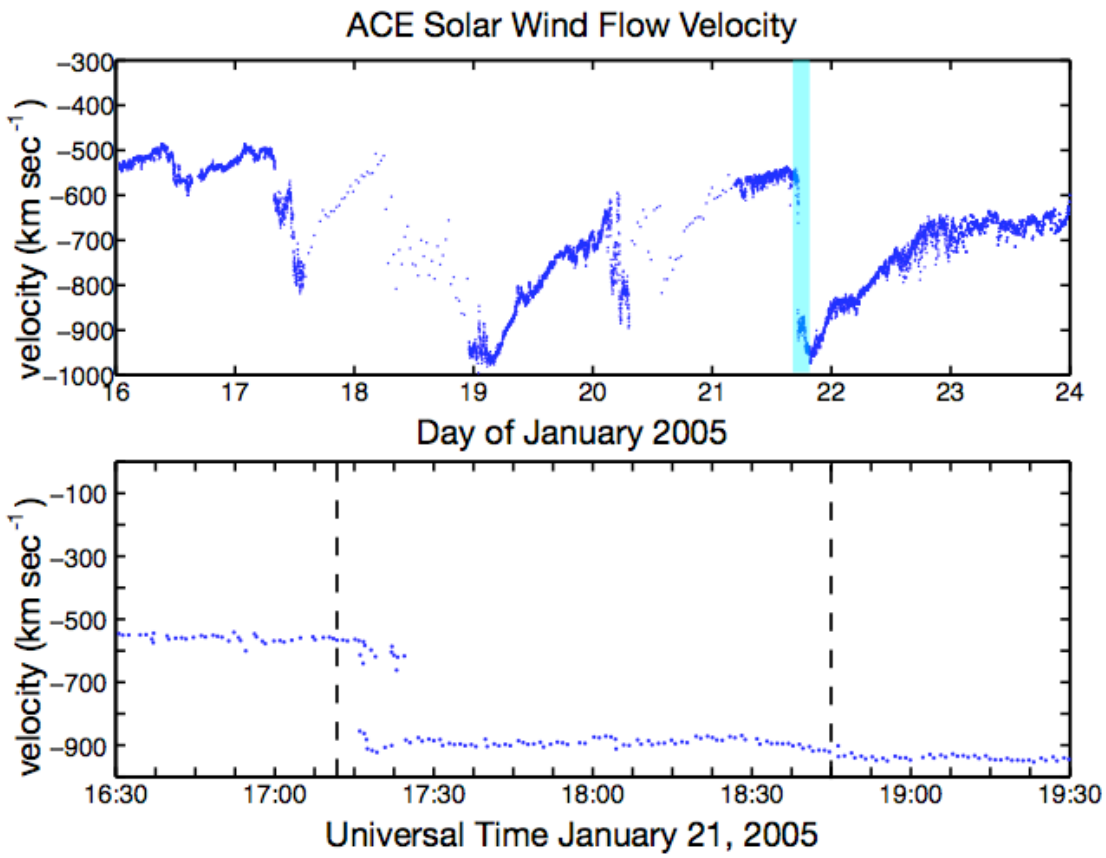

Figure 6.1.2 ACE solar wind velocity in January 2005. The top panel shows the time between January 16th and 24th. The shaded region indicates the time represented in the bottom panel. The bottom panel ranges from 16:30 UT to 19:30 UT on January 21st, 2005. The two vertical dashed lines indicate general earth arrival times of the two impulses at 17:12 UT and 18:45 UT.

When a shock impulse passes by ACE, time-delays suddenly shift. This causes an apparent "back track" in the observational data. This effect is clearly seen after the first impulse between 17:15 UT and 17:25 UT. At the later impulse, there is no "back track" because there is no change in velocity (shown in Figure 6.1.2), only in density. At the first impulse, the density increases nearly three-fold from 6 protons cm^{-3} to 20 protons cm^{-3}. At the second impulse, the density again nearly triples from 13 protons cm^{-3} to 45 protons cm^{-3}. This same "back track" feature is seen in the solar wind velocity data shown in Figure 6.1.2. The solar wind velocity only changes once, at the first impulse, and remains relatively constant at the second. The velocity shift at the first impulse is from 550 km s^{-1} to 925 km s^{-1}.

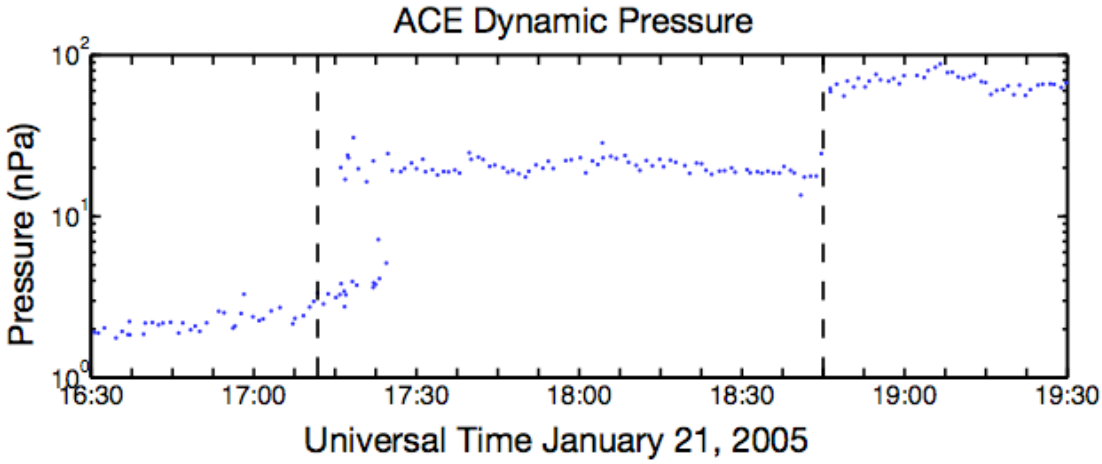

Figure 6.1.3 ACE solar wind dynamic pressure for three hours after 16:30 UT January 21st, 2005. The two vertical dashed lines indicate general earth arrival times of the two impulses at 17:12 UT and 18:45 UT.

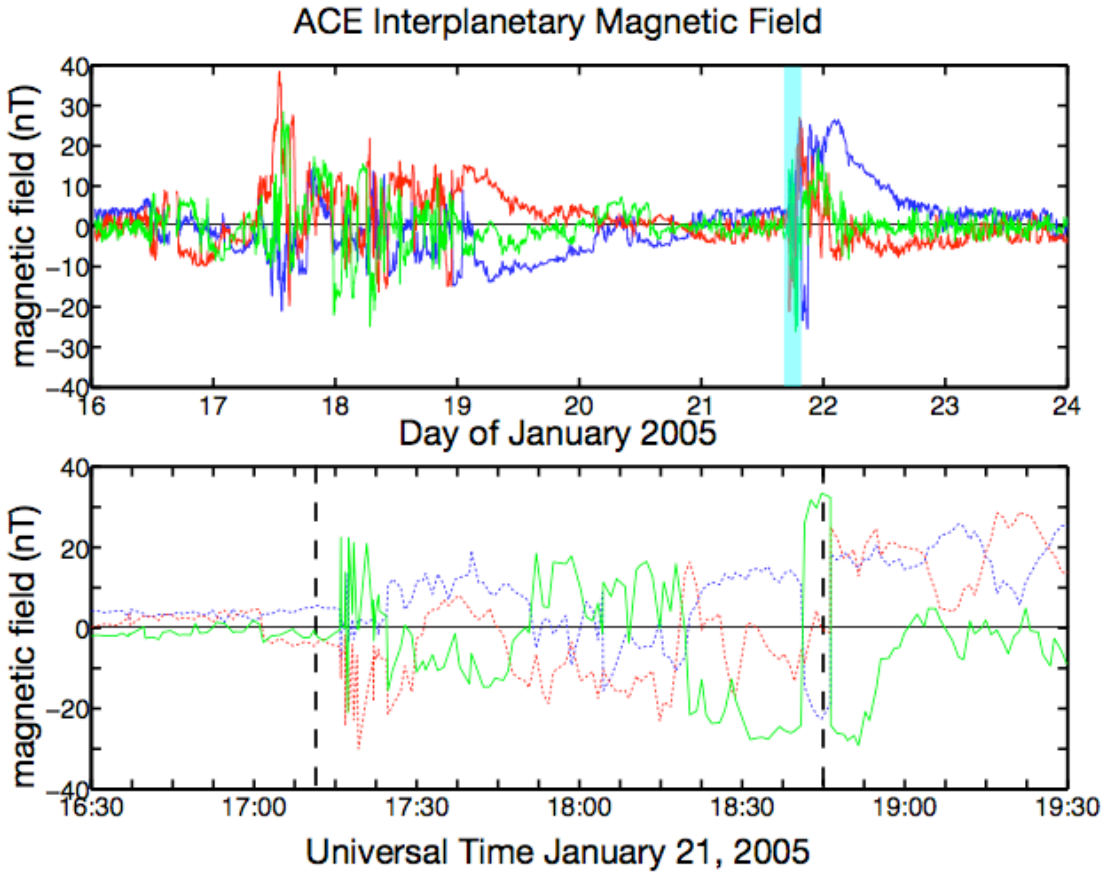

Figure 6.1.4 ACE IMF in January 2005. The shaded region in the top panel indicates the time represented in the bottom panel. The bottom panel ranges from 16:30 UT to 19:30 UT on January 21st, 2005. The two vertical dashed lines indicate general earth arrival times of the two impulses at 17:12 UT and 18:45 UT. IMF x, y and z components are shown in blue, red and green, respectively.

Combining the density and velocity observations, we can calculate the solar wind

dynamic pressure show in Figure 6.1.3. At the first impulse, there is a pressure increase from 4 nPa to 20 nPa and at the second there is an increase from 20 nPa to 60 nPa.

The final solar wind parameter we show is the magnetic field, IMF. At the second impulse arrival, Figure 6.1.4 shows a rapid increase in magnetic field magnitude as well as a reversal of the *z*-component (green). The impulsive magnetic field enhancement is caused by the imbedded magnetic field in the solar wind piling up in front of a propagating shock. Due to the arrival time delay at the first impulse, a similar pile-up is not as noticeable. However, there is a sudden shift in IMF magnitude and direction. The IMF is strongly southward starting at 17:32 UT and is even stronger at 18:18 UT.

6.1.2 Magnetospheric Compression and Storm Development

Because the solar wind dynamic pressure is balanced by magnetic pressure at the magnetopause, we expect to observe a magnetospheric compression resulting from the sudden impulses described in Section 6.1.1. In this section, we present magnetic field data from GOES 10 and 12. We also show model results showing magnetopause location that help solidify our interpretation of the GOES data.

Figure 6.1.5 shows three components of GOES 10 (top panel) and GOES 12 (bottom panel) magnetic field data. Each panel has H_p in blue (parallel to earth's rotation axis), H_e in red (earthward) and H_n in green (normal to H_p and H_e, westward). Again, the vertical dashed lines mark the two impulses arriving at earth. By looking just at the H_p components at each GOES satellite, we can get a better idea of the compression state of the magnetosphere as well as the spacecraft magnetic region. Figure 6.1.6 shows just the H_p components from GOES 10 (red) and GOES 12 (blue). There are three different magnetic regions that each spacecraft enters. Before the first impulse arrival, both GOES satellites are in an undisturbed magnetosphere, with a magnitude just above 100 nT.

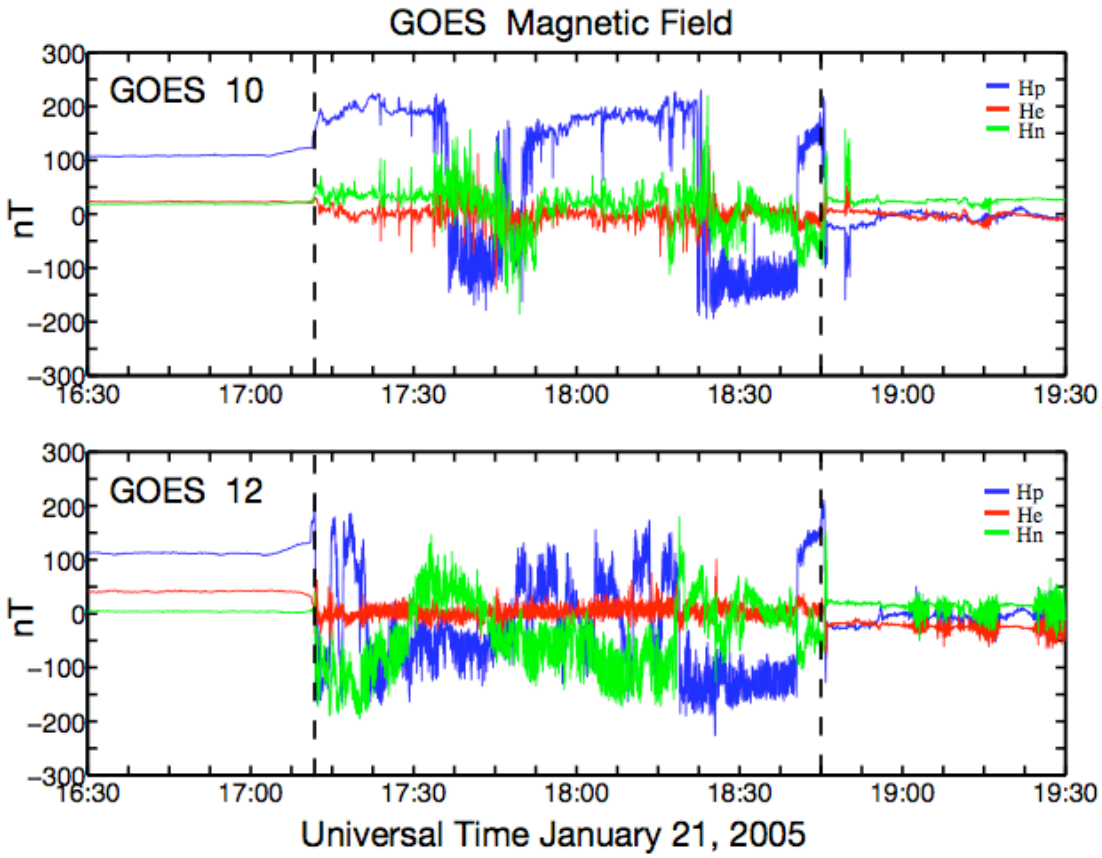

Figure 6.1.5 GOES magnetic field data for three hours after 16:30 UT January 21st, 2005. GOES 10 data are in the top panel and Goes 12 are in the bottom. H_p is blue (parallel to earth's rotation axis), H_e is red (earthward) and H_n in green (normal to H_p and H_e, westward). The two vertical dashed lines indicate general earth arrival times of the two impulses at 17:12 UT and 18:45 UT.

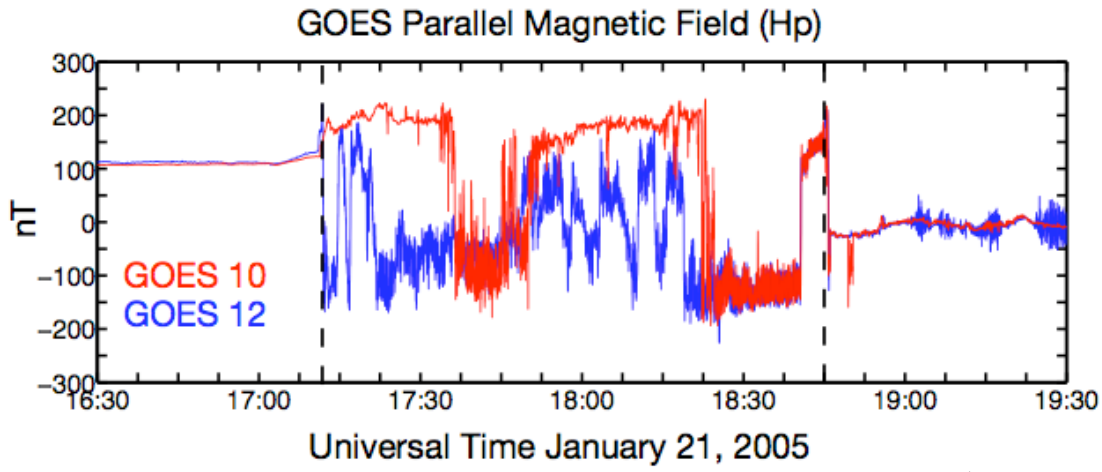

Figure 6.1.6 GOES parallel magnetic field data for three hours after 16:30 UT January 21st, 2005. GOES 10 (red) and 12 (blue) H_p (parallel to earth's rotation axis). The two vertical dashed lines indicate general earth arrival times of the two impulses at 17:12 UT and 18:45 UT.

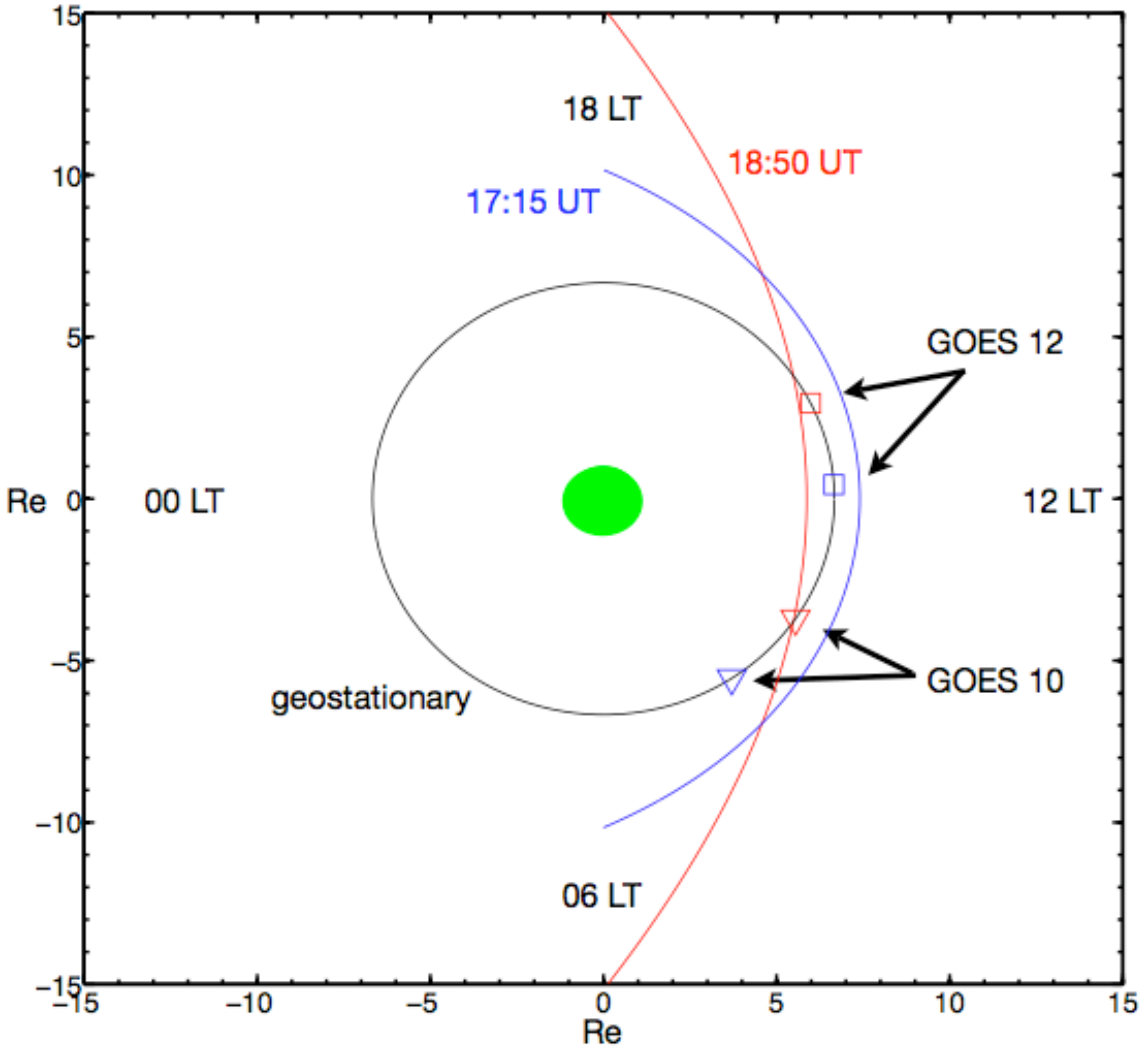

Figure 6.1.7 Modeled magnetopause with GOES locations. GOES 10 (triangles) and GOES 12 (squares) are marked in blue (model output at 17:15 UT) and red (model output at 18:50 UT). GOES 10 is westward of (and toward the bottom of the figure from) GOES 12.

Between 17:12 UT and 18:45 UT, both satellites move between the earthward side and solar wind side of a magnetic pile-up region. After the second impulse, both satellites enter the solar wind itself and are completely outside the magnetosphere.

Figure 6.1.7 shows the locations of GOES 10 and 12 and a model of the equatorial magnetopause at 17:15 UT (blue) and 18:50 UT (red), minutes after each impulse arrival. The equatorial magnetopause location was calculated using a model dependent on IMF and dynamic pressure from *Shue et al.* [1998]. The radial location of the magnetopause, *r*,

is given as a function of sub-solar zenith angle, θ (such that $\theta = 0$ at the sub-solar point).

$$r = r_0\left(\frac{2}{1+\cos\theta}\right)^{\alpha} \tag{6-1}$$

Here, r_0 and α are functions of the dynamic pressure and the z-component of the IMF.

$$\begin{aligned} r_0 &= (11.4 + 0.013B_z)D_p^{-\frac{1}{6.6}} \qquad for \quad B_z > 0 \\ r_0 &= (11.4 + 0.014B_z)D_p^{-\frac{1}{6.6}} \qquad for \quad B_z < 0 \end{aligned} \tag{6-2}$$

$$\alpha = \left(0.58 - 0.010B_z\right)\left(1 + D_p\right) \tag{6-3}$$

In Equations (6-2) and (6-3), D_p is the dynamic pressure in nPa and B_z is the IMF z-component in nT. The r_0 term controls the sub-solar magnetopause standoff location and α determines the flaring of the magnetopause. The model output in Figure 6.1.7 generally agrees with the GOES data in Figure 6.1.6. After the first impulse, both satellites are near the magnetopause boundary. The data suggest that GOES 12 is outside the magnetopause, which is not reflected in the model. After the second impulse, both GOES spacecraft are outside the magnetosphere entirely. The model appears to estimate slightly larger magnetopause radii than the data suggest. However, the general agreement between the data and the model gives us a good idea of the severity of compression during this time period.

As part of our investigation of relativistic electron precipitation (REP), we examine the flux of energetic electrons in the magnetosphere. GOES 10 and 12 have integral electron flux detectors sensitive to > 2 MeV electrons. Following the first impulse at 17:12 UT, the electron flux levels drop (Figure 6.1.8). GOES 12, closer to local noon, observes a rapid decrease of over an order of magnitude whereas flux at GOES 10 takes one half of an hour for a similar decrease. This is consistent with a rapid magnetospheric compression where the electron populations move earthward.

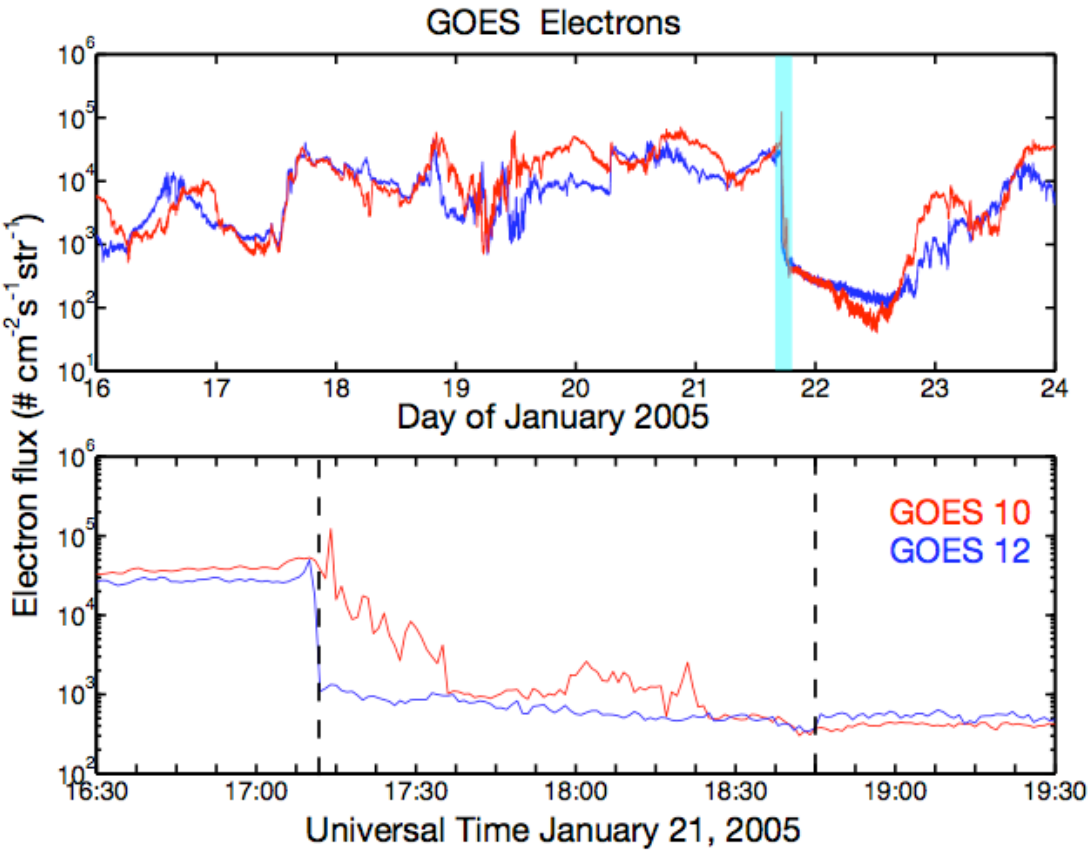

Figure 6.1.8 GOES 10 and 12 >2 MeV electron flux. Data from Goes 10 is in red and GOES 12 is in blue. The shaded region in the top panel indicates the time represented in the bottom panel. The bottom panel ranges from 16:30 UT to 19:30 UT on January 21st, 2005. The two vertical dashed lines indicate general earth arrival times of the two impulses at 17:12 UT and 18:45 UT.

The last piece of data we present is Sym-H. Sym-H is a global geomagnetic storm index, calculated in much the same way as the Dst index. To calculate Sym-H, deviations from the nominal magnetic field (caused by ring current dynamics and related phenomena) are gathered using a chain of ground-based magnetometers and normalized for direct comparison to Dst. A recent study shows that there is good agreement (within 10 nT) between Sym-H and Dst above -300 nT (and within 20 nT below -300 nT) [*Wanliss and Showalter*, 2006]. The main difference between the two indices is that Sym-H is calculated in 1-minute increments, whereas Dst is an hourly index. Thus, with Sym-H, we can get better time resolution for comparison with events that occur on a shorter

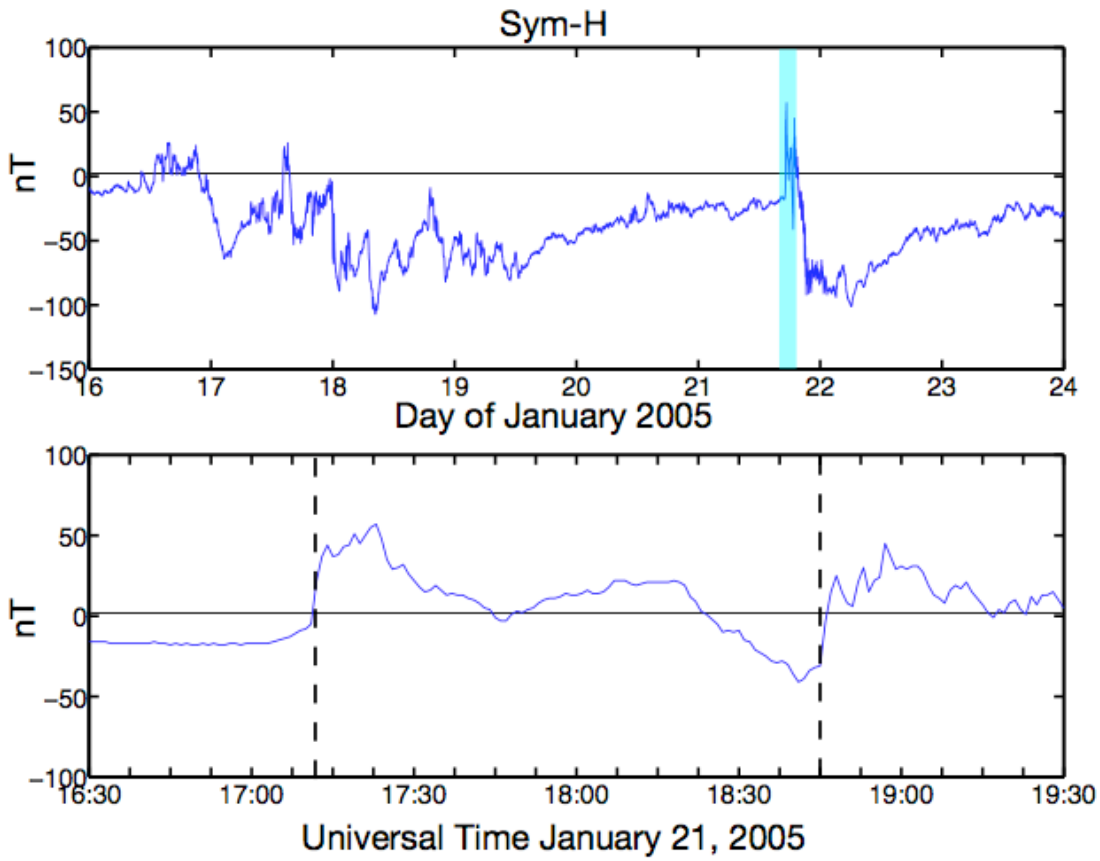

Figure 6.1.9 Sym-H index during January 2005. Sym-H is essentially like Dst, but with a faster time resolution. The shaded region in the top panel indicates the time represented in the bottom panel. The bottom panel ranges from 16:30 UT to 19:30 UT on January 21st, 2005. The two vertical dashed lines indicate general earth arrival times of the two impulses at 17:12 UT and 18:45 UT.

timescale. Figure 6.1.9 shows Sym-H data during January 2005 (top) and a close up of 16:30 UT to 19:30 UT on January 21st (bottom). Each of the impulse arrivals causes Sym-H to increase rapidly, a sign of magnetospheric compression. Following the first impulse, Sym-H decreases when IMF B_z is negative and increases when B_z is positive. This is consistent with storm time ring current injection during times of southward IMF.

We have now shown two separate dynamic pressure impulses in the solar wind that are associated with rapid fluctuations in the IMF. These impulses cause a compression of the dayside inner magnetosphere, as evidenced by the fluctuations in the GOES magnetometers, the drop in the energetic electron flux and by the rapid increase in Sym-H.

Using this description of the solar wind forcing on the magnetosphere, we can now proceed with presenting the MINIS balloon data within the appropriate context.

6.2 MINIS Observations Near Impulse Events

In this section, we present MINIS balloon data from three different balloon flights: Flight 1 North, Flight 2 South and Flight 3 South. We primarily focus on the two southern balloons because the northern payloads did not include electric field instrumentation.

6.2.1 Relativistic Electron Precipitation Observations

On January 21st, 2005, MINIS Flight 2 South was located at L=3.5 and Flight 3 South was at L=4.1. Both balloons remained at nearly the same L-shell during the 3-hour interval we are focusing on. Flight 1 North began the interval at ~L=10 and quickly drifted to much higher magnetic latitude. The southern payloads were separated by 38 minutes of MLT as calculated by the IGRF/DGRF model. X-ray spectrometers on all of the balloons observed intense periods of hard bremsstrahlung in the interval shown in Figure 6.2.1 between 16:30 UT and 19:30 UT. Each panel of Figure 6.2.1 shows high time-resolution data from the x-ray detectors during this precipitation interval from MINIS Flight 1 North (top), 2 South (middle) and 3 South (bottom). There are four energy channels shown in blue (20-175 keV), red (175-540keV), green (540-825keV) and magenta (825-1500keV) that were sampled 20 times per second. At 17:12 UT, coincident with the first impulse arrival at earth, all three balloons observed REP x-rays. Due to data gaps, we can place an upper limit of 3 minutes on this coincidence. At the second impulse arrival time (18:45 UT), there are coincident REP observations at the two southern payloads only. At this time, Flight 1 North had moved to an L-shell much greater than 10. In this case, the two southern payloads observed a rise in x-ray counts within 3 seconds of each other. This time is too fast to be a precipitation region that is drifting in MLT. Additionally, there is rapid onset REP marked in the bottom panel seen by only Flight 3 South at 18:33 UT.

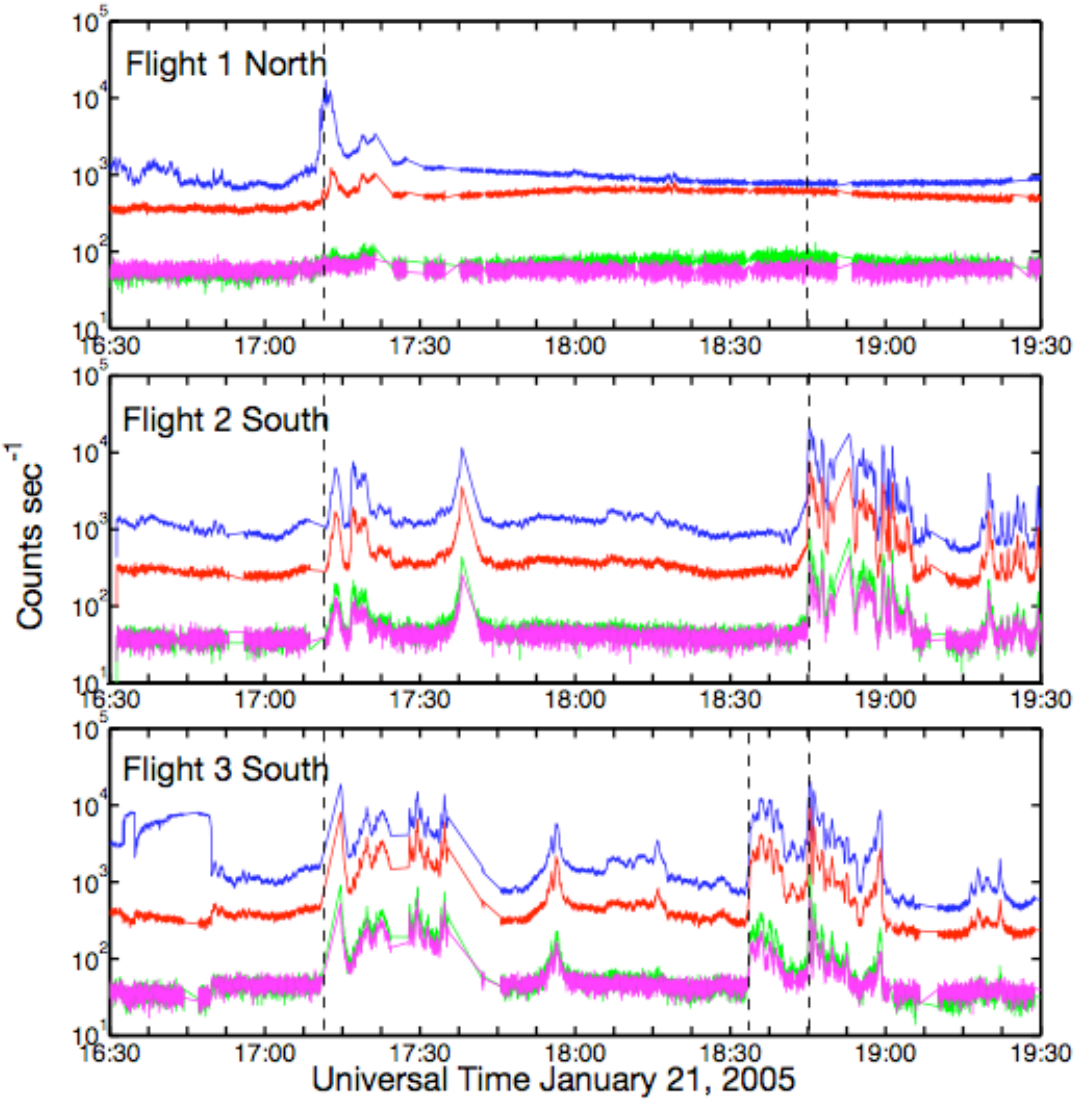

Figure 6.2.1 MINIS high time-resolution x-ray counts from three different balloons. Data from Flight 1 North (top), Flight 2 South (middle) and Flight 3 South (bottom) are shown. There are four energy channels shown in blue (20-175 keV), red (175-540keV), green (540-825keV) and magenta (825-1500keV). Each channel was sampled 20 times per second. The two vertical dashed lines indicate general earth arrival times of the two impulses at 17:12 UT and 18:45 UT. In the bottom panel, there is an extra line at 18:33 UT marking the beginning of a precipitation interval at Flight 3 South only.

Figure 6.2.2 shows high energy-resolution spectra from each MINIS flight between 17:10 UT and 17:50 UT on January 21st [adapted from *Sample et al.,* 2008]). The inset has colored squares at the two southern balloon locations (Flight 2 South in red; Flight 3 South in blue) as well as the location magnetically conjugate to Flight 1 North (green).

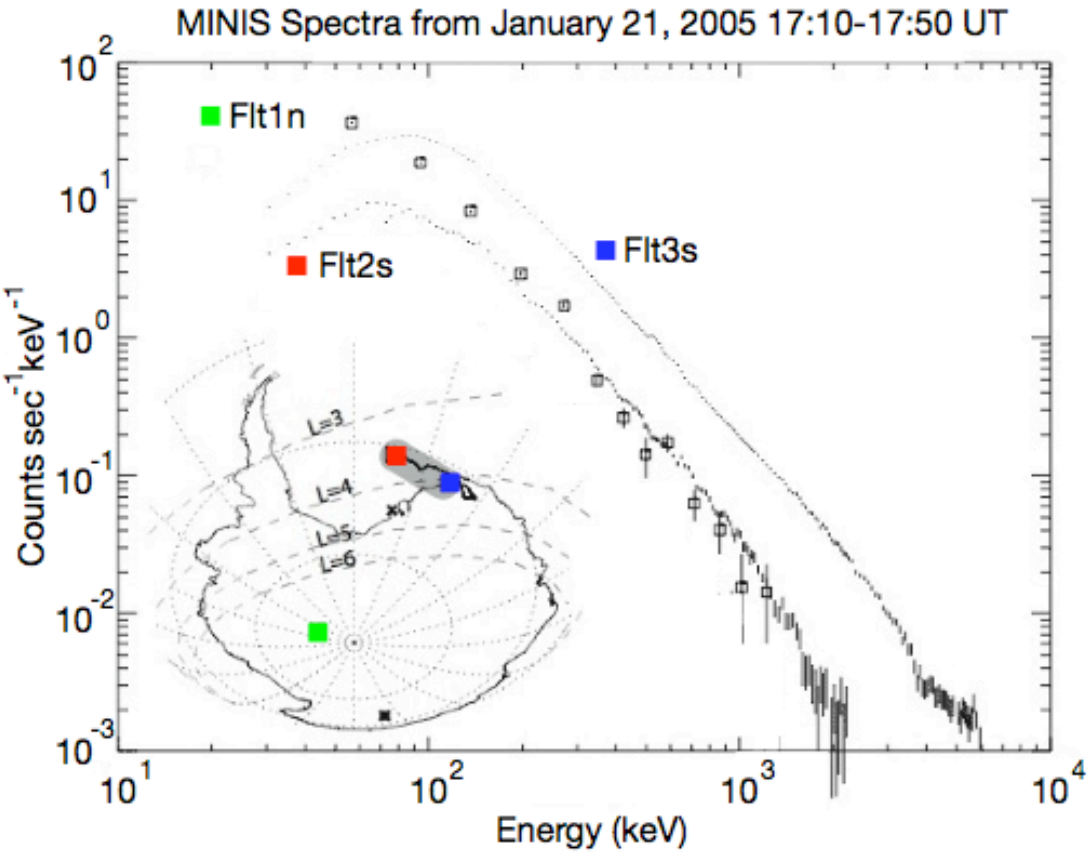

Figure 6.2.2 MINIS observed x-ray spectra for Flight 1 North, Flight 2 South and Flight 3 South between 17:10 UT and 17:50 UT on January 21st, 2005. The locations of the two southern balloons are marked by red (Flight 2 South) and blue (Flight 3 South) squares. The point magnetically conjugate to Flight 1 North is marked by a green square. The spectrum of Flight 1 North is shown by open squares and the two southern payload spectra are simple lines. The total flux is greater for Flight 3 South. [Adapted from *Sample et al.*, 2008]).

Table 6-1 Calculated incident REP spectra parameters for Flight 2 South and Flight 3 South between 17:12 UT and 18:55 UT.

Payload	Time range (UT)	Mono-E (keV)	E-folding (keV)	>500 keV flux for exp. fit	Flux at mono-energetic
Flt 2 S	17:12-17:38	2800	830	1277	400
Flt 3 S	17:14-18:00	----	1500	2180	---
Flt 2 S	18:44-19:09	2700	800	5760	1100
Flt 3 S	18:33-18:41	---	780	8650	---
Flt 3 S	18:44-18:55	---	820	6000	---

The spectrum from Flight 1 North is shown by squares, while simple lines mark Flight 2 South and Flight 3 South. The spectrum from Flight 3 South has a greater flux than Flight 2 South. Modeling efforts by J. Sample and other MINIS team members using a method based on *Smith et al.* [*1995*], have produced incident electron flux spectra for the various REP intervals. The basic framework of the model is to assume an incident electron spectral shape and flux and then propagate the electrons through a model atmosphere. The GEANT Monte-Carlo code [*Allison et al.,* 2006] is used to process the bremsstrahlung x-rays through the remaining atmosphere and a payload-detector mass model. Varying the angular distribution of the x-rays was found to be of only minor importance. (See *Sample, et al.* [2008] and *Sample* [2008] for a detailed description of this work.) The result of this effort for the two southern payloads is outlined in Table 6-1.

Again, we focus on the two southern payloads because they both made electric field observations, which we discuss later. Table 6-1 gives the payload name, time range over which the spectra is modeled and characteristics of the incident spectra. Each of the REP event spectra fit well to exponential models (see error estimates below). Two of the events (beginning at 17:12 UT and 18:45 UT) at Flight 2 South, however, were also fit well by mono-energetic electron spectra. We are less confident in the mono-energetic spectra. The two balloons each observe REP onset near simultaneously 17:12 UT and 18:45 UT, suggesting that the two balloon payloads are observing the same precipitation event [*Sample et al.*, 2008]. There is no mono-energetic spectrum fit for Flight 3 South observations at 17:12 UT and 18:44 UT. Since we believe that both balloon payloads are observing the same large REP event, we lean towards the exponential fit to the spectra. The exponential differential spectra, f, are fit to the following form:

$$f = f_0 e^{-\frac{E}{E_0}} \ (electrons\, cm^{-2}\ s^{-1}\ keV^{-1}). \qquad \textbf{(6-4)}$$

Here, E is the electron energy, E_0 is the e-folding energy and f_0 is a constant determined

by the total flux. The error in the e-folding energy is +/- 50 keV. The low energy cutoffs for these model fits are not well defined. To the best of our knowledge, the cutoff is between 100 keV and 200 keV. Below this energy, the incident electron flux may not follow Equation (6-4).

6.2.2 Horizontal DC Electric Field Observations

The dc horizontal electric field observations by MINIS Flight 2 South and Flight 3 South in the polar stratosphere are assumed to be indicative of the large-scale potential differences in the ionosphere above. Potential differences in the ionosphere can be mapped out into the magnetosphere because of the extremely high conductivity parallel to

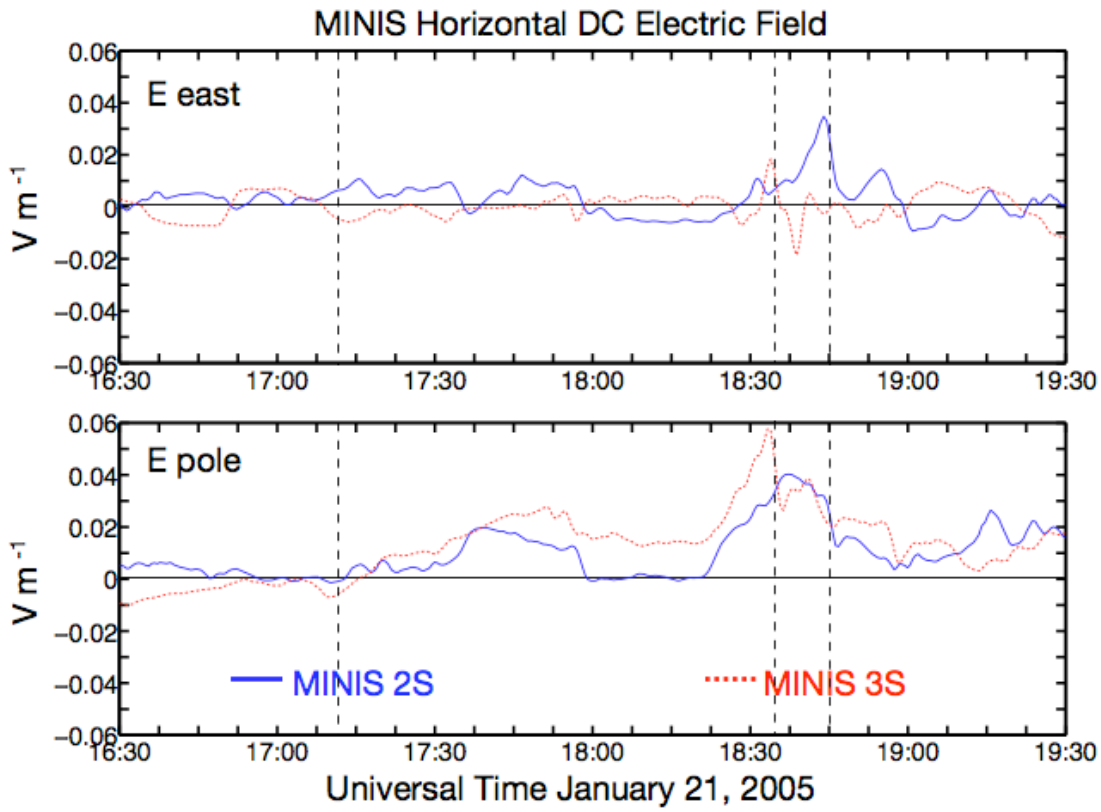

Figure 6.2.3 Horizontal dc electric field observations from MINIS Flight 2 South (blue) and Flight 3 South (red). The top panel shows the eastward component and the bottom panel shows the south poleward component. The two vertical dashed lines indicate general earth arrival times of the two impulses at 17:12 UT and 18:45 UT. Additionally, there is a vertical dashed line at 18:33 UT. This is the same time marked in the bottom panel of Figure 6.2.1.

magnetic field lines. Therefore, by presenting horizontal dc electric field observations, we assume that these potential differences map out into the magnetosphere and the source region for the relativistic electrons that precipitated above the balloon payloads.

Figure 6.2.3 shows the eastward and south poleward components of the horizontal dc electric field measured at MINIS Flight 2 South and Flight 3 South. There are noticeable periods of poleward enhancement after 18:20 UT at both balloons. Flight 3 South data also show a relatively moderate increase following the first impulse arrival at 17:12 UT. There is a period of sustained enhancement in the poleward component at Flight 2 South between 17:33 UT and 17:58 UT. There are rapid decreases in the magnitude of both horizontal components at Flight 2 South (18:45 UT) and Flight 3 South (18:33 UT). These decreases are coincident with periods of rapid-onset REP at each balloon (Figure 6.2.1).

6.2.3 MINIS Field Line Mapping into the Magnetosphere

The final piece of observational data we show are the MINIS balloon locations mapped into the equatorial magnetosphere. We use the IGRF magnetosphere model to trace the field line from the balloon location to the magnetic equator. Figure 6.2.4 shows the mapped equatorial location of MINIS Flight 2 South and Flight 3 South payloads overlaid on an IMAGE EUV picture taken before the first impulse. The EUV green 30.4 nm emission is assumed to be proportional to the integrated line of sight He^+ density. Since the plasmasphere is optically thin to 30.4 nm emission, this assumption should be valid [*Sandel, et al.*, 2000; *Sandel, et al.*, 2001]. He^+ density is then assumed to be a qualitative proxy for the entire plasmasphere based on measurements of He^+ and H^+ [*Horwitz et al.*, 1984; 1990]. Qualitatively, we take the green emission to show where there is cold, dense plasma in the plasmasphere. The green circles indicate one of two things: a) the sharp plasmapause location; or b) a diffuse plasmasphere edge near the low energy threshold. When the green dots are aligned in a tight line (as in the lower and left-hand portion of

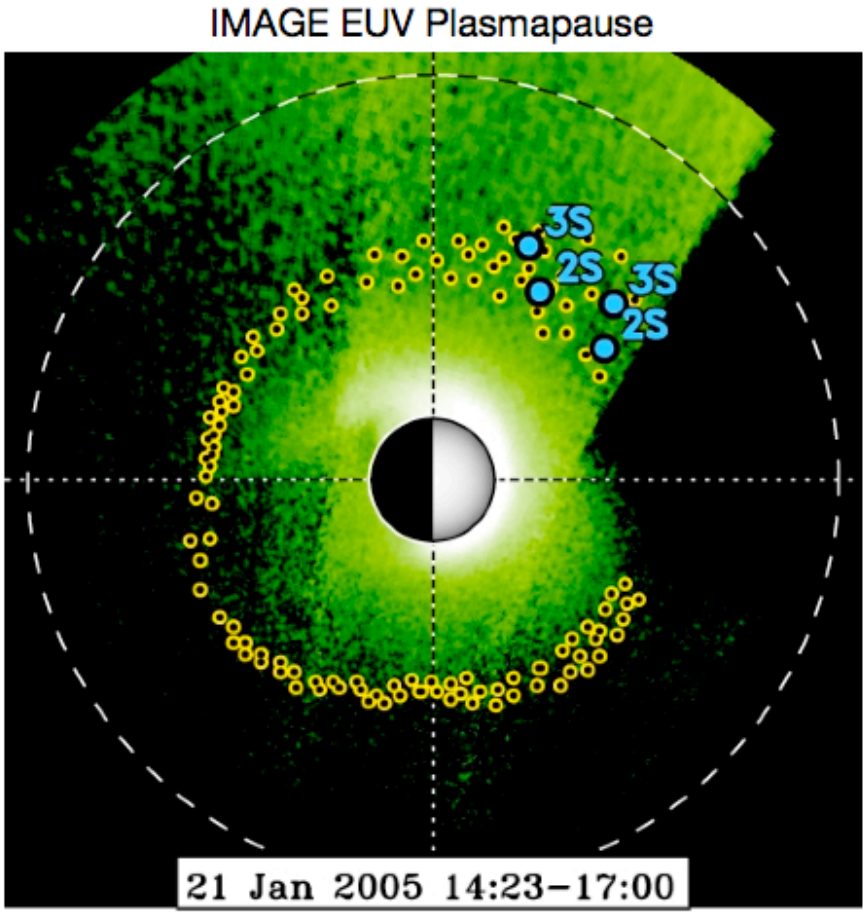

Figure 6.2.4 IMAGE EUV plasmasphere picture taken just before the first compression event. The green circles mark the edge of the cold, dense plasmasphere. MINIS balloon magnetic locations are mapped onto the magnetic equator. [Adapted from *Woodger et al.*, 2005]; IMAGE EUV overlay courtesy of *J. Goldstein*.]

Figure 6.2.4), then there is a sharp boundary. If there is not a sharp boundary (the upper right-hand side of Figure 6.2.4), then the boundary is more diffuse. The lower energy threshold corresponds to ~ 40 electrons cm^{-3}. Each point was found by a semi-automated system administered by J. Goldstein [*Goldstein et al.*, 2003b]. The MINIS payload locations are indicated at the beginning of the exposure (closer to noon) and at the end of the exposure (closer to dusk). We notice that the equatorially-mapped MINIS balloon field lines are in a region where the plasmapause does not have a sharp boundary and is more diffuse. Dusk-side plasmaspheric bulges, as well as the dayside plasmasphere, can erode causing a plasmaspheric plume if the separatrix shifts and cold plasma $\vec{E} \times \vec{B}$

convects sunward. Both of the MINIS balloon payloads are located in afternoon/evening local time during this exposure and during the REP observations. At the time of the IMAGE exposure, the payloads are in a diffuse boundary region. For the case we are investigating, the pressure impulses cause sudden storm commencement compressions. This differs from traditional geomagnetic storm evolution, which generally has a slower onset time. After the impulse-driven magnetic compression events take place, the MINIS field line locations are in a prime spot in the afternoon/evening for the development of an eroding plasmaspheric plume region. (See *Goldstein and Sandel* [2005b] for further discussion on storm-time plume formation and erosion.)

7 Discussion of MINIS Relativistic Electron Precipitation Observations

In this chapter, we discuss the relationship between the MINIS horizontal dc electric field and x-ray observations. We perform a quantitative correlation analysis in Section 7.1, searching for similarities in measurements between MINIS Flight 2 South and Flight 3 South. We find that there is no one-to-one correlation between the electric field and x-ray data at each individual balloon location. In Section 7.2 we use a gyroresonance analysis to place constraints on the magnetospheric plasma waves responsible for the REP observations. We show that hiss and EMIC waves are scattering mechanisms, while chorus are not. We then investigate the extent to which the horizontal dc electric field data can act as an indicator of precipitation mechanisms. We determine that there is a qualitative connection, but that by itself, the electric field is not a robust indicator of electron precipitation. This finding is in agreement with the correlation analysis discussed in Section 7.1.

7.1 Correlation Between Horizontal DC Electric Field and REP Observations

Questions addressed in this section: 1) how well correlated are the MINIS Flight 2 South and Flight 3 South x-ray and horizontal dc electric field observations between 17:00 UT and 19:30 UT; and 2) what can this tell us about the spatial scale size, temporal variability and the global nature of REP events?

Answer summary: There is a moderate, statistically significant (< 5% chance correlation was caused by random noise) correlation between: a) the magnitude; and b) the poleward component of the horizontal electric field observations at Flight 2 South and 3 South (magnitude: R = 0.68, poleward component: R = 0.66). There is only a small statistically significant correlation between x-ray light curve counts from Flight 2 South and Flight 3 South (R = 0.26). There is no correlation between electric field and x-ray counts to speak

of. We determine that the general scale size of REP regions is: a) smaller than the scale size of the electric field; and b) smaller than the 660 km balloon separation. The one exception is directly following the second impulse event, when the x-ray correlation is much larger (R = 0.65). With generally small REP x-ray correlation, multi-point measurements are important for an accurate global observation.

The simultaneous REP observations by MINIS Flight 2 South, Flight 3 South and Flight 1 North are the first multi-point measurements of REP by balloon-borne instrumentation. As such, they present the first opportunity to separate spatial and temporal observational differences. During the observed REP events between 16:30 UT and 19:30 UT on January, 21st, 2005, MINIS Flight 2 South and Flight 3 South were separated by about 660 km. Flight 2 South was at L = 3.5 and Flight 2 South was at L = 4.1. In this section, we examine the correlation between REP events and horizontal dc electric field magnitude and direction. In Section 7.2.2, we examine in more detail what specific horizontal dc electric field measurements imply about precipitation mechanisms. Here, we simply search for statistical correlations between the data sets from each balloon in an effort to judge the reasonability of extrapolating point measurements to larger areas.

In the sub-auroral zone, where the MINIS south balloons were located on January 21st, currents flow into and out of the ionosphere. The spatial scale size of these currents is dynamic and dependent on solar wind forcing and magnetospheric activity. However, auroral arcs and Region 1 and Region 2 currents can all have scale sizes smaller than the balloon separation of 660 km. Therefore, we cannot assume a priori that the horizontal dc electric field observations will be uniform. Scale sizes of REP regions are not well constrained because, until MINIS, there have been no definite measurements that could separate temporal and spatial differences in precipitation. By using a statistical analysis, we can explore correlations between the vector horizontal dc electric field and REP observations at the two southern MINIS balloons.

Table 7-1 Parameters used in horizontal electric field and x-ray light curve correlation study.

	Flight 2 South	Flight 3 South
E east	Ee2	Ee3
E south	Es2	Es3
E magnitude	Em2	Em3
E theta	Et2	Et3
Light Curve channel 1	LC12	LC13
Light Curve channel 2	LC22	LC23
Light Curve channel 3	LC32	LC33
Light Curve channel 4	LC42	LC43

Our analysis compares eight different variables each from MINIS Flight 2 South and Flight 3 South for a total of 16 variables. This produces a total of 256 correlation calculations in a given time period. The variables we compare are listed in Table 7-1 along with their abbreviation used in Appendix E, where the full correlation tables are provided. To perform our analysis, we modified the horizontal electric field and high time-resolution light curve data. We took the one-minute average horizontal dc electric field data from Flight 2 South as our base time series. We took linear interpolations of the Flight 3 South electric field data to match the time markers from Flight 2 South. This has the effect of smoothing the Flight 3 South data slightly by removing the maxima and minima values. Comparisons between the data presented in Figure 7.1.1 with those in Figure 6.2.3 show only minimal perturbation. Then, we took one-minute averages of each of the light curve channels on both flights, again using the time markers from the Flight 2 South electric field data set. A simple visual plotting check was made to ensure that missing data did not appreciably skew the light curve averages. If, at any time, there was missing data or the averages did not appear to capture the nature of the original data in any individual set, that time was removed from all of the data sets. Figure 7.1.1 and Figure 7.1.2 show the data used in our correlation study. Each figure shows the x-ray light curve counts in the top two panels. The lower panels show the geomagnetic components of the horizontal dc electric field (Figure 7.1.1) and the magnitude and direction of the horizontal field

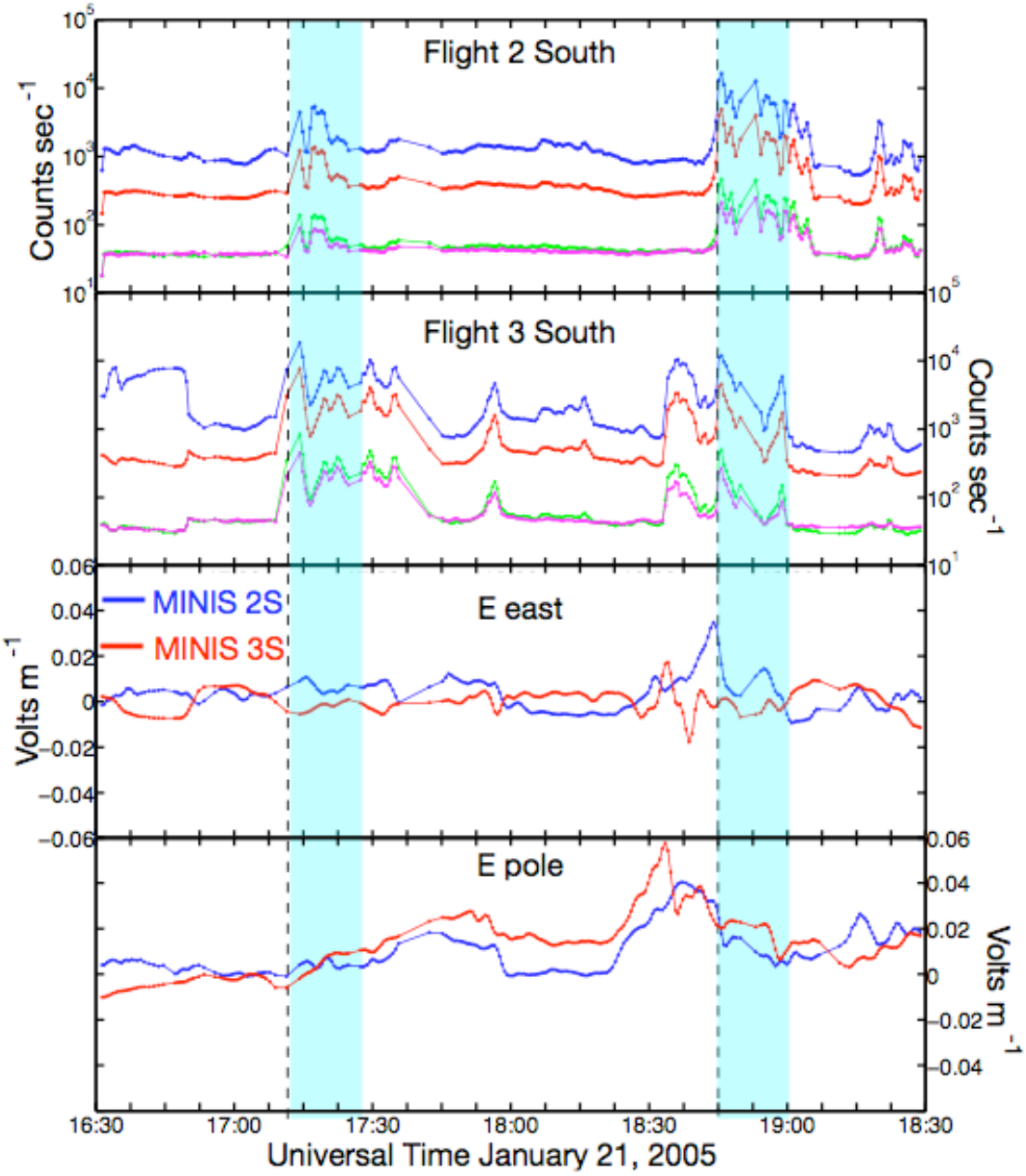

Figure 7.1.1 MINIS light curve and horizontal electric field comparisons. Light curve x-ray data from Flight 2 South (top) and Flight 3 South (second from top). Horizontal electric field from Flight 2 South (blue) and Flight 3 South (red) are shown in the bottom two panels. The third panel shows the eastward components and the bottom panel shows the south poleward components. The vertical dashed lines show the impulse arrival times and the shaded areas mark the time periods 15 minutes after the impulses.

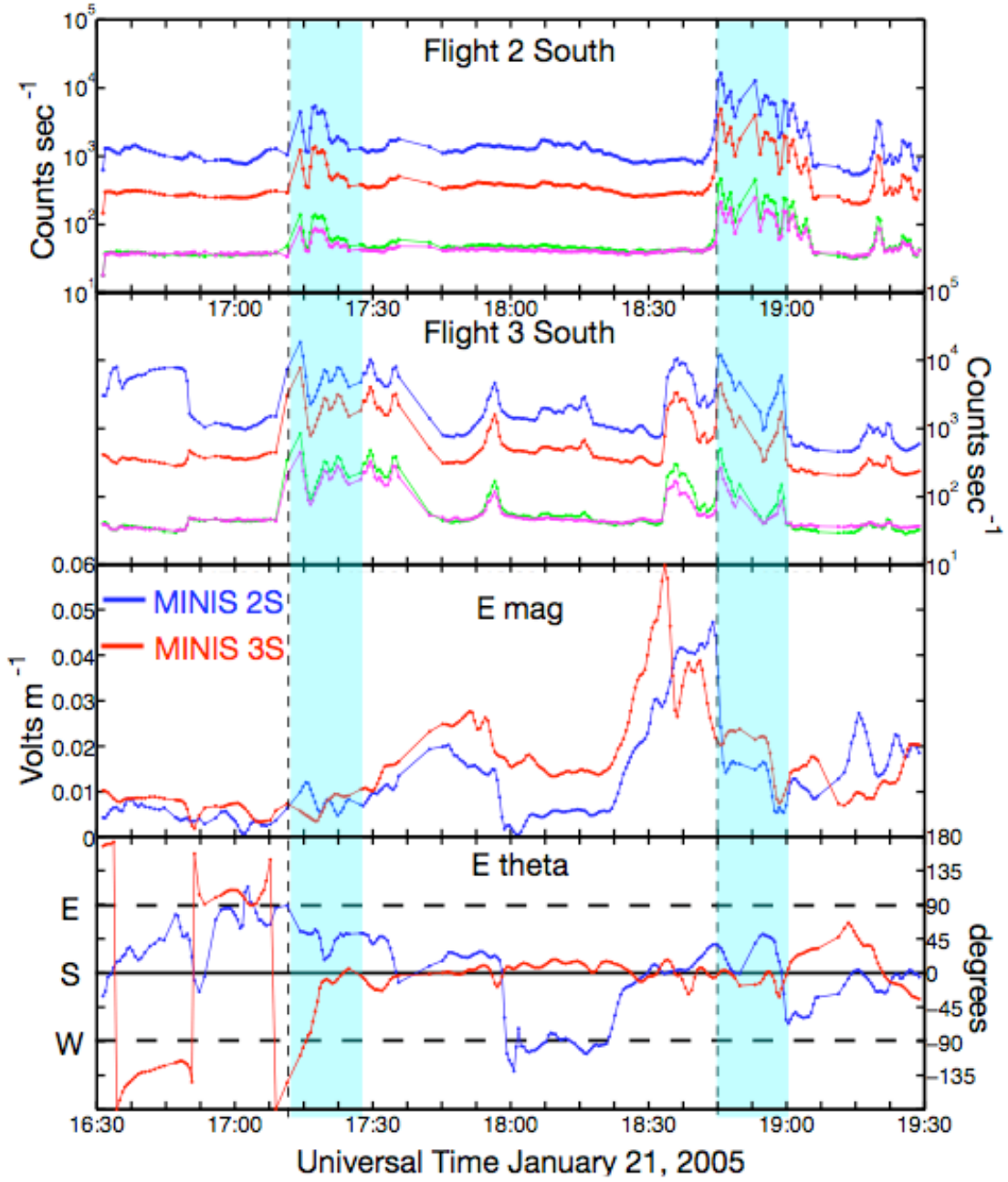

Figure 7.1.2 MINIS light curve and horizontal electric field magnitude and angle comparison. Light curve x-ray data from Flight 2 South (top) and Flight 3 South (second from top). Horizontal electric field from Flight 2 South (blue) and Flight 3 South (red) are shown in the bottom two panels. The third panel shows the electric field magnitude and the bottom panel shows the direction of the electric field. The vertical dashed lines show the impulse arrival times and the shaded areas mark the time periods 15 minutes after the impulses.

Table 7-2 Correlation coefficients for horizontal dc electric field and x-ray light curve observations. Each value has a probability of correlation that is less than 5 percent. The dashed markers indicate where there were no statistically significant correlations made. In the bottom row, N is the number of data points in the correlation calculation. Each correlation involving light curve data is the average of the significant correlations to each light curve channel.

		1700 UT - 1930 UT	1712 UT – 1727 UT (impulse 1)	1845 UT - 1900 UT (impulse 2)	1700 UT - 1930 UT (no impulse 2)
Correlation between Flight 2 South and Flight 3 South	Ee23	-0.33	-0.72	--	-0.33
	Es23	0.66	--	--	0.67
	Em23	0.68	-0.45	--	0.67
	Et23	--	-0.49	--	--
	LC23	0.26	--	0.65	0.21
Flight 2 South only	EeLC2	0.17	--	0.69	-0.14
	EsLC2	--	--	0.60	-0.21
	EmLC2	--	--	0.71	-0.19
	EtLC2	0.14	--	--	--
Flight 3 South only	EeLC3	-0.29	--	--	-0.32
	EsLC3	-0.14	--	--	-0.16
	EmLC3	-0.15	--	--	-0.16
	EtLC3	-0.38	--	--	-0.40
	N	228	20	21	206

(Figure 7.1.2). The vertical dashed lines mark the arrival of the two impulse events at earth. The shaded regions behind each line show a 15-minute period following each of the impulses. We computed the correlation between each variable over several different time periods. We looked at (nearly) the entire time shown in Figure 6.2.1 and Figure 6.2.3 (neglecting data before 17:00 UT because of the abnormal count rate in Flight 2 South light curve channel 1), times directly following the two impulses at 17:12 UT and 18:45 UT and (nearly) the entire time omitting the second impulse. The results are shown in Table 7-2.

From the first column of correlation coefficients show in Table 7-2, we see that there is no consistent connection between the horizontal dc electric field variables and the light

curve variables. We cannot use one as a direct indicator of the other. Indeed, we are only looking at the time period where we already know there is precipitation occurring at both balloons. If we did see a correlation, we would have needed to extend the observation time series to confirm its usefulness. In this case, there is no need. There is a lasting, moderate correlation between the horizontal dc electric field magnitudes (R = 0.68) and southward components (R = 0.66) measured at the two separate balloon locations. The southward component is often nearly equal to the magnitude of the horizontal electric field, so it is expected that the magnitude and southward components have similar correlation coefficients.

There was only a small statistically significant correlation between x-ray light curve counts from Flight 2 South and Flight 3 South (R = 0.26). The one exception is directly following the second impulse event when the x-ray correlation is much larger (R = 0.65). From this, we determine that the general scale size of REP regions was: a) smaller than the scale size of the electric field; and b) smaller than the 660 km balloon separation. Since the impulse events are expected to affect the magnetosphere on large scales, it is not surprising that there is a greater correlation directly after the second impulse at 18:45 UT. It is unfortunate that the correlation statistics following the first impulse at 17:12 are too poor to make a similar (or counter) statement. The notion that the impulses affect large areas and may be the trigger for very large-scale particle precipitation is in agreement with VLF ionosphere observations reported by *Clilverd et al.* [2007]. However, if we ignore the impulse event, we see that the correlation between x-ray counts at Flight 2 South and Flight 3 South is even smaller (R = 0.21). Since REP is thought to be such an important loss mechanism for energetic radiation belt electrons, the generally small REP x-ray correlation insists that multi-point measurements are vital for accurate global observations.

7.2 Placing Constraints on MINIS-Observed REP Mechanisms

Question addressed in this section: assuming wave-particle interactions are the dominant mechanism responsible for the MINIS-observed REP events, can we place reasonable constraints on which type of waves were responsible?

Answer summary: We use a simple analysis to place constraints on which types of plasma waves are responsible for the MINIS-observed REP from a gyroresonance perspective. We find that: a) chorus emissions are unlikely candidates; b) hiss waves are likely to be responsible for precipitation of < 1MeV electrons; and c) EMIC waves may cause some precipitation > 1 MeV. However, these results are based on general estimates of the plasma density and assume that pitch angle scattering occurs only at the equator, leaving large uncertainties. We examine a method for estimating the equatorial number density using the MINIS horizontal dc electric field data and find that this method is not very robust and is currently limited to qualitative analysis.

7.2.1 Wave-Particle Interactions From a Gyroresoance Perspective

In order to gain a complete understanding of energetic particle dynamics, specifically loss terms, it is important to know what physical mechanisms are responsible for any loss observations. Wave-particle interactions leading to rapid pitch angle scattering and drift losses to the magnetopause are the two main loss mechanisms for energetic electrons in the radiation belts. Of these, only wave-particle leads to precipitation and atmospheric loss. There have been numerous studies to date which have examined different wave-particle interactions including whistler chorus [e.g., *Lorentzen, et al.*, 2001; *O'Brien et al.*, 2004; *Meredith et al.*, 2003], plasmaspheric hiss [e.g., *Thorne et al.*, 1973; *Lyons and Thorne* 1973; *Albert*, 1994], EMIC waves [e.g., *Thorne and Horne*, 1997; *Jordanova et al.*, 1998] and balloon observations of precipitation [e.g., *Foat et al.*, 1998 *Lorentzen et al.*, 2000; *Millan et al.*, 2002]. Even with all of this effort, there is not a complete understanding of REP processes. Our goal in the following discussion is to see what

Table 7-3 Summary of general wave characteristics for likely responsible for REP.

	Chorus	***Hiss***	***EMIC***
energy source	*e^- cyclotron resonance with anisotropic 10-100 keV electrons injected from the plasmasheet near midnight* [4,12]	*evolution of chorus waves*[1]*, e^- cyclotron resonance with anisotropic 10-100 keV electrons injected from the plasmasheet near midnight* [4]	*anisotropic, low energy (~kev) H^+ from the ring current*[3]
frequency	*0.05 $\|\Omega_e\|$ - 0.8 $\|\Omega_e\|$* [13]	*100 Hz – several kHz* [10]	*0.1 – 5.0 Hz* [2]
local time	*~2300 – 1300* [6,12]	*all* [10]	*dusk side plasmapause and drainage plume* [2,3,10]
L - shell *(quiet)*	*> 6* [6,8]	*< 6* [7]	
(active)	*> 3* [6,8]	*< 3* [7]	

1. Bortnik et al. [2008]
2. Fraser et al. [1996]
3. Jordanova et al. [2001]
4. Kennel and Petschek [1966]
5. Meredith et al. [2004]
6. Meredith et al. [2001]
7. Parrot and Lefeuvre [1986]
8. Santolik et al. [2005]
9. Smith et al. [1974]
10. Summers et al. [2007]
11. Thorne et al. [1974]
12. Tsurutani and Smith [1977]
12. Tsurutani and Smith [1974]

horizontal dc electric field information can add to our understanding of REP processes, not to provide a completely unique explanation of the MINIS balloon observations.

Here we briefly define the general characteristics associated with each class of plasma wave expected to be responsible for some cases of REP, including whistler mode chorus and hiss as well as electromagnetic ion-cyclotron (EMIC) waves. All of these waves are circularly polarized electromagnetic waves that propagate parallel to the base magnetic field. It is possible to have some off-parallel propagation, but for the simplest case, we assume that there is no perpendicular component to the propagation. Chorus and hiss rotate in a left-handed sense with respect to the magnetic field whereas EMIC waves are right-handed. Chorus emissions are repeated, narrow band pulses of VLF, which is strongest outside the plasmasphere. Hiss, a broadband VLF emission, generally occupies the entirety of the plasmasphere and can also be observed in dense drainage plumes. EMIC waves are found in a narrow region of the dusk side plasmapause and again in drainage plumes. Table 7-3 summarizes some wave properties of chorus, hiss and EMIC waves. This summary gives a basic idea of what plasma waves are responsible for REP at

various local times, L – shells and geomagnetic conditions.

Each type of wave must satisfy the gyroresonance condition in order to interact with energetic electrons. The basic condition for a wave to exchange energy with a particle is

$$\omega - k_{\|} v_{\|} = \frac{n\Omega_s}{\gamma}; \quad \gamma = \left(1 - \frac{v^2}{c^2}\right)^{-\frac{1}{2}}. \tag{7-1}$$

Here, ω is the wave angular frequency, $k_{||}$ is the wave vector parallel to the magnetic field line, $v_{||}$ is the particle velocity along the field line, n is an integer harmonic number, Ω_s is the particle gyrofrequency and γ is the Lorentz factor. In this simple case, we assume waves are propagating parallel such that $k_{\|} = k$.

The dispersion relations for right and left-handed circularly polarized electromagnetic waves are given by the following expressions [from *Krall and Trivelpiece*, 1973]:

$$\begin{aligned} k_R &= \frac{\omega}{c}\left(1 - \frac{\omega_p^2}{\omega(\omega - \Omega_e)}\right)^{\frac{1}{2}} \\ k_L &= \frac{\omega}{c}\left(1 - \frac{\omega_p^2}{\omega(\omega + \Omega_e)}\right)^{\frac{1}{2}} \end{aligned} \tag{7-2}$$

Here, ω_p is the plasma frequency and Ω_e is the electron cyclotron frequency. These dispersion relationships assume that ions are infinitely massive compared to electrons. We can make a substitution and include a useful parameter α^*, such that

$$\begin{aligned} k_R &= \frac{\omega}{c}\left(1 - \frac{1}{\alpha^*}\frac{\Omega_e^2}{\omega(\omega - \Omega_e)}\right)^{\frac{1}{2}} \\ k_L &= \frac{\omega}{c}\left(1 - \frac{1}{\alpha^*}\frac{\Omega_e^2}{\omega(\omega + \Omega_e)}\right)^{\frac{1}{2}} \end{aligned} \tag{7-3}$$

where

$$\alpha^* = \frac{\Omega_e^2}{\omega_{pe}^2} = \frac{\left(\frac{eB}{m_e}\right)^2}{\left(\frac{ne^2}{m_e\varepsilon_0}\right)} = \frac{\varepsilon_0 B^2}{m_e n}. \qquad \textbf{(7-4)}$$

Here, B is the magnetic field, m_e is the mass of an electron and n is the electron number density. In more complete theoretical studies, which include a cold plasma composed of multiple ion species, it has been shown that the resonance condition in Equation (7-4) can be met only if $\alpha^* \leq 0.02$ [*Summers et al.*, 2007a; 2007b and references therein]. This provides a limit on the gyroresonance condition in terms of two measurable parameters B and n.

Using the α^* limit on the gyroresonance conditions, we attempt to eliminate possible wave mechanisms responsible for the MINIS observed REP events by building a simple model. Figure 7.2.1 shows the parameter α^* as a function of equatorial L-shell for various electron densities assuming a dipole magnetic field. The two vertical dashed lines mark the estimated MINIS balloon field lines. In the shaded area below about $\alpha^* = 0.02$, there is a chance for resonant energy transfer. We show multiple number density contours because we do not know the number density at the magnetic equator along the field lines mapped to the MINIS payloads. Chorus emissions, which exists outside the plasmasphere where there is a low ($n < 30$ cm^{-3}) plasma density, are not expected to undergo significant gyroresonance until $L > 5$. This is an indicator that chorus emissions are not causing the REP observed by MINIS. We are left with hiss and EMIC waves as the two remaining possibilities.

The Lorentz factor in Equation (7-1) introduces an energy dependence to the resonance condition. We apply minimum energy arguments in attempt to eliminate either hiss or EMIC waves as possible mechanisms that caused the MINIS-observed REP. *Summers et al.* [2007a] show that there is a minimum energy resonance for hiss waves given by:

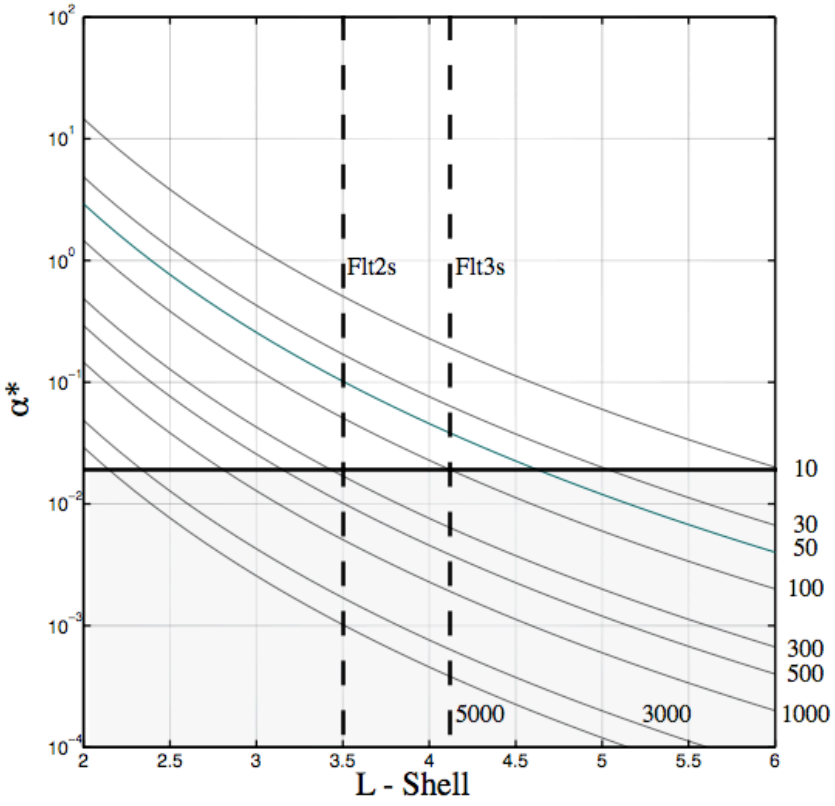

Figure 7.2.1 α^* as a function of L-shell on the magnetic equator assuming a dipole magnetic field for various plasma number densities. Curves for varying density between 10 cm^{-3} and 5000 cm^{-3} are shown. The horizontal line is near the maximum α^* suitable for gyroresonance. The vertical dashed lines are the approximate L-shells for MINIS Flight 2 South and Flight 3 South between 16:30 UT – 19:30 UT on January 21st, 2005.

$$E_{\min} = \left[1 - \frac{(v_{||})_{\min}^{\ 2}}{c^2}\right]^{-1/2} - 1, \qquad \textbf{(7-5)}$$

where $v_{||}$ is the component of particle velocity parallel to the magnetic field and c is the speed of light. *Summers et al.* [2007b] provide examples of E_{min} in the several to tens of keV range. EMIC waves, on the other hand, have a much higher minimum resonant energy. For $\alpha^*= 0.01$, *Summers and Thorne* [2003], show that E_{min} for a gyroresonant electron is near 1 MeV. From minimum energy considerations, only hiss waves can interact with electrons and cause REP in the hundreds of keV range, EMIC waves cannot. Both MINIS Flight 2 South and Flight 3 South observed REP events consistent with exponential spectra that include hundreds of keV electrons. Therefore, is appears that

hiss has to be contributing to the REP observations, while EMIC waves may or may not cause precipitation at higher energies (> 1 MeV).

7.2.2 Qualitative Usefulness of Horizontal DC Electric Field

We have IMAGE plasmasphere exposures from a few hours before the MINIS REP events. From this data, we can extract the location of either the sharp plasmapause boundary or identify diffuse edges of the plasmasphere. However, we do not have the same information during the REP events because the IMAGE spacecraft was not near the apogee of its orbit and could not take an exposure. Here we show that we can get a qualitative idea of how the boundary moves by using electric field drift velocity data.

Here we examine the local time and L-shell locations of the MINIS balloons with respect to where we expect to see chorus, hiss and EMIC plasma waves. The top two panes in Figure 7.2.2 show cartoon schematics [based on Figure 21 of *Summers et al.*, 2007b] for the distribution of these waves for: (Case A) a compressed plasmasphere; and (Case B) during the development of a plasmaspheric plume. The plasmapause locations were taken from IMAGE data during the appropriate conditions and the wave regions are assumed based on observational studies. The equatorial location of magnetic field lines that map to MINIS Flight 2 South (blue square) and Flight 3 South (red square) at 17:12 UT and 18:45 UT on January 21st, 2005 are also shown. Clearly, the geomagnetic activity and the location of the plasmasphere are important when trying to determine which wave is likely to cause REP observations. In the lower portion of Figure 7.2.2, we show a rotated view of the IMAGE-observed plasmasphere from Figure 6.2.4 and a schematic of the plasmapause location. The MINIS balloons are within the shaded gray region. This region represents a gradual slope in cold plasmasphere density in a dusk-afternoon plasmaspheric bulge. The cold, dense plasmasphere is radially inward from the balloon-mapped field line locations. Eastward and outward of the balloon-mapped field lines the plasma density drops. There is no information to the west. The time stamp for

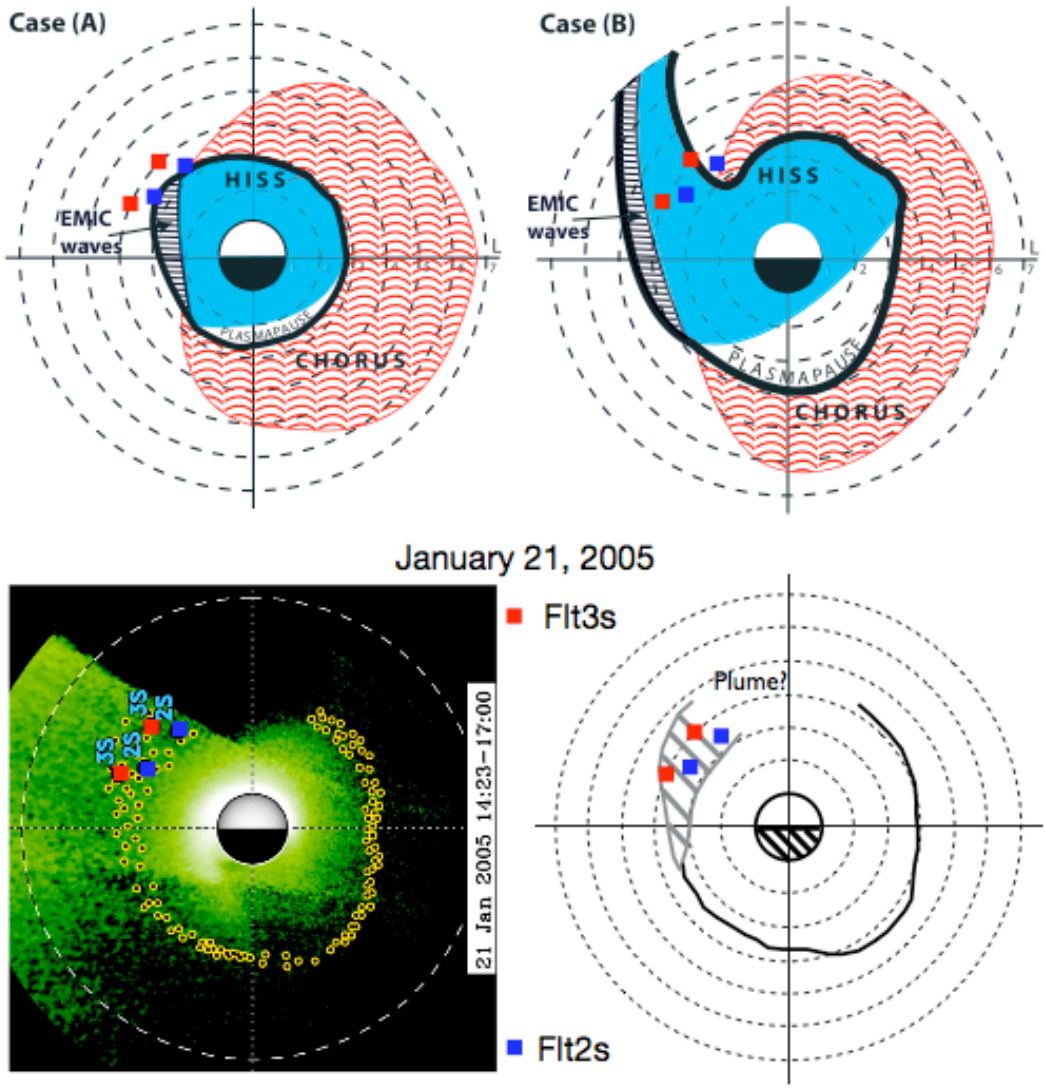

Figure 7.2.2 Regions of the magnetosphere where chorus, hiss and EMIC waves are expected to exist for various conditions. Each panel shows the approximate position of MINIS Flight 2 South (blue square) and Flight 3 South (red square) at 17:12 UT and 18:45 UT on January 21st, 2005. The top two panels are schematics of characteristic magnetospheres [from *Summers et al.*, 2007b]. The top left panel shows a compressed plasmapause during an active geomagnetic period. The top right panel shows a slightly less compressed plasmasphere with a large drainage plume. The bottom left panel shows an IMAGE view of the plasmasphere and plasmapause just before MINI-observed REP. The bottom right shows the MINIS locations and the plasmapause location.

the IMAGE observation (14:23 UT to 17:00 UT) is slightly before the MINIS REP observations (17:12 UT to 19:30 UT). Essentially, the exposure represents the baseline plasmasphere before any compression events. To investigate what happens over the next

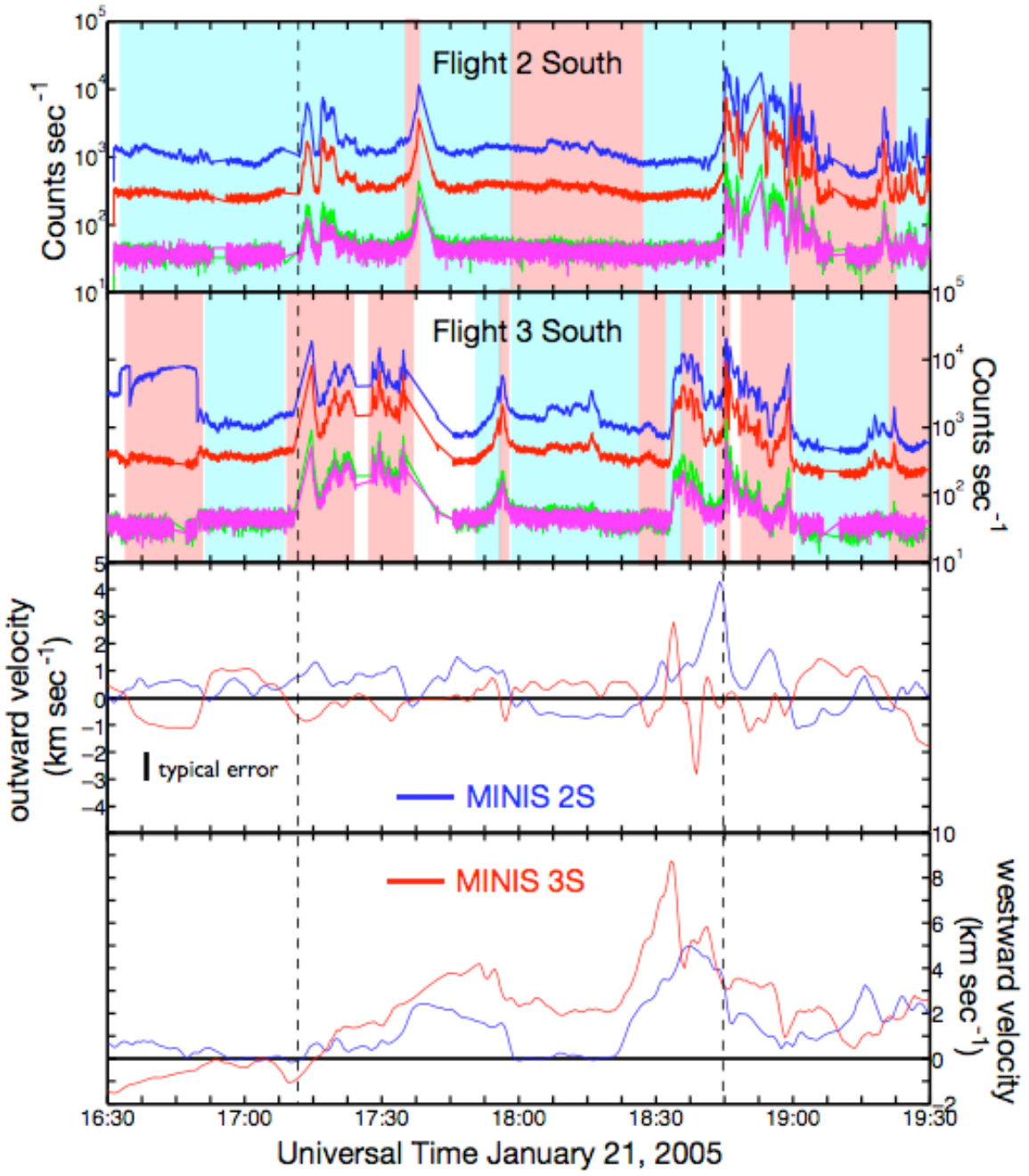

Figure 7.2.3 MINIS light curve and electric field data comparison with outward and inward bulk plasma motion highlighted**.** MINIS Flight 2 South (top) and Flight 3 South (second from top) REP x-ray data as shown in Figure 6.2.1. The bottom two panels show the outward (third panel from top) and westward (bottom) drift velocities at the equator of the field lines, which the balloons are on estimated from the horizontal electric field data. The shaded regions show times when plasma flow has a component outward (blue) and inward (red). The vertical dashed lines mark the arrival time of the impulses at 17:13 UT and 18:45 UT).

few hours when there is no IMAGE exposure (because of spacecraft location), we use the horizontal dc electric field data to get an estimate for the movement of cold dense plasma after the IMAGE plasmasphere picture was taken. Figure 7.2.3 shows MINIS Flight 2 South and Flight 3 South REP x-ray data in the top two panels and estimated equatorial drift velocities for cold plasma on the same field lines as the balloon payloads. The shaded regions show when there is a drift component radially inward (blue) or outward (red). There is no one-to-one correlation between the electric field and the REP observations as we showed in Section 7.1. From Figure 7.2.3, we can get a qualitative idea of the direction the cold plasma is moving in the equatorial magnetosphere along the MINIS balloons' field lines. The mean drift velocities between 17:15 UT and 19:30 UT for equatorial plasma mapped to Flight 2 South was 1.5 km s^{-1} westward and 0.4 km s^{-1} outward. For Flight 3 South the velocities were 2.3 km s^{-1} westward and 0.05 km s^{-1} outward. Looking at the bottom right panel of Figure 7.2.2, we can see that radially outward drift will move cold, dense plasmasphere plasma toward higher L-shells. Westward drift should eventually move the balloon-mapped locations to regions of lower density as the plasmaspheric bulge erodes. With this analysis, but without knowing the density upstream in the drifting plasma, we can only add a refined qualitative intuition characterizing plasma parameters.

The horizontal dc electric field data set, by itself, is not sufficient to determine what the plasma parameters are along magnetic field lines mapped to the MINIS balloon locations. All we can realistically glean is a sense of the plasma drift direction, not a quantitative measure of plasma parameters.

8 Conclusion and Future Work

In this section, we recap the work presented in this thesis and then highlight areas where future efforts could be placed. We examine the advancements made in the areas of atmosphere-ionosphere conductivity modeling, SEP precipitation effects on the coupled atmosphere-ionosphere electrodynamics and the relationship between stratospheric electric field and REP observations.

8.1 A Global Conductivity Model

In Chapter 3, we discussed the theory behind conductivity in the collisional atmosphere and the ionosphere. From this theory, we built a global conductivity model based on a combination of density, composition and temperature from several other models that are not specific to electrodynamics. We used the MSISE-90 model for neutral atmosphere parameters, the IRI model for ionospheric temperature and density, the IGRF model for magnetic field and the Sodankylä Ion Chemistry (SIC) model for atmospheric ion and electron abundances. One of the main advantages of the SIC model is the ability to include effects from precipitating particles into its ion chemistry computations. The work presented in this thesis is the first time the SIC model has been applied directly to conductivity. Other space physics applications related to precipitation-induced ionization have recently been made [e.g., *Clilverd et al.*, 2005; 2007]. Thus, the SIC model is beginning to evolve into a more universal tool for space physics applications. With the appropriate parameters, calculating conductivity, in and of itself, is not difficult. The hard part is to ensure that the parameters used are as accurate as possible. Thus, much of the work presented in this thesis has dealt with how to handle particle precipitation in the best ion chemistry model available.

In light of the relatively recent application to precipitation effects on the electrical and chemical atmosphere and lower ionosphere, we examined several areas for improving/expanding how the SIC model handles precipitation. Specifically, we looked at

A) using polar orbiting satellite instead of geosynchronous measurements of energetic protons for incident flux estimates, B) the applicability and error estimation associated with a piece-wise construction of a differential incident proton spectrum and C) the addition of including ionization from precipitating relativistic electrons. These modifications could be built into future version of the SIC model.

Currently, the SIC model uses GOES geosynchronous measurements of energetic protons to estimate the flux incident on the polar atmosphere during SEP events. We compared the flux measurements from the polar-orbiting POES satellites to those made by GOES. There are several advantages to using the POES data set. They sample various L-shells in rapid succession, providing insight on the geographical extent of the precipitation region. Also, they sample the proton spectrum much closer (< 1000 km) to the precipitation region itself as opposed to the inferring the flux spectrum from 6.7 R_e away, providing a degree of confidence in the incident particle spectrum. However, there are some disadvantages to using POES as opposed to GOES proton observations. Since POES satellites cross each polar cap once during a 90-minute orbit, a significant period of time is spent not observing SEP proton flux. This problem is curtailed with multiple spacecraft, but there is no constant, uniform coverage like that received with GOES measurements. The energetic particle sensors on GOES have better energy resolution than those on POES. Multiple instruments on POES cover a similar energy range as a single instrument on GOES (down to 1 MeV). However the instruments on POES have different look angles and responses, making interpretation much more difficult. Assumptions about the proton pitch-angle distribution must be made in order to generate differential flux spectra. Limitations can be placed on the angular distribution based on magnetic mirroring altitudes, but there is no intrinsic measure of the distribution function on GOES or POES. In the end, using POES instead of GOES energetic proton data would be useful in certain situations. POES would be better for analysis of latitude-dependent studies and in any cases where proton flux at geosynchronous is not expected to be similar to the flux

incident on the polar caps – SEP events with a high fluence of low energy (<1 MeV) protons for example.

The current method for changing the integral proton spectrum measured at GOES into a differential spectrum does not allow for a good estimate of the error associated with the transformation. The differential spectrum relies on several two-point fits to and exponential curve. If the measured spectrum does not fit the assumed spectrum, discontinuities appear. Directly after the January 20th, 2005 SEP event, these discontinuities were as large as two orders of magnitude. Our alternative method assumes that the entire SEP spectrum has to fit an exponential decay curve, as was the assertion by *Freier and Webber* [1963]. With this approach, we can use the multiple points to get some measure of the goodness of fit statistics as well as avoid any discontinuities. However, this is only one alternative. It is impossible to avoid the intrinsic problem of limited integral flux data points without changing the spacecraft instrumentation.

The last modification to precipitation input to the SIC model suggested is the addition ionization due to of precipitating electrons. Although ionization from proton precipitation has been included in the SIC model already, energetic electrons have not yet been added. One of the difficulties in adding relativistic electron effects is the lack of incident electron spectra. The MINIS balloon x-ray dataset provides us with a measurement-based estimation of incident electrons. Using on a method described by *Rees* [1989], we developed an REP-induced ionization model that produces ionization rate profiles given an incident precipitating electron spectrum. For the MINIS observations, it appears that the REP-induced ionization rate is much smaller than the background. It may be possible to apply this model to future electron precipitation events after some validity tests are run.

8.2 Effects of the January 20th, 2005 Solar Energetic Particle Event on the Coupled Magnetosphere-Ionosphere-Atmosphere

In Chapter 4, we presented particle and field data from various sources during a large solar flare (X 7.1) and an extremely hard SEP event on January 20th, 2005, which resulted in the largest GLE since 1956 [*Bieber et al.*, 2005]. We presented solar activity as well as solar wind and magnetospheric conditions to place the events on January 20th, into context. Within this context, we presented the effects on the electrical environment from the point of view of the MINIS balloon observations. These effects include an increase in electrical conductivity and a vanishing of the dc electric field in the polar stratosphere. In Chapter 5, we looked at what physical mechanisms are responsible for the MINIS observations during the SEP event. We present a summary of the results below.

1) Precipitating SEP protons were the dominant source of ionization, and therefore conductivity enhancement, in the polar stratosphere on January 20th, 2005. We took the MINIS Flight 2 South conductivity observations, and compared them with our SIC-driven conductivity model that includes SEP proton precipitation. We showed that there is good agreement between the data and model at balloon altitude. Based on our conductivity model, we show that the maximum conductivity enhancements are centered near 45 km altitude and that there is essentially no enhancement higher than 80 km altitude.

2) The vanishing of the vertical dc electric field at SEP event onset is consistent with enhanced local conductivity and a constant (or slowly varying) fair-weather current density. One of two subsequent rapid vertical jumps (at 13:56 UT, but not at 15:54 UT) can be explained with the same mechanisms. However, the final jump was accompanied with an electric field direction reversal, which is not consistent with shorting the fair-weather return electric field. We present a plausibility example of SEP-induced charge separation that could account for a field direction reversal. For an SEP-induced, upward-

pointing quasi-static field plausibly to reasonably explain a vertical field reversal, the characteristic relaxation time would need to be on the order of 100 seconds or more.

3) Vanishing of the horizontal electric field at SEP onset cannot be explained by SEP-induced enhanced conductivity in the ionosphere. Applying our conductivity model, we find that there is no significant conductivity increase near 120 km at an ionospheric source altitude. There is no evidence to suggest an enhanced electron precipitation, which could possible affect the ionospheric conductivity, coincident with SEP event onset. It is possible that lower-altitude sources heavily influence the MINIS horizontal electric field measurements on January 20th, 2005. We present a plausibility argument that is consistent with the MINIS observations of vanishing lower-altitude sources.

8.3 Relativistic Electron Precipitation and Ionospheric Electrodynamics During the January 21st, 2005 Storm Sudden Commencement

In Chapters 6 and 7, we discuss the MINIS-observed REP and examined the electric field data for physical connections and insight into the precipitation mechanism(s) responsible. Fast moving CME plasma caused a two-step impulsive solar wind dynamic pressure observed at earth beginning at 17:11 UT and 18:45 UT on January 21st, 2005. These impulses resulted in rapid compression of the magnetosphere and a storm sudden commencement (SSC). With three MINIS balloons aloft in the dusk side polar stratosphere (although only two had electric field instrumentation), we observed bremsstrahlung x-rays from relativistic electron precipitation (REP) coincident with these impulse events. Additionally, for several hours after the first impulse arrival REP observations were made at both southern payloads. We presented data describing the impulse events and SSC in the solar wind and within the magnetosphere. Then, we presented the MINIS x-ray and electric field observations. Last, we discussed specific questions, which fall under the larger umbrella: what is the relationship between the horizontal dc electric field and the REP events observed by MINIS? Specifically, we 1)

examined the correlation between the x-ray and electric field measurements at the two southern balloons and 2) presented the minimal quantitative value of horizontal dc electric field observations for identification of typical REP wave-particle precipitation mechanisms. This case study is the first to look multi-point REP and the relationship to stratospheric horizontal dc electric field. Fortunately, we observed REP in coincident with sudden compression events as well as REP that occurred more than an hour after a compression event. REP not associated with a compression event may represent a more typical observation mainly because sudden compressions are not frequent. There have been multiple previous balloon REP observations associated with geomagnetic storm and substorm activity and no previous compression-related measurements.

1) We preformed a correlation analysis comparing the x-ray and horizontal dc electric field observations at the two southern MINIS balloon payloads between 17:00 UT and 19:30 UT on January 21st, 2005. There was a moderate, statistically significant correlation between the magnitude and poleward component of the horizontal electric field observations at Flight 2 South and 3 South (magnitude: R = 0.68, pole: R = 0.66). There was only a small statistically significant correlation between x-ray light curve counts from Flight 2 South and Flight 3 South (R = 0.26). There was no correlation between electric field and x-ray counts to speak of. We determine that the general scale size of REP regions was A) smaller than the scale size of the electric field and B) smaller than the 660 km balloon separation. The one exception is directly following the second impulse event, where the x-ray correlation is much larger (R = 0.65). With generally small REP x-ray correlation, multi-point measurements are important for an accurate global observation.

2) Horizontal dc electric field observations, on their own, cannot conclusively narrow REP wave-particle mechanisms to any single wave type. The horizontal electric field data does not provide sufficient constraints that can conclusively determine what the plasma parameters are along magnetic field lines mapped to the MINIS balloon locations.

All we can realistically glean is a sense of the plasma drift direction, not a quantitative measure of plasma parameters.

8.4 Future Work

8.4.1 Particle Precipitation and Energetic Photon Additions to the SIC Model

As outlined in Section 8.1, we have made cases for several modifications to the way that particle precipitation is included as an ionization source for the SIC model. Already, the SIC model has a huge advantage in that it includes precipitation effects at all. The suggestions made here might help with some of the rough edges. We have not presented a methodology for how to include effects of energetic photon ionization effects into the SIC model. However, we do suggest that the effects of solar flare-related energetic photon enhancement may cause conductivity near 120 km to decrease. As of this writing, there are efforts underway by researchers at the Sodankylä Geophysical Observatory to add flare radiation effects. If a version of the SIC model becomes freely distributed, then a full, stand-alone conductivity model could be made. This full model would be able to calculate a conductivity profile at any fair-weather location at any time and include precipitation effects. The custodians of the SIC have significantly improved the model over the past 20 years and will hopefully continue to expand the usefulness of this incredible tool.

8.4.2 Conductivity Modeling of Multiple SEP Events.

In this thesis, we have presented a single case study of SEP effects on electrical conductivity for the January 20th, 2005 event. Although similar stratospheric electric field data sets during SEP events are rare, two other data sets do exist from a large event in August 1974 and a shorter, softer event in February 1984 [*Holzworth and Mozer*, 1979; *Holzworth*, 1981; *Holzworth et al.*, 1987]. The total fluence of 1-100 MeV protons was more than an order of magnitude larger during the August 1974 SEP event then it was for the January 2005 event discussed in this text. However, the January, 2005 event had a much harder spectrum, such that there were more >200 MeV protons [*Mewaldt, et al.*,

2005]. During the August 1974 event, the horizontal electric field did not immediately disappear as they did at MINIS Flight 2 South. Earlier, we concluded that the SEP protons did not cause a conductivity increase at 120 km and therefore were not responsible for vanishing horizontal dc electric field on January 20th, 2005. Would application of our new conductivity model using energetic proton data from August 1974 produce consistent results? Would our model suggest a conductivity increase only below ~80 km?

During the short, soft February 1984 SEP event, there were two balloons aloft at different latitudes. One balloon payload (-56.3° invariant latitude) measured a local conductivity enhancement from precipitating particles, the other (-48.8° invariant latitude) did not. We could use these data to test rigidity cut-off models which depend on magnetospheric activity like the one presented by *Rodger et al.* [2006]. We can use our new conductivity model and satellite proton flux measurements to determine the rigidity cutoff at the poleward balloon location and see how well it matches with the model prediction.

8.4.3 Comparison of Plasmasphere Models with Long-Duration Balloon Horizontal DC Electric Field

Recently, there has been an increased focus on plasmasphere dynamics [e.g., *Burch et al.*, 2001; *Sandel et al.,* 2001; *Goldstein et al.*, 2003a]]. Many of the advances have stemmed from imaging from the (now defunct) IMAGE spacecraft. Plasmaspheric plume development and erosion are areas of particular interest. *Goldstein and Sandel* [2005b] provide an example of observation and modeling of one particular erosion event. The model used was a plasmapause test particle (PTP) simulation, similar to those which had previously been used to model plasmaspheric dynamics [*Grebowsky*, 1970; *Chen and Wolf*, 1972]. These models can output plasmapause location as a function of time. If the cold, dense plasmaspheric particle are E x B drifting , then we should be able to connect the plasmapause movement to electric fields that are mapped into the middle-high latitude

ionosphere. Horizontal stratospheric dc electric field observations from long-duration balloons could provide ground-truth to plasmasphere models.

There are two ideal data sets which could be used to test a PTP plasmasphere model. The IMAGE data set has been used for these kinds of simulations in many cases. Fortunately there was (at least) one long-duration balloon campaign with dc electric field instrumentation that overlaps with the IMAGE spacecraft lifetime. The Polar Patrol Balloon (PPB) campaign had three payloads that flew in the southern hemisphere during early 2003. PPB horizontal dc electric field could be analyzed in combination with IMAGE data to test a PTP model's accuracy.

8.4.4 Stratospheric Current Density Fluctuations During an SEP-Induced Vertical DC Electric Field Decrease and Conductivity Increase

The effect of SEP events on the large-scale Global Electric Circuit (GEC) remains largely unstudied. There have only been three balloon-borne vertical dc electric field observations made during an SEP event. The calculated change in current density during each event varies dramatically. Thus, there is no established standard for expected future measurements or the general effect of SEP events on the total GEC. MINIS Flight 2 South observations suggest long timescale (longer than the GEC relaxation time) perturbations to the polar fair weather return current can occur.

As illustrated in Figure 4.2.6, there is an obvious, rapid decrease in the vertical dc electric field measured at MINIS Flight 2 South coincident with the SEP event onset. This is only the second instance a long time-scale decrease in the vertical dc electric field has been observed by balloon-borne instrumentation in the stratosphere in conjunction with a large SEP event. The previous measurement was taken in August of 1974 [*Holzworth and Mozer*, 1979]. The mechanism postulated to describe that observation was that the SEP-induced ionization caused an increase in the local conductivity, which shorted out the fair-weather global electric circuit (GEC) electric field. To within the instrumentation error,

the idea of a slowly varying current density fit with the observations. During the August 1974 SEP event, there was no direct measurement of conductivity near the balloon. Rather, conductivity was inferred from measurements of radiation intensity by an onboard x-ray detector. In a separate instance, a shorter duration (~ 1 hour) SEP event observed by stratospheric balloons with dc electric field and conductivity instrumentation, the vertical current density was shown to change by a factor of 2.25 [*Holzworth et al.*, 1987]. Since that event was both geographically constrained to the polar regions and short lived, significant perturbations to the large scale GEC were not expected or observed.

Utilizing direct observation of both the vertical electric field and conductivity from MINIS Flight 2 South, we apply Ohm's law to see how the vertical current density changed during the January 20th, 2005 SEP event. Over the course of January 20th, 2005, neither the magnitude nor the direction of the current remained constant, varying between +/- 5 pA/m^2. One global study by *Holzworth et al.* [2005] has shown that current density can change on a diurnal cycle by a factor of ~2-3 due to global lightning with a maximum downward field occurring near 18:00 UT. However, factors of five increases, rapid fluctuations and reversals are not consistent with a nominal GEC model.

Based on the GEC leaky capacitor model described by *Chalmers* [1967], if the total GEC current is assumed constant over the timescale of enhanced current density, and if we also assume global thunderstorm activity was not changed by precipitating SEPs, then an increased current density near the poles would lead to decreases everywhere else. Both

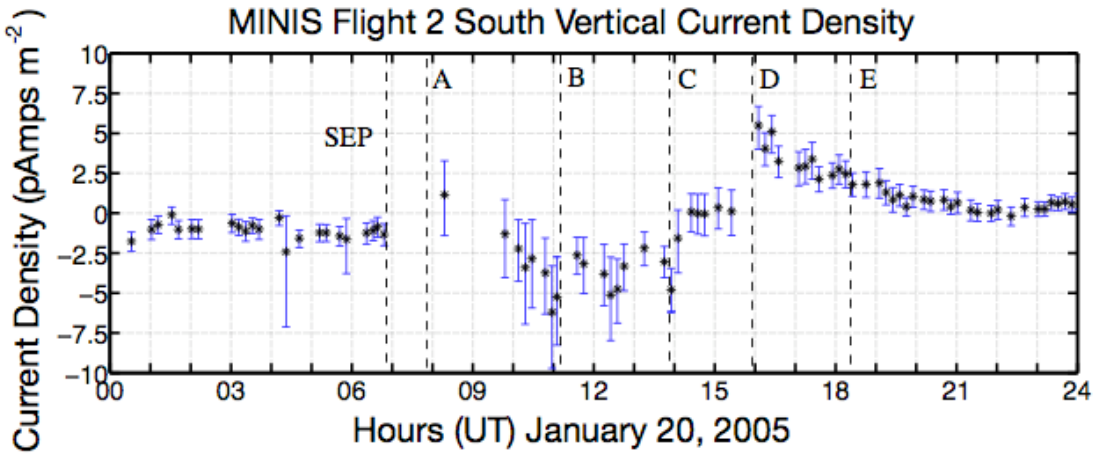

Figure 8.4.1 Vertical current density at MINIS Flight 2 South on January 20th, 2005. The top panel shows the entire day, while the lower panel focuses on the first half of the day and the SEP event onset. The error bars come from estimated vertical dc uncertainties and the 95% confidence bounds from the conductivity fitting routine. The vertical dashed lines are at the same times as in previous figures (A – 07:53 UT, B – 11:10 UT C - 13:56 UT, D - 15:54 UT and E - 18:22 UT).

previous sets of balloon measurements of dc vertical electric field decreases and conductivity enhancements during an SEP event gave no indication of large-scale effects on the GEC. The MINIS Flight 2 South data, on the other hand, show current density perturbations on timescales much longer than the maximum suggested GEC relaxation time of 40 minutes (based on the relaxation of an equivalent circuit). The January 20th, 2005 event could have affected the GEC as a whole and not just the polar regions. If it can be determined that low-latitude current density decreased globally at the same time as high-latitude current density increased during an SEP event, this would lend support to a model of the GEC as a constant current source. However, multi-point measurements (which do not exist for January 20th) are required to add more insight into the possible dynamics of the GEC during such an SEP event. In order to account for the observed magnitude fluctuations, calculations of the total current density changes may need to include current arising from the precipitating SEPs themselves. *Reagan et al.* [1983] suggest that the proton and electron current may be sizable during large SEP events and could, in part, cause an upward vertical current.

References

Albert, J. M. (1994), Quasi-Linear Pitch-Angle Diffusion-Coefficients - Retaining High Harmonics, *J. Geophys. Res-Space Phys.*, *99*, 23741-23745.

Allison, J., Amako, K. Apostolakis, J., et al. (2006), GEANT4 developments and applications, *IEEE Trans. Nuc. Sci.*, 53, 270-278, doi: 10.1109/TNS.2006.869826.

Anderson, B. J., K. Takahashi, and B. A. Toth (2000), Sensing global Birkeland currents with Iridium (R) engineering magnetometer data, *Geophys. Res. Lett.*, *27*, 4045-4048.

Anderson, P. C., W. B. Hanson, R. A. Heelis, et al. (1993), A Proposed Production-Model Of Rapid Subauroral Ion Drifts And Their Relationship To Substorm Evolution, *J. Geophys. Res-Space Phys.*, *98*, 6069-6078.

Bailey, D. K. (1964), Polar-Cap Absorption, *Planet Space Sci.*, *12*, 495-541.

Baker, D. N., J. B. Blake, L. B. Callis, et al. (1989), Relativistic Electrons Near Geostationary Orbit - Evidence For Internal Magnetospheric Acceleration, *Geophys. Res. Lett.*, *16*, 559-562.

Balcewicz, P. T., J. M. Bodeau, M. A. Frey, et al. (1998), Environment on-orbit anomaly correation efforts at Hughes, paper presented at Spacecraft Charging Technology Conference, AFRL-VS-TR-20001578, Air Force Research Laboratory, Hanscom Air Force Base, Massachusetts.

Barnett, J., and M. Corney (1985), Middle atmosphere reference model derived from satellite data, in *Middle Atmosphere Program 16*, edited by K. Labitzke, et al., pp. 47-85, Sci. Comm. for Sol.-Terr. Phys. Secr., Univ. of Ill., Urbana.

Barnum, B., H. (1999), Electromagnetic and optical characteristics of lightning measured in the earth's ionosphere, Ph.D. thesis, Geophysics Program, University of Washington, Seattle, WA.

Berger, M. J., and S. M. Seltzer (1982), Stopping Powers and Ranges of Electrons and Positrons (2nd Ed.), edited, p. 110, U.S. Department of Commerce National Bureau of Standards.

Bering, E. A., J. R. Benbrook, R. Haacke, et al. (1991), The Intense Magnetic Storm Of December 19, 1980 - Observations At L = 4, *J. Geophys. Res-Space Phys.*, *96*, 5597-5617.

Bering, E. A., A. A. Few, and J. R. Benbrook (1998), The global circuit, *Physics Today*, *51(10)*, 24-30.

Bethe, A. H., and J. Ashkin (1953), Passage of Radiations through Matter, in *Experimental Nuclear Physics, vol. 1*, edited by E. Segre, pp. 166-251, John Wiley & Sons, New York.

Bieber, J. W., J. Clem, P. Evenson, et al. (2005), Largest GLE in Half a Century: Neutron Monitor Observations of January 20, 2005 Event, *29th International Cosmic Ray Conference Pune*, *1*, 237-240.

Bilitza, D. (2001), International Reference Ionosphere 2000, *Radio Sci.*, *36*, 261-275.

Bilitza, D., and A. f. R. a. S. World Data Center (1990), *International reference ionosphere 1990*, National Space Science Data Center, World Data Center A for Rockets and Satellites, [Greenbelt, Md.].

Brandt, P. C., J. Goldstein, B. J. Anderson, et al. (2005),
On the Relation Between Electric Fiels in the Inner Magnetosphere, Ring Current, Auroral Conductance, and Plasmapause Motion, in *Inner Magnetosphere Interactions; New Perspectives from Imaging*, edited by J. Burch, et al., American Geophyical Union, Washington D. C.

Burch, J. L. (2000), Image Mission Overview, *Space Science Reviews*, *91*, 1-14.

Burch, J. L., D. G. Mitchell, B. R. Sandel, et al. (2001), Global dynamics of the plasmasphere and ring current during magnetic storms, *Geophys. Res. Lett.*, *28*, 1159-1162.

Byrne, G. J., J. R. Benbrook, E. a. Bering, et al. (1988), Observations of the Stratospheric Conductivity and Its Variation at 3 Latitudes, *J. Geophys. Res.-Atmos.*, *93*, 3879-3891.

Byrne, G. J., J. R. Benbrook, E. A. Bering, et al. (1990), Solar-Radiation (190-230 Nm) In The Stratosphere - Implications For Photoelectric Emissions From Instrumentation At Balloon Altitudes, *J. Geophys. Res.-Atmos.*, *95*, 5557-5566.

Chalmers, J. A. (1967), *Atmospheric Electricity*, 34. pp., Pergamon Press, New York.

Chappell, C. R., K. K. Harris, and G. W. Sharp (1970), A Study Of Influence Of Magnetic Activity On Location Of Plasmapause As Measured By Ogo-5, *J. Geophys. Res.*, *75*, 50.

Chen, A. J., and R. A. Wolf (1972), Effects On Plasmasphere Of A Time-Varying Convection Electric-Field, *Planet Space Sci.*, *20*, 483.

Chisham, G., M. Lester, S. E. Milan, et al. (2007), A decade of the Super Dual Auroral Radar Network (SuperDARN): scientific achievements, new techniques and future directions, *Surveys in Geophysics*, *28*, 33-109.

Clilverd, M. A., C. J. Rodger, R. Gamble, et al. (2008), Ground-based transmitter signals observed from space: Ducted or nonducted? *J. Geophys. Res-Space Phys.*, *113*.

Clilverd, M. A., C. J. Rodger, R. M. Millan, et al. (2007), Energetic particle precipitation into the middle atmosphere triggered by a coronal mass ejection, *J. Geophys. Res-Space Phys.*, *112*.

Clilverd, M. A., C. J. Rodger, T. Ulich, et al. (2005), Modeling a large solar proton event in the southern polar atmosphere, *J. Geophys. Res-Space Phys.*, *110*.

Clilverd, M. A., A. Seppälä, C. J. Rodger, et al. (2006), Modeling polar ionospheric effects during the October-November 2003 solar proton events, *Radio Sci.*, *41*.

Danilov, A. D., A. Y. Rodevich, and N. V. Smirnova (1995), Problems with incorporating a new D-region model into the IRI, *Advances in Space Research*, *15*, 165.

Degenstein, D. A., N. D. Lloyd, A. E. Bourassa, et al. (2005), Observations of mesospheric ozone depletion during the October 28, 2003 solar proton event by OSIRIS, *Geophys. Res. Lett.*, *32*.

Dejnakarintra, M. (1974), A theoretical study of electrical coupling between the troposphere, ionosphere and magnetosphere, Ph.D. thesis, Dept. of Electrical Engineering, Stanford University, Palo Alto, CA.

Delabeaujardiere, O., R. Vondrak, R. Heelis, et al. (1981), Auroral Arc Electrodynamic Parameters Measured By Ae-C And The Chatanika Radar, *J. Geophys. Res-Space Phys.*, *86*, 4671-4685.

Driscoll, K. T., R. J. Blakeslee, and M. E. Baginski (1992), A Modeling Study Of The Time-Averaged Electric Currents In The Vicinity Of Isolated Thunderstorms, *J. Geophys. Res.-Atmos.*, *97*, 11535-11551.

Dungey, J. W. (1961), Interplanetary Magnetic Field And Auroral Zones, *Phys. Rev. Lett.*, *6*, 47-48.

Elkington, S. R., M. K. Hudson, and A. A. Chan (2003), Resonant acceleration and diffusion of outer zone electrons in an asymmetric geomagnetic field, *J. Geophys. Res-Space Phys.*, *108*.

Evans, D. S., and M. S. Greer (2000), Polar Orbiting Environmental Satellite Space Environment Monitor -2: Instrument Descriptions and Archive Data Documentation, edited, NOAA Technical Memoradum, Space Environment Center, Boulder, Colorado.

Feuerbac.B, and B. Fitton (1972), Experimental Investigation Of Photoemission From Satellite Surface Materials, *Journal Of Applied Physics*, *43*, 1563.

Few, A. A., and a. J. Weinheimer (1986), Factor of 2 Error in Balloon-Borne Atmospheric Conduction Current Measurements, *J. Geophys. Res.-Atmos.*, *91*, 937-948.

FMI (2008), IMAGE Magnetometer Network, Finnish Meteorological Institue, http://www.space.fmi.fi/image/index.html, edited.

Foat, J. E., R. P. Lin, D. M. Smith, et al. (1998), First detection of a terrestrial MeV X-ray burst, *Geophys. Res. Lett.*, *25*, 4109-4112.

Forbush, S. E. (1946), Three Unusual Cosmic-Ray Increases Possibly Due to Charged Particles from the Sun, *Physical Review*, *70*, 771-772.

Frederickson, A. R., E. G. Holeman, and E. G. Mullen (1992), Characteristics Of Spontaneous Electrical Discharging Of Various Insulators In Space Radiations, *IEEE Trans. Nucl. Sci.*, *39*, 1773-1782.

Freier, P. S., and W. R. Webber (1963), Exponential Rigidity Spectrums For Solar-Flare Cosmic Rays, *J. Geophys. Res.*, *68*, 1605-1629.

Friedel, R. H. W., G. D. Reeves, and T. Obara (2002), Relativistic electron dynamics in the inner magnetosphere - a review, *J. Atmos. Sol.-Terr. Phys.*, *64*, 265-282.

Friedrich, M., and K. M. Torkar (2001), FIRI: A semiempirical model of the lower ionosphere, *J. Geophys. Res-Space Phys.*, *106*, 21409-21418.

Fujimoto, M., and A. Nishida (1990), Energization And Anisotropization Of Energetic Electrons In The Earths Radiation Belt By The Recirculation Process, *J. Geophys. Res-Space Phys.*, *95*, 4265-4270.

Galand, M., and A. D. Richmond (2001), Ionospheric electrical conductances produced by auroral proton precipitation, *J. Geophys. Res-Space Phys.*, *106*, 117-125.

Goldstein, J., S. G. Kanekal, D. N. Baker, et al. (2005), Dynamic relationship between the outer radiation belt and the plasmapause during March-May 2001, *Geophys. Res. Lett.*, *32*.

Goldstein, J., and B. R. Sandel (2005a), The Global Pattern of Evolution of Plasmaspheric Drainage Plumes, in *Inner Magnetosphere Interactions: New Perspectives form Imaging*, edited by J. Burch, et al., pp. 1-22, American Geophysical Union, Washington D. C.

Goldstein, J., and B. R. Sandel (2005b), The golbal patter of evolution of plasmaspheric drainage plumes, in *Inner Magnetosphere Interactions: New Perspectives from Imaging*, edited by J. L. Burch, et al., pp. 1-22, American Geophysical Union, Washington DC.

Goldstein, J., B. R. Sandel, W. T. Forrester, et al. (2003a), IMF-driven plasmasphere erosion of 10 July 2000, *Geophys. Res. Lett.*, *30*.

Goldstein, J., M. Spasojevic, P. H. Reiff, et al. (2003b), Identifying the plasmapause in IMAGE EUV data using IMAGE RPI in situ steep density gradients, *J. Geophys. Res-Space Phys.*, *108*.

Grebowsky, J. M. (1970), Model Study Of Plasmapause Motion, *J. Geophys. Res.*, *75*, p4329.

GSFC (2008), Community Coordinaged Modeling Center Model Web, http://ccmc.gsfc.nasa.gov/modelweb/, edited.

Hale, L. C., C. L. Croskey, and J. D. Mitchell (1981), Measurements Of Middle-Atmosphere Electric-Fields And Associated Electrical Conductivities, *Geophys. Res. Lett.*, *8*, 927-930.

Hargreaves, J. K. (1992), *The solar-terrestrial environment*, Cambridge University Press, Cambridge, England.

Hawkins, J. (1996), GOES I-M DataBook, edited, Loral Space Systems NASA Goddard Space Flight Center.

Hedin, A. E. (1983), A Revised Thermospheric Model Based On Mass-Spectrometer And Incoherent-Scatter Data - Msis-83, *J. Geophys. Res-Space Phys.*, *88*, 170-188.

Hedin, A. E. (1987), Msis-86 Thermospheric Model, *J. Geophys. Res-Space Phys.*, *92*, 4649-4662.

Hedin, A. E. (1991), Extension Of The Msis Thermosphere Model Into The Middle And Lower Atmosphere, *J. Geophys. Res-Space Phys.*, *96*, 1159-1172.

Hedin, A. E., C. A. Reber, G. P. Newton, et al. (1977a), Global Thermospheric Model Based On Mass-Spectrometer And Incoherent-Scatter Data Msis-2 - Composition, *J. Geophys. Res-Space Phys.*, *82*, 2148-2156.

Hedin, A. E., J. E. Salah, J. V. Evans, et al. (1977b), Global Thermospheric Model Based On Mass-Spectrometer And Incoherent-Scatter Data Msis-1 - N2 Density And Temperature, *J. Geophys. Res-Space Phys.*, *82*, 2139-2147.

Holzworth, R. H. (1981), High-Latitude Stratospheric Electrical Measurements In Fair And Foul Weather Under Various Solar Conditions, *J. Atmos. Terr. Phys.*, *43*, 1115-1125.

Holzworth, R. H. (1989), A New Source Of Horizontal Electric-Fields In The Mid-Latitude Stratosphere, *J. Geophys. Res.-Atmos.*, *94*, 12795-12802.

Holzworth, R. H. (1991), Conductivity And Electric-Field Variations With Altitude In The Stratosphere, *J. Geophys. Res.-Atmos.*, *96*, 12857-12864.

Holzworth, R. H., and E. A. Bering (1998), Ionospheric electric fields from stratospheric balloon borne probes., in *Measurement Techniques for Space Plasmas, Fields*, edited by R. Pfaff, et al., American Geophysical Union, Washington DC.

Holzworth, R. H., E. A. Bering, M. F. Kokorowski, et al. (2005), Balloon observations of temporal variation in the global circuit compared to global lightning activity, in *Planetary Atmospheres, Ionospheres, And Magnetospheres*, edited, pp. 2223-2228, Elsevier Science Ltd, Oxford.

Holzworth, R. H., and R. A. Goldberg (2004), Electric field measurements in noctilucent clouds, *J. Geophys. Res.-Atmos.*, *109*.

Holzworth, R. H., M. C. Kelley, C. L. Siefring, et al. (1985), Electrical Measurements In The Atmosphere And The Ionosphere Over An Active Thunderstorm.2. Direct-Current Electric-Fields And Conductivity, *J. Geophys. Res-Space Phys.*, *90*, 9824-9830.

Holzworth, R. H., and F. S. Mozer (1979), Direct Evidence Of Solar-Flare Modification Of Stratospheric Electric-Fields, *Journal Of Geophysical Research-Oceans And Atmospheres*, *84*, 363-367.

Holzworth, R. H., K. W. Norville, P. M. Kintner, et al. (1986), Stratospheric Conductivity Variations Over Thunderstorms, *J. Geophys. Res.-Atmos.*, *91*, 13257-13263.

Holzworth, R. H., K. W. Norville, and P. R. Williamson (1987), Solar-Flare Perturbations In Stratospheric Current Systems, *Geophys. Res. Lett.*, *14*, 852-855.

Horne, R. B., and R. M. Thorne (2003), Relativistic electron acceleration and precipitation during resonant interactions with whistler-mode chorus, *Geophys. Res. Lett.*, *30*.

Horwitz, J. L., R. H. Comfort, and C. R. Chappell (1984), Thermal Ion Composition Measurements Of The Formation Of The New Outer Plasmasphere And Double Plasmapause During Storm Recovery Phase, *Geophys. Res. Lett.*, *11*, 701-704.

Horwitz, J. L., R. H. Comfort, P. G. Richards, et al. (1990), Plasmasphere-Ionosphere Coupling.2. Ion Composition Measurements At Plasmaspheric And Ionospheric Altitudes And Comparison With Modeling Results, *J. Geophys. Res-Space Phys.*, *95*, 7949-7959.

Hu, H. (1994), Global and local electrical phenomena in the stratosphere, Ph.D. thesis. Geophysics Program, University of Washington, Seattle, WA.

Hu, H., and R. H. Holzworth (1996), Observations and parameterization of the stratospheric electrical conductivity, *J. Geophys. Res.-Atmos.*, *101*, 29539-29552.

Hu, H., and R. H. Holzworth (1997), An inertial wave-driven stratospheric horizontal electric field: New evidence, *J. Geophys. Res.-Atmos.*, *102*, 19717-19727.

Hudson, M. K., S. R. Elkington, J. G. Lyon, et al. (2001), Radiation belt electron acceleratio by ULF wave drift resonance: Simulation of 1997 and 1998 storms, in *Space Weather*, edited by P. Song, et al., pp. 289-296, American Geophysical Union, Washington D.C.

Iijima, T., and T. A. Potemra (1978), Large-Scale Characteristics Of Field-Aligned Currents Associated With Substorms, *J. Geophys. Res-Space Phys.*, *83*, 599-615.

Iucci, N., L. I. Dorman, A. E. Levitin, et al. (2006), Spacecraft operational anomalies and space weather impact hazards, *Advances in Space Research*, *37*, 184.

Jackman, C. H., M. T. DeLand, G. J. Labow, et al. (2005a), The influence of the several very large solar proton events in years 2000-2003 on the neutral middle atmosphere, in *Influence Of The Sun's Radiation And Particles On The Earth's Atmosphere And Climate*, edited, pp. 445-450, Pergamon-Elsevier Science Ltd, Kidlington.

Jackman, C. H., M. T. DeLand, G. J. Labow, et al. (2005b), Neutral atmospheric influences of the solar proton events in October-November 2003, *J. Geophys. Res-Space Phys.*, *110*.

Jackson, J. D. (1975), *Classical Electrodynamics*, Wiley and Sons, New York.

JHU/APL (2008), Super Dual Auroral Radar Network, http://superdarn.jhuapl.edu., edited.

Jones, J. B. L., R. D. Bentley, R. Hunter, et al. (2005), Space weather and commercial airlines, *Advances in Space Research*, *36*, 2258-2267.

Jordanova, V. K., C. J. Farrugia, J. M. Quinn, et al. (1998), Effect of wave-particle interactions on ring current evolution for January 10-11, 1997: Initial results, *Geophys. Res. Lett.*, *25*, 2971-2974.

Kahler, S. W., N. R. Sheeley, R. A. Howard, et al. (1984), Associations Between Coronal Mass Ejections And Solar Energetic Proton Events, *J. Geophys. Res-Space Phys.*, *89*, 9683-9693.

Kavanagh, A. J., S. R. Marple, F. Honary, et al. (2004), On solar protons and polar cap absorption: constraints on an empirical relationship, *Ann. Geophys.*, *22*, 1133-1147.

Kellogg, P. J., and M. Weed (1968), Balloon measurements of ionospheric electric fields, paper presented at Fourth International Conference on the Universal Aspects of Atmospheric Electricity, Tokyo.

Kirkwood, S., H. Opgenoorth, and J. S. Murphree (1988), Ionospheric Conductivities, Electric-Fields And Currents Associated With Auroral Substorms Measured By The Eiscat Radar, *Planet Space Sci.*, *36*, 1359-1380.

Krall, N. A., and A. W. Trivelpiece (1973), *Principles of Plasma Physics*, McGraw Hill, New York.

Lay, E. H., R. H. Holzworth, C. J. Rodger, et al. (2004), WWLL global lightning detection system: Regional validation study in Brazil, *Geophys. Res. Lett.*, *31*.

Lemme, P. W., S. M. Glenister, and A. W. Miller (1999), Iridium((R)) - Aeronautical satellite communications, *IEEE Aerosp. Electron. Syst. Mag.*, *14*, 11-16.

Li, X. L., D. N. Baker, M. Temerin, et al. (1997), Multisatellite observations of the outer zone electron variation during the November 3-4, 1993, magnetic storm, *J. Geophys. Res-Space Phys.*, *102*, 14123-14140.

Liu, R. Y., P. A. Smith, and J. W. King (1983), A New Solar Index Which Leads To Improved Fof2 Predictions Using The Ccir Atlas, *Telecommunication Journal*, *50*, 408-414.

Lorentzen, K. R., J. B. Blake, U. S. Inan, et al. (2001), Observations of relativistic electron microbursts in association with VLF chorus, *J. Geophys. Res-Space Phys.*, *106*, 6017-6027.

Lorentzen, K. R., M. P. McCarthy, G. K. Parks, et al. (2000), Precipitation of relativistic electrons by interaction with electromagnetic ion cyclotron waves, *J. Geophys. Res-Space Phys.*, *105*, 5381-5389.

Lyons, L. R., and R. M. Thorne (1973), Equilibrium Structure Of Radiation Belt Electrons, *J. Geophys. Res.*, *78*, 2142-2149.

Markson, R. (1981), Modulation Of The Earths Electric-Field By Cosmic-Radiation, *Nature*, *291*, 304-308.

McCarthy, M., and G. K. Parks (1985), Further Observations Of X-Rays Inside Thunderstorms, *Geophys. Res. Lett.*, *12*, 393-396.

McCracken, K. G. (1962), The Cosmic-Ray Flare Effect: 3. Deductions regarding the Interplanetary Magnetic Field, *J. Geophys. Res.*, *67*, 447-458.

McIlwain, C. E. (1961), Coordinates For Mapping Distribution Of Magnetically Trapped Particles, *J. Geophys. Res.*, *66*, 3681.

McPherron, R. L. (1970), Growth Phase of Magnetospheric Substorms, *J. Geophys. Res.*, *75*, 5592-5599.

Meredith, N. P., R. B. Horne, R. M. Thorne, et al. (2003), Favored regions for chorus-driven electron acceleration to relativistic energies in the Earth's outer radiation belt, *Geophys. Res. Lett.*, *30*.

Mewaldt, R. A., M. D. Looper, C. M. S. Cohen, et al. (2005), Solar-Particle Energy Spectra during the Large Events of October-November 2003 and January 2005., *29th International Cosmic Ray Conference Pune*, *1*.

Millan, R. M., R. P. Lin, D. M. Smith, et al. (2002), X-ray observations of MeV electron precipitation with a balloon-borne germanium spectrometer, *Geophys. Res. Lett.*, *29*.

Mozer, F. S. (1971), Balloon Measurement Of Vertical And Horizontal Atmospheric Electric Fields, *Pure Appl. Geophys.*, *84*, 32-45.

Mozer, F. S. (1973), Analyses Of Techniques For Measuring Dc And Ac Electric-Fields In Magnetosphere, *Space Science Reviews*, *14*, 272-313.

Mozer, F. S., and R. Serlin (1969), Magnetospheric Electric Field Measurements With Balloons, *J. Geophys. Res.*, *74*, 4739-4754.

NASA/GOES (2008), GOES Project, edited, NASA Goddard Space Flight Center, http://goespoes.gsfc.nasa.gov/goes/index.html.

NASA/POES (2008), POES Project, edited, NASA Goddard Space Flight Center, http://goespoes.gsfc.nasa.gov/poes/index.html.

Nishida, A. (1976), Outward Diffusion Of Energetic Particles From Jovian-Radiation-Belt, *J. Geophys. Res-Space Phys.*, *81*, 1771-1773.

NOAA/SEC (2008), ACE Real Time Solar Wind, edited, http://www.swpc.noaa.gov/ace/.

O'Brien, T. P., M. D. Looper, and J. B. Blake (2004), Quantification of relativistic electron microburst losses during the GEM storms, *Geophys. Res. Lett.*, *31*.

Park, C. G., and M. Dejnakarintra (1977a), The Effects of Magnetospheric Convection on Atmospheric Electric Fields in the Polar Cap, in *Electrical Processes in Atmospheres*, edited by H. Dolezalek and R. Reiter, pp. 536-543, Steinkopff-Verlag, Darmstadt.

Park, C. G., and M. Dejnakarintra (1977b), Thundercloud Electric Fields in the Ionosphere, in *Electrical Processes in Atmospheres*, edited by H. Dolezalek and R. Reiter, pp. 544-551, Steinkopff-Verlag, Darmstadt.

Parks, G. K. (1991), *Physics of Space Plasmas*, Westview Press.

Patterson, J. D., T. P. Armstrong, C. M. Laird, et al. (2001), Correlation of solar energetic protons and polar cap absorption, *J. Geophys. Res-Space Phys.*, *106*, 149-163.

Prölss, G. W. (2004), *Physics of the Earth's Space Environment*, Springer, Berlin.

Randall, C. E., V. L. Harvey, C. S. Singleton, et al. (2007), Energetic particle precipitation effects on the Southern Hemisphere stratosphere in 1992-2005, *J. Geophys. Res.-Atmos.*, *112*.

Reames, D. V. (1999), Particle acceleration at the Sun and in the heliosphere, *Space Science Reviews*, *90*, 413-491.

Rees, M. H. (1982), On The Interaction Of Auroral Protons With The Earths Atmosphere, *Planet Space Sci.*, *30*, 463-472.

Rees, M. H. (1989), *Physics and chemistry of the upper atmosphere*, Cambridge University Press, Cambridge [Cambridgeshire]; New York.

Reeves, G. D., K. L. McAdams, R. H. W. Friedel, et al. (2003), Acceleration and loss of relativistic electrons during geomagnetic storms, *Geophys. Res. Lett.*, *30*.

Reid, G. C. (1961), Study Of Enhanced Ionization Produced By Solar Protons During A Polar Cap Absorption Event, *J. Geophys. Res.*, *66*, 4071-4085.

Rodger, C. J., J. B. Brundell, R. L. Dowden, et al. (2004), Location accuracy of long distance VLF lightning location network, *Ann. Geophys.*, *22*, 747-758.

Rodger, C. J., M. A. Clilverd, P. T. Verronen, et al. (2006), Dynamic geomagnetic rigidity cutoff variations during a solar proton event, *J. Geophys. Res-Space Phys.*, *111*.

Rodger, C. J., C. F. Enell, E. Turunen, et al. (2007), Lightning-driven inner radiation belt energy deposition into the atmosphere: Implications for ionisation-levels and neutral chemistry, *Ann. Geophys.*, *25*, 1745-1757.

Rycroft, M. J., S. Israelsson, and C. Price (2000), The global atmospheric electric circuit, solar activity and climate change, *J. Atmos. Sol.-Terr. Phys.*, *62*, 1563-1576.

Sample, J. G., Kokorowski, M., Smith, D. M., et al., (2008), First Observations of MeV Electron Precipitation form Multiple Balloon-Borne Spectrometers, *Geophys. Res. Lett. (Submitted.)*

Sample, J. G. (2008), Ph.D. thesis, Department of Physics, University of California at Berkeley, Berkeley, CA.

Sandel, B. R., A. L. Broadfoot, C. C. Curtis, et al. (2000), The extreme ultraviolet imager investigation for the IMAGE mission, *Space Science Reviews*, *91*, 197-242.

Sandel, B. R., R. A. King, W. T. Forrester, et al. (2001), Initial results from the IMAGE extreme ultraviolet imager, *Geophys. Res. Lett.*, *28*, 1439-1442.

Schield, M. A., J. W. Freeman, and A. J. Dessler (1969), A Source For Field-Aligned Currents At Auroral Latitudes, *J. Geophys. Res.*, *74*, 247.

Seppälä, A., M. A. Clilverd, and C. J. Rodger (2007), NOx enhancements in the middle atmosphere during 2003-2004 polar winter: Relative significance of solar proton events and the aurora as a source, *J. Geophys. Res.-Atmos.*, *112*.

Seppälä, A., P. T. Verronen, V. F. Sofieva, et al. (2006), Destruction of the tertiary ozone maximum during a solar proton event, *Geophys. Res. Lett.*, *33*.

Shprits, Y. Y., R. M. Thorne, R. Friedel, et al. (2006), Outward radial diffusion driven by losses at magnetopause, *J. Geophys. Res-Space Phys.*, *111*.

Shue, J. H., P. Song, C. T. Russell, et al. (1998), Magnetopause location under extreme solar wind conditions, *J. Geophys. Res-Space Phys.*, *103*, 17691-17700.

Siscoe, G. L., G. M. Erickson, B. U. O. Sonnerup, et al. (2002), Hill model of transpolar potential saturation: Comparisons with MHD simulations, *J. Geophys. Res-Space Phys.*, *107*.

Smart, D. F., and M. A. Shea (2001), Comparison of the Tsyganenko model predicted and measured geomagnetic cutoff latitudes, in *Validation Of Magnetospheric Models*, edited, pp. 1733-1738.

Smith, D. M., R. P. Lin, K. A. Anderson, et al. (1995), High-Resolution Spectra Of 20-300-Kev Hard X-Rays From Electron-Precipitation Over Antarctica, *J. Geophys. Res-Space Phys.*, *100*, 19675-19685.

Sonnerup, B. U. Ö., and K. D. Siebert (2003), Theory of the Low Latitude Boundary Layer and Its Coupling to the Ionosphere: A Tutorial Review, in *Earth's Low-Latitude Boundary Layer*, edited by P. T. Newell and T. Onsager, pp. 13-32, American Geophysical Union, Washington D.C.

Spiro, R. W., R. A. Heelis, W. B. Hanson (1978), Ion convection and the formation of the mid-latitude F-region ionization trough, *J. Geophys. Res.*, 83, 4255-4264.

Sternheimer, R. M. (1959), Range-Energy Relations for Protons in Be, C, Al, Cu, Pb, and Air, *Physical Review*, *115*, 137.

Stoker, P. H. (1995), Riometer Absorption Events At Sanae, L=4.0, *Astrophysics And Space Science*, *230*, 405-413.

Stone, E. C., A. M. Frandsen, R. A. Mewaldt, et al. (1998), The Advanced Composition Explorer, *Space Science Reviews*, *86*, 1-22.

Summers, D., B. Ni, and N. P. Meredith (2007a), Timescales for radiation belt electron acceleration and loss due to resonant wave-particle interactions: 1. Theory, *J. Geophys. Res-Space Phys.*, *112*.

Summers, D., B. Ni, and N. P. Meredith (2007b), Timescales for radiation belt electron acceleration and loss due to resonant wave-particle interactions: 2. Evaluation for VLF chorus, ELF hiss, and electromagnetic ion cyclotron waves, *J. Geophys. Res-Space Phys.*, *112*.

Summers, D., and R. M. Thorne (2003), Relativistic electron pitch-angle scattering by electromagnetic ion cyclotron waves during geomagnetic storms, *J. Geophys. Res-Space Phys.*, *108*.

SwRI (2008), Official SwRI IMAGE Mission Web Site, http://pluto.space.swri.edu/IMAGE.

Thomas, J. N. (2005), Lightning-Driven Electric and Magnetic Fields Measured in the Stratosphere: Implications for Sprites, Ph.D. thesis, Earth and Space Science Department, University of Washington, Seattle, WA.

Thomas, J. N., R. H. Holzworth, M. P. McCarthy, et al. (2005), Lightning sferics and stroke-delayed pulses measured in the stratosphere: Implications for mesospheric currents, *Geophys. Res. Lett.*, *32*.

Thomas, L., and M. R. Bowman (1986), A Study of Pre-Sunrise Changes in Negative-Ions and Electrons in the D-Region, *Annales Geophysicae Series a-Upper Atmosphere and Space Sciences*, *4*, 219-228.

Thorne, R. M., and R. B. Horne (1997), Modulation of electromagnetic ion cyclotron instability due to interaction with ring current O+ during magnetic storms, *J. Geophys. Res-Space Phys.*, *102*, 14155-14163.

Thorne, R. M., R. B. Horne, S. A. Glauert, et al. (2005), The influence of wave-particle interactions on relativistic electron dynamics during storms, in *Inner Magnetosphere*

Interactions: New Perspectives form Imaging, edited by J. Burch, et al., pp. 101-112, American Geophysical Union, Washington D. C.

Thorne, R. M., E. J. Smith, R. K. Burton, et al. (1973), Plasmaspheric Hiss, *J. Geophys. Res.*, *78*, 1581-1596.

Tobiska, W. K., T. Woods, F. Eparvier, et al. (2000), The SOLAR2000 empirical solar irradiance model and forecast tool, *J. Atmos. Sol.-Terr. Phys.*, *62*, 1233-1250.

Treilhou, J. P., C. Jacquey, J. Coutelier, et al. (2002), INTERBOA: A balloon project for auroral studies and magnetosphere/ionosphere research, *Scientific Ballooning In The Next Century: Goals And Challenges*, *30*, 1371-1380.

Treilhou, J. P., K. Lorentzen, M. McCarthy, et al. (2000), Hard X-rays and electric field in the subauroral afternoon sector, *Scientific Ballooning*, *26*, 1393-1396.

Turunen, E., H. Matveinen, J. Tolvanen, et al. (1996), D-region ion chemistry model, in *STEP Handbook of Ionospheric Models*, edited by R. W. Schunk, pp. 1-25, SCOSTEP Secretariat, Boulder, Colorado, USA.

Vampola, V. M. (1969), Energetic Electrons at Latitudes above the Outer-Zone Cutoff, *J. Geophys. Res-Space Phys.*, *74*, 1254-1269.

Verronen, P. T. (2006), Ionosphere-Atmosphere Interaction During Solar Proton Events, Ph.D. thesis, Department of Physicical Scienes, University of Helsinki, Helsinki, Finland.

Verronen, P. T., A. Seppälä, M. A. Clilverd, et al. (2005), Diurnal variation of ozone depletion during the October-November 2003 solar proton events, *J. Geophys. Res-Space Phys.*, *110*.

Volland, H. (1984), Atmospheric Electricity, 132-154.

Walker, R. J., and M. G. Kivelson (1975), Energization Of Electrons At Synchronous Orbit By Substorm-Associated Cross-Magnetosphere Electric-Fields, *J. Geophys. Res-Space Phys.*, *80*, 2074-2082.

Wanliss, J. A., and K. M. Showalter (2006), High-resolution global storm index: Dst Versus SYM-H, *J. Geophys. Res.*, *111*, doi:10.1029/2005JA011034.

Wild, J. P., A. A. Weiss, and S. F. Smerd (1963), Solar Bursts, *Annual Review Of Astronomy And Astrophysics*, *1*, p291.

Wilson, C. T. R. (1920), Investigations on lightning discharges and on the electric field of thunderstorms., *Philos. Trans. A*, 73-115.

Wissing, J. M., J. P. Bornebusch, and M. B. Kallenrode (2008), Variation of energetic particle precipitation with local magnetic time, *Advances in Space Research*, *41*, 1274.

Woodger, L. A., R. M. Millan, J. G. Sample, et al. (2005), Investigating EMIC waves as a relativistic electron
precipitation mechanism during the MINIS balloon campaign, abstract #SH23A-0330, paper presented at American Geophysical Union, Fall Meeting 2005, San Francisco, CA.

Wrenn, G. L. (1995), Conclusive Evidence For Internal Dielectric Charging Anomalies On Geosynchronous Communications Spacecraft, *Journal Of Spacecraft And Rockets*, *32*, 514-520.

Wygant, J. R., R. B. Torbert, and F. S. Mozer (1983), Comparison Of S3-3 Polar-Cap Potential Drops With The Interplanetary Magnetic-Field And Models Of Magnetopause Reconnection, *J. Geophys. Res-Space Phys.*, *88*, 5727-5735.

Appendix A: MINIS DC Electric Field Instrument

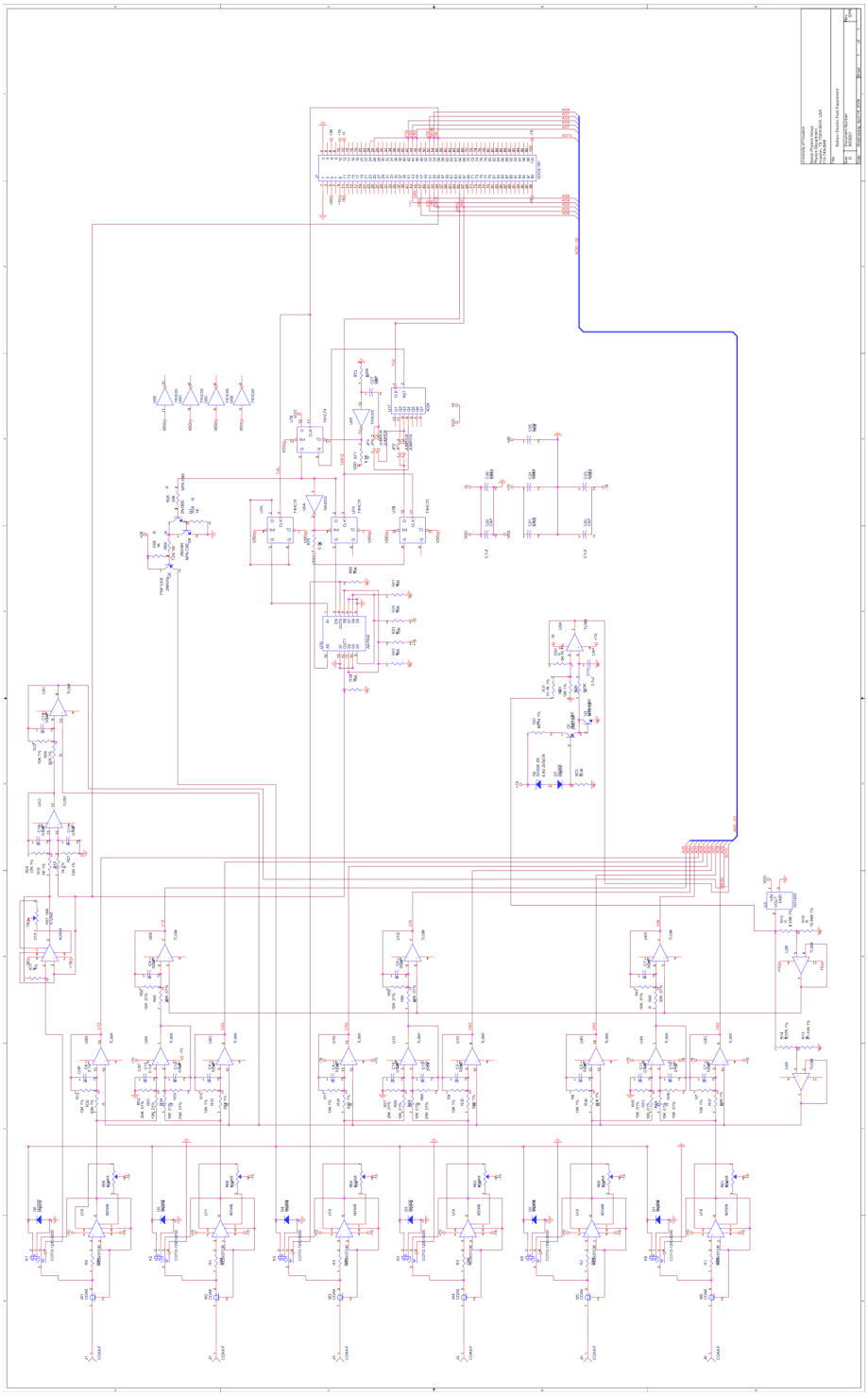

Figure A.1 Full schematic for the MINIS dc electric field circuit.

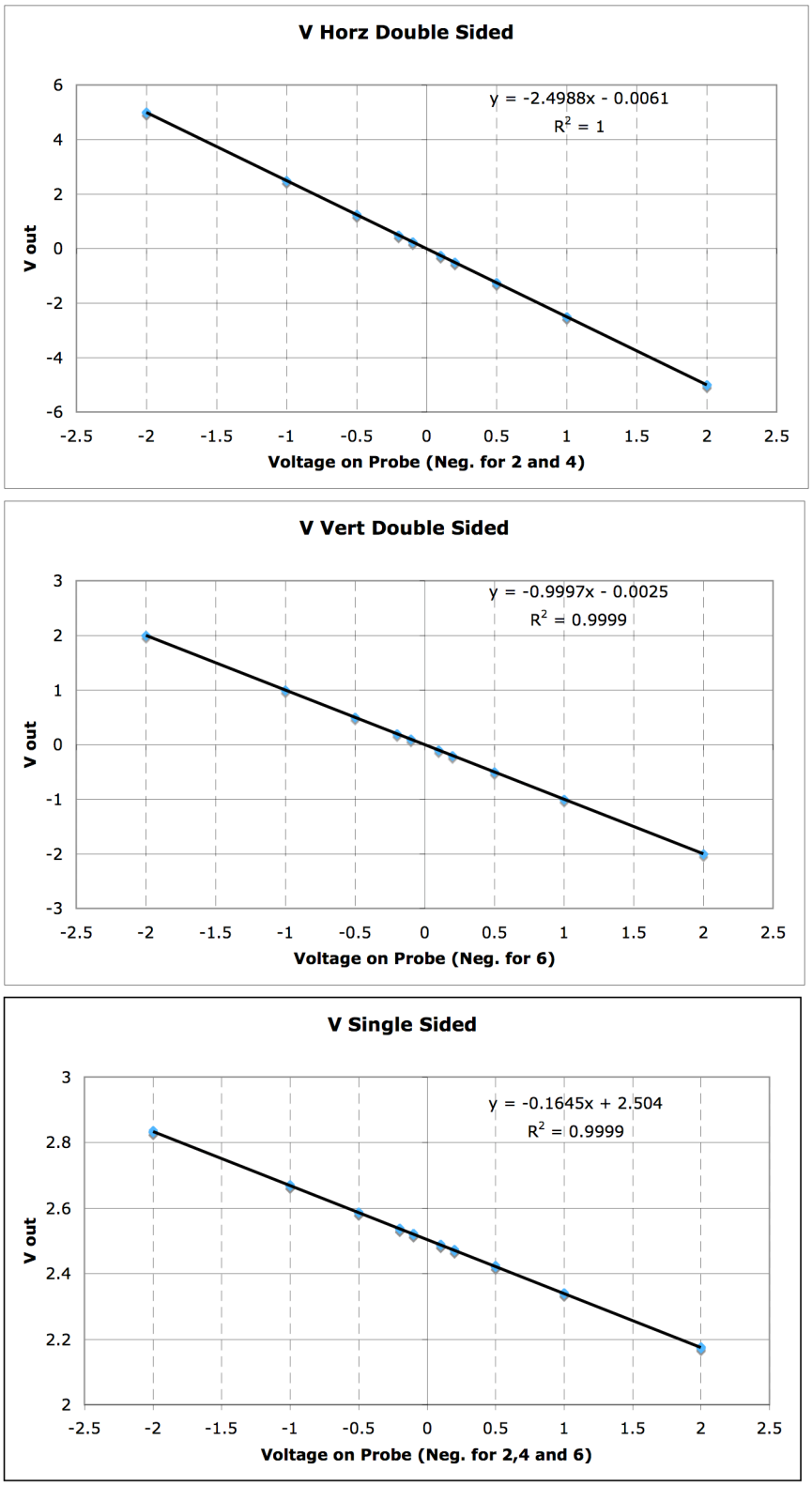

Figure A.2 MINIS dc double and single sided calibration plots. All data taken at room temperature.

Appendix B: MINIS Telemetry Allocation

Table B-1 MINIS telemetry allocation table.

MINIS TELEMETRY ALLOCATION					
Version L / MINIS 2004-5					
11.18.2004 / RWS					
OFFSET	**NBYTES**	**DESCRIPTION**	**DATA TYPE**	**D to A**	**COMMENTS**
0	2	Sync 0xEB90	uint		START
2	2	Frame Counter	uint		Low 15 bits = frame counter; high bit set for CAL CYCLE.
4	4	Time	long		Tick Counter running at 100 Hz.
8	8	4 Sun Sensors	4 uint		0 - 0xFFFF
16	8	4 Thermistors	4 uint	YES	10 mV per degree K. ON EVEN FRAME NUMBERS
16	8	TILT DATA	2 float		TCM_P followed by TCM_R ON ODD FRAME NUMBERS
24	2	Thermistor	1 int	YES	10 mV per degree K. (shielded thermistor)
26	4	HKP INFO	see below		See below
30	4	ENGR INFO	see below		See below
34	4	EF Horiz Axes	2 int	YES	V12, V34 at 1 Hz
34	20	PHOTOMETER DATA	PACKED		20 12-BIT DATA PACKED INTO 30 BYTES (ROBYN FLIGHT ONLY)
38	8	EF Z Axis	4 int	YES	V56 at 4 Hz
46	12	6 Spheres	6 int	YES	V1 - V6 at 1 Hz
58	6	3 Freq VLF	3 int	YES	VLF1, VLF2, VLF3 at 1 Hz
64	6	3 Search Coil	3 int	YES	Single Axis measurements B1, B2, B3
70	4	Bx	float		TCM2 - Bx uT
74	4	By	float		TCM2 - By uT
78	4	Bz	float		TCM2 - Bz uT
82	52	Spectra	uint		208 Channels accumulated for 8 seconds. 52 bytes per frame.
134	120	Lightcurves	uint		2 16-bit channels plus 2 8-bit channels at 20 hz. Channels are grouped as follows: 16BIT: CH0-74, CH75-229. 8BIT:CH230-349 CH350-619. Serial output is ch0low, ch0hi, ch1lo, ch1hi, ch2, ch3.
254	2	N	uint		END Checksum is calculated by starting with zero and sequentially adding contents as 128 unsigned integers. Example where frame counter = 0x01F: EB90 + 01FF = ED8F + NEXT 126 VALUES.
	256				
Multiplex following Hkp information according to low nibble FrameCntr					
Frame%16	**NBYTES**	**DESCRIPTION**			**NOTES**
0	4	GPS X	float		LAT IN RADIANS (+North; -South). See below.
1	4	GPS Y	float		LONG IN RADIANS.
2	4	GPS Z	float		ALTITUDE IN METERS. MSL.

3	4	GPS TIME	long		UTC time of week in seconds.
4	4	computer time	long		UTC in seconds
5	4	EF Therm , Batt+28	int	YES	TBD (ef_therm from Gar), Batt+28 = val*4.3636
6	4	12VA, -12VA	int	YES	val * 2
7	4	5VA, 3.3VGPS	int	YES	val
8	4	Irid5V, FILTER5V	int	YES	val
9	4	Filter-5V, Boom+12	int	YES	val
10	4	Boom+5,Boom-12V	int	YES	val * 2
11	4	SC+12,SC-12	int	YES	val * 2
12	4	PMT+5,PMT-5	uint	YES	
13	4	PMT RATE CNTR1	long		Accumulate rate counters at 20 hz
14	4	PMT RATE CNTR2	long		
15	4	PMT RATE CNTR3	long		

CALIBRATION DATA

Calibration cycle occurs once every 10 minutes. We collect 4 readings at10 Hz. The sequence is as follows: every ten minutes, send CAL PULSE trigger. Wait six seconds. Then start 12 seconds of data acquisition. The total data set fills FOUR FRAMES of 256 bytes each. The calibration data is sent out at each three second period during the 12 second total period. Calibration frames are indicated by the high bit of the frame counter being set. The data format for each calibration data frame is as follows: sync (2 bytes),framecounter(2 bytes), 100 hz tickcounter (4 bytes), three i-mon readings at 1 hz for three seconds (6 bytes), data (V12, V1,V34,V3)(240 bytes for the three second period), checksum (2 bytes). Tickcounter is time when the frame is put together and written to output buffer.

A/D CONVERSION NOTES

Column titled "D to A" indicates whether the value needs conversion to volts. If yes, voltage = Val * 0.000305175 where Val is in two's complement form. Data type for 'val' is signed integer. Voltages that are over 10 volts were scaled down to be within the 0 to 10 volt range. They need to be multiplied by two to show the true value. This applies to +12, -12 etc..

For GPS Radian conversion use pi = 3.1415926535898.

Multiplex following ENGR INFORMATION according to low nibble FrameCntr ie Modulo 16.

Frame%16	NBYTES	DESCRIPTION			NOTES
0	4	computer startup time	long		time when system powered up
1	4	errors, errtype	uint, uint		number of errors, last error type
2	4	nloops, nloops/2	int, int		number of loops, half way couter
3	4	S/W VERSION	float+A1		version number
4 to 15	4	write_ptr, rd_ptr	uint, uint		write pointer location, read pointer location

Appendix C: Model Specifics

IRI Model input parameters used.
January 20, 2005 70 South 345 E geographic

URSI maps are used for the F2 peak density (NmF2)
CCIR maps are used for the F2 peak height (hmF2)
B0-Table option is used for the bottomside thickness parameter B0
Danilov- option is used for the ion composition
The foF2 STORM model is turned on
IRI-95 option is used for the electron temperature
IRI-95 option is used for the D-region Ne
Scotto-97 no L option is used for the F1 occurrence probability
Peak Densities/cm-3: NmF2= 320870.6 NmF1= 0.0 NmE= 58100.6
Peak Heights/km: hmF2= 289.73 hmF1= 0.00 hmE= 110.00

Solar Zenith Angle/degree 77.0
Dip (Magnetic Inclination)/degree 62.83
Modip (Modified Dip)/degree 61.93
Solar Sunspot Number (12-months running mean) Rz12 34.5
Ionospheric-Effective Solar Index IG12 38.5

Appendix D: Electron Ionization Matlab Code

```
function[q] = minis_rep_ionization_rates(disp, e_min, epoch)
%This function will calculate ionization rates as a function of
altitude
%given the minis REP flux spectra.
%
%The inout 'disp' determines the assumed incident REP dispersion.
%1 -> a unidirectional dispersion and 2 -> an isotropic dispersion
%from 0 to xx degrees.
%
%flt_num will either be 2 or 3 flr minis flight 2s and flight 3s
%
%e_min = the minimum electron energy
%
%epoch will determine the specific time and assumed spectrum: from
J.Sample

%                                                    #/cm2/sec
%   1 = flt2s 17:12-17:38 UT  monoenergetic 2.8MeV   400
%   2 = flt2s 17:12-17:38 UT  E-folding     830keV   1277 >500 keV
%   3 = flt3s 17:14-18:00 UT  E-folding     1500keV  2180 >500 keV
%   4 = flt2s 18:44-19:09 UT  monoenergetic 2.7MeV   1100
%   5 = flt2s 18:44-19:09 UT  E-folding     800keV   5760 >500 keV
%   6 = flt3s 18:33-18:41 UT  E-folding     780keV   8650 >500 keV
%   7 = flt3s 18:44-18:55 UT  E-folding     820keV   6000 >500 keV
%
%mkoko Feb 2008


%% Define maximum distributed source angle in degrees
isotropic_max = 60;


%% Load msise-90 atmosphere for desired balloon
%  needs to be changed for appropriate application
%
%  check flight number and load appropriate msise atmos

    path1 = '/Applications/MATLAB7/sepmodel/std_atm.mat';

    if epoch == 1 | epoch == 2 | epoch == 4 | epoch == 5;
        var_name = 'flt2s_msis_200501211800';
    elseif epoch == 3 | epoch == 6 | epoch == 7;
        var_name = 'flt3s_msis_200501211800';
    else
        error('Not a valid flight.  Must be flight 2 or 3.');
    end;

    %load msise-90 atmos_var
    msis = load(path1, '-regexp', var_name);
```

```
    %convert to matrix array
    msis = cell2mat(struct2cell(msis));


%% Load Stopping Power .mat file
%  file location needs to be changed for appropriate application
%
%  define .mat file name
    fn = '/Applications/MATLAB7/minis05/rep_efld/e_stopping_power.mat';

     %load Energy vector (10keV to 1GeV, Range (g/cm^2) and stopping
         power
    %spt = total stopping power and spc =  collision stopping power
    %(MeV cm^2 / g)
    [E]   = load(fn, '-regexp', 'E');
    [R]   = load(fn, '-regexp', 'R');
    [spt] = load(fn, '-regexp', 'spt');
    [spc] = load(fn, '-regexp', 'spc');

    %convert to matrix array
    E   = cell2mat(struct2cell(E));
    R   = cell2mat(struct2cell(R));
    spt = cell2mat(struct2cell(spt));
    spc = cell2mat(struct2cell(spc));


%% Create z-atmospheric depth array
%
    %initialize z atmospheric depth array
    L_msis = length(msis(:,1));
    %z = zeros(L_msis,2);


    %create array of alt(km) and mass density(g/cm^3)
    alt_mass_density = zeros(L_msis,2);
    alt_mass_density(:,1) = msis(:,1);
    alt_mass_density(:,2) = msis(:,5);


    %flip alt_mass_density array
    alt_mass_density_fud = flipud(alt_mass_density);


    %sum mass into units of g/cm^2*km
    alt_mass_sum = alt_mass_density_fud;

    for i = 1:L_msis;
        alt_mass_sum(i,2) = sum(alt_mass_density_fud(1:i,2))*10^5;
    end;


    %define atmospheric depth, Z (gm/cm^2)
    Z = flipud(alt_mass_sum);


%% Flux and Energy
%
```

```
    %Use the MINIS-determined         initial spectra to define energy
flux
    [F0] = flux_energy(e_min, epoch);


%% Energy Deposition and Ionization
%
%This section will calculate the energy deposited in the atmosphere due
%to collisions and estimate the ionization as a function of altitude.
%
%We have two cases, monodirectional(1 degree half-angle cone) and
%isotropic

    %Call monodirectional ionization function - dispersion (input var.
        disp ==1)
    if disp == 1;

        %assume monodirectional flux with 0 degrees incidence
        iangle = 0;

        %use dummy iangle_N value of 45 degrees - can be anything
        iangle_N = 45;

       [q_angle, test_check] = ionization_rate . . .
                           (F0,L_msis,E,spt,spc,. . .
                              alt_mass_density_fud,iangle, iangle_N);

        %must un-normalize q_angle because ionization_rate normalizes
        for isotropic flux
        %unnormalize q_angle by N based on size of the solid angle of
        annulus
        iangle_min = iangle;
        iangle_max = iangle + 1;
        N = (cosd(iangle_min) - cosd(iangle_max))/(1-cosd(iangle_N));

        q = q_angle/N;

    elseif disp == 2;

        %assume isotropic flux between 0 and isotropic_max degrees
        incidence
        iangle = [0:isotropic_max]';
        iangle_N = iangle(end);

        %initialize q
        q = zeros(L_msis,1);

        %loop over angles
        L_iangle = length(iangle(:,1));

        for i = 1:L_iangle;
            [q_angle, test_check] = ionization_rate . .
                            (F0,L_msis,E,spt,spc, . . .
                            alt_mass_density_fud,iangle(i,1),iangle_N);

            %add ionization rates from each angle to total q
            q = q + q_angle;
```

```
        end;
    end;

    %create output array with altitude and q
    q = horzcat([0:200]',q);


%%  *******  END OF MAIN FUNCTION *******



%% Ionization Rate as a function of angle
function[q_angle, test_check] = ionization_rate . . .
                 (F0,L_msis,E,spt,spc,. . .
                 alt_mass_density_fud,iangle,iangle_N)
%This function will calculate an ionization rate as a function of
%altitude give an initial angle of incidence, iangle;
%iangle will be the minimum angle of incidence

    %define length of F0 electron flux array
    L_F0 = length(F0(:,1));

    %initialize Energy_deposition, Electron_Flux and Ionization arrays
    E_dep = zeros(L_msis,L_F0 + 1);
    EE    = zeros(L_msis,L_F0);
    Q     = zeros(L_msis,L_F0 + 1);

    EE(1,:) = F0(:,1);

    %Define Ionization Energy I_energy =  35eV in keV
    I_energy = 35.0E-3;

    %transform E,spt,spc from MeV and MeV cm^2/g to keV and keV cm^2/g
    E   = E*1E3;
    spt = spt*1E3;
    spc = spc*1E3;

    %make initial interpolated spc and spt arrays
      spc_int(F) and spt_int(F)
    X     = E;
    Y_spt = spt;
    Y_spc = spc;
    Xi    = F0(:,1);

    spt_int = interp1(X,Y_spt,Xi);
    spc_int = interp1(X,Y_spc,Xi);


    %define iangle_step iangle_min, iangle_max,
            iangle_ave (all in degrees)
    iangle_step = 1;
    iangle_min = iangle;
    iangle_max = iangle + iangle_step;
    iangle_ave = iangle + iangle_step/2;
```

```
%loop over altitude and          energies
for i = 2:L_msis;

    %delta Z = integral of mass density between
    %assume a linear relationship
    rho_i       = alt_mass_density_fud(i,2);
    rho_iminus1 = alt_mass_density_fud(i - 1,2);

    delta_Z = mean([rho_iminus1,rho_i])*1E5/cosd(iangle_ave);


    %loop over energies in incident flux spectra
    for j = 1:L_F0;

        %electron stopping power
        spt_j     = spt_int(j);
        spc_j     = spc_int(j);


        %energy deposited through collisions
        E_dep_j    = spc_j*delta_Z;
        E_dep(i,j) = E_dep_j;

        %Energy in jth energy bin
        E_jminus1 = EE(i-1,j);

        E_j = E_jminus1 - spt_j*delta_Z;

        %check for negative energy
        if E_j >= 0;
            EE(i,j) = E_j;
        else
            EE(i,j) = 0;
            E_dep_j = EE(i-1,j);
            E_dep(i,j) = E_dep_j;
        end


        %ionization through collisions
        Q_j    = E_dep_j/I_energy;
        Q(i,j) = Q_j;

    end;

    %normalize q_angle by N based on size of the
        solid angle of annulus
    N = (cosd(iangle_min) - cosd(iangle_max))/(1-cosd(iangle_N));



    %combine Flux and Q and sum over all energy bins in last column
    E_dep(i,end) = F0(:,2)'*E_dep(i,1:end-1)';
    E_dep(i,end) = E_dep(i,end)*N;

    Q(i,end) = F0(:,2)'*Q(i,1:end-1)';
    Q(i,end) = Q(i,end)*N;
```

```
        %make interpolated spc and spt arrays
            spc_int(F) and spt_int(F) for new energy spectrum
        X     = E;
        Y_spt = spt;
        Y_spc = spc;
        Xi    = EE(i,:)';

        spt_int = interp1(X,Y_spt,Xi);
        spc_int = interp1(X,Y_spc,Xi);


    end;

    %arrange q_angle for output
    q_angle = Q(:,end)*1E-5;
    q_angle = flipud(q_angle);



%% Flux-Energy Function
function[F] = flux_energy(e_min, epoch)
%
%This function will produce an array for flux as a function of energy
for given balloon
%
%                                                    #/cm2/sec
%   1 = flt2s 17:12-17:38 UT  monoenergetic 2.8MeV   400
%   2 = flt2s 17:12-17:38 UT  E-folding     830keV   1277 >500 keV
%   3 = flt3s 17:14-18:00 UT  E-folding     1500keV  2180 >500 keV
%   4 = flt2s 18:44-19:09 UT  monoenergetic 2.7MeV   1100
%   5 = flt2s 18:44-19:09 UT  E-folding     800keV   5760 >500 keV
%   6 = flt3s 18:33-18:41 UT  E-folding     780keV   8650 >500 keV
%   7 = flt3s 18:44-18:55 UT  E-folding     820keV   6000 >500 keV
%


    %initialize flux (F) array
    e_step = 1;
    energy = [e_min:e_step:10000]';
    L_energy = length(energy);

    F = zeros(L_energy,2);
    F(:,1) = energy;


    %determine epoch and calculate Flux vs energy
    if epoch == 1;
        display('Epoch1 = flt2s 17:12-17:38 UT  monoenergetic 2.8MeV
                                                    400 #/cm2/sec');
        F_loc = find(F(:,1) == 2800);
        F(F_loc,2) = 400;

    elseif epoch == 2;
        display('Epoch2 = flt2s 17:12-17:38 UT  E-folding     830keV
                                              1277 >500 keV #/cm2/sec');
```

```
    for i = 1:L_energy;
        C  = 2.81;
        E0 = 830;
        F(i,2) = e_step * C * exp(-energy(i,1)/E0);
    end;

elseif epoch == 3;
    display('Epoch3 = flt3s 17:14-18:00 UT  E-folding     1500keV
                                          2180 >500 keV #/cm2/sec');
    for i = 1:L_energy;
        C  = 2.03;
        E0 = 1500;
        F(i,2) = e_step * C * exp(-energy(i,1)/E0);
    end;

elseif epoch == 4;
    display('Epoch4 = flt2s 18:44-19:09 UT  monoenergetic 2.7MeV
                                             1100 #/cm2/sec');
    F_loc = find(F(:,1) == 2700);
    F(F_loc,2) = 1100;

elseif epoch == 5;
    display('Epoch5 = flt2s 18:44-19:09 UT  E-folding     800keV
                                           5760 >500 keV #/cm2/sec');
    for i = 1:L_energy;
        C  = 13.45;
        E0 = 800;
        F(i,2) = e_step * C * exp(-energy(i,1)/E0);
    end;

elseif epoch == 6;
    display('Epoch6 = flt3s 18:33-18:41 UT  E-folding     780keV
                                          8650 >500 keV #/cm2/sec');
    for i = 1:L_energy;
        C  = 21.05;
        E0 = 780;
        F(i,2) = e_step * C * exp(-energy(i,1)/E0);
    end;

elseif epoch == 7;
    display('Epoch7 = flt3s 18:44-18:55 UT  E-folding     820keV
                                           6000 >500 keV #/cm2/sec');
    for i = 1:L_energy;
        C  = 13.47;
        E0 = 820;
        F(i,2) = e_step * C * exp(-energy(i,1)/E0);
    end;
end;
```

Appendix E: Electric Field and REP Correlation Study Results

Table E-1 Full correlation study results between 17:00 UT and 19:30 UT on January 21st, 2005.

1700-1930	Ee2	Es2	Em2	Et2	lc12	lc22	lc32	lc42	Ee3	Es3	Em3	Et3	lc13	lc23	lc33	lc43
Ee2	--	0.55	0.66	0.67	0.19	0.19	0.17	0.14	-0.33	0.32	0.34	-0.23	0.36	0.34	0.32	0.29
Es2	0.55	--	0.97	0.23	--	--	--	--	-0.18	0.66	0.69	--	--	--	--	--
Em2	0.66	0.97	--	0.23	--	--	--	--	-0.18	0.66	0.68	-0.16	0.16	--	--	--
Et2	0.67	0.23	0.23	--	0.14	0.14	0.14	0.13	-0.27	--	--	--	0.31	0.34	0.36	0.38
lc12	0.19	--	--	0.14	--	1.00	0.98	0.95	--	--	--	-0.16	0.34	0.32	0.30	0.25
lc22	0.19	--	--	0.14	1.00	--	0.99	0.96	--	--	--	-0.15	0.33	0.31	0.29	0.23
lc32	0.17	--	--	0.14	0.98	0.99	--	0.99	--	--	--	-0.15	0.29	0.27	0.25	0.19
lc42	0.14	--	--	0.13	0.95	0.96	0.99	--	--	--	--	-0.15	0.24	0.22	0.20	0.15
Ee3	-0.33	-0.18	-0.18	-0.27	--	--	--	--	--	--	--	0.59	-0.31	-0.30	-0.29	-0.28
Es3	0.32	0.66	0.66	--	--	--	--	--	--	--	0.98	-0.15	--	--	--	-0.14
Em3	0.34	0.69	0.68	--	--	--	--	--	--	0.98	--	--	--	--	--	-0.15
Et3	-0.23	--	-0.16	--	-0.16	-0.15	-0.15	-0.15	0.59	-0.15	--	--	-0.38	-0.39	-0.38	-0.36
lc13	0.36	--	0.16	0.31	0.34	0.33	0.29	0.24	-0.31	--	--	-0.38	--	0.99	0.95	0.90
lc23	0.34	--	--	0.34	0.32	0.31	0.27	0.22	-0.30	--	--	-0.39	0.99	--	0.99	0.95
lc33	0.32	--	--	0.36	0.30	0.29	0.25	0.20	-0.29	--	--	-0.38	0.95	0.99	--	0.98
lc43	0.29	--	--	0.38	0.25	0.23	0.19	0.15	-0.28	-0.14	-0.15	-0.36	0.90	0.95	0.98	--

Table E-2 Full correlation study results between 17:12 UT and 17:27 UT on January 21st, 2005.

1712-1727	Ee2	Es2	Em2	Et2	lc12	lc22	lc32	lc42	Ee3	Es3	Em3	Et3	lc13	lc23	lc33	lc43
Ee2	--	--	0.89	0.67	--	--	--	--	-0.72	-0.77	-0.50	-0.84	--	--	--	--
Es2	--	--	0.52	-0.69	--	--	--	--	--	--	--	--	--	--	--	--
Em2	0.89	0.52	--	--	--	--	--	--	-0.71	-0.72	-0.45	-0.79	--	--	--	--
Et2	0.67	-0.69	--	--	--	--	--	--	--	-0.46	--	-0.49	--	--	--	--
lc12	--	--	--	--	--	1.00	0.99	0.98	--	--	-0.64	--	--	--	--	--
lc22	--	--	--	--	1.00	--	0.99	0.99	--	--	-0.63	--	--	--	--	--
lc32	--	--	--	--	0.99	0.99	--	1.00	--	--	-0.61	--	--	--	--	--
lc42	--	--	--	--	0.98	0.99	1.00	--	--	--	-0.59	--	--	--	--	--
Ee3	-0.72	--	-0.71	--	--	--	--	--	--	0.90	0.66	0.97	--	--	--	--
Es3	-0.77	--	-0.72	-0.46	--	--	--	--	0.90	--	0.86	0.96	--	--	--	--
Em3	-0.50	--	-0.45	--	-0.64	-0.63	-0.61	-0.59	0.66	0.86	--	0.71	--	--	--	--
Et3	-0.84	--	-0.79	-0.49	--	--	--	--	0.97	0.96	0.71	--	--	--	--	--
lc13	--	--	--	--	--	--	--	--	--	--	--	--	--	1.00	0.98	0.93
lc23	--	--	--	--	--	--	--	--	--	--	--	--	1.00	--	0.99	0.95
lc33	--	--	--	--	--	--	--	--	--	--	--	--	0.98	0.99	--	0.98
lc43	--	--	--	--	--	--	--	--	--	--	--	--	0.93	0.95	0.98	--

Table E-3 Full correlation study results between 18:45 UT and 19:00 UT on January 21st, 2005.

1845-1900	Ee2	Es2	Em2	Et2	lc12	lc22	lc32	lc42	Ee3	Es3	Em3	Et3	lc13	lc23	lc33	lc43
Ee2	--	--	0.79	0.72	0.72	0.72	0.70	0.60	--	--	--	--	--	0.46	0.52	0.51
Es2	--	--	0.88	--	0.64	0.63	0.53	--	--	--	--	--	0.74	0.75	0.76	0.77
Em2	0.79	0.88	--	--	0.79	0.78	0.71	0.56	--	--	--	--	0.63	0.70	0.74	0.75
Et2	0.72	--	--	--	--	--	--	--	--	--	--	--	--	--	--	--
lc12	0.72	0.64	0.79	--	--	1.00	0.97	0.90	--	--	--	--	0.66	0.73	0.77	0.77
lc22	0.72	0.63	0.78	--	1.00	--	0.98	0.91	--	--	--	--	0.64	0.72	0.76	0.76
lc32	0.70	0.53	0.71	--	0.97	0.98	--	0.97	--	--	--	--	0.53	0.60	0.65	0.65
lc42	0.60	--	0.56	--	0.90	0.91	0.97	--	--	--	--	--	--	--	0.46	0.47
Ee3	--	--	--	--	--	--	--	--	--	--	--	--	--	--	--	--
Es3	--	--	--	--	--	--	--	--	--	--	--	--	--	--	--	--
Em3	--	--	--	--	--	--	--	--	--	--	--	--	--	--	--	--
Et3	--	--	--	--	--	--	--	--	--	--	--	--	--	--	--	--
lc13	--	0.74	0.63	--	0.66	0.64	0.53	--	--	--	--	--	--	0.99	0.97	0.98
lc23	0.46	0.75	0.70	--	0.73	0.72	0.60	--	--	--	--	--	0.99	--	1.00	1.00
lc33	0.52	0.76	0.74	--	0.77	0.76	0.65	0.46	--	--	--	--	0.97	1.00	--	1.00
lc43	0.51	0.77	0.75	--	0.77	0.76	0.65	0.47	--	--	--	--	0.98	1.00	1.00	--

Table E-4 Full correlation study results between 17:00 UT and 19:30 UT on January 21st, 2005, omitting the impulse events.

1700-1930C	Ee2	Es2	Em2	Et2	Ic12	Ic22	Ic32	Ic42	Ee3	Es3	Em3	Et3	Ic13	Ic23	Ic33	Ic43
Ee2	--	0.58	0.67	0.66	--	--	--	-0.14	-0.33	0.31	0.34	-0.24	0.33	0.31	0.29	0.27
Es2	0.58	--	0.98	0.24	-0.27	-0.20	-0.16	--	-0.19	0.67	0.69	--	--	--	--	--
Em2	0.67	0.98	--	0.23	-0.22	-0.16	--	--	-0.20	0.66	0.67	-0.17	0.14	--	--	--
Et2	0.66	0.24	0.23	--	--	--	--	--	-0.26	--	--	--	0.31	0.35	0.38	0.40
Ic12	--	-0.27	-0.22	--	--	0.99	0.95	0.91	--	-0.26	-0.30	-0.26	0.21	0.24	0.26	0.27
Ic22	--	-0.20	-0.16	--	0.99	--	0.99	0.96	--	-0.23	-0.27	-0.25	0.19	0.22	0.25	0.26
Ic32	--	-0.16	--	--	0.95	0.99	--	0.99	--	-0.19	-0.23	-0.23	0.15	0.19	0.21	0.22
Ic42	-0.14	--	--	--	0.91	0.96	0.99	--	--	-0.16	-0.19	-0.18	--	0.15	0.17	0.16
Ee3	-0.33	-0.19	-0.20	-0.26	--	--	--	--	--	--	--	0.59	-0.33	-0.33	-0.32	-0.31
Es3	0.31	0.67	0.66	--	-0.26	-0.23	-0.19	-0.16	--	--	0.98	-0.16	--	--	--	-0.16
Em3	0.34	0.69	0.67	--	-0.30	-0.27	-0.23	-0.19	--	0.98	--	-0.14	--	--	-0.14	-0.18
Et3	-0.24	--	-0.17	--	-0.26	-0.25	-0.23	-0.18	0.59	-0.16	-0.14	--	-0.40	-0.41	-0.41	-0.38
Ic13	0.33	--	0.14	0.31	0.21	0.19	0.15	--	-0.33	--	--	-0.40	--	0.99	0.95	0.90
Ic23	0.31	--	--	0.35	0.24	0.22	0.19	0.15	-0.33	--	--	-0.41	0.99	--	0.99	0.95
Ic33	0.29	--	--	0.38	0.26	0.25	0.21	0.17	-0.32	--	-0.14	-0.41	0.95	0.99	--	0.98
Ic43	0.27	--	--	0.40	0.27	0.26	0.22	0.16	-0.31	-0.16	-0.18	-0.38	0.90	0.95	0.98	--

VITA

Michael Kokorowski, son of Stan and Therese Kokorowski, grew up in West Hills, California. He graduated from Chaminade College Preparatory in 1998. Eager to move away from the Los Angeles area, Michael headed north to attend the University of California at Berkeley. While at Berkeley, he worked in the Ion Beam Technology group at Lawrence Berkeley National Laboratory studying the production of negative boron ions from a multi-cusp plasma source. After receiving a Bachelor's degree in Physics (2002), Michael continued further north to attend the University of Washington. He was a member of the Space Physics group in the Earth and Space Science Department from 2002 until the completion of his Ph.D in 2008. Michael accepted a position in the Mission Environments group at the Jet Propulsion Laboratory in Pasadena, California in 2008.